

# The University of Sheffield



## Investigation of High Speed Permanent Magnet Motors

**Jie Ma**

**A thesis submitted for the degree of Doctor of Philosophy**

Department of Electronic and Electrical Engineering

The University of Sheffield

Sheffield, UK

**February 2019**

# ABSTRACT

This thesis investigates the electromagnetic performance of high speed permanent magnet (PM) motors, with particular reference to the mitigation of parasitic effects, the influence of key design parameters and the improved optimization method.

In order to reduce the parasitic effects, i.e. unbalanced magnetic force (UMF) and on-load magnet eddy current loss which are the most undesirable drawbacks of 3-slot/2-pole high speed PM motors, the motors with several different types of auxiliary slots are investigated and compared. It shows that the auxiliary slots with the optimal size and position can reduce the rated on-load UMF and the rated on-load magnet eddy current loss over 95% and 80%, respectively, with only a slight sacrifice of output torque. In addition, the influence of working conditions, drive modes, slot opening widths and rotating directions on the parasitic effects is studied as well. Moreover, the proposed magnet eddy current loss reduction method can be also applied to other motors with different slot/pole number combinations and winding configurations.

In addition, as one of the most important design parameters, the influence of magnet thickness is investigated comprehensively. It shows that 3-slot/2-pole high speed PM motors with thicker magnet can benefit from lower on-load UMF, lower magnet eddy current loss as well as better demagnetization withstand capability. The influence of magnet thickness on other performances, e.g. the flux linkage, the back electromotive force (EMF) and the inductance, etc., is also studied.

Finally, a new analytical optimization method is presented. Different loss constraints are taken into account in the optimisation, i.e. stator loss limitation only, rotor loss limitation only and both stator and rotor loss limitations. It shows that these loss constraints can significantly affect the optimal split ratio and the motor performance. By considering the influence of rotor loss, especially the rotor eddy current loss, the optimal split ratio is increased significantly in some scenarios. The output torque is calculated analytically and the influences of several key design parameters on the optimal split ratio, e.g. the maximum stator flux density, slot/pole number combinations and magnet materials, etc., are investigated in details.

## **ACKNOWLEDGEMENTS**

I would like to express my deepest gratitude to my supervisor, Professor Zi-Qiang Zhu, for his invaluable guidance, patience and continuous encouragement throughout the duration of my PhD study.

I would also like to thank all members of Electrical Machines and Drives Group for their support and inspired discussion. Particularly, I would like to extend my sincere thanks to Mr. H. Y. Li, Mr. Y. Liu, Mrs Y. W. Shi and Mr. L. Wang who give me a lot of help for both the academy and the daily life. I would like to thank Mr. John A. Wilkinson, Mr. Lawrence Obodo and Mr. Karl Rotchell for their help with the prototype machine construction.

I would also like to thank Welling Motor Manufacturing Co., Ltd, China, for their technical support and the internship opportunity.

Finally, a special thanks to my parents for their love and support in these years which give me the faith and the courage to face and overcome all the difficulties.

# CONTENTS

<b>ABSTRACT</b> .....	<b>I</b>
<b>ACKNOWLEDGEMENTS</b> .....	<b>II</b>
<b>CONTENTS</b> .....	<b>III</b>
<b>NOMENCLATURE</b> .....	<b>VIII</b>
<b>CHAPTER 1 GENERAL INTRODUCTION</b> .....	<b>1</b>
1.1 Introduction.....	1
1.2 Review of High Speed Machines .....	2
1.2.1 Induction Machines.....	2
1.2.2 Reluctance Machines .....	4
1.2.3 Permanent Magnet Machines.....	6
1.3 Design Considerations Applicable to High Speed Machines .....	24
1.3.1 Mechanical Consideration .....	24
1.3.2 Thermal Consideration.....	27
1.4 Optimization Methods in High Speed Machines .....	32
1.5 Scope of Research and Contribution of the Thesis .....	33
<b>CHAPTER 2 UNBALANCED MAGNETIC FORCE MITIGATION IN HIGH SPEED PM MACHINES BY USING AUXILIARY SLOTS</b> .....	<b>37</b>
2.1 Introduction.....	37
2.2 UMF of Conventional 3-Slot/2-Pole Machines .....	38
2.2.1 Prototype .....	38
2.2.2 UMF Decomposition in Conventional 3-Slot/2-Pole Machines.....	39
2.3 UMF Mitigation in 3-Slot/2-Pole Machines .....	44
2.3.1 Auxiliary Slots in Middle of Stator Tooth Having Optimal Size .....	44
2.3.2 Auxiliary Slots with Optimal Size and Position .....	49
2.4 Electromagnetic Performance Comparison .....	54



2.4.1 Flux Linkage and Back EMF .....	54
2.4.2 Torque Characteristics .....	56
2.5 Influence of Working Conditions .....	58
2.5.1 Comparison of Torques and UMFs in Machines with and without Auxiliary Slots.....	58
2.5.2 Influence of Current Amplitude on Machine 3 .....	61
2.5.3 Influence of Current Angle on Machine 3 .....	62
2.6 Influence of Slot Opening Width .....	64
2.6.1 Influence of Slot Opening Width on UMFs in Conventional Machines .....	65
2.6.2. Effectiveness of Different Auxiliary Slots on Rated On-Load UMF Reduction in Machines Having Different Slot Opening Widths .....	67
2.7 Influence of Rotating Direction .....	70
2.7.1 Influence of Rotating Direction on Machine 3 .....	71
2.7.2 Rated On-Load UMF Mitigation in Bidirectional Rotating Machines .....	76
2.7.3 Influence of Working Conditions .....	80
2.8 Influence of Drive Mode.....	82
2.9 Experimental Validation .....	86
2.9.1 Prototype Machines and Test Rig .....	86
2.9.2 Back EMF Waveforms .....	87
2.9.3 Static Torque Waveforms .....	88
2.9.4 UMF waveforms .....	89
2.10 Summary .....	94
<b>CHAPTER 3 MAGNET EDDY CURRENT LOSS REDUCTION IN HIGH SPEED PM MACHINES BY USING AUXILIARY SLOTS .....</b>	<b>95</b>
3.1 Introduction.....	95
3.2 Field Analysis in 3-slot/2-pole Permanent Magnet Machines.....	97
3.2.1 Prototype .....	97

3.2.2 Open Circuit Air Gap Flux Density .....	98
3.2.3 Armature Reaction Air-Gap Flux Density .....	99
3.2.4 Resultant Air-Gap Flux Density .....	102
3.3 Effect of Auxiliary Slots on Magnet Eddy Current Loss .....	102
3.4 Machine Performance .....	113
3.4.1 Flux Linkage and Back EMF .....	113
3.4.2 Torque Characteristics .....	114
3.5 Effect of Working Condition .....	115
3.6 Influence of Airgap Length.....	118
3.7 Influence of Drive Mode.....	122
3.8 Influence of Slot/Pole Number Combinations .....	126
3.5 Experimental Validation .....	133
3.6 Summary .....	137
<b>CHAPTER 4 INFLUENCE OF MAGNET THICKNESS ON ELECTROMAGNETIC PERFORMANCE OF HIGH SPEED PM MACHINES</b> .....	<b>139</b>
4.1 Introduction.....	139
4.2 Prototype Machines .....	141
4.3 Effect of Magnet Thickness on Magnetic Fields .....	142
4.4 Effect of Magnet Thickness on Machine Performance.....	147
4.4.1 Phase Flux Linkage and Phase Back EMF .....	147
4.4.2 On-load Torque Characteristics .....	150
4.4.3 Unbalanced Magnetic Force .....	151
4.4.4 Self and Mutual Inductances.....	155
4.4.5 Stator Iron Loss and Magnet Eddy Current Loss.....	156
4.4.6 Demagnetization .....	160
4.4.7 Economic Issue .....	162

4.5 Experimental Validation .....	164
4.6 Summary .....	168
<b>CHAPTER 5 OPTIMIZATION OF SPLIT RATIO IN SMALL HIGH SPEED PM MACHINES CONSIDERING DIFFERENT LOSS LIMITATIONS.....</b>	<b>170</b>
5.1 Introduction.....	170
5.2 Split Ratio Optimization in Small High Speed Machine Considering Stator Loss Limitation Only.....	172
5.2.1 Loss Calculation.....	172
5.2.2 Torque Calculation.....	176
5.2.3 Influence of Key Design Parameters .....	180
5.2.4 FE Validation .....	191
5.3. Split Ratio Optimization in Small High Speed Machine Considering Rotor Loss Limitation Only.....	193
5.3.1 Loss Calculation.....	193
5.3.2 Torque Calculation Considering Rotor Loss Only .....	195
5.4 Split Ratio Optimization in Small High Speed Machine Considering Both Stator and Rotor Loss Limitations.....	197
5.4.1 Optimal split ratio Calculation and Its Characteristics .....	197
5.4.2 Influence of Design Parameters .....	201
5.4.3 FE Validation .....	215
5.4.4 General Determination of Optimal Split Ratio in Small High Speed Permanent Magnet Machine Considering Both Stator and Rotor Loss .....	217
5.5. Summary .....	218
<b>CHAPTER 6 GENERAL CONCLUSIONS AND FUTURE WORK.....</b>	<b>220</b>
6.2 Future Work .....	226
<b>REFERENCES .....</b>	<b>227</b>
<b>APPENDIX I FROZEN PERMEABILITY METHOD .....</b>	<b>251</b>
<b>APPENDIX II STATIC TORQUE MEASURING METHOD .....</b>	<b>252</b>

<b>APPENDIX III CAD DRAWINGS OF PROTOTYPES .....</b>	<b>253</b>
<b>APPENDIX IV CALCULATION OF THE OPTIMAL SLEEVE THICKNESS .....</b>	<b>256</b>
<b>APPENDIX V PUBLICATION RESULTED FROM PHD STUDY .....</b>	<b>260</b>

# NOMENCLATURE

## *Symbol*

$A_a$	Airgap cross section area (m <sup>2</sup> )
$A_{coil}$	Conductor area (m <sup>2</sup> )
$A_{fe}$	Stator iron area (m <sup>2</sup> )
$ah_t$	Auxiliary slot depth (m)
$A_s$	Slot area (m <sup>2</sup> )
$as_o$	Auxiliary slot width (m)
$B$	Flux density (T)
$B_{ABC,har,aux}$	Armature field airgap flux density caused by auxiliary slots (T)
$B_{ar}$	Radial airgap flux density of armature field (T)
$B_{at}$	Tangential airgap flux density of armature field (T)
$B_g$	Airgap flux density of BLDC machines (T)
$B_{gmax}$	Peak value of airgap flux density (T)
$B_{har,aux}$	Resultant airgap flux density harmonics caused by auxiliary slots (T)
$B_{max}$	Maximum stator flux density (T)
$B_{mr}$	Radial airgap flux density of PM field (T)
$B_{mt}$	Tangential airgap flux density of PM field (T)
$B_{PM,har,aux}$	PM field airgap flux density harmonics caused by auxiliary slots (T)
$B_r$	Magnet remanence under room temperature (T)
$B_{r,temp}$	Magnet remanence with specific temperature (T)
$B_{radial}$	Radial airgap flux density (T)
$B_{resultant}$	On-load airgap flux density (T)
$b_t$	Tooth width (m)
$B_{tan}$	Tangential airgap flux density (T)
$C_a$	Coolant specific heat capacity (J/(kg·°C))
$C_f$	Friction coefficient
$D_{ag}$	Diameter of middle of equivalent airgap (m)
$Direction_{ar}$	Armature field direction
$Direction_{eddy}$	Rotor eddy current direction
$Direction_{PM}$	PM field direction

$Direction_{rotating}$	Rotating direction
$D_{mo}$	Magnet outer diameter (m)
$D_{sh}$	Shaft diameter (m)
$D_{si}$	Stator inner diameter (m)
$D_{so}$	Stator outer diameter (m)
$E$	Young's modulus (Gpa)
$f$	Electrical frequency (Hz)
$F$	Unbalanced magnetic force (N)
$F_1$	Unbalanced magnetic force caused by self-interaction of PM field (N)
$F_1'$	Unbalanced magnetic force caused by self-interaction of PM field considering the effect of auxiliary slots (N)
$F_2$	Unbalanced magnetic force caused by mutual interaction between PM and armature fields (N)
$F_2'$	Unbalanced magnetic force caused by mutual interaction between PM and armature fields considering the effect of auxiliary slots (N)
$F_{2r}$	Radial component of F2 (N)
$F_{2r1}$	Unbalanced magnetic force caused by $\sigma_{2,1}$
$F_{2r2}$	Unbalanced magnetic force caused by $\sigma_{2,2}$
$F_{2t}$	Tangential component of F2 (N)
$F_{2t1}$	Unbalanced magnetic force caused by $\tau_{2,1}$
$F_{2t2}$	Unbalanced magnetic force caused by $\tau_{2,2}$
$F_3$	Unbalanced magnetic force caused by self-interaction of armature field (N)
$F_a$	Magneto-motive force of phase A (A)
$F_{ABC}$	Magneto-motive force of armature field (A)
$F_b$	Magneto-motive force of phase B (A)
$F_c$	Magneto-motive force of phase C (A)
$F_{PM}$	Magneto-motive force of PM field (A)
$F_x$	X-direction unbalanced magnetic force (N)
$F_y$	Y-direction unbalanced magnetic force (N)
$h_c$	Stator back-iron thickness (m)

$H_{PM}$	Distance between the radial position of magnet and the central of shaft (m)
$h_{rotor}$	Rotor overall heat transfer coefficient (W/(m <sup>2</sup> ·°C))
$h_{stator}$	Stator overall heat transfer coefficient (W/(m <sup>2</sup> ·°C))
$h_t$	Tooth tip height (m)
$I$	Phase current (A)
$I_d$	D-axis phase current
$I_{max}$	Maximum phase current (A)
$I_q$	Q-axis phase current
$I_{source}$	Current of current source (A)
$J$	Eddy current density (W/m <sup>2</sup> )
$k_a$	Coefficient depending on the slot/pole number combinations
$K_c$	Classic eddy current loss coefficient
$K_{dp}$	Winding factor
$K_e$	Excess loss coefficient (W/m <sup>2</sup> )
$K_h$	Hysteresis loss coefficient (W/m <sup>2</sup> )
$K_s$	Filling factor
$l_a$	Active length (m)
$l_e$	End winding length (m)
$l_g$	Airgap length (m)
$l_{sleeve}$	Sleeve thickness (m)
$m_{fe}$	Stator iron mass (kg/m <sup>3</sup> )
$N_s$	Number of stator tooth
$N_w$	Number of turns per phase
$P$	Permeance distribution (H)
$p$	Number of pole pairs
$P_0$	DC permeance component (H)
$P_{cu}$	Copper loss (W)
$P_{fe}$	Stator iron loss (W)
$P_{knr}$	Permeance coefficient for $knr^{\text{th}}$ harmonic (H)
$P_{rotor,eddy}$	Rotor eddy current loss (W)
$P_{rotor,lim}$	Maximum allowed rotor loss (W)
$P_{stator,lim}$	Maximum allowed stator loss (W)

$P_{windage}$	Windage loss (W)
$r$	Radius (m)
$Re_a$	Reynolds number for the axial flow
$Re_\delta$	Couette Reynolds number for the tangential flow
$r_{rotor}$	Rotor outer radius (m)
$s_o$	Slot opening width (m)
$t$	Time (s)
$T$	Output torque (Nm)
$THD$	Total harmonic distortion (%)
$u$	Displacement (m)
$V$	Motor volume (m <sup>3</sup> )
$v_a$	Airgap coolant axial speed (m/s)
$W_{fe}$	Iron loss density (W/kg)
$\alpha$	Shift angle of auxiliary slots (Mech. Deg.)
$\beta$	Current angle (Elec. Deg.)
$\gamma$	Flux density ratio
$\delta$	Skin depth (m)
$\delta_{fit}$	Pre fit (m)
$\theta$	Rotor position (Mech. Deg.)
$\theta_0$	Phase difference (Mech. Deg.)
$\lambda$	Split ratio
$\mu$	Permeability (H/m)
$\mu_0$	Vacuum permeability (H/m)
$\mu_{air}$	Air dynamic viscosity (Pa·s)
$\rho$	Density (Kg/m <sup>3</sup> )
$\rho_{air}$	Air mass density (kg/m <sup>3</sup> )
$\rho_{fe}$	Iron mass density (kg/m <sup>3</sup> )
$\rho_{r,c}$	Resistance of conductor ( $\Omega/m$ )
$\sigma$	Radial traveling stress (Pa)
$\sigma_1$	Radial traveling stress caused by self-interaction of PM field (Pa)
$\sigma_2$	Radial traveling stress caused by mutual interaction between PM and armature fields (Pa)
$\sigma_{2,1}$	Radial traveling stress caused by $B_{mr}$ and $B_{ar}$



$\sigma_{2,2}$	Radial traveling stress caused by $B_{mt}$ and $B_{at}$
$\sigma_3$	Radial traveling stress caused by self-interaction of armature field (Pa)
$\sigma_e$	Electrical conductivity (S/m)
$\sigma_{R,lim}$	Maximum normal stress in the inner surface of magnet
$\sigma_{radial}$	Radial stress (Pa)
$\sigma_U$	Yield strength (Pa)
$\sigma_{ref}^{vM}$	Von-Mises reference stress (Pa)
$\sigma_\theta$	Tangential stress (Pa)
$\tau$	Circumferential traveling stress (Pa)
$\tau_1$	Tangential traveling stress due to self-interaction of PM field (Pa)
$\tau_2$	Tangential traveling stress caused by mutual interaction between PM and armature fields (Pa)
$\tau_{2,1}$	Tangential traveling stress caused by $B_{mr}$ and $B_{at}$
$\tau_{2,2}$	Tangential traveling stress caused by $B_{mt}$ and $B_{ar}$
$\tau_3$	Tangential traveling stress due to self-interaction of armature field (Pa)
$\nu$	Poisson's ratio
$\omega$	Electrical angular speed (rad/s)
$\Omega$	Angular velocity (rad/s)
$\omega_{mech}$	Rotor mechanical angular velocity (rad/s)
$\Delta T$	Sleeve emperature variation (°C)
$\Delta \tau_a$	Coolant temperature variation (°C)
$\Delta \tau_{rotor,max}$	Maximum allowed rotor temperature rise (°C)
$\Delta \tau_{stator,max}$	Maximum allowed stator temperature rise (°C)

### **Abbreviation**

BLAC	Brushless AC
BLDC	Brushless DC
CFD	Computational fluid dynamics
Co-Fe	Cobalt-iron
Dy	Dysprosium

EMF	Electromagnetic force
FE	Finite element
HSPM	High speed permanent magnet
IM	Induction machine
IPM	Interior permanent magnet
LPTN	Lumped-parameter thermal network
MMF	Magneto-motive force
MTPA	Maximum torque per ampere
NdFeB	Neodymium-iron-boron
PM	Permanent magnet
Si-Fe	Silicon-iron
SMC	Soft magnetic composite
SmCo	Samarium-cobalt
SPM	Surface mounted permanent magnet
SR	Switched-reluctance
SynR	Synchronous reluctance
UMF	Unbalanced magnetic force

# CHAPTER 1

## GENERAL INTRODUCTION

### 1.1 Introduction

In last decades, thanks to the development of converter and bearing technologies, high speed machines have been gaining popularities in academies and used in many industry applications. Since the output power in an electrical machine is proportional to the rotating speed and the volume, high speed machines can effectively increase the output power or reduce the size. Consequently, high speed machines become very competitive in numerous applications, e.g. flywheel energy storage systems [ACA96] [NAG06], heat pumps, blowers, centrifugal compressor [JAN07] [SOO00] [GIE12], micro turbines [GOL03], domestics and medical equipment applications [LEI11] [ZWY09]. Moreover, high speed machines can also offer a direct drive solution for some applications, e.g. power generation [ZYW05] [DAN08], which can increase the efficiency, reduce the weight and cost of the whole system.

In terms of the definition of high speed machines. The circumferential velocity of rotor outer surface is used as the criterion in [BIN07], which mainly considers the mechanical constrain. In contrast, the relationship between the output power and the rotating speed is employed as the definition in [RAH04] and [MAE95], which use an empirical equation to describe the speed limitation for the specific output power. Nevertheless, as stated in [BOR10], all definitions have their own merits and the selection mainly depends on the specific application.

This thesis will investigate the electromagnetic performance of high speed permanent magnet motors with due consideration of mechanical aspects.

This chapter will review the background and literatures for high speed machines comprehensively. Different types of high speed machines will be introduced at first including induction, reluctance and permanent magnet (PM) machines. The PM machine will be emphasized and its key design aspects will be reviewed systematically, e.g. stator and rotor structures, PM materials, magnetizations, sleeve materials and sleeve structures. Then, the key issues applicable to high speed machines will be introduced in next section, in which the mechanical and thermal considerations are emphasized. In addition, different design optimization methods for high speed

machines will also be introduced. Finally, the outline and the main contributions of this PhD thesis will be detailed.

## **1.2 Review of High Speed Machines**

There are many different types of electrical machines which can be applied to high speed applications, e.g. induction machines (IM), switched-reluctance (SR) machines, synchronous reluctance (SynR), and PM machines.

### **1.2.1 Induction Machines**

The IM is very popular in many high speed applications due to its robust structure and great economic performance. In terms of its rotor structures, the possible solid rotors are introduced at first which are shown in Fig. 1. 1 [GER14].

The IM with the smooth solid rotor shown in Fig. 1. 1 (a) is studied comprehensively in [BUM06] and [BUM06a]. Both analytical and numerical analyses are carried out for investigation and design guidance. It shows the smooth solid rotor has the simplest rotor structure and very low cost which are the main advantages. Nevertheless, the electromagnetic performance of IMs with the smooth solid rotor is relative poor due to the low steel electrical conductivity.

In contrast, the slitted solid rotor shown in Fig. 1. 1 (b) can offer higher output torque and efficiency. Moreover, the power factor can be also improved by introducing slits at a lower slip [PYR10] [AHO07] [HUP04] [IKE90]. It should be noticed that the design of rotor slits has significant influence on the machine performance. Both the number and the depth of slits should be optimized carefully. Nevertheless, the slitted solid rotor has relatively worse mechanical performance comparing with the smooth one. As a result, the electromagnetic and mechanical performance should be balanced when a slitted solid rotor is employed.

In addition, the solid rotor with coating layers shown in Fig. 1. 1 (c) is also a competitive candidate [PYR94], in which a low resistance layer, e.g. copper layer, is adopted at the outer surface of the solid rotor, so that the electromagnetic anisotropy can be introduced [GER14]. The machine performance can be increased further by using a double coating layers structure [SHA96], in which the selection of layer material and thickness should be optimized, since they can affect the torque and the power factor significantly. A top layer with higher permeability and a lower layer with higher conductivity are advised

to obtain decent machine performance. Nevertheless, it is reported that due to the existence of extra layer, the equivalent airgap length in this kind of IMs can be relatively larger, which can result in relatively lower power factor [GER14].

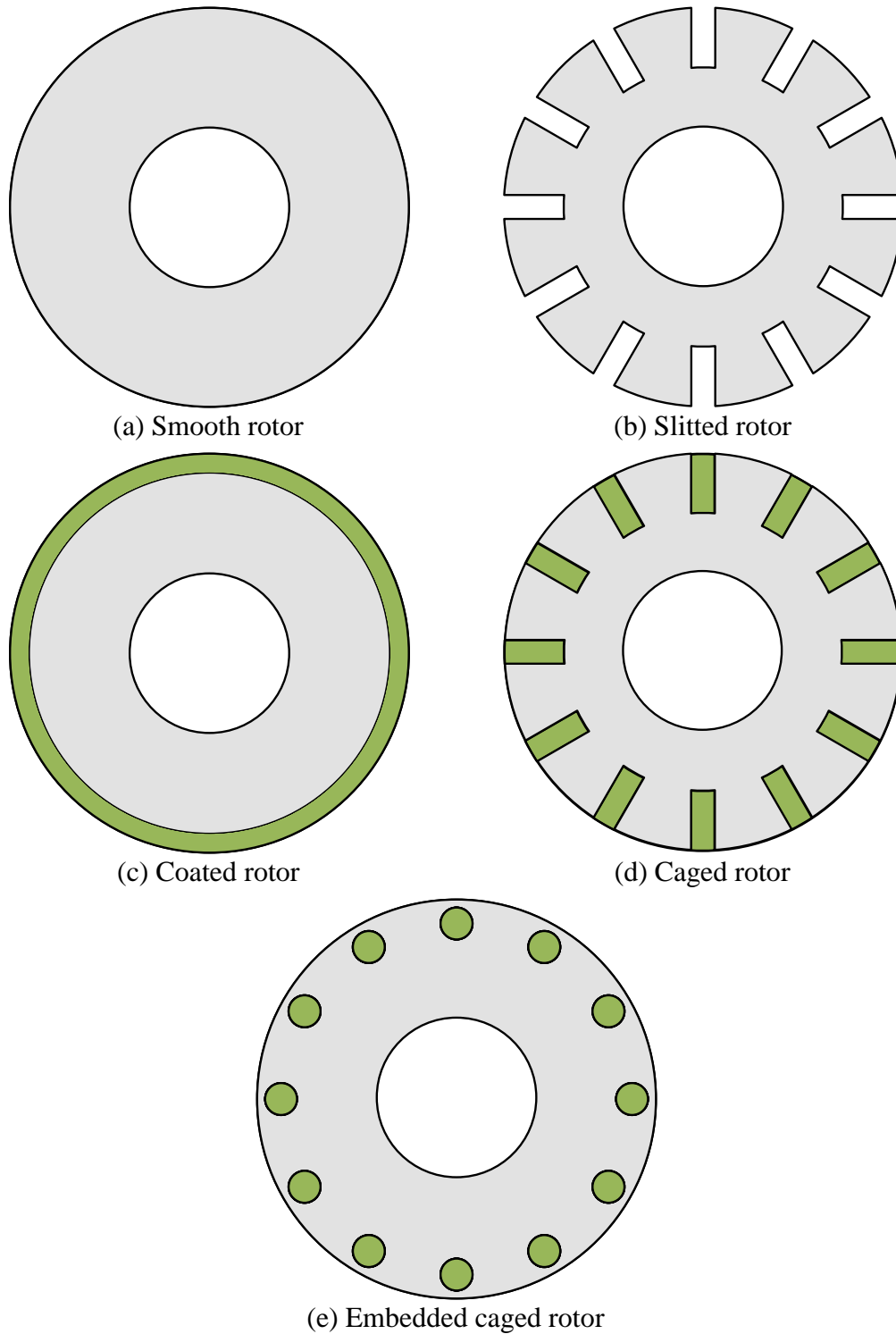


Fig. 1. 1 High speed IM solid rotor structures [GER14].

The solid rotor also can be equipped with a squirrel cage as shown in Fig. 1. 1 (d) and (e), which is investigated in [LAH00] and [PYR10]. Comparing with the rotor structures mentioned above, this rotor balances the electromagnetic and mechanical performances to a certain extent, and can offer the highest output torque. The main disadvantage of this kind of rotor is the complicated manufacture, especially the embedded caged one which needs to drill holes in a solid iron. Consequently, the cost of caged rotor is relative high.

In terms of the comparison among different IM rotors, slitted and caged rotors are compared comprehensively in [LAT09] [SAA94]. It shows the slitted rotor has much higher mechanical loss due to the increased surface roughness and lower output torque, which indicates the caged rotor is more favourable. Nevertheless, solid and coated rotors are used in the applications having the highest peripheral velocity due to the excellent mechanical performance [GER14]. However, it also shows that the caged rotor has much higher output torque as well as less loss comparing with the solid and coated rotors [LAH00]. Consequently, the caged rotor will be the best choice if power and efficiency are more important.

In [LAT09], solid and laminated caged rotors are compared in depth. The laminated rotor shares the same rotor structure comparing with the solid one except that the lamination is used. It shows the laminated rotor has much higher efficiency due to the significantly decreased rotor loss.

Several other literatures investigate the optimization and design of IMs with the laminated rotor. The rotor topology is optimized in [GER11] and [GER12]; the selection of rotor lamination material is studied in detail in [CEN10] and the end ring optimization is investigated in [CAP05].

### **1.2.2 Reluctance Machines**

In addition to IMs, the reluctance machine can be also applied to high speed applications. Two different kinds of reluctance machines are introduced in this section, i.e. SRs and SynRs, of which typical rotor structures are shown in Fig. 1. 2.

The SR machine has great advantages such as high fault tolerance, low cost and high working temperature. In addition, different from PM machines and some kinds of IMs, there is not additional auxiliary parts on the rotor in SR machines, which results in great

simplicity. However, several critical problems exist, e.g. high torque ripple, high level of noise and vibration, high mechanical loss, as well as relatively low torque density.

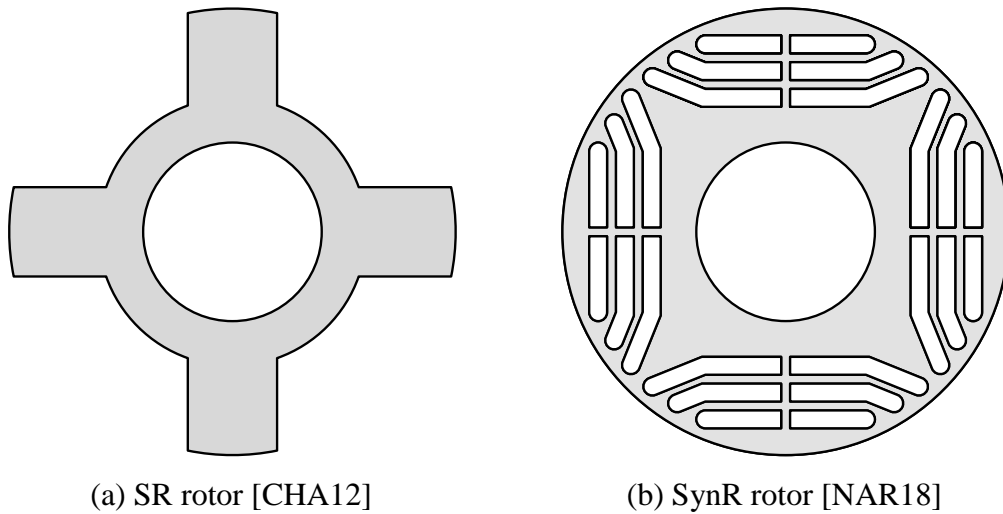


Fig. 1. 2. Rotor structures for high speed reluctance machines.

In these disadvantages, the high mechanical loss, especially the high windage loss, is very undesirable. To reduce this part of loss, a reluctance rotor with extra rib is proposed in [WON08] which is shown in Fig. 1. 3 (a).

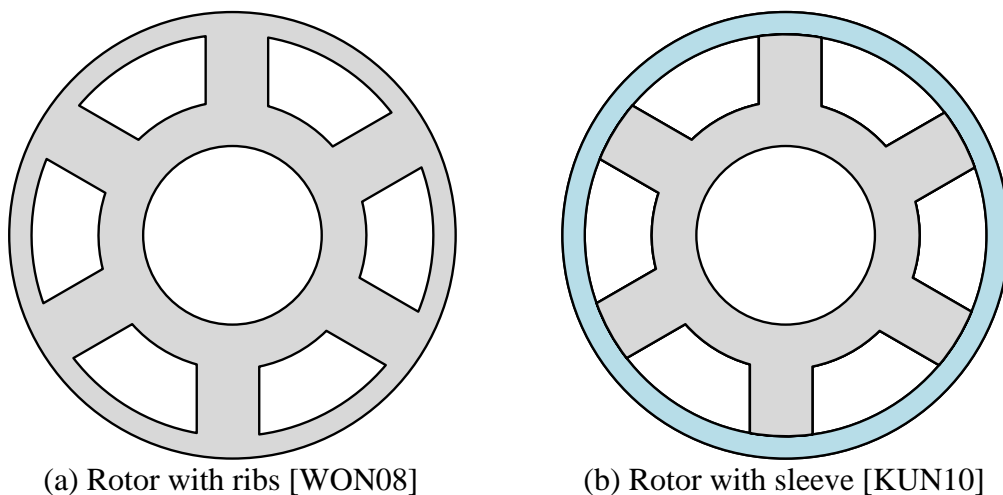


Fig. 1. 3. Rotors in SR machines for windage loss reduction.

It shows that the proposed rotor can decrease the windage loss significantly, and hence, improve the efficiency, which is due to the smooth rotor outer surface. Nevertheless, the output torque is also descended due to lower airgap field. A similar rotor structure is proposed in [DON13], which also confirms the effectiveness of the auxiliary rib on windage loss reduction. Moreover, the asymmetric air gap is introduced and optimized in [DON13] to improve the machine performance, which makes the rotor with rib can achieve even higher torque. In [KUN10], the rotor is equipped with a carbon fibre

sleeve which is shown in Fig. 1. 3 (b). This rotor can also significantly decrease the windage loss. Moreover, it can reduce the stress in the laminations, which boosts the mechanical performance. Nevertheless, due to the existence of the extra sleeve, the cost and the difficulty of manufacture process also ascend. Moreover, the two pole SR rotor is proposed and analysed in [MOR00] and [GON17], which achieve the highest rotating speed for SR machines, i.e. 200krpm and 1000krpm, respectively.

As for the SynR machine whose typical rotor is shown in Fig. 1. 2 (b), it is marked as low cost, low windage loss and high reliability [NAR15]. However, the relatively low power factor and the complicated rotor optimization are the main drawbacks. The rotor mechanical design is very critical for this kind of machines, since the stress will focus on the magnetic bridges, which may cause failure of the machine when it operates under the high speed condition. As a result, the electromagnetic and mechanical performance should be balanced carefully, and the multi-physics optimization is very necessary for high speed SynR machines. In [NAR18], [NAR15] and [DZI16], different multi-physical methods are proposed to optimize the torque and mechanical performances simultaneously. In these literatures, different shape and number of flux barriers are proposed and optimized to get the best overall machine performance.

### **1.2.3 Permanent Magnet Machines**

Comparing with other types of high speed machines, thanks to the PM material characterized as high energy density, e.g. neodymium-iron-boron (NdFeB) and samarium-cobalt (SmCo), PM machines exhibit the highest torque density as well as efficiency which is very desirable for high speed applications. As a result, the review of high speed PM machines will be emphasized.

In this part, the development and the design of high speed PM machines will be detailed. All stator structures, rotor structures, PM materials, magnetizations, sleeve materials and sleeve structures will be reviewed.

#### **1.2.3.1 Review of Stator Types**

For high speed PM machines, several stator structures are very popular as shown in Fig. 1. 4 and Fig. 1. 5. Generally, they can be divided into two different types, i.e. the slotless and the slotted stators.



### A. Slotless Stator

In terms of the slotless machine, since its structure is very different comparing with the traditional PM machine equipped with the slotted stator, its design consideration, field analysis and optimization have received much attention in last few decades.

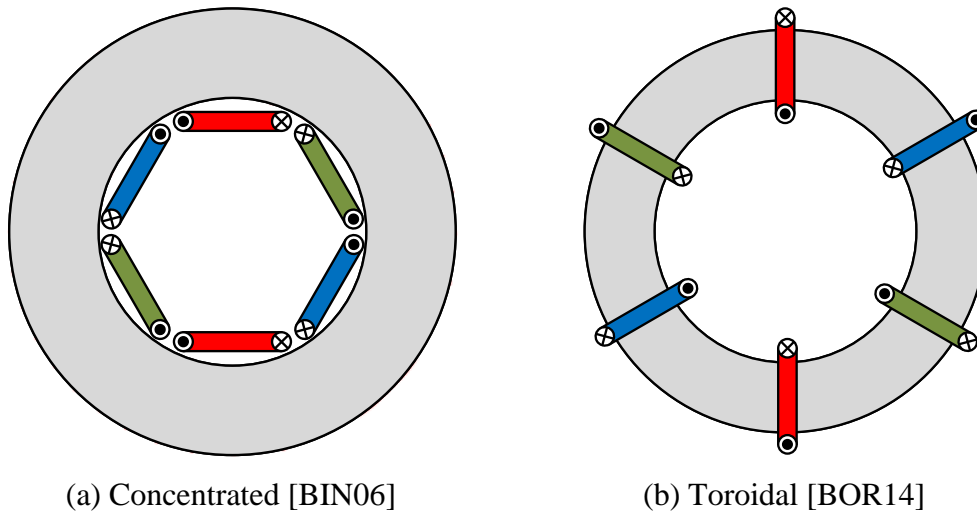


Fig. 1. 4 Stator structures for high speed PM slotless machines.

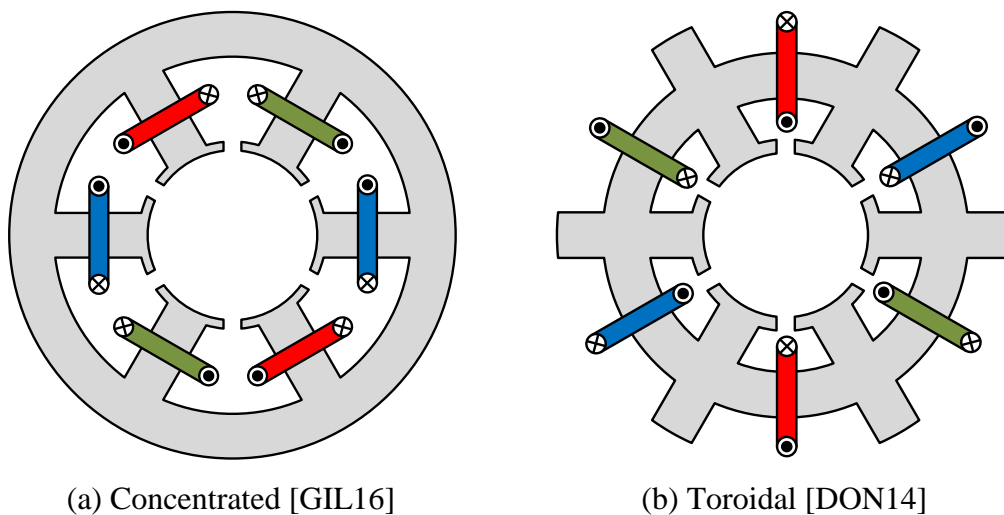


Fig. 1. 5 Stator structures for high speed PM slotted machines.

For high speed slotless machines with concentrated windings, the design consideration is investigated comprehensively in [BIA06]. All the amplitude selection of input phase currents, the PM demagnetization and the thermal consideration are taken into account. In addition, its typical control strategy is also presented and several methods for increasing the drive reliability are summarized. In [CHE07], an analytical model is proposed. Both PM and armature fields are calculated analytically. In addition, the rotor eddy current loss and the stator iron loss are investigated by analytical methods as well. An extension work is finished in [CHE15], in which the accuracy is increased by using

an improved analytical model and the torque is also calculated analytically. Another analytical method is proposed in [PFI10]. Comparing with [CHE07] and [CHE15], more loss components, e.g. the windage loss and the bearing loss, are considered in this paper. In addition, the mechanical stress is also calculated. In [MER15], both PM and armature fields are solved simultaneously based on a harmonics model solution in machines with voltage supply, which does not need accurate inductance calculation. In order to improve the output torque, the slotless machine with concentrated winding and Halbach array is investigated in [JAN01] and [JAN10]. The airgap flux density is analytically determined and the winding thickness is optimized.

For slotless machines with toroidal windings, the windings are wound on the back iron as shown in Fig. 1. 4 (b). The inductance and several loss components are also calculated in [BOR14]. As stated, the eddy current loss in the frame can be measurable when the toroidal winding structure is used, which is mainly due to external flux leakage. Consequently, the material and the thickness of the frame should be selected carefully. Moreover, it also shows that machines with the toroidal winding are more sensitive to manufacture tolerance, especially the unequal number of turns in the serially connected coil, which can result in significantly higher stator iron loss and measurable output torque reduction. In [JUM15], the rotor eddy current loss is analytically determined. The voltage supply is used and the influence of PWM harmonics is also considered.

Different winding configurations in slotless high speed PM machines are compared in [JUM13] and [JUM13a], in which the typical prototype machines with the same stator and rotor specifications are used. In addition, the output torques are kept as the same to make the comparison fair. It shows the machine with concentrated winding has higher rotor eddy current loss due to richer armature magneto-motive force (MMF) harmonics, which indicates the toroidal winding configuration is more favourable when the rotor eddy current loss is the main concern. Moreover, the winding manufacture is more difficult for the slotless machine with concentrated winding, which is mainly caused by the complicated shaping and assembling process [BIA06].

### *B. Slotted stator*

In terms of the PM machine with a slotted stator, its structure is the same comparing with the conventional low speed machines. Nevertheless, for the machine with tooth-

coil windings, the one slot pitch winding is more favourable for high speed applications, even though the output torque may not be maximized due to the relatively low winding factor for some slot/pole number combinations, e.g. the 6-slot/2-pole machine. This is mainly due to the mechanical consideration, since the overlapped winding can significantly increase the end winding and shaft length, which can decrease the natural frequency of rotor and may cause mechanical problems. It should be noticed that in the relatively large high speed machines, the slot number can be relative high, thanks to relative high winding factor but short end winding length, the toroidal winding is more favourable in this case.

Different from the slotless machines, the slot design is very critical when the slotted stator is used. Since the inappropriate slot opening width selection can significantly increase rotor eddy current loss due to the slotted effect, which worsens the thermal condition of rotor [UZH14]. Secondly, the slot design also has significant influence on the AC copper loss, e.g. the proximity loss. In [GON14], the impact of slot flux leakage on this part of losses is investigated in depth. It shows the proximity loss is higher in the winding closer to the slot opening due to the stronger alternating magnetic field. Moreover, in this paper, two different slot shapes are compared in terms of their influence on the proximity loss, i.e. the open slot and the semi-closed one. It shows although semi-closed slots can result in lower rotor eddy current loss but higher proximity loss due to higher flux leakage concentration in slot opening area.

In addition to the conventional slotted stator, several novel slotted stator structures are proposed in literatures for increasing the machine performance.

In [DON16a], the high speed PM slotted machine with stator flux barriers is employed for aircraft applications. The cross section is shown in Fig. 1. 6. It shows the existence of stator flux barriers can effectively reduce the low order spatial harmonics, which results in rotor eddy current loss reduction. The similar stator structure is studied in [LIG14] [LIG14a] [DAJ12] [DAJ12a] [DAJ13] and [DAJ14]. It also indicates that the flux barrier can increase the output torque in machines with specific slot/pole number combinations due to the higher winding factor and the flux focusing effect.

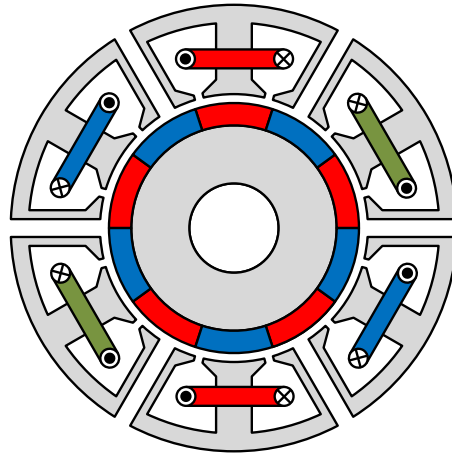
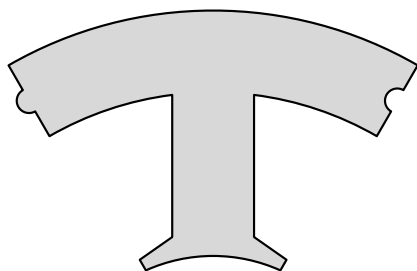


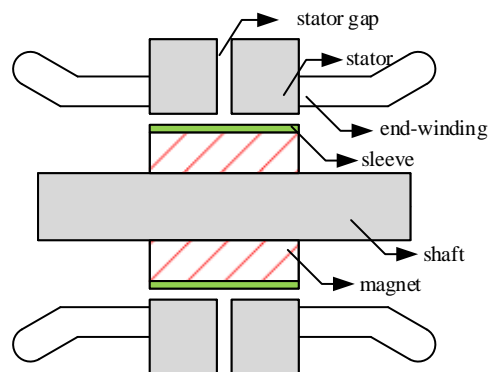
Fig. 1. 6 Cross section of high speed SPM machines with stator flux barriers [DON16a].

The circumferential segmented stator structure is used in [UZH14] which is shown in Fig. 1. 7 (a). It indicates that the modular structure can significantly ease the manufacture process, especially the winding process. In addition, it also results in higher packing factor. Consequently, the current density, and hence, the copper loss can be decreased.

In [SUN17], an axial segmented stator structure is proposed to increase the cooling ability as shown in Fig. 1. 7 (b). The air can be forced to flow through the auxiliary gap between the segmented stator parts, which leads to better cooling capability. Moreover, due to the increased end effect caused by the gap, the iron loss and the rotor eddy current loss can be decreased. Nevertheless, this technology will decrease the active stator length, which can result in torque reduction. As a consequence, the cooling ability, the loss and the output torque should be balanced well when the axial segmented stator is employed.



(a) Circumferential segmented [UZH14]



(b) Axial segmented [SUN17]

Fig. 1. 7 Different segmented slotted stator structures.

### C. Comparison between Slotless and Slotted Stators

In terms of the comparison of slotless and slotted high speed machines, literatures show that the slotless structure has several favourable advantages [BIA04], e.g. great demagnetization performance and low rotor losses. These advantages are mainly achieved by the relative large equivalent airgap length, and hence, low no-load airgap flux density and weak armature reaction. In addition, due to the toothless stator structure, the rotor loss caused by slotted effect can be eliminated and the torque ripple can be reduced, which are also desirable for high speed applications. Nevertheless, comparing with the slotless stator structure, the slotted machine has significantly higher torque density. In addition, the higher inductance in slotted machines also results in lower on-load current distortion [LIY16].

#### 1.2.3.2 Review of Rotor Topologies

In high speed PM machines, both the surface mounted permanent magnet (SPM) rotor and the interior permanent magnet (IPM) rotor can be used. The selection of rotor types highly depends on detailed applications. The typical rotor structures are shown in Fig. 1. 8.

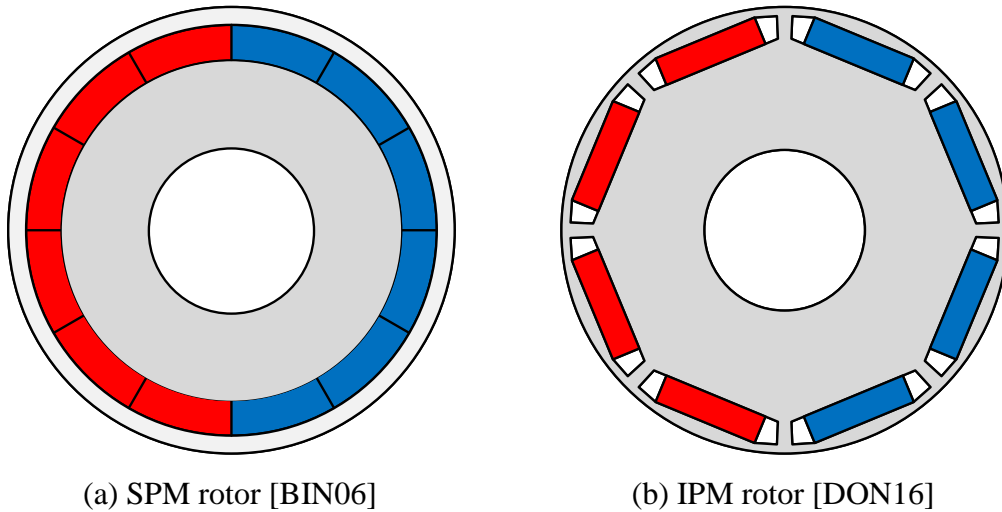


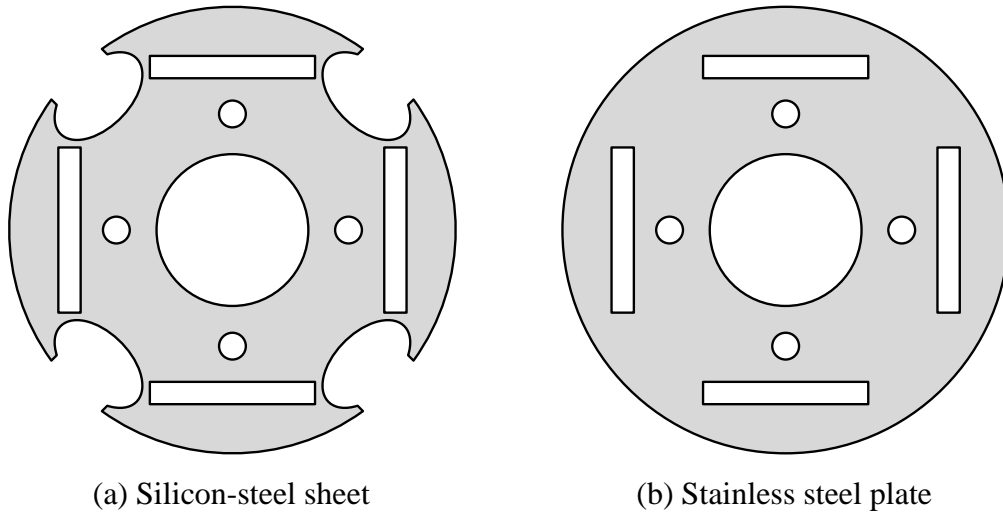
Fig. 1. 8. Typical rotor structures for SPM and IPM machines.

#### A. IPM Rotor

The high speed PM machine with IPM rotor has several advantages, such as no sleeve, low magnet usage, etc. However, it always has to face the crucial mechanical challenge, which comes from several different aspects. One of them is that the force caused by high rotating speed focuses on the magnetic bridge. In addition, the low rotor mechanical strength due to the laminations is also undesirable.

Nevertheless, several literatures try to optimize the IPM rotor to increase its mechanical performance so that its advantages can be utilized. In [RAO14], the impact of magnetic bridge on both electromagnetic and mechanical performances is investigated comprehensively. Several design parameters are studied and optimized, i.e. the number, the direction, the position and the width, respectively. It shows with the same output torque, the machine with optimized multiple magnetic bridges can offer better mechanical performance.

In [ZHA15], a novel IPM rotor is proposed which is named as the “retaining shield” rotor. This rotor consists two parts, i.e. silicon-steel and stainless steel plates, which are shown in Fig. 1. 9. The stainless steel plate inter-stacks with the proposed rotor. By this way, the rotor mechanical strength can be increased significantly. The proportion of the stainless steel plate along axial direction is 17% in the prototype rotor. It shows that this proportion can offer a satisfactory mechanical performance, which is validated by FE method. In terms of the electromagnetic performance, although the rated torque of the prototype machine with 17% stainless steel plate is not given, the output torques of several machines with different stainless steel plate proportions are calculated by 3D FE method. The minimum stainless steel proportion is zero while the maximum value is 33.3%. It shows that due to the influence of end effect as well as relative small proportion of reluctance torque, the reduction of the output torque is smaller than 3% even in the machine with 33.3% proportion of stainless steel plate. Nevertheless, as stated in this paper, since the existence of the stainless steel plate could decrease the difference between the d-axis and q-axis reluctances, it may cause more significant torque reduction when the proportion of reluctance torque is relative high.



(a) Silicon-steel sheet

(b) Stainless steel plate

Fig. 1. 9 Cross sections of the improved IPM rotor in [ZHA15].

In [REF14], a novel spoke type IPM rotor as shown in Fig. 1. 10 is proposed, in which the magnetic bridge is removed and the structure is optimized by finite-element (FE) method. As a result, the proposed rotor can offer excellent mechanical performance under high speed operation. Moreover, the flux leakage is also reduced due to the lack of magnetic bridges, which increases the torque and power density significantly. The influence of magnet materials with the same motor is investigated comprehensively in [GAL15], two different Dysprosium (Dy) free NdFeB magnets are compared with the conventional Dy-NdFeB material. All mechanical, electromagnetic and demagnetization performances are considered. It shows the Dy-free-NdFeB with higher remanence can even offer better performance comparing with Dy-NdFeB in the proposed machine, while it leads to higher cost and slightly worse demagnetization performance. In contrast, the Dy-free-NdFeB material with lower remanence has great advantage in terms of the efficiency under high speed situation.

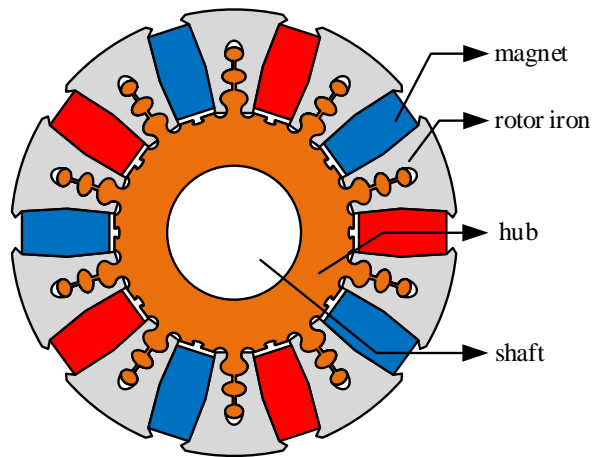


Fig. 1. 10 Improved spoke type IPM rotor in [REF14].

### B. SPM Rotor

The SPM rotor is also very popular for high speed machines. Different from the IPM rotor and the conventional SPM rotor under low speed situation, the retaining sleeve is usually required for high speed SPM machines to keep the rotor mechanical integrity. SPM rotors with different pole arc coefficients are compared in terms of the mechanical performance in [BIN06], of which the cross sections are shown in Fig. 1. 11.

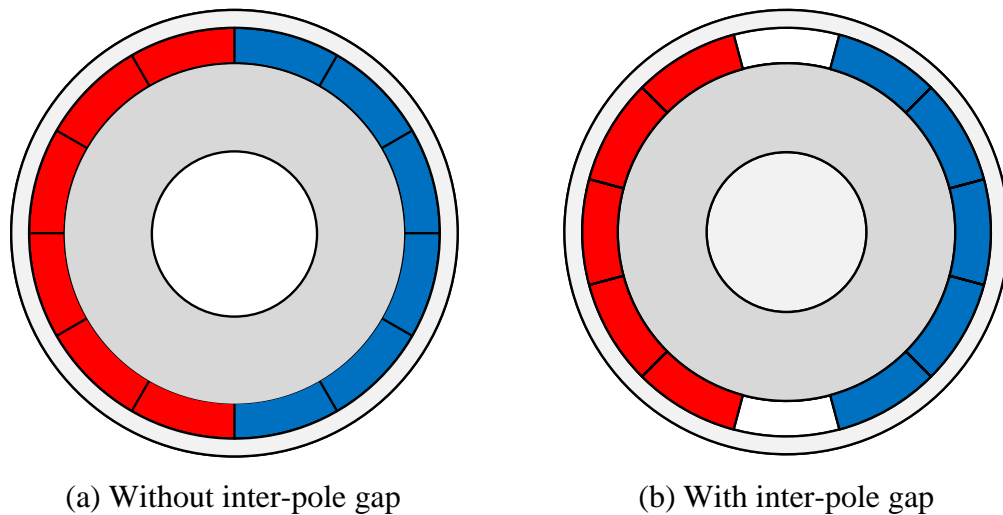


Fig. 1. 11. SPM rotors with different pole arc coefficient [BIN06].

It shows that the inter-pole gap may result in failure of sleeve due to the additional stress on the edge of magnet material and bending effect. Consequently, the SPM rotor with pole arc coefficient equals to one can offer much better mechanical performance. In addition, it also points that the bending effect can be significantly decreased by filling the inter-pole gap with the material having similar mechanical characteristics comparing with the magnet.

In [FOD14], three different SPM rotors are compared which are shown in Fig. 1. 12, i.e. the traditional SPM rotor, the half-buried rotor, and the half-buried rotor with outer profile shaping. As for the electromagnetic performance, it shows that traditional SPM rotor has the highest output torque while the half-buried rotor with shaping has the lowest torque ripple. Moreover, the traditional SPM rotor also leads to highest stator iron loss. In contrast, the half-buried rotor can offer relative small stator iron loss but the largest rotor eddy current loss.



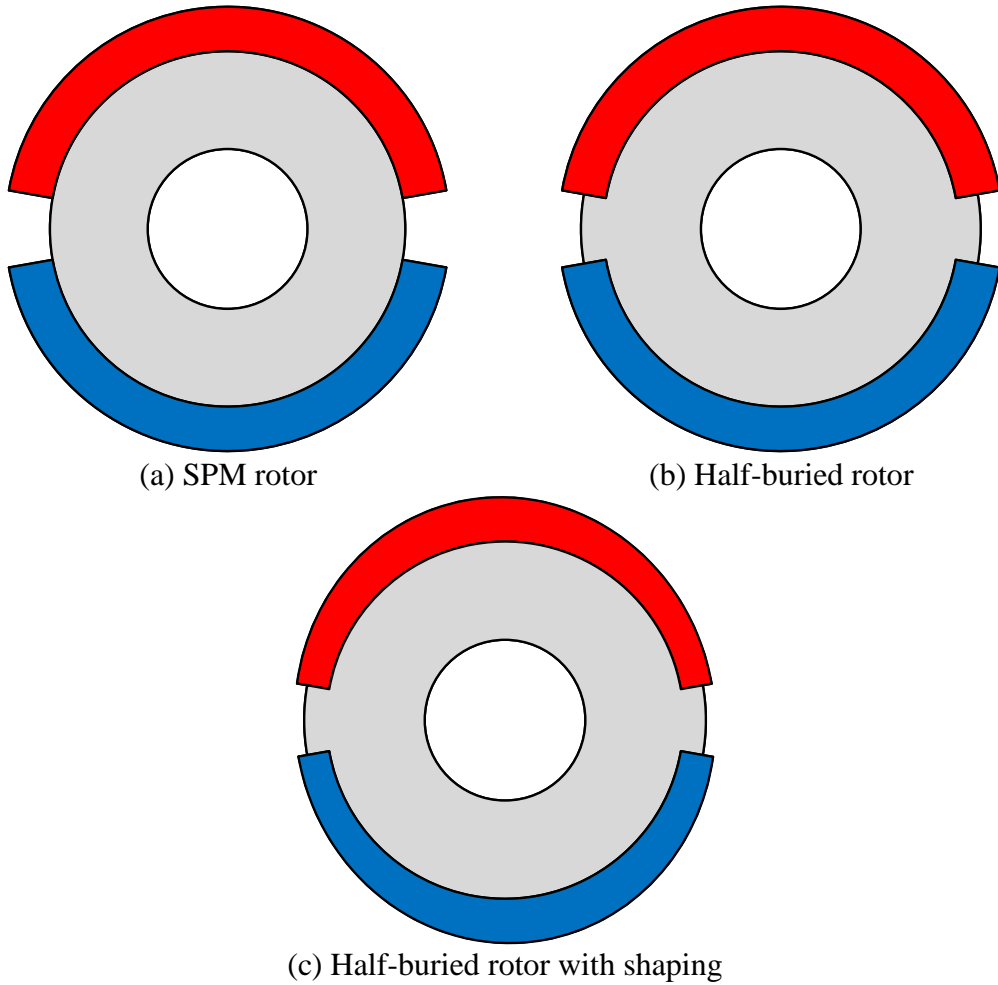


Fig. 1. 12 Different SPM rotors in [FOD14].

In addition to traditional SPM rotor, the solid PM rotor is also a competitive candidate for high speed applications, of which the topology is shown in Fig. 1. 13. The analytical strength analysis for the solid PM rotor is finished in [CHE14], and in [FAN19], the solid PM rotor is optimized by considering mechanical constrains and speed limitations. In addition, several methods are introduced for rotor eddy current loss reduction, i.e. the hybrid sleeve adoption, the copper shield and the sleeve groove. It should be noticed that the segmentation can be hardly employed for loss reduction in solid PM rotor, since the segmentation will decrease the rigidity of rotor, which may cause the mechanical problem.

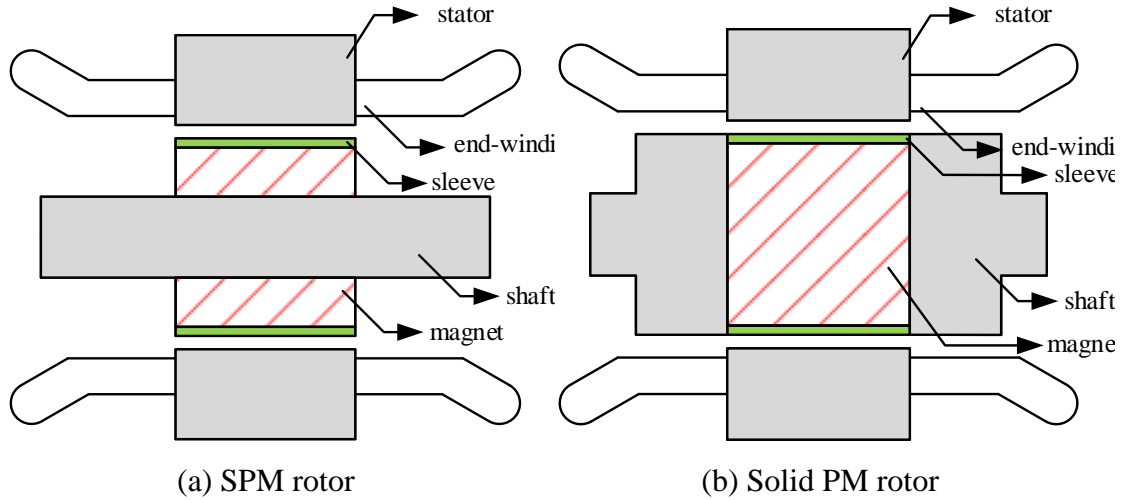


Fig. 1. 13 Different rotor topologies [XIA16].

The comparison between the traditional SPM and solid PM rotors is finished in [XIA16]. It shows the carbon fibre can be used as the sleeve material for SPM rotor, while the metallic material should be used for solid PM rotor to ensure the rigid connection between the PM material and the shaft. Since the carbon fibre has better mechanical characteristics, the equivalent airgap length for conventional SPM rotor can be smaller, which is desirable for torque production. In addition, due to the high conductivity of metallic material, the rotor eddy current loss of solid PM rotor can be significantly higher. As a consequence, the machine with a solid PM rotor may have lower efficiency. A similar work is done in [XUS17], it shows the solid PM rotor can offer higher PM field generally due to the thick magnet. Consequently, if the output torque is fixed, the machine with solid PM rotor can have smaller size, which is the main advantage. Nevertheless, all literatures indicate that the solid PM rotor has relatively lower PM usage efficiency, which is not desirable for economic consideration.

### C. Comparison between IPM and SPM Rotors

The comparison of SPM and IPM rotors for high speed PM machines is investigated in [BIN06]. It shows the IPM machine has several distinct advantages. The elimination of retaining sleeve, which is necessary in SPM machines due to mechanical requirement, is one of the most significant merits, thus the equivalent airgap length can be reduced and the manufacture process can be simplified. Nevertheless, since more force caused by high rotating speed focuses on the magnetic bridge in IPM machines, it states that the IPM machine has relative worse mechanical performance. Consequently, the SPM machine with retaining sleeve is more suitable for ultra-high speed applications. Similar conclusions are drawn in [DON16]. In addition, it also indicates that the nature

frequency in IPM rotors is relatively low due to the low bending stiffness of laminated rotor [LAH02]. As a consequence, the IPM rotor more likely suffers from the noise and vibration under high speed conditions. In contrast, the proper design of retaining sleeve in SPM rotors can increase the total stiffness, which can result in higher natural frequency.

### **1.2.3.3 Review of Soft Magnetic Materials**

The selection of soft magnetic material for high speed machines highly depends on detailed applications and machine designs, since the weight of each consideration, e.g. the saturation, the iron loss, the mechanical strength and the cost, etc., varies from one situation to another.

Among the numerous choices, the cobalt-iron (Co-Fe) material can offer the highest saturation flux density, which indicates it could maximize the power density or minimize the machine size [POW05]. Nevertheless, it suffers from the relative high iron loss and the expensive price, which makes it less favourable for adopting as stator material in many high speed applications, e.g. high speed aircraft generator, etc. [FER17] [GER14]. However, the Co-Fe alloys exhibit the highest mechanical strength comparing with other available commercial materials. As a result, it is more suitable for using as the rotor core in high speed machines to improve the rotor mechanical performance.

In contrast, silicon-iron (Si-Fe) alloys are applied on high speed applications widely. It should be noticed that the characteristics of Si-Fe alloys can be very different depending on the Si content which typically varies from 2% to 6.5%. With the increasing of the Si content, the Si-Fe alloys show lower saturation flux density, smaller permeability but higher electrical resistivity, and hence, smaller eddy current loss [ZHA15a] [PET10]. Nevertheless, comparing with conventional Si-Fe alloys, several new Si-Fe grade materials are proposed in last decades to enhance the machine performance further. One example is 15JNSF950, which has very low iron loss due to 6.5% Si content but almost the same saturation flux density comparing with the conventional Si-Fe alloys having 3% Si [SHO16].

Another material suitable for high speed machines is the amorphous material, which is characterized as extremely low iron losses as well as low manufacture costs [GAV02]. It shows the amorphous material has even higher electrical resistivity comparing with

high Si content Si-Fe alloys. Consequently, this material is favourable for small high speed machines [MEY94] [KOL13]. Nevertheless, there are also several drawbacks of the amorphous material. The most important one is the difficult manufacture process when it is used as the stator material, which is mainly due to its brittleness. Moreover, the advised annealing process can make the material more brittle which initially aims to get better magnetic performance.

In addition, another key parameter is very important for the soft magnetic material selection, i.e. the thickness of laminations. Typically, the iron loss is proportional to the square of lamination thickness, which indicates that the relative thin lamination should be used for high speed applications. However, the yield strength decreases with the lamination thickness as well. As a result, the electromagnetic and mechanical performances should be balanced. However, different from the Co-Fe and Si-Fe alloys, the thickness of the amorphous material is usually very thin, typically 0.025mm, which makes it have very high electrical resistivity but also different for stack and manufacture process.

The materials mentioned above are usually made as thin sheets. In contrast, another competitive choice is the soft magnetic composite (SMC) material, which is produced by powder metallurgical technology [SCH14]. Although this material has relative lower permeability and higher hysteresis loss comparing with conventional Si-Fe materials, it benefits from very low eddy current loss, which can decrease the total iron loss significantly under high speed situations [ZHU97] [CHU07]. Consequently, this type of materials is also very suitable for high speed applications. Nevertheless, the SMC material has low mechanical strength [GUO03]. As a consequence, the mechanical requirement should be checked when SMC material is used for high speed machines.

#### **1.2.3.4 Review of PM Materials and Magnetizations**

The PM material is very critical for all types of PM machines. Moreover, its selection is extremely important for high speed PM machines, since all electromagnetic performance, operating temperature, demagnetization and mechanical consideration need to be taken into account. Typically, high energy density magnet material, e.g. NdFeB and SmCo families are adopted for high speed machines [GER14]. The key characteristics of representative materials are listed in Table 1. 1. As can be seen, both the material type and the detailed grade have significant influence on the characteristics.

The highest operating temperature for NdFeB can be as much as 180°C. It is also reported that when Dy is alloyed with NdFeB, the working temperature can be even increased [GER14]. Comparing with NdFeB, SmCo presents higher working temperature but lower remanence. The maximum operating temperature for typical SmCo material can be as high as 350°C. Consequently, SmCo is better for the applications with hash environment.

Table 1. 1  
Characteristics of typical PM materials

Name	Remanence (T)	Coactivity (kA/m)	Maximum operating temperature (°C)
NdFeB N35	1.22	920	80
NdFeB N38	1.26	920	80
NdFeB N35H	1.22	920	120
NdFeB N35UH	1.22	920	180
SmCo 18	0.87	650	250
SmCo 26HE	1.07	800	350

In terms of the magnetization, different magnetizations are summarized in Fig. 1. 14, in which 4-pole segmented rotors is used to show the characteristics clearly. In addition, the different magnetizations in 2-pole segmented rotors are shown in Fig. 1. 15. It should be noticed that the parallel magnetization is identical to the Halbach array when pole number equals to two.

Its influence is investigated comprehensively in [PHY12], which shows the Halbach array can offer the highest torque, especially when the magnet is relative thick. In addition, the Halbach array also can provide more sinusoidal airgap flux density due to the sinusoidal PM MMF

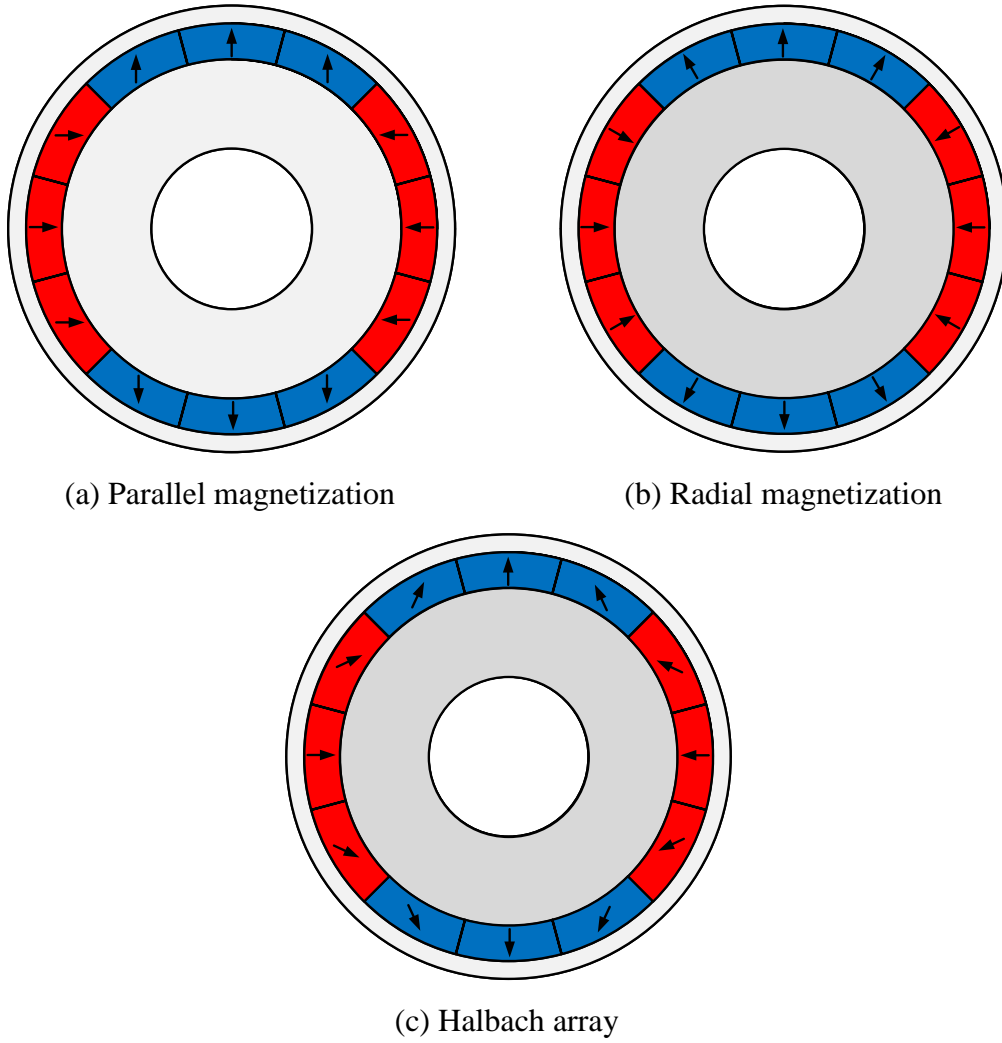


Fig. 1. 14 Different magnetizations in 4-pole rotors.

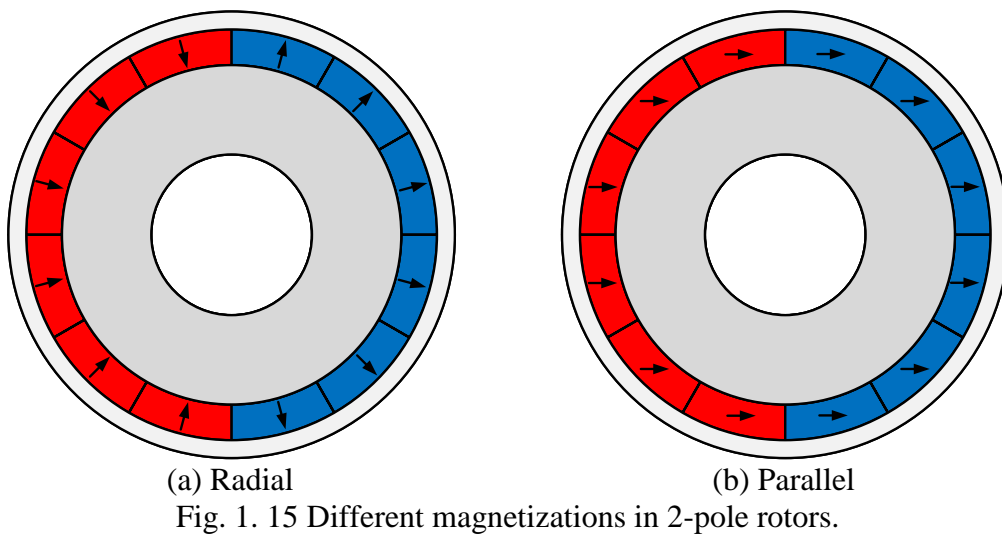


Fig. 1. 15 Different magnetizations in 2-pole rotors.

### 1.2.3.5 Review of Sleeves

Different from the low speed machines, the rotor mechanical integrity is very important for high speed machines due to the high rotating speed and the centrifugal force. As a

result, the retaining sleeve is often employed. Although all the material selection, the design and the structure are very important, only the material and the structure are reviewed here. Since the sleeve design is mainly about the mechanical consideration, it will be detailed in next section with other mechanical design issues, e.g. resonance and vibration, etc.

#### *A. Sleeve Materials*

In terms of the sleeve material, there are numerous choices, e.g. Inconel 718, carbon fibre, glass fibre, copper, stainless steel and Ti-alloy, etc. These materials have their own merits and demerits. For example, the carbon fibre can offer the best mechanical performance, and it has negligible sleeve eddy current loss due to the extremely low electrical conductivity. Nevertheless, it also has poor thermal conductivity, which can isolate the heat and may cause the overheat problem of PM materials. In [BOR10a], it states that the carbon fibre is sensitive to bending although it can withstand extreme tension. Consequently, the rotor with carbon fibre sleeve should be well designed so that the bending effect appeared on the edge of adjacent materials can be avoided. Moreover, the carbon fibres has anisotropy mechanical characteristics, which indicates it has different characteristics on tangential and radial directions. As a result, the mechanical analytical model for carbon fibre sleeves can be much more complicated comparing with other isotropy sleeve materials if the high accuracy is required [BOR10a]. In contrast, the glass fibre has great economic advantage due to its low price. Nevertheless, as stated in [BIN06], the strength of glass fibre bandages cannot be used for keeping the magnet to the rotor surface safely when the circumferential speed of rotor exceeds 150m/s typically.

The high strength metallic materials can be also applied, e.g. the Inconel 718 and the titanium, etc. Although these kinds of materials have relative large eddy current loss due to their high electrical conductivity, which may worsen the total efficiency and the rotor thermal condition, their high rigidity is desirable for rotor mechanical consideration.

The semipermeable material is also proposed in several literatures. In [JAS12], it shows the employment of typical materials with low permeability results in large equivalent airgap length, which indicates the relative thick magnet should be used to maintain the PM field. Nevertheless, the large rotor flux leakage will be introduced if the material

with high permeability is used. Consequently, it shows the sleeve with reasonable permeability should be employed to utilize the PM material. The optimal relative permeability of sleeve material is optimized analytically in [JAS12], and the FE results are carried out for validation. The similar conclusion is drawn in [LIW14] where the influence of sleeve conductivity and permeability is investigated comprehensively. It shows the rotor eddy current loss increases with conductivity at first but then decreases significantly. This is mainly since the penetration depth varies with the conductivity significantly. As a result, when the material with very high conductivity is used, the loss will more focus on the edge of sleeve, and the eddy current loss of magnet will be decreased measurably, which decreases the total rotor eddy current loss. Moreover, the influence of relative permeability is studied as well, which has the same conclusion of [JAS12]

### *B. Sleeve Structures*

The sleeve for high speed SPM machines is usually bounded on the rotor outer surface directly. Nevertheless, there are also several other sleeve structures which can be used. The copper shield is one of the candidates. The adoption of copper shield for reducing the rotor eddy current loss is proposed in [VAN97]. Since the copper has much higher electrical conductivity comparing with sleeve and magnet materials, the proper design of copper shield can make the eddy current loss focuses on the shield itself, while the total rotor eddy current loss can be decreased due to more significantly reduced loss in the sleeve and the magnet. In [ALA17], the influence of several key design parameters is investigated in depth. The impact of copper shield location is studied at first, of which the cross sections are shown in Fig. 1. 16.

It shows that the rotor with inner copper shield has the better performance in terms of the rotor eddy current loss reduction, since the outer copper shield will result in very high eddy current loss due to the abundant flux density harmonics, which is even higher than the reduced loss in other rotor parts. In addition, the influence of sleeve material is also studied, it indicates the metallic sleeve could benefit more from the copper shield rather than the carbon fibre sleeve due to the negligible loss in the carbon fibre material.



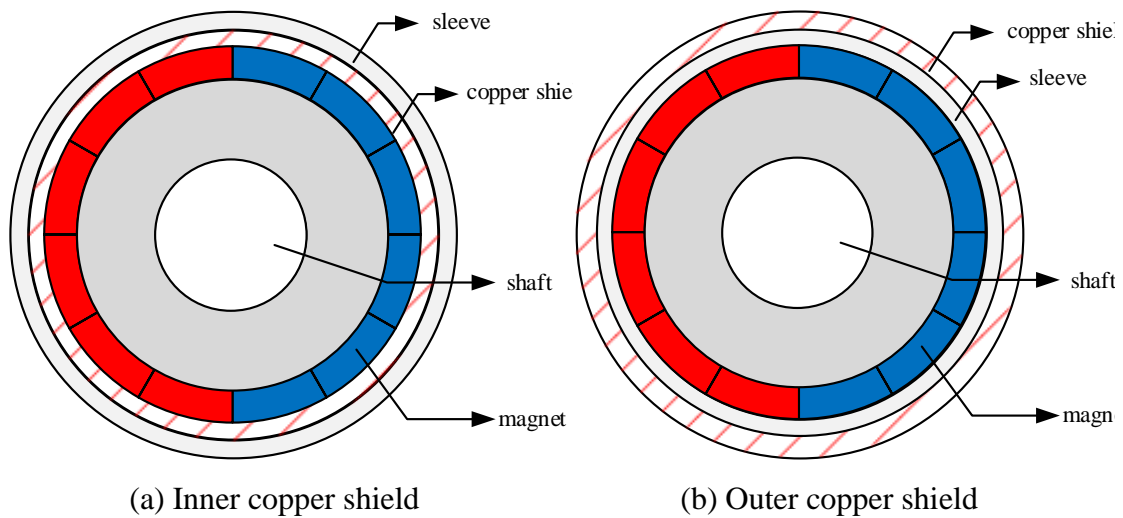


Fig. 1. 16 Cross section of rotors with copper shield [ALA17].

In [SHE13], the grooved sleeve structure is used to decrease the eddy current loss. Extra grooves are added in the surface of sleeve so that the equivalent resistance can be increased. Both circumferentially and axially grooved titanium sleeves are considered, of which the illustration figures are shown in Fig. 1. 17. It indicates the circumferentially grooved sleeve can decrease the sleeve eddy current loss over 20%. Nevertheless, due to the decrease of sleeve rigidity, the rotor dynamic performance needs to be checked. Moreover, the strength of sleeve may also be reduced, which should be considered well in the design stage. In contrast, the axial grooved sleeve has relative worse performance as for eddy current suppression and mechanical strength. In addition, this literature also states that the circumferentially grooved sleeve is easier for manufacture process.

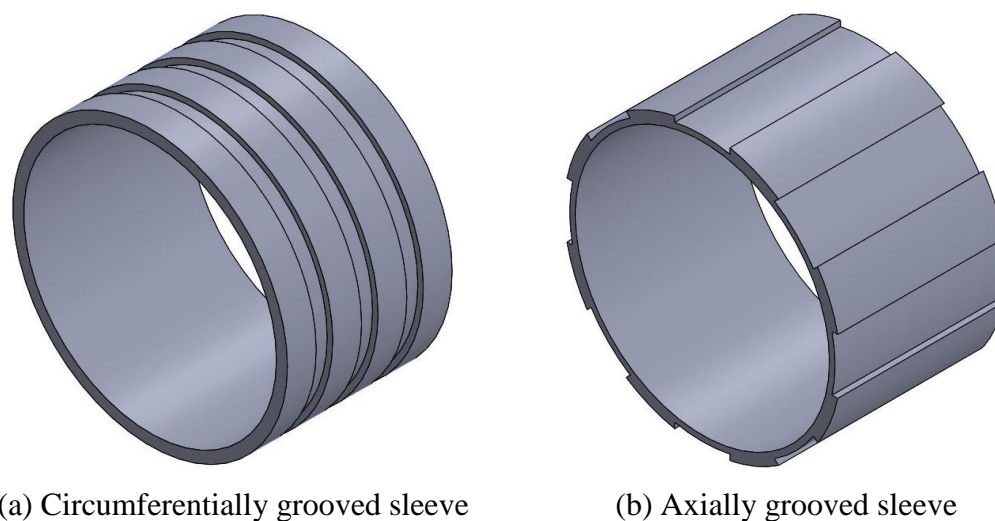


Fig. 1. 17 Sleeves with different groove types [SHE13].

Another sleeve structure is proposed in [JUN15] which uses slotted sleeve, and the illustration figure is shown in Fig. 1. 18. The influence of the slot is similar to the groove shown in [SHE13]. Nevertheless, all width, depth, number and skew angle of the sleeve slots are optimized in [JUN15], and it shows the sleeve eddy current loss can be decreased by over 70%. Although this method can offer great performance for loss reduction, it also decreases the mechanical strength and rigidity significantly, which should be paid attention.

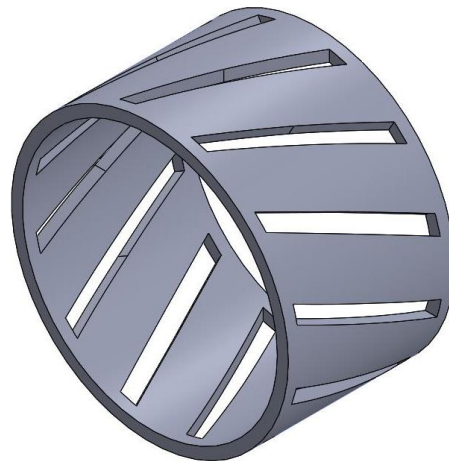


Fig. 1. 18 Slotted sleeve in [JUN15].

### **1.3 Design Considerations Applicable to High Speed Machines**

#### **1.3.1 Mechanical Consideration**

In high speed machines, due to the high rotating frequency, there might be mechanical problems which decreases the machine performance significantly. One of them is the rotor integrity. As stated in Section 1.2.3.4, the retaining sleeve should be used for keeping the rotor structure integrity under the maximum rotating speed [BOR10]. Consequently, the design of sleeve should be based on the mechanical requirement. Moreover, as stated in Section 1.2.3.2, the IPM rotor needs to face the crucial mechanical changes, which indicates the rotor stress calculation is also very important for IPM machines. In addition, the vibration and shaft bending are also very critical for high speed machines. Comparing with the overheat problem caused by more significant loss due to high rotating speed, the mechanical problem is more likely to result in the failure of high speed machines [BOR10].

### 1.3.1.1 Rotor Mechanical Stress Calculation

In terms of sleeves, the sleeve material and the structure are reviewed in Section 1.2.3.4. Nevertheless, the basic requirement of sleeve is to provide sufficient mechanical support. In [BIN06], several detailed requirements of sleeve are summarized, it indicates that the sleeve must provide residual contact pressure between the magnet and the adjacent rotor parts, i.e. rotor iron or shaft. In addition, the stress in the sleeve cannot exceed the maximum allowed value. As can be seen, in order to design the sleeve properly, the accurate rotor stress calculation is required. Although the FE method can be employed, it is relatively complicated and time-consuming. As a result, the analytical model is more favourable at the beginning design stage.

Several analytical models for SPM and solid rotors stress calculation are proposed in [BIN06], [BOR08], [BOR10] as well as [CHE14]. Sufficient accuracy can be obtained by these analytical models, and the influence of temperature can be also considered. However, these models assume the mechanical property of sleeve is isotropic, which indicates that the measurable error may occur when the carbon fibre is used due to its anisotropic mechanical characteristics. In [BOR12], an analytical model is proposed which considers anisotropy of several materials, it shows for small size high speed machines, the influence of anisotropy can be very small and the isotropy model can be also used even though the sleeve is made of carbon fibre.

Nevertheless, the analytical model is only suitable for conventional sleeve structures, which indicates the FE method should be used if novel sleeve structures are employed, e.g. the grooved and slotted sleeves.

For IPM machines, although the sleeve is not necessary, the high pressure usually occurs at the iron bridge which should be considered in the rotor design. Comparing with SPM machines, the accurate stress model is very difficult for IPM machines due to the complex rotor configuration. Consequently, the FE method is more proper [LOV04]. Nevertheless, the analytical method can still offer acceptable accuracy if the IPM rotor structure is relative simple. In [BIN06], an analytical approach is proposed to calculate the rotor stress in a simple IPM machine shown in Fig. 1. 19. This method divides the IPM rotor into several different parts, i.e. magnet, rotor iron bridge, rotor iron and shaft. Then, the IPM rotor is equated as a ring so that the maximum stress in the original IPM rotor can be estimated.

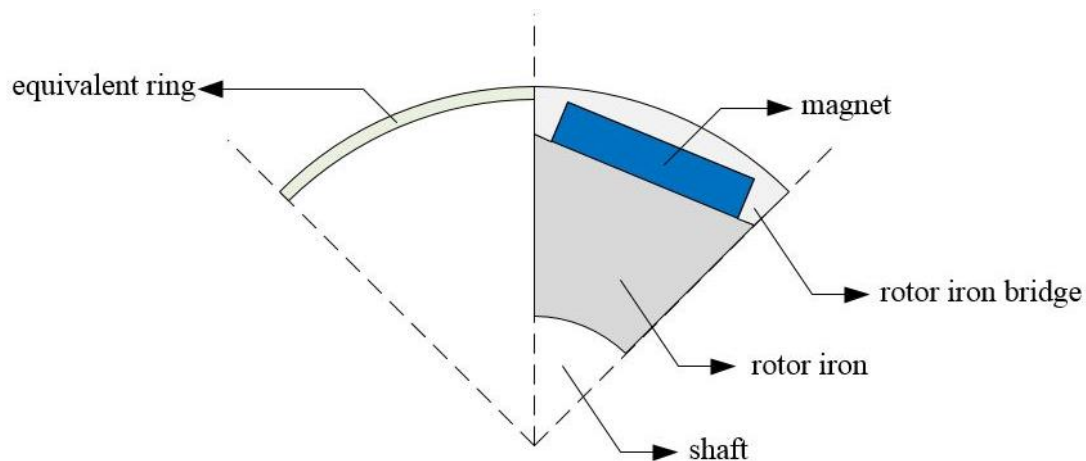


Fig. 1. 19 Analytical model for simple IPM rotor stress calculation using equivalent ring [BIN06].

### 1.3.1.2 Vibration of Machines

The vibration of PM machines mainly results from the stator part [YUS06], and several reasons resulting in vibration are summarized in [BOI14]:

- Magnetic reasons which are due to the stress caused by the variation of magnetic fields, e.g. cogging torque, torque ripple, unbalanced magnetic force, etc.
- Mechanical reasons which are caused by the frictions.
- Aerodynamic reasons which are caused by the airflow within the high speed machines.

In terms of the investigation method, the FE approach can offer the highest accuracy. Nevertheless, the analytical methods are still very important and useful for the high speed machine design.

In [LEC04] and [LIQ11], the stator vibration problem is investigated by analytical method comprehensively. It equates the stator with tooth to an equivalent ring. Both stator tooth and windings are taken into account by varying the mass of equivalent ring. The similar models are used in [CRE10] and [WIT11], but the influence of stator tooth and winding is considered by using a coefficient. Nevertheless, these methods can offer good accuracy only when the stator yoke is relative thin. A more accurate model is proposed in [BOI14], which can be applied for machines with relatively thick stator yokes.

### **1.3.1.3 Shaft Bending**

The shaft bending is mainly caused by the rotor resonant vibration, which occurs when the machine rotates close to the shaft nature frequency. The shaft bending problem is very critical for high speed machines, since it can cause significant deformation of shaft or even the failure of machines.

In order to avoid this problem, the shaft nature frequency should be calculated accurately. Although the FE method can be used, which provides the high accuracy and is suitable for complicated rotor structures. It is relatively time consuming and the influence of design parameters is not intuitive. In contrast, the shaft nature frequency is calculated analytically in many literatures [EDE02] [BOR10] [TEN14] [GIE14] [CHO11]. It shows both the diameter and the length of shaft have significant influence on its nature frequency. Generally, a larger shaft diameter can improve the nature frequency significantly due to the increased axial strength. Nevertheless, the diameter of shaft also depends on the detailed rotor design as well as the bearing. In contrast, the shaft length is inversely related to the nature frequency. Moreover, the other parts of rotor also can affect the shaft nature frequency. It is reported that the rotor lamination and the end-cap can decrease the shaft nature frequency, which is due to the increased mass but low level of axial stiffness [EDE02]. In contrast, the PM material has the opposite function which thanks to its high axial stiffness.

In addition, the influence of unbalanced magnetic force is investigated in [BOR10] and [FAN14]. It shows the unbalanced magnetic force has noticeable impact on the critical speed, since the unbalanced attraction force between rotor and stator parts can decrease the rotor stiffness significantly.

### **1.3.2 Thermal Consideration**

In addition to the mechanical considerations, the thermal issue is also very critical to the high speed machine. Since the high temperature may cause demagnetization of PM material, which will decrease the machine performance significantly. In addition, the high temperature can also shorten the life of isolations, and hence, the life of machines. Moreover, the electromagnetic field and the mechanical field are also highly coupled with the thermal condition. Consequently, the accurate evaluation of machine temperature is important for high speed PM machines.

Due to the fact that the variation of temperature is mainly caused by the various loss components, the different losses in high speed PM machines will be reviewed at first. Then, the different methods for temperature distribution calculation will be presented.

### 1.3.2.1 Loss Components

In this part, various loss components will be reviewed. It should be noticed that there are generally two different parts of losses, i.e. the electromagnetic loss and the mechanical loss, respectively. The electromagnetic loss will be reviewed at first, which includes the copper loss, the stator iron loss and the rotor eddy current loss. Then, the mechanical loss including the windage loss and the bearing friction loss will be introduced.

#### *A Copper Loss*

In high speed machines, not only the DC copper loss, but also other copper loss components have significantly influence on the machine performance, e.g. skin effect losses and proximity losses, etc.

The skin effect is defined as the phenomenon that the current density decreases from the edge of conductor to the centre, which is caused by the alternating magnet field due to the AC current flowing though the conductor itself. Consequently, the effective conductor area is decreased by skin effect, which increases the copper loss. The skin effect can be evaluated by using the skin depth, which can be expressed as

$$\delta = \frac{1}{\sqrt{\pi f \mu \sigma_e}} \quad (1.1)$$

where  $\delta$  denotes the skin depth,  $f$  indicates the electrical frequency,  $\mu$  is the permeability of the conductor and  $\sigma_e$  indicates the conductivity of conductors.

As can be seen, with the increase of frequency, the skin depth is decreased significantly, which denotes that the skin effect will be more notable [FAN15].

In addition to the skin effect, the proximity effect also has great influence when the machine rotates under high speed situation. The proximity effect indicates the phenomenon that the current distribution in one conductor is affected by the alternating magnetic field caused by adjacent conductors or flux leakages.

The influence of skin and proximity effects can be estimated by either analytical or FE methods. The FE method can offer higher accuracy and consider more complicated slot structure as well as winding configurations, which is employed for many scholars. Nevertheless, the analytical approach is relative simple and time saving, which also received a lot of attentions in academics. Generally, two different analytical models can be used, i.e. 1-D and 2-D models, respectively. The 1-D model is relative simple, and can roughly consider the flux variation in the slot area [PER79] [FER94]. Nevertheless, the 1-D analytical model may have relatively large error, since it cannot consider the impact of flux leakage crossing the slot opening. As a result, the 2-D model is more suitable for accurate AC copper loss prediction in high speed machines [RED08].

In addition, the slot design as well as the conductor position have significant influence on the proximity loss distribution [GON14]. In addition, the end winding and PWM also have significant impact on the evaluation of AC copper losses [IWA09].

In terms of the AC copper loss reduction, several method can be used, e.g. using Litz wire [GON14], transposing the coil along the slot [GON14], twisting the parallel connected wires [VET15] and leaving sufficient place between the coil and the slot opening [BOR10].

### *B. Stator Iron Loss and Rotor Eddy Current Loss*

The stator iron loss plays a more significant role in high speed machines as its value is proportional to the frequency, which can be calculated accurately by using FE method. Nevertheless, the stator iron loss is estimated analytically in [LIQ14] and [WAN18], in which the maximum flux density in all stator area is assumed to be the same, and the stator iron loss can be calculated by timing the stator iron area and the loss density. This method can achieve acceptable results in terms of open circuit iron loss calculation. The main drawback of this method is that it cannot take the effect of the armature field into account. However, since the armature reaction in high speed machines is relative weak, especially for small high speed machines, which is due to the large equivalent airgap length, this method can still have reasonable results for on-load stator iron loss calculation.

As for the rotor eddy current loss, it mainly results from three reasons:

- Airgap flux density harmonics caused by slotted effect
- Airgap flux density harmonics caused by MMF of the armature field

- Time harmonics in the armature field.

The rotor eddy current loss can be estimated accurately by using either FE or analytical methods. As for the analytical approach, the equivalent current sheet method is usually used for considering the influence of the armature field, which is shown in Fig. 1. 20. Both the contributions of time and spatial harmonics are calculated analytically in [ZHU01]. A further study is finished in [ZHU01a], in which the influence of eddy currents on the magnetic field is considered. A more accurate analytical model is proposed in [ISH05], which takes the different rotor components and winding configurations into account. The influence of segmentations is investigated in [WAN10], it shows the segmentation can decrease the eddy current loss, but when the number of segmentation is higher than two, the loss distribution in different segments can be significantly uneven.

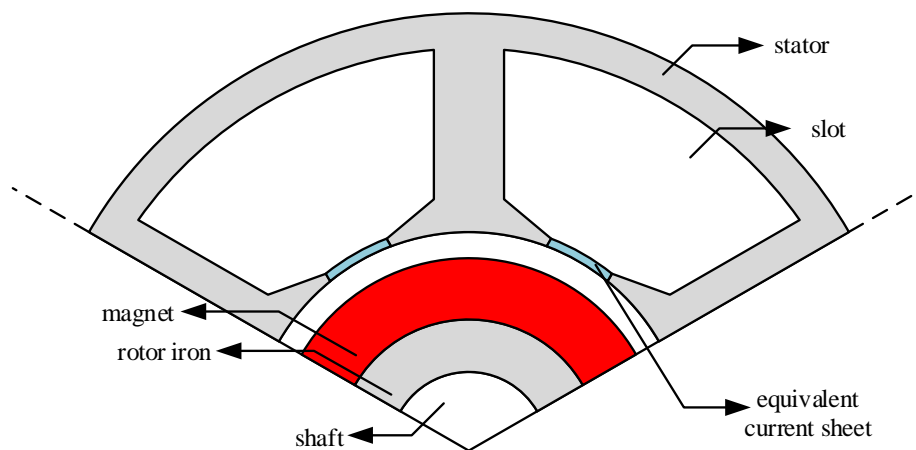


Fig. 1. 20 Illustration of equivalent current sheet method [ISH05].

### C. Mechanical Loss

Mechanical losses are also important for high speed PM machines. Generally, two different kinds of mechanical losses should be considered during the design process, i.e. the windage loss and the bearing friction loss, respectively.

The windage loss originates from the friction loss between the coolant as well as the airgap. Its value depends on many different factors, i.e. the roughness of rotor outer surface, the slot opening width, the pressure of coolant, the physical characteristics of the coolant, the length of rotor, the radius of rotor and the rotating speed, etc. As for the estimation of windage loss, a simple equation is proposed in [VRA68], which has acceptable accuracy for machines with relative small slot opening and smooth rotor



surface. Consequently, this equation is applied widely in academics [WAN09] [PFI10]. It shows windage loss is proportional to the rotating speed, the rotor diameter as well as the active length. Nevertheless, this equation does not consider the axial flow of coolant which may increase the windage loss notably. As a result, the high speed machines with forced airgap cooling system is not suitable for this equation. An improved model is proposed in [AGL03], which considers the axial flow of coolant by modifying several coefficients. However, the analytical method still has several limitations. The most important one is the significant error when the rotor surface roughness is high or the slot opening width is relative large. As a result, the computational fluid dynamics (CFD) method is more suitable when higher accuracy is required.

In addition, the bearing loss is also important, which highly depends on the type of bearings. In terms of its estimation, an analytical method is proposed in [PAL59], in which the friction torque in bearing is divided into two parts, i.e. the viscous and load dependent torques, respectively. The detailed calculating methods for two torque components are also illustrated. Nevertheless, the value of coefficients in the proposed equations vary from one kind of bearings to another. Consequently, detailed empirical data are required to evaluate the bearing friction loss accurately.

### **1.3.2.2 Temperature Distribution Calculation**

In terms of the temperature distribution calculation, generally two different methods are very popular, i.e. lumped-parameter thermal network (LPTN) and CFD methods.

The LPTN method estimates the temperature distribution by treating the loss components as the heat source and calculating the thermal resistance based on geometries and material properties of different machine components. This method is relatively simple but can still offer reasonable accuracy. Due to its simplicity, this method is applied widely in academics [MEL91] [DON16b].

Based on the LPTN method, a simpler model is proposed in [BIA04] for estimating the stator temperature distribution, in which the overall heat transfer coefficient is used and the relationship between the stator loss and temperature can be roughly estimated. Nevertheless, this method assumes the stator temperature distributes evenly, which indicates that more accurate method should be employed if the high accuracy is required.

Nevertheless, the empirical data are required for coefficients assignment in LPTN methods, which may result in reduced accuracy when the specification and material of machines vary. In contrast, the CFD method can offer the highest accuracy, which can also consider the influence of fluid in the machine. However, this method is very time consuming since the 3-D model is required. As a result, the CFD method is not favourable if many candidates need to be checked.

#### **1.4 Optimization Methods in High Speed Machines**

The optimization of high speed machines is more complicated comparing with the low speed one, since many different issues need to be taken into account simultaneously, e.g. the electromagnetic performance, the mechanical consideration, the thermal consideration and the economic issue, etc.

Both analytical and numerical methods can be applied on the high speed machine optimizations. The high speed machine topology is optimized analytically in [ZHU97] and [EDE01] by setting the stator copper loss as a constant. The influence of other loss components and design parameters are also considered. The similar method is also used in [LIQ15] [WAN18], while the stator total loss is considered as the limitation and the mechanical constrain is also taken into account.

In addition to the analytical method, the numerical method is also very popular, which uses FE software to couple the different fields together. It is widely applied for the situation where the accurate solution and the multi-objective optimum are required [JAN11] [AUB12].

Comparing with the analytical method, the numerical method can offer very high accuracy, but it is also very time consuming, especially for multi-physics analysis due to the complicated iteration process among different physical fields. In contrast, the analytical method can offer good insight of the influence of design parameters, and it costs a very short time. As a result, the analytical method is usually used at the first design stage so that the number of candidates can be reduced effectively. Then, the numerically method is necessary for further optimization and checking.

## 1.5 Scope of Research and Contribution of the Thesis

Due to the high torque/power density and relative simple structures, this thesis focuses on the investigation of high speed slotted SPM machines. The outline of each chapter is illustrated in Fig. 1. 21, and the detailed contents are summarized as follows.

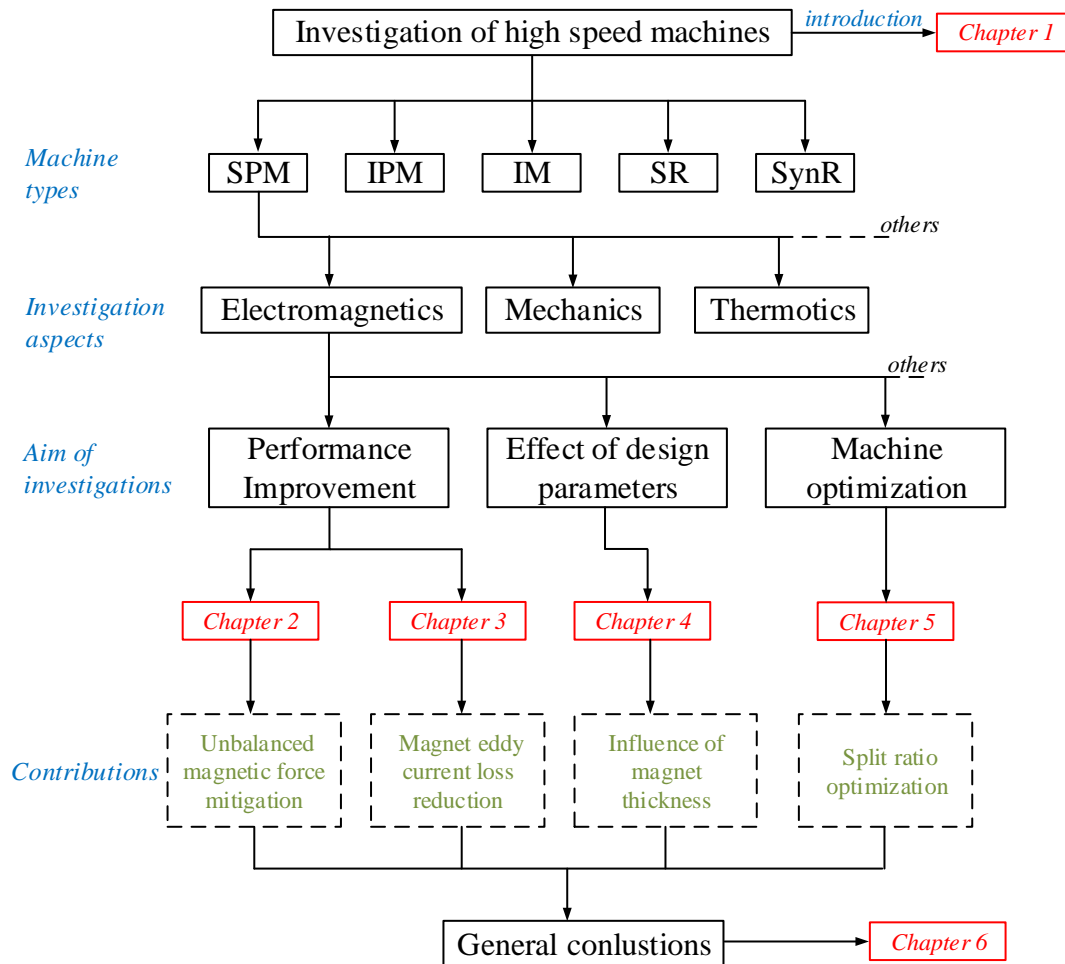


Fig. 1. 21 Research scope and outline of each chapter.

### **Chapter 1: General Introduction**

In this chapter, the background and related literatures are reviewed comprehensively.

### **Chapter 2: Unbalanced Magnetic Force Mitigation in High Speed PM machines by Using Auxiliary Slots**

This chapter focuses on the rated on-load UMF reduction by using auxiliary slots. An existing 3-slot/2-pole machine is chosen as the prototype, and several different types of auxiliary slots are compared. It shows that the auxiliary slots with the optimal size and position can almost eliminate the rated on-load UMF in the prototype machine.

Moreover, the electromagnetic performance in machines with different types of auxiliary slots is compared. In addition, the influence of working conditions, slot opening widths and drive modes will also be discussed. Finally, three different prototype machines are built to verify the FE predictions. All back EMFs, static torques and UMFs are measured.

### ***Chapter 3: Magnet Eddy Current Loss Reduction in High Speed PM machines by Using Auxiliary Slots /***

In this chapter, the rated on-load magnet eddy current loss reduction is the topic. A 3-slot/2-pole machine is still used as the prototype machine, and the auxiliary slots with the optimal size and position are employed. It shows that the proposed method can significantly decrease the rated on-load magnet eddy current loss. The mechanism is explained by a simple analytical model from the harmonics reduction perspective. In addition, the electromagnetic performance between the conventional and the proposed machines are compared comprehensively. Moreover, the influence of working conditions, slot/pole combinations and airgap lengths are also investigated. The prototype machines are built and tested finally. Although the magnet eddy current loss is too complicated to be tested, several other key electromagnetic performance are measured for verification.

### ***Chapter 4: Influence of Magnet Thickness on Electromagnetic Performance of High Speed PM Machines***

As one of the most important parameters for high speed machines, the magnet thickness has not been investigated comprehensively. As a consequence, the influence of magnet thickness on the electromagnetic performance of high speed machines will be investigated in this chapter, e.g. the flux linkage, the phase back EMF, the on-load torque, the unbalanced magnetic force, the self and mutual inductance, the stator iron loss, the magnet eddy current loss, the demagnetization and the economic issue. Finally, two prototype machines with different magnet thicknesses are built and tested. The on-load test is also finished under high speed conditions.

## ***Chapter 5: Optimization of Split Ratio in Small High Speed PM Machines Considering Different Loss Limitations***

In this chapter, the optimization of split ratio in small high speed PM machines is investigated. The split ratio is optimized by the analytical method. Comparing with other literatures, more loss limitations are considered, which is based on the thermal consideration. Different models considering stator loss limitation only, rotor loss limitation only, and both stator and rotor loss limitations are investigated in detail. It shows the machine structure varies significantly when the loss limitation is different. Especially, different from the low speed and large high speed machines, the rotor loss limitation is critical for small high speed machines, since the magnet ring and metallic sleeve are usually used in this case, which results in more significant rotor losses. In addition, the influence of several design parameters is also studied, and the FE validations are carried out for the verification.

## ***Chapter 6: General Conclusion***

Several general conclusions in terms of the investigation of high speed slotted SPM machines are drawn, and the future work based on this thesis are also suggested.

### ***Appendix A:***

The illustration of the frozen permeability method employed in this thesis is explained.

### ***Appendix B:***

The principle and the detailed method for static torque measurement is introduced.

### ***Appendix C:***

CAD drawings for all prototype machines.

### ***Appendix D:***

Publications during the PhD study.

### **Major Contributions of the Thesis:**

1. Successfully reduced the rated on-load UMF in the 3-slot/2-pole prototype high speed PM machine over 95% by using optimal auxiliary slots.

2. Successfully decreased the rated on-load magnet eddy current loss in the 3-slot/2-pole prototype PM high speed machine over 85% by using optimal auxiliary slots.
3. Comprehensively investigated the influence of magnet thickness on the electromagnetic performance in high speed machines.
4. Optimized the split ratio in small high speed machines considering different loss limitations.

## **CHAPTER 2**

# **UNBALANCED MAGNETIC FORCE MITIGATION IN HIGH SPEED PM MACHINES BY USING AUXILIARY SLOTS**

The unbalanced magnetic force (UMF) occurs in machines with specific slot/pole number combinations even if there is no rotor eccentricity. This parasitic effect is critical for 3-slot/2-pole high speed machines, since it has significant influence on noise, vibration and life of bearings. In this chapter, auxiliary slots are employed to mitigate the maximum rated on-load UMF. The characteristics of UMF, the optimization of different auxiliary slots, the machine performance comparison and the influence of several key design parameters, i.e. working conditions, slot opening widths, rotating directions as well as drive modes, will be discussed as well.

This chapter was published on International Conference on Electrical Machines and Drives (IEMDC) 2017, and Transactions on Industry Applications, which are referred as [MAJ17b] and [MAJ18] listed in the references.

### **2.1 Introduction**

PM machines have received much attention recently due to their high efficiency, high torque density and high power factor [GER14], [TEN14]. However, due to the asymmetric stator topology and the unbalanced winding distribution, UMF occurs under both no-load and on-load conditions in machines with specific slot/pole number combinations [ZHU07], which can cause high vibration as well as noise, and significantly reduce the life of bearings.

Many papers have investigated the UMF. The production mechanism of UMF is given in [BIC96] and it shows that two field harmonics differed by one could result in the UMF. The UMFs in machines with axial even and axial-varying eccentricities are calculated by analytical methods in [LIY17], [LIY17a], [LIJ07]. In [ALA17a], a 2-D conformal mapping method is used to calculate the UMF caused by eccentricities in surface mounted PM machines. The difference of UMF between internal and external fractional-slot PM machines is studied in [WUL17]. [WUL13], [ZHU13] and [WUL10] compare the UMF in SPM machines having different slot/pole number combinations,

and the influence of design parameters on UMF is investigated in [WUL16], [MAJ17], [MAJ17a].

The reduction of UMF has been also widely investigated for decades. Various methods have been proposed which can be classified as machine control methods and machine design optimizations [KRO11]. As for machine control methods, the field weakening commutation strategy can be used to minimize the on-load UMF [JIA04]. A similar method is introduced in [YAN14] which injects appropriate current to compensate the low order spatial harmonics of air-gap flux density. In terms of machine design optimizations, both rotor and stator shape optimizations can be used. An effective method of rotor optimization is shaping and magnetizing magnets properly [JAN91], [JAN93]. In [KAN09], another method is proposed by adding notches in the rotor of interior permeant magnet machines. However, these methods lead to complex machining process which increases the cost significantly. The shaped rotor may also have mechanical problem when it runs under high-speed conditions [BIN06]. In addition to rotor shape optimizations, UMF can also be reduced by stator structure optimizations. In [PAN14], the no-load UMF is decreased by adding auxiliary slots into the middle of stator teeth with the same size comparing with slot openings. However, this method has very limited influence on the rated on-load UMF.

The aim of this chapter is to compare the electromagnetic performance of several machines with different auxiliary slots, with emphasis on the maximum rated on-load UMF reduction. Although there are many different slot/pole combinations, the 3-slot/2-pole machine is chosen due to the simple rotor and stator structures.

Moreover, the influence of several factors, e.g. working conditions, slot opening widths, rotating directions and drive modes will be investigated in detail as well. Finally, the prototypes with the same dimensions of analysis models are manufactured and tested. The experimental results are carried out for validations.

## **2.2 UMF of Conventional 3-Slot/2-Pole Machines**

### **2.2.1 Prototype**

The cross section of an existing conventional 3-slot/2-pole PM prototype machine is shown in Fig. 2. 1, and its detailed parameters are listed in Table 2. 1. In the prototype machine, the concentrated winding and a 2-pole PM ring with diametric magnetization



are employed. The brushless AC (BLAC) drive mode is used at first, while the influence of different drive modes will be investigated in later sections.

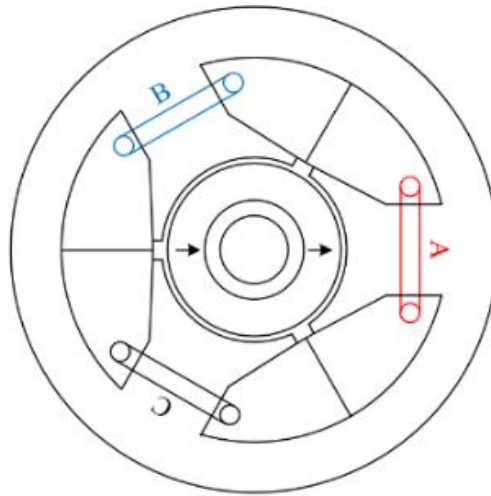


Fig. 2. 1 Cross section of prototype 3-slot/2-pole PM machine.

Table 2. 1

Basic Parameters of 3-slot/2-pole Prototype Machine

Slot number	3	Shaft diameter (mm)	7
Pole number	2	Magnet thickness (mm)	4
Stator outer diameter (mm)	50	Axial length (mm)	30
Stator inner diameter (mm)	19	Magnet remanence (T)	1.2
Stator yoke height (mm)	5.2	Rated current (A)	10
Slot opening (mm)	2	Current angle (Elec. Deg.)	0
Air-gap length (mm)	0.6	Rated speed (rpm)	14000
Rotor outer diameter (mm)	17.8	Number of turns per phase	32

### 2.2.2 UMF Decomposition in Conventional 3-Slot/2-Pole Machines

To obtain the characteristics of UMF, the field distribution needs to be investigated at first as UMF essentially originates from the asymmetric magnetic field distribution. The no-load and the rated on-load flux density distributions are shown in Fig. 2. 2, and the corresponding field distributions are shown in Fig. 2. 3.

It should be noticed that the field distributions are the results of transient analysis. Consequently, the rotor position and the excitation should be specified. In this thesis,

the initial position of rotor is defined as the situation that the North Pole is aligned with phase A. To ease the investigation and the comparison, all field analysis results in this thesis are obtained at zero second except for specific situations, abbreviated as 0s, which indicates that the rotor is set as its initial position. Moreover, the rated working condition denotes that the amplitude of current equals to its rated value, viz. 10A in this chapter, and the current angle is zero, which means the fundamental component of the PM flux linkage is aligned with the d-axis.

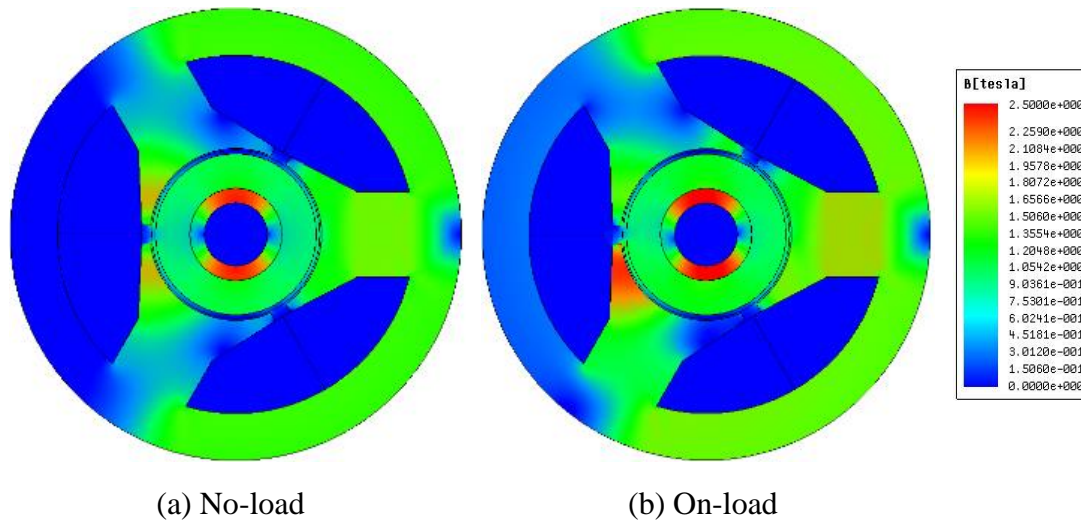


Fig. 2. 2 No-load and rated on-load flux density distributions of a conventional 3-slot/2-pole PM machine at 0s.

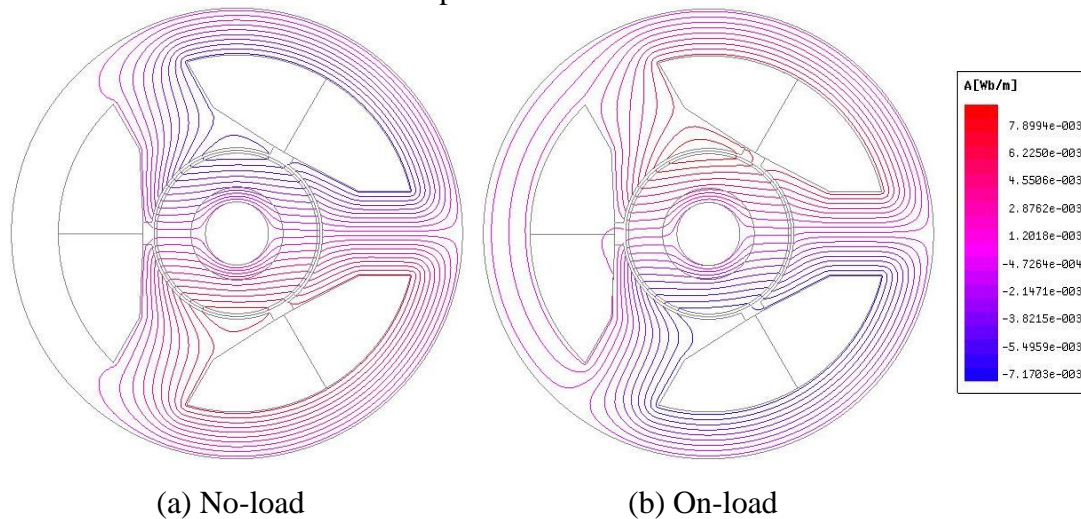


Fig. 2. 3 No-load and rated on-load field distributions of a conventional 3-slot/2-pole PM machine at 0s.

It is found that the field is symmetrical along the x-axis at 0s under the no-load condition, which means there is only x-axis direction UMF component. However, the field is

modified when the currents are excited. Armature field makes the on-load field not symmetrical along the x-axis any more, and hence there will be an extra UMF component in y-axis which does not only affect the amplitude but also the phase of total UMF.

By way of example, the comparison of UMFs under no-load and on-load conditions is shown in Fig. 2. 4.

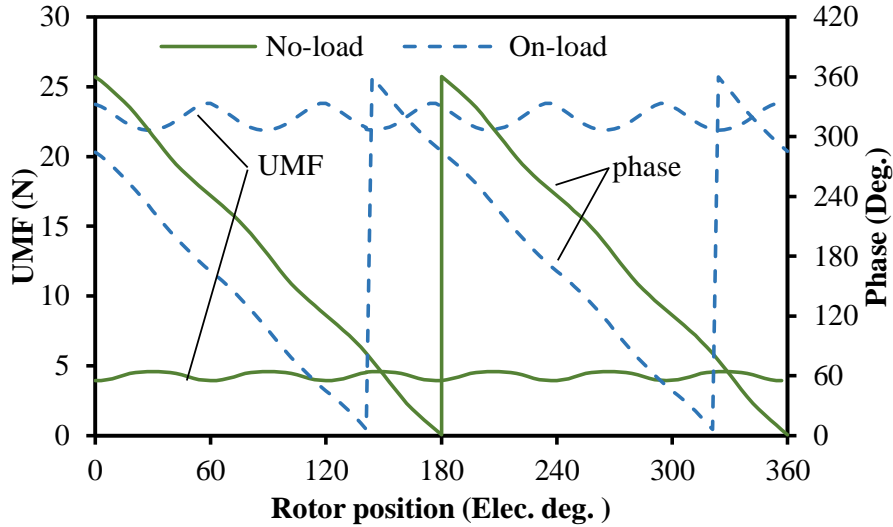


Fig. 2. 4 UMF comparison between no-load and on-load condition of conventional 3-slot/2-pole machine.

It is found that the amplitude of UMF is significantly increased by the input current. Meanwhile, the phase of on-load UMF lags behind no-load one about 90 degrees, which confirms that a measurable y-axis UMF component is introduced due to the enhancement of armature field. The phase of UMF indicates the angle between the specific UMF component and the x-axis in anti-clockwise direction. In addition, the x-axis is in a stationary coordinate which is aligned with phase A, and the y-axis is defined as the axis advancing x-axis by 90 mechanical degrees in anti-clockwise direction.

Since both PM and armature fields have significant influence on the on-load UMF, it has to be decomposed according to the source so that the contribution of each magnetic field can be studied in details.

The UMF based on the Maxwell stress tensor can be calculated by [WUL10]

$$F_x = rl_a \int_0^{2\pi} (\sigma \cdot \cos \theta + \tau \cdot \sin \theta) d\theta \quad .(2.1)$$

$$F_y = rl_a \int_0^{2\pi} (\sigma \cdot \sin \theta - \tau \cdot \cos \theta) d\theta \quad (2.2)$$

where  $F_x$  and  $F_y$  are UMF components in  $x$  and  $y$  directions,  $r$  is the radial of middle air-gap,  $\theta$  is the rotor position in mechanical degree,  $l_a$  is the active length of machines,  $\sigma$  and  $\tau$  are the radial and circumferential traveling stresses, respectively, which can be calculated by

$$\sigma = \frac{B_{radial}^2 - B_{tan}^2}{2\mu_0} \quad (2.3)$$

$$\tau = \frac{B_{radial} \cdot B_{tan}}{\mu_0} \quad (2.4)$$

where  $\mu_0$  is the vacuum permeability,  $B_{radial}$  and  $B_{tan}$  are the radial and tangential components of air-gap flux density, which can be expressed as

$$B_{radial} = B_{mr} + B_{ar} \quad (2.5)$$

$$B_{tan} = B_{mt} + B_{at} \quad (2.6)$$

where  $B_{mr}$ ,  $B_{ar}$  and  $B_{mt}$ ,  $B_{at}$  are the radial and tangential flux densities of PM and armature fields. Since both these two field components are affected by saturation, the frozen permeability method is used here for separating the flux densities [CHU13], which could be calculated as follows: at a specific working condition, the permeability distributions of soft magnetic materials under on-load condition can be predicted and saved by FE method. Then, the PM field is calculated by setting current as zero and employing the permeability distributions just obtained. By this means, the PM field considering the influence of armature field on saturation can be predicted precisely. Following the same procedure, the corresponding armature field can be also calculated. It should be noticed that while calculating  $B_{ar}$  and  $B_{at}$ , the remanence of magnet material should be set as zero, but the relative permeability of the magnet should not be changed. In this way, the radial and tangential travelling stresses can be decomposed as:

$$\sigma = \overbrace{\left( B_{mr}^2 - B_{mt}^2 \right) / 2\mu_0}^{\sigma_1} + \overbrace{\left( B_{ar}^2 - B_{at}^2 \right) / 2\mu_0}^{\sigma_3} + \overbrace{\left[ \left( B_{mr} \cdot B_{ar} \right) - \left( B_{mt} \cdot B_{at} \right) \right] / \mu_0}^{\sigma_2} \quad (2.7)$$

$$\tau = \overbrace{B_{mr} \cdot B_{mt} / \mu_0}^{\tau_1} + \overbrace{B_{ar} \cdot B_{at} / \mu_0}^{\tau_3} + \overbrace{\left( B_{mr} \cdot B_{at} + B_{ar} \cdot B_{mt} \right) / \mu_0}^{\tau_2} \quad (2.8)$$

Where  $\sigma_1$ ,  $\tau_1$ ,  $\sigma_3$ ,  $\tau_3$  and  $\sigma_2$ ,  $\tau_2$  are the radial and tangential traveling stresses caused by the self-interaction of PM field, the self-interaction of armature field, and the mutual interaction between these two fields, respectively. The UMF caused by the self-interaction of PM field introduces the UMF under the open-circuit condition, and the UMF caused by the interaction between armature and PM fields aggravates the UMF under on-load situation.

For convenience,  $F_1$  and  $F_2$  are used here to represent the UMFs resulted from  $\sigma_1$ ,  $\tau_1$  and  $\sigma_2$ ,  $\tau_2$  under on-load conditions, which indicates the influence of saturation is taken into account. Although the self-interaction of armature field can also affect the on-load UMF, its value is much lower comparing with the other two UMF components due to the large equivalent airgap length caused by relative thick magnet thickness, and therefore, this part of UMFs is neglected in following analysis. For instance, the amplitude and phase of  $F_1$  and  $F_2$  are calculated and shown in Fig. 2. 5.

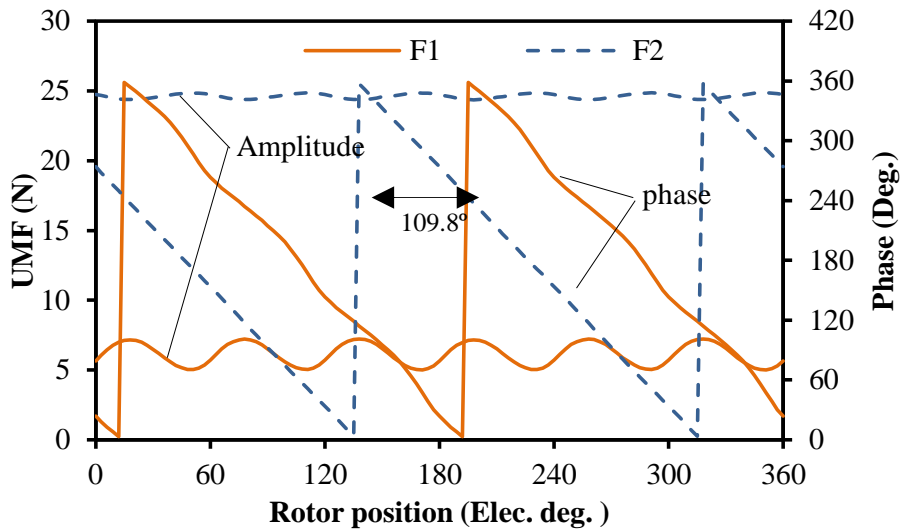


Fig. 2. 5 Comparison of  $F_1$  and  $F_2$  of the conventional 3-slot/2-pole PM machine.

It can be seen that  $F_1$  has great difference comparing with no-load UMF no matter for amplitude or phase as shown in Fig. 2. 4, even if both them are caused by the self-interaction of PM field. In order to explain this phenomenon, the PM field flux density distributions under no-load and rated on-load conditions are shown in Fig. 2. 6. As can be seen, the PM field flux distribution under rated on-load condition is not symmetrical along x-axis anymore which is due to the modified permeability distribution caused by armature field. Consequently, the phase difference between  $F_1$  and  $F_2$  is slightly bigger than 90 degrees, and there is a small cancelling effect between  $F_1$  and  $F_2$ .

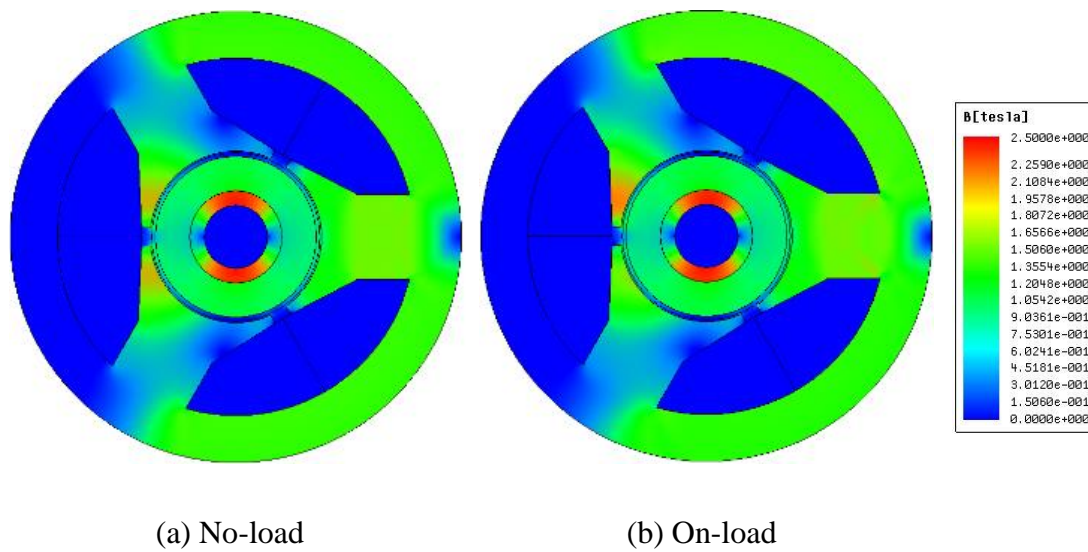


Fig. 2. 6 No-load and rated on-load PM field flux density distributions of a conventional 3-slot/2-pole PM machine at 0s.

## 2.3 UMF Mitigation in 3-Slot/2-Pole Machines

### 2.3.1 Auxiliary Slots in Middle of Stator Tooth Having Optimal Size

Since the main reason for no-load UMF is the asymmetric distributed slot openings rather than stator slots [PAN14], the auxiliary slots with the same size as slot openings can be inserted into the middle of stator teeth to balance the slot opening distribution, and no-load UMF can be almost eliminated by this means.

Although  $F_1$  is different from the no-load UMF as stated in last section,  $F_1$  is still related to the no-load UMF significantly. As a result, this kind of auxiliary slots can also reduce  $F_1$  notably. However, since  $F_2$  is much higher comparing with  $F_1$  as shown in the last section, the rated on-load UMF is just slightly reduced by this method. In other words,

the optimization goal of this method is the minimum no-load UMF instead of the minimum rated on-load UMF.

Alternatively, the optimization goal can be changed to the minimum rated on-load UMF. As a result, the size of auxiliary slots could be modified significantly. By way of example, the topologies of these two machines, namely Machine 1 and Machine 2, are shown in Fig. 2. 7, whose optimization goals are the minimum no-load and rated on-load UMFs, respectively. The optimization of Machine 2 is carried out by FE method, both height and width of auxiliary slots have been optimized. The detailed parameters of their auxiliary slots are listed in Table 2. 2. It can be seen that Machine 2 has much larger auxiliary slots comparing with Machine 1.

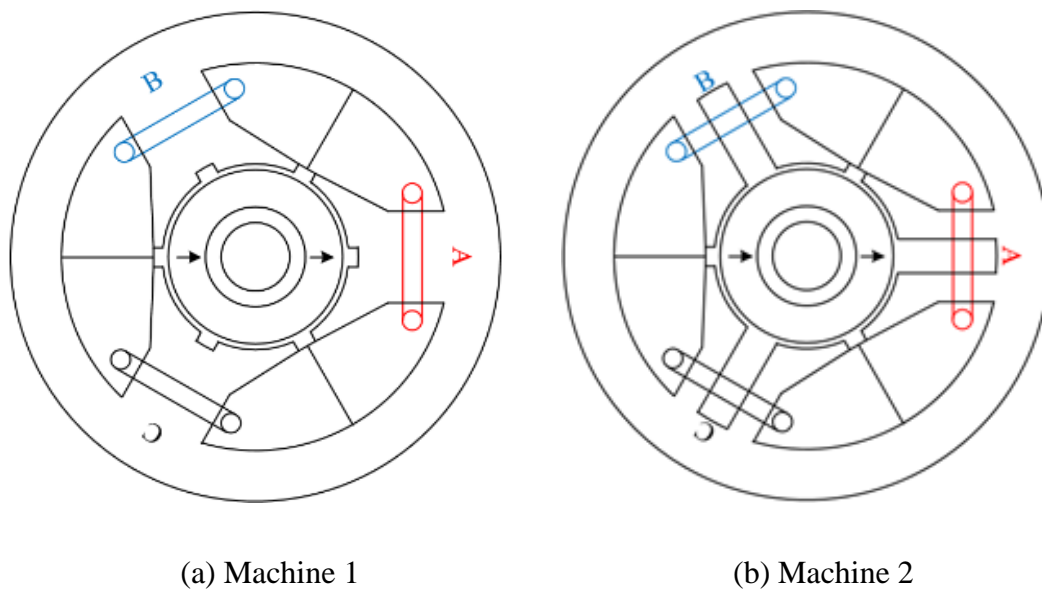


Fig. 2. 7 Optimized topologies of Machine 1 and Machine 2.

Table 2. 2

Specification Comparison of Optimal Auxiliary Slots

Parameters	Machine 1	Machine 2
Auxiliary slot opening width (mm)	2	3.5
Auxiliary slot opening height (mm)	1	10.1

The comparison of UMFs between Machine 1 and Machine 2 is shown in Fig. 2. 8 and their rated on-load flux density distributions are shown in Fig. 2. 9. It should be



mentioned that the auxiliary slots change not only the air-gap permeance distribution but also the saturation of stator, i.e. stator tooth body. Therefore, both  $F_1$  and  $F_2$  are affected by auxiliary slots. As a result,  $F_1'$  and  $F_2'$  are employed here to represent those two UMF components considering the influence of auxiliary slots.

As shown in Fig. 2. 8, both Machine 1 and Machine 2 can reduce the maximum rated on-load UMF, but the reduction of Machine 1 is much lower than that of Machine 2, which is due to different functions of auxiliary slots in these two machines. In Machine 1, the auxiliary slots is mainly for balancing the slot opening distributions, and hence, the asymmetric air-gap permeance variation. However, the main function of auxiliary slots in Machine 2 is reducing the harmonic content of armature field and fundamental PM field, which is achieved by larger equivalent air-gap length.

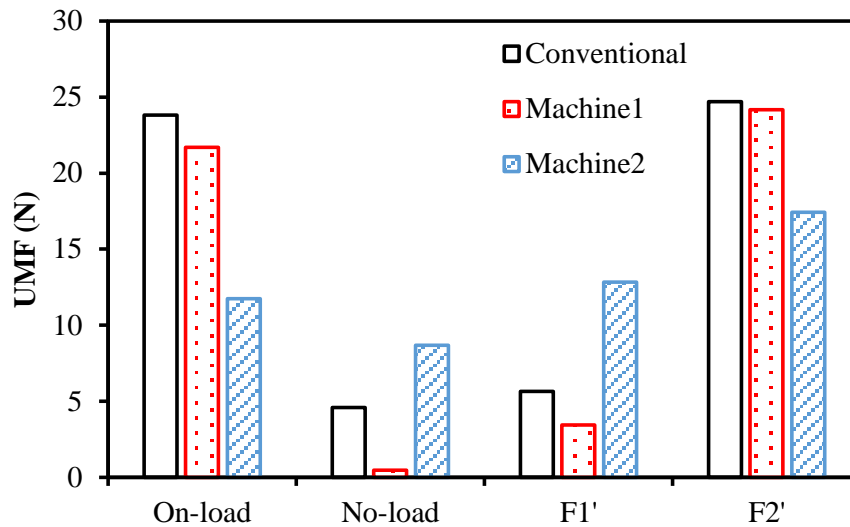


Fig. 2. 8 Comparison of maximum value of UMFs.



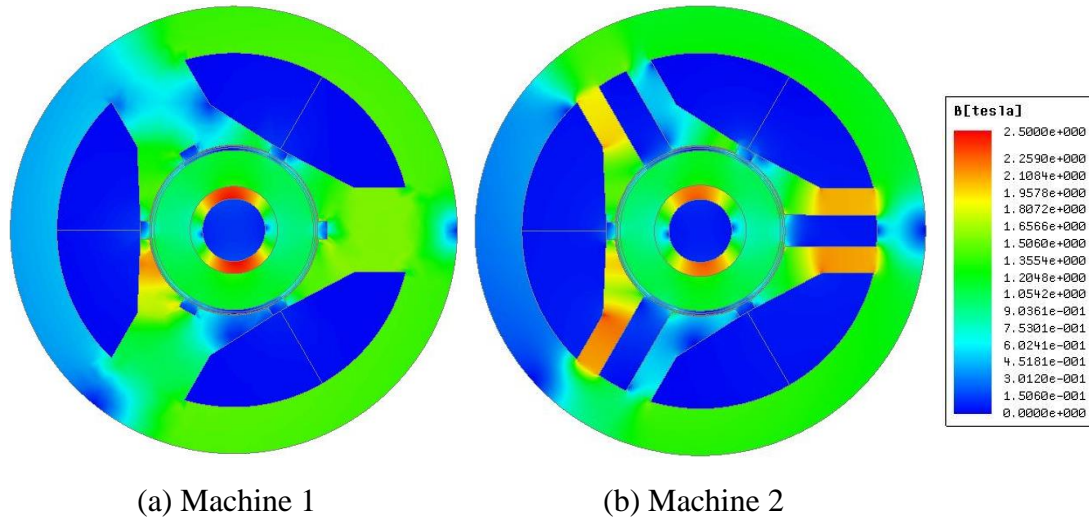
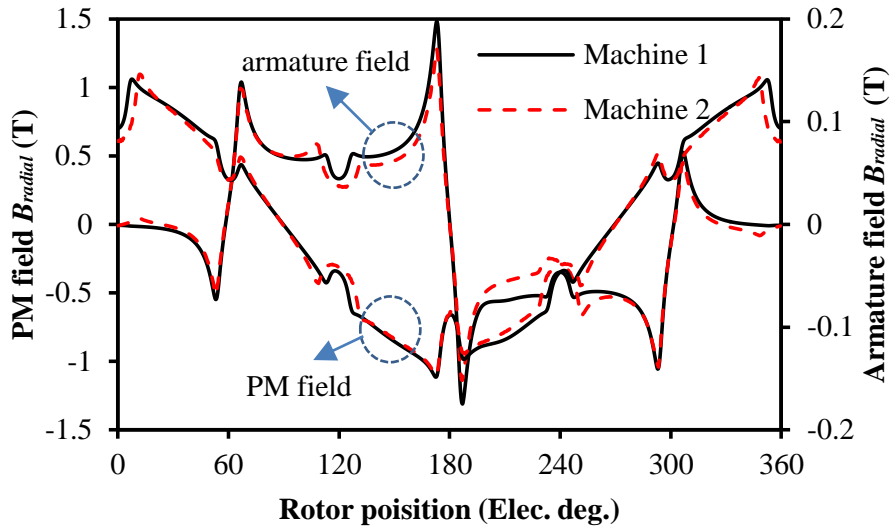


Fig. 2. 9 Rated on-load flux density distributions at 0s.

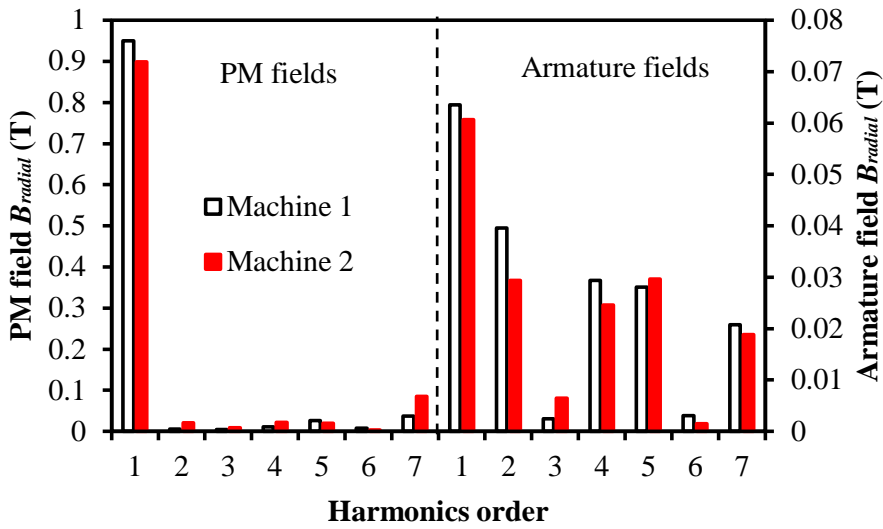
By way of examples, the airgap flux densities in different fields of Machine 1 and Machine 2 are calculated by the frozen permeability method and shown in Fig. 2. 10.

Due to the fact that UMF is resulted from any two adjacent field harmonics, although there are abundant harmonic contents, according to (2.1) to (2.8), the main parts of  $F_1'$  and  $F_2'$  origin from the interaction between the fundamental PM radial field and the 2nd PM tangential harmonic as well as the 2nd armature harmonics, respectively.

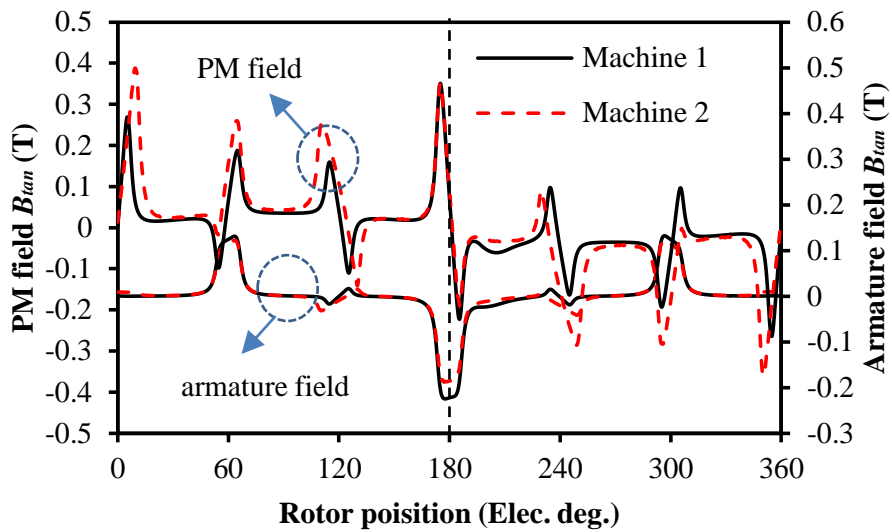
It can be seen that the PM field harmonics content of Machine 1 is much lower comparing with Machine 2, which results in lower  $F_1'$ . However, the armature field harmonic content of Machine 1 is much higher which makes  $F_2'$  of Machine 1 is larger than that of Machine 2. In contrast, the armature field harmonics as well as the fundamental PM field are lower in Machine 2. As a consequence, Machine 2 has relative larger  $F_1'$  but lower  $F_2'$ .



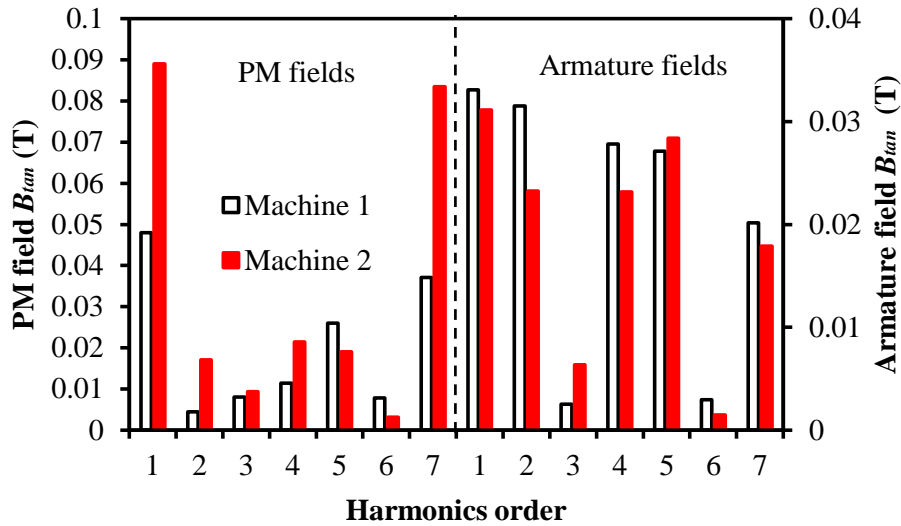
(a) Radial field waveforms



(b) Radial field spectra



(c) Tangential field waveforms



(d) Tangential field spectra

Fig. 2. 10 Comparison of PM and armature fields of Machine 1 and Machine 2 under rated working condition at 0s.

### 2.3.2 Auxiliary Slots with Optimal Size and Position

Since  $F_1$  is caused by the self-interaction of PM field, its phase mainly depends on the saturation condition and rotor position. From another perspective, if the rotor position and load conditions are fixed, the phase of  $F_1$  can be treated as a function of the slot openings position. Since the auxiliary slots have almost the same function as the conventional slots for no-load UMF, this rule can be also applied to auxiliary slots. Since the amplitude of  $F_1'$  can be adjusted by modifying the size of auxiliary slots, and its phase can be modified by shifting position of auxiliary slots, it is possible to make  $F_1'$  and  $F_2'$  have the same amplitude but opposite direction by using auxiliary slots with the optimized size and position, and hence the rated on-load UMF can be eliminated by this means.

The parameters of auxiliary slots used in this method are shown in Fig. 2. 11, where  $w_t$  and  $aw_t$  are the width of conventional and auxiliary slots, respectively;  $h_t$ ,  $ah_t$  are the height of conventional and auxiliary slots, and  $\alpha$  is the shift angle of auxiliary slots, which is defined as the mechanical angle between the middle of the auxiliary slots as well as the middle of corresponding tooth in clockwise direction. Machine 3 represents the machine optimized by this method, the FE method is employed for global optimization, and the auxiliary slots are optimized under rated on-load condition. The

optimized variables are  $aw_o$ ,  $ah_t$  as well as  $\alpha$ , and the optimization goal is the minimum rated on-load UMF.

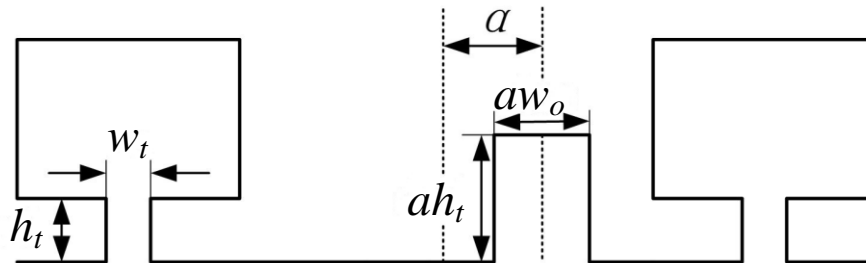


Fig. 2. 11 Auxiliary slots with shift angle.

However, it should be noticed that the existence of auxiliary slots can result in torque reduction due to the increased equivalent airgap length, while significant torque decrease is usually unacceptable in practice. As a result, only the candidates of which the torque decrease is smaller than 5% will be considered further, and the machine having minimum rated on-load UMF among the qualified candidates will be chosen as the optimal one. The cross section and rated on-load flux density distributions of Machine 3 are shown in Fig. 2. 12 and Fig. 2. 13, respectively. Moreover, the parameters of auxiliary slots in Machine 3 are listed in Table 2. 3.

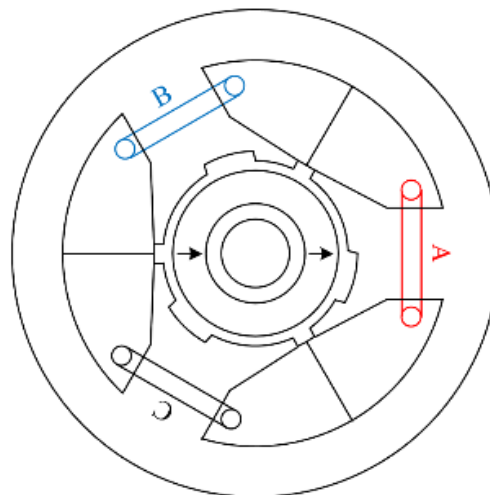


Fig. 2. 12 Cross section of Machine 3.

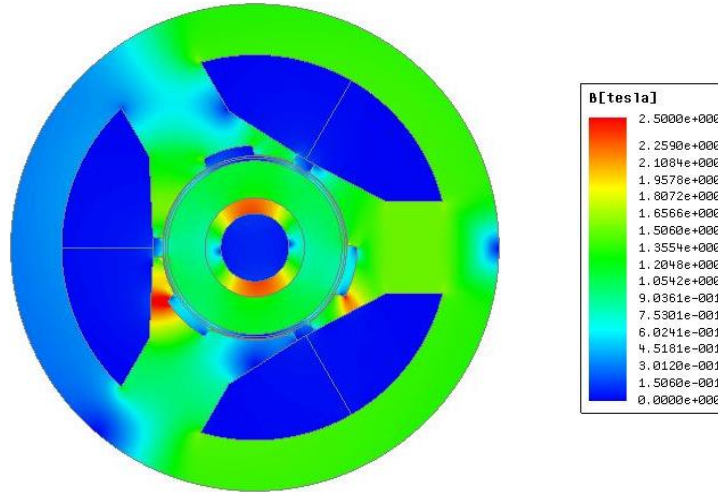


Fig. 2. 13 Rated on-load flux density distribution of Machine 3 at 0s.

Table 2. 3

Specification of Optimal Auxiliary Slots in Machine 3

Auxiliary slot opening width (mm)	4.98	Auxiliary slot opening height (mm)	0.98
Auxiliary slots shift angle (Deg.)	14.18		

Fig. 2. 14 compares the maximum UMFs of Machine 3 under different input currents. It can be found that the maximum UMF achieves almost zero in Machine 3 under the rated on-load condition. In other working conditions, the maximum UMF of Machine 3 is not zero any more due to the variation of the armature field and the modified permeability distribution. In contrast, the maximum UMF of conventional machines increases over the whole current range due to the fact that the phase between  $F_1$  and  $F_2$  is close to 90 degrees. Consequently,  $F_1$  and  $F_2$  have very small cancelling effect comparing with Machine 3.

The maximum rated on-load UMF is 0.8N in Machine 3 but 23.8N in the conventional one, the reduction is about 96.6%, which shows the great effectiveness of this method. It is worth noting that  $F_2'$  highly depends on working conditions. Therefore,  $F_1'$  needs to be modified according to different input currents to obtain a low UMF. As a result, the optimal size and position of auxiliary slots vary with working conditions as shown in Fig. 2. 15.

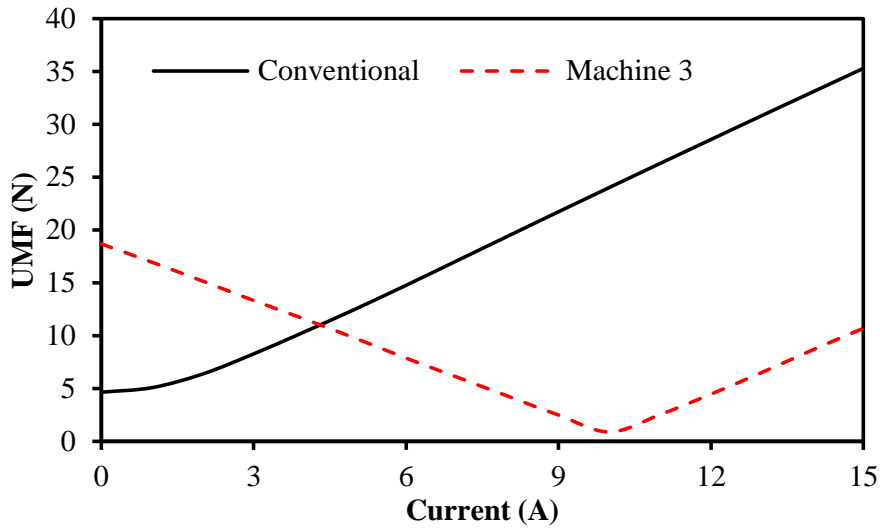


Fig. 2. 14 Comparison of maximum UMFs of conventional machine and Machine 3 under different working conditions.

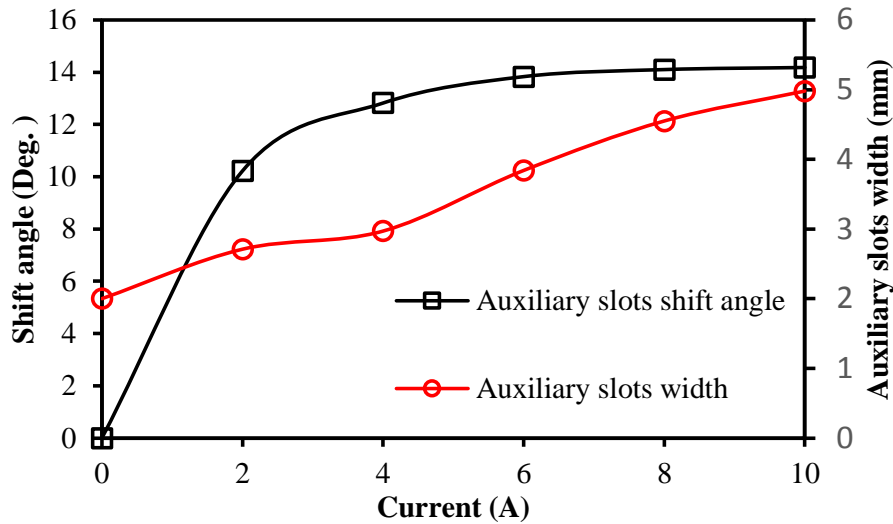
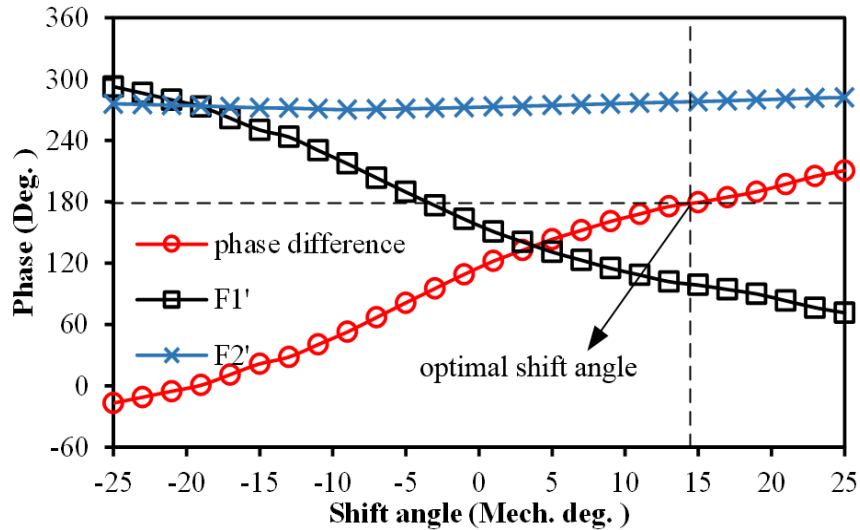


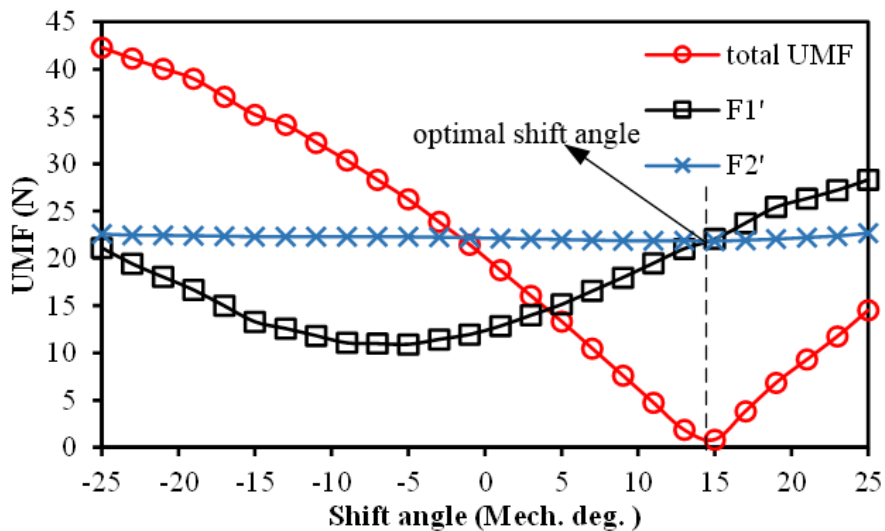
Fig. 2. 15 Optimal shift angle and width of auxiliary slots for minimum UMF with different currents.

To show more detail,  $F_1'$  and  $F_2'$  in Machine 3 against auxiliary slots shift angle are shown in Fig. 2. 16. The rated current is 10A and current angle is 0 electrical degree. It can be seen that the position of auxiliary slots has a great effect on  $F_1'$  for both phase and amplitude. In contrast,  $F_2'$  is much less sensitive as for the position of auxiliary slots. This is due to the fact that  $F_1'$  is caused by the self-interaction of PM field, in which all harmonics except the fundamental are caused by slotting effect, and therefore the permeance variation affected by auxiliary slots has great impact on the PM field harmonics in addition to the fundamental. As for the fundamental PM field, its amplitude and phase are related to the equivalent air-gap length and the initial position of rotor, respectively. Hence, the auxiliary slots can only decrease its amplitude slightly

but have very small effect on its phase. On the contrary,  $F_2'$  is mainly caused by the fundamental PM field and the second harmonics of armature field [WUL10], and the armature field harmonics mainly origin from the MMF harmonics of the armature field instead of slot harmonics. Therefore, the auxiliary slots have the similar influence on armature field comparing with the fundamental of PM field.



(a) Phase

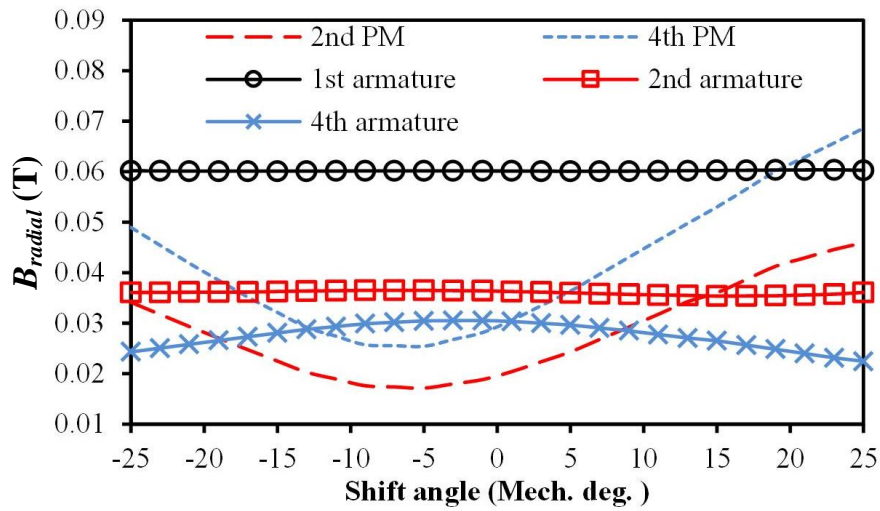


(b) Amplitude

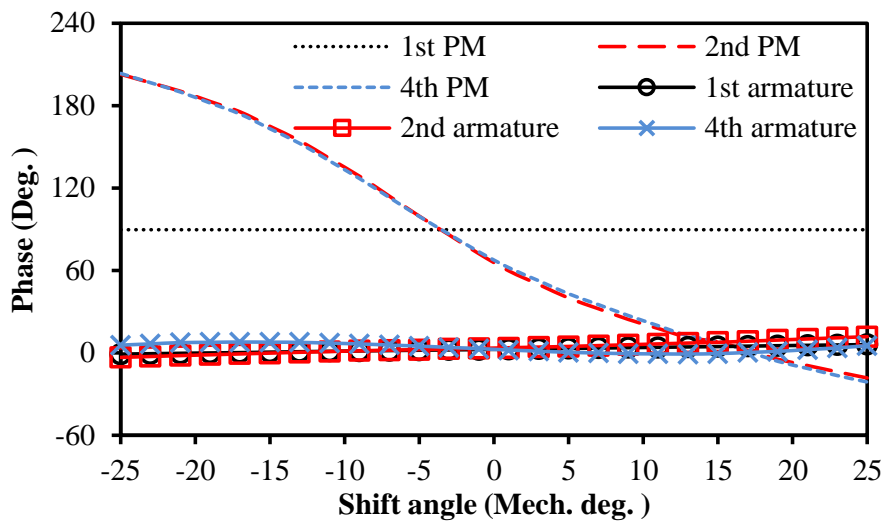
Fig. 2. 16  $F_1'$  and  $F_2'$  versus auxiliary slots shift angle at 0s under rated working condition.

By way of example, the harmonics in PM field and armature field with different shift angles are shown in Fig. 2. 17. It is worth mentioning that since the fundamental PM field is very insensitive to the shift angle of auxiliary slots, and its value is much larger

than the other harmonics, it is not shown here so that the other harmonics can be observed more clearly.



(a) Amplitude



(b) Phase

Fig. 2. 17 Flux density harmonics versus shift angle of auxiliary slots at 0s under rated working condition.

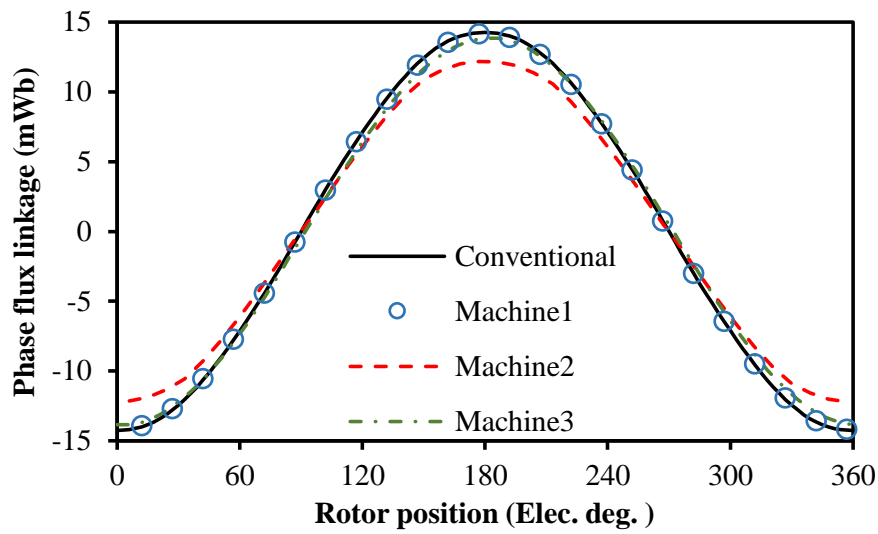
## 2.4 Electromagnetic Performance Comparison

### 2.4.1 Flux Linkage and Back EMF

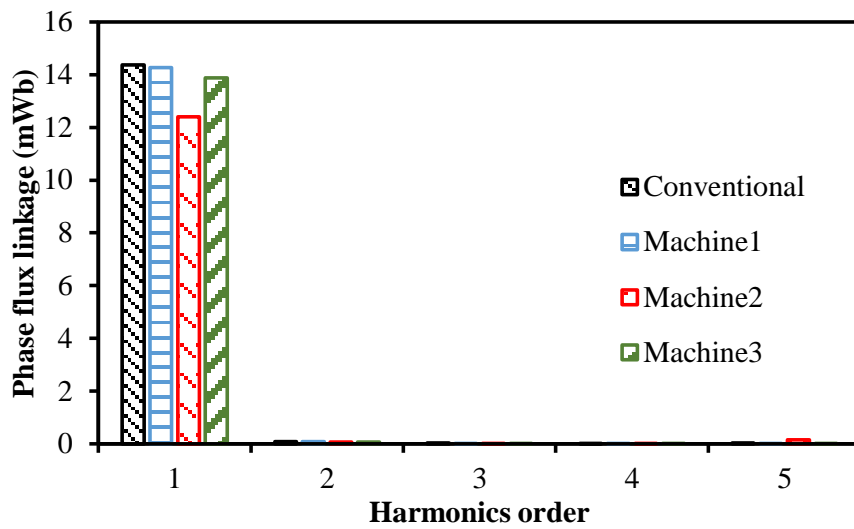
Fig. 2. 18 shows the comparison of phase flux linkages. It is found that Machine 1 and Machine 3 have almost the same phase flux linkage comparing with the conventional one, the slight reduction is mainly due to the increased airgap length caused by auxiliary



slots. In contrast, flux linkage in Machine 2 is much lower, which is mainly due to the much larger auxiliary slots, hence the larger equivalent air-gap length.



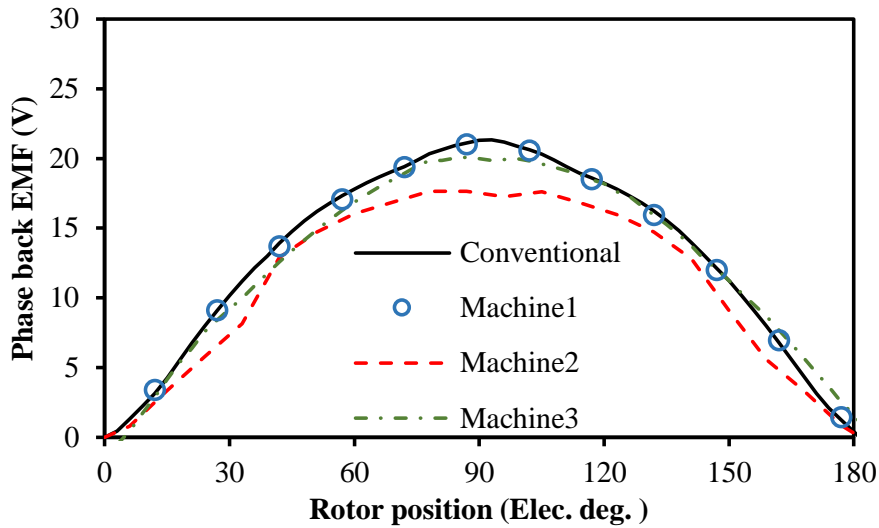
(a) Waveforms



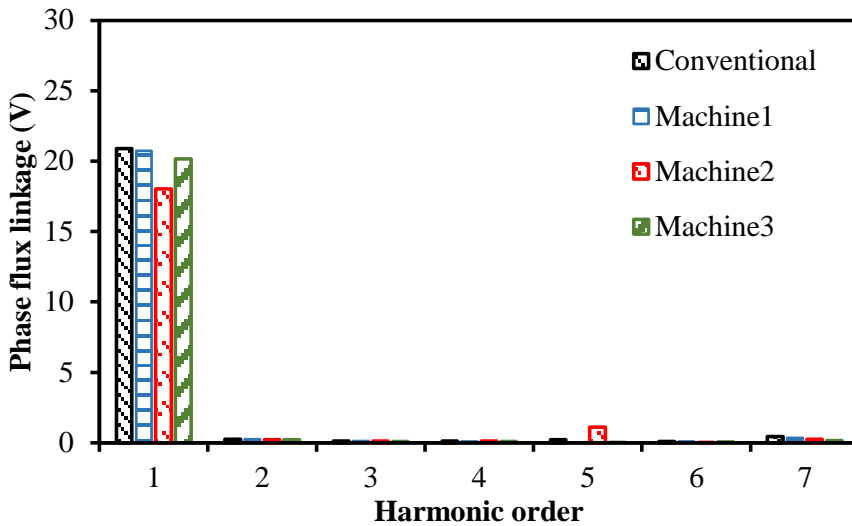
(b) Spectra

Fig. 2. 18 Phase flux linkage comparison.

The phase back EMF are compared in Fig. 2. 19.



(a) Waveforms



(b) Spectra

Fig. 2. 19 Phase back EMF comparison.

Since the back EMF is proportional to the phase flux linkage, the auxiliary slots have the similar effect on the back EMF comparing with the flux linkage. In terms of the harmonics content, all machines have a very sinusoidal waveform except for Machine 2 in which the 5th harmonic is more measurable comparing with other machines. As a result, the torque ripple of Machine 2 is aggravated.

### 2.4.2 Torque Characteristics

Fig. 2. 20 compares the cogging torques. It can be seen that Machine 1 has the lowest cogging torque which is due to the balanced air-gap permeance distribution caused by auxiliary slots.

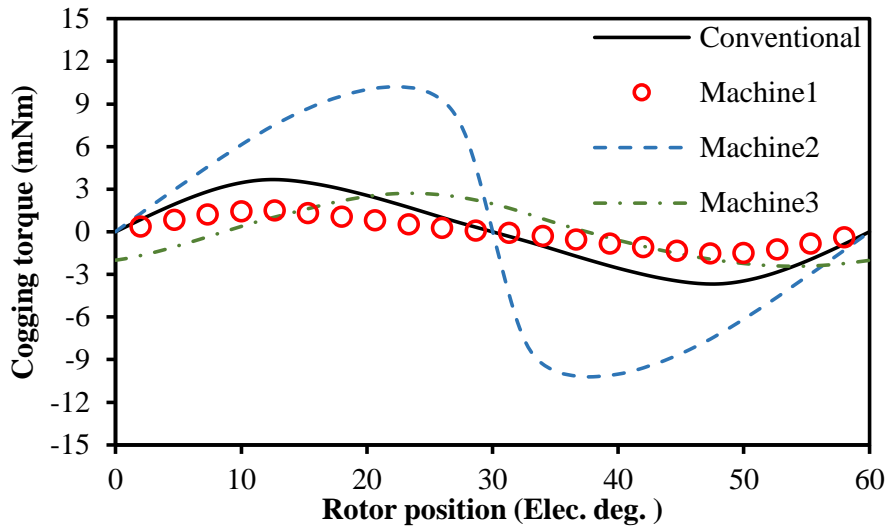


Fig. 2. 20 Cogging torque comparison.

Moreover, the difference between the conventional machine, Machine 1 and Machine 3 is very small. In contrast, the cogging torque of Machine 2 is much higher, which is mainly caused by the much larger auxiliary slots.

In addition, the on-load torques are calculated and shown in Fig. 2. 21.

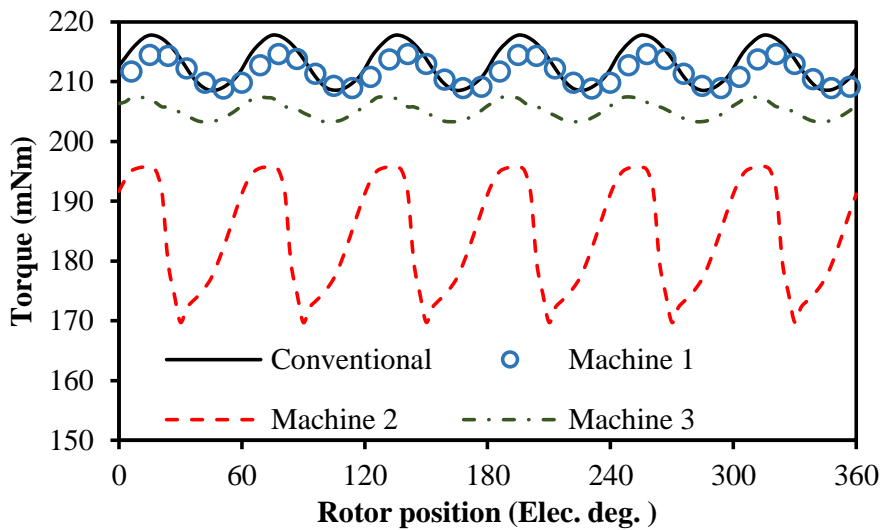


Fig. 2. 21 On-load torque comparison.

It is found that since the auxiliary slots are very small, there is only very slight difference between the conventional machine and Machine 1. However, since the auxiliary slots increase the equivalent air-gap length much more significantly in Machine 2 and Machine 3 comparing with Machine 1, the reduction of rated on-load torque in Machine 2 and Machine 3 is more measurable. In addition, the saturation in Machine 2 is much heavier due to the thinner tooth width. Consequently, the Machine

2 has the lowest output torque. The rated output torques are decreased by 0.7%, 11.5% and 4% in three machines, respectively.

The comparison of rated on-load torque ripple is shown in Table 2. 4. It shows the difference between Machine 1, Machine 3 and the conventional machine is very small, the slight reduction is mainly due to the mitigation of cogging torque. In contrast, Machine 2 has the largest torque ripple which is due to the increased cogging torque and the relative measurable back EMF harmonics.

Table 2. 4

Torque Ripple Comparison

Conventional	9.27 (mNm)	Machine2	26.14 (mNm)
Machine1	5.81 (mNm)	Machine3	4.20 (mNm)

## 2.5 Influence of Working Conditions

### 2.5.1 Comparison of Torques and UMFs in Machines with and without Auxiliary Slots

Previous sections investigated the performance of three machines with different auxiliary slots under rated working conditions according to the maximum torque per ampere (MTPA) control strategy. Since the machine mostly operates under rated working condition in various applications, e.g. vacuum cleaner, etc. The best performance under rated working condition is usually the most important. However, the load may change in some situations. Therefore, the effect of working conditions is also important which will be investigated in this section.

The maximum on-load UMFs and average torques of three machines with different working conditions are shown in Fig. 2. 22, in which  $\beta$  represents the current angle. It can be found that all of the machines have similar torque characteristics which are proportional to current amplitude but inversely proportional to current angle. However, since the on-load torque is inversely proportional to the equivalent air-gap length affected by auxiliary slots, Machine 2 has the lowest on-load torque and the conventional one has the highest on-load torque. It is worth noting that the Machine 1 has almost the same torque as the conventional machine, this is due to the auxiliary

slots in Machine 1 are very small, which, as a result, have negligible influence on the equivalent airgap length as well as tooth saturation.

As for the maximum UMFs, four machines have very different behaviors. It can be seen that the maximum UMF in the conventional machine is proportional to current amplitude but almost irrelevant to current angle in most situations. This is due to the fact that the slot openings are too small to affect UMF notably, and  $F_2$  dominates the value of on-load UMF. For the same reason, Machine 1 has very similar characteristics as the conventional one when the current is not too small. However, Machine 1 has very low UMF when the current is small, this is due to  $F_1'$  dominates the whole value of UMF in this condition, and  $F_1'$  is very small in Machine 1 due to the balanced airgap permeance distribution. In contrast, auxiliary slots have significant influence on the maximum UMF in Machine 2 and Machine 3. In Machine 2, the phase difference between  $F_1'$  and  $F_2'$  is reduced gradually with the increasing of current angle, and the additive effect makes on-load UMF increase significantly. Machine 3 can almost eliminate the UMF on rated working condition, and the reason has been detailed in Section 2.3.2. However, it should be noticed that since the proposed method employed in Machine 3 is using  $F_1'$  to cancel out  $F_2'$ , it is very hard to make Machine 3 have better overall performance, which is due to the amplitude and phase of  $F_2'$  vary with different working conditions. Nevertheless, the proposed method could offer better performance in a relative wide range as shown in Fig. 2. 22.

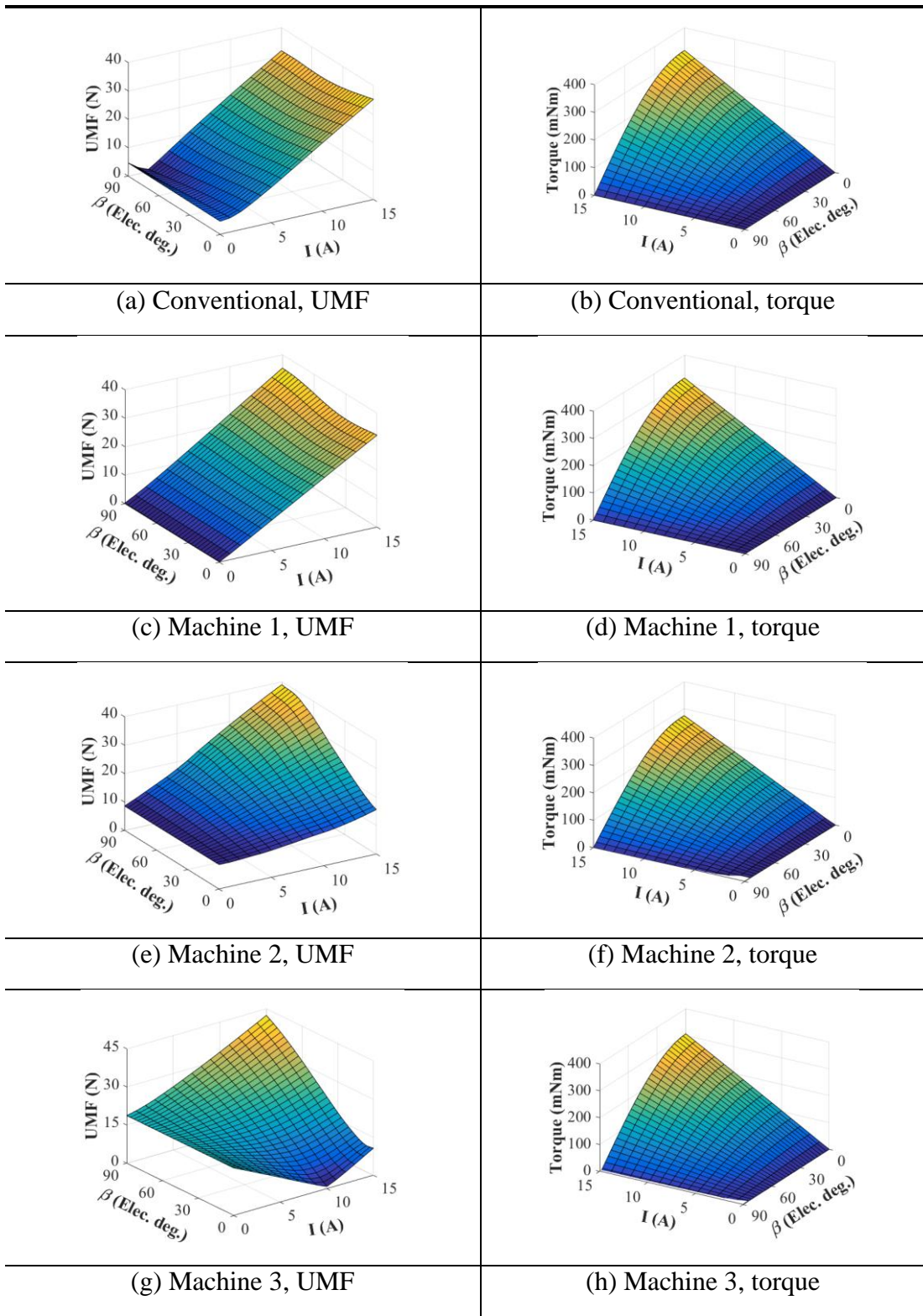


Fig. 2. 22 Performance of machines under different working conditions.

### 2.5.2 Influence of Current Amplitude on Machine 3

Since Machine 3 can reduce the most of the maximum rated on-load UMF, the influence of working condition on Machine 3 will be emphasized in this part. Although both current amplitude and current angle can affect the on-load UMF of Machine 3 significantly, the reasons are different. The influence of current amplitude is investigated at first. It should be noticed that the current angle is fixed as zero when the influence of current amplitude is investigated, and the current amplitude is fixed as 10 A when the effect of current angle is studied.

By way of example, the field distributions of Machine 3 with different input currents, i.e. 2A, 10A and 15A, are given in Fig. 2. 23, and the UMF components with different current amplitudes are shown in Fig. 2. 24.

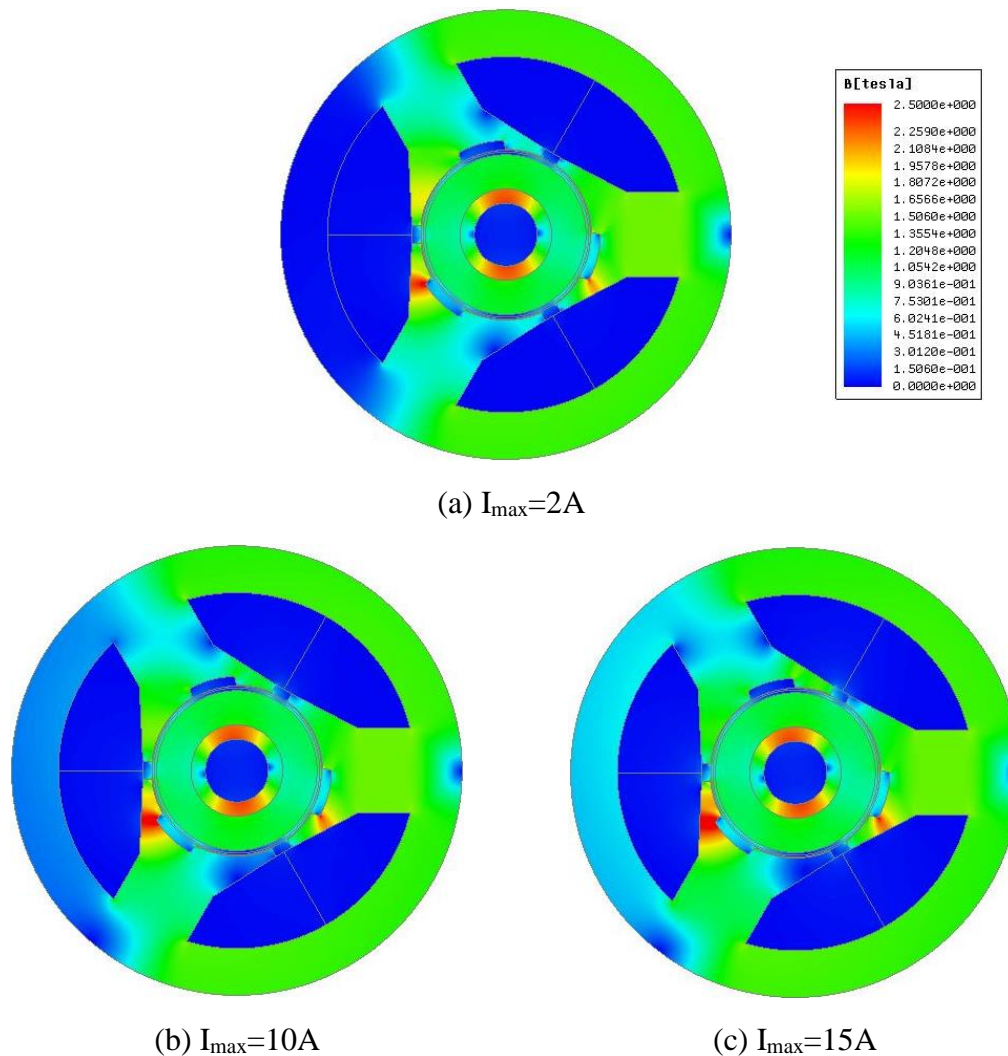


Fig. 2. 23 Field distributions with different input currents at 0s.

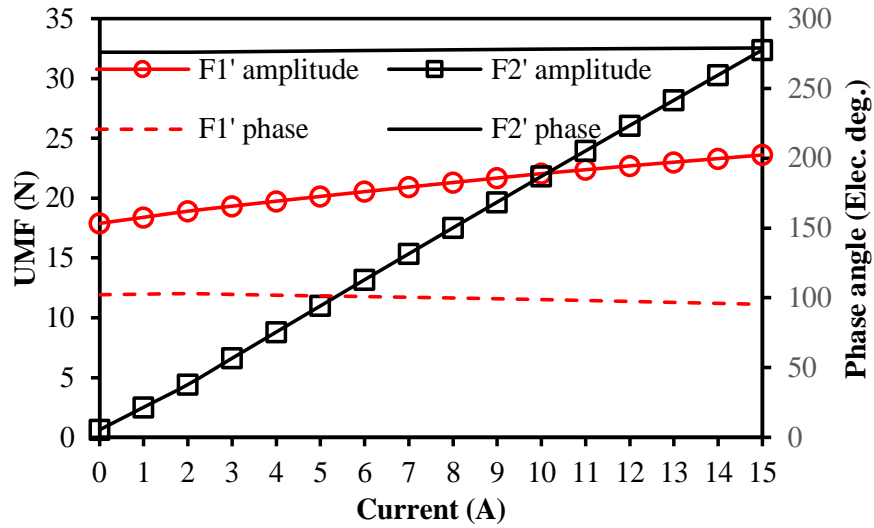


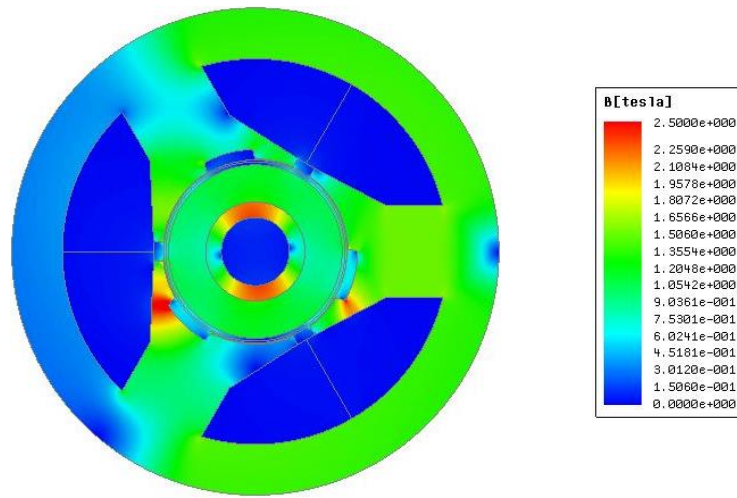
Fig. 2. 24  $F_1'$  and  $F_2'$  with different input current value at 0s.

It can be seen that the both  $F_1'$  and  $F_2'$  rise with the increase of input current. The increase of  $F_1'$  is mainly due to the aggravated saturation and the growth of  $F_2'$  is mainly caused by the improved armature field. As for their phase, since the rotor position and current angle are kept as the same, both of  $F_1'$  and  $F_2'$  remain the almost same phases during whole current interval.

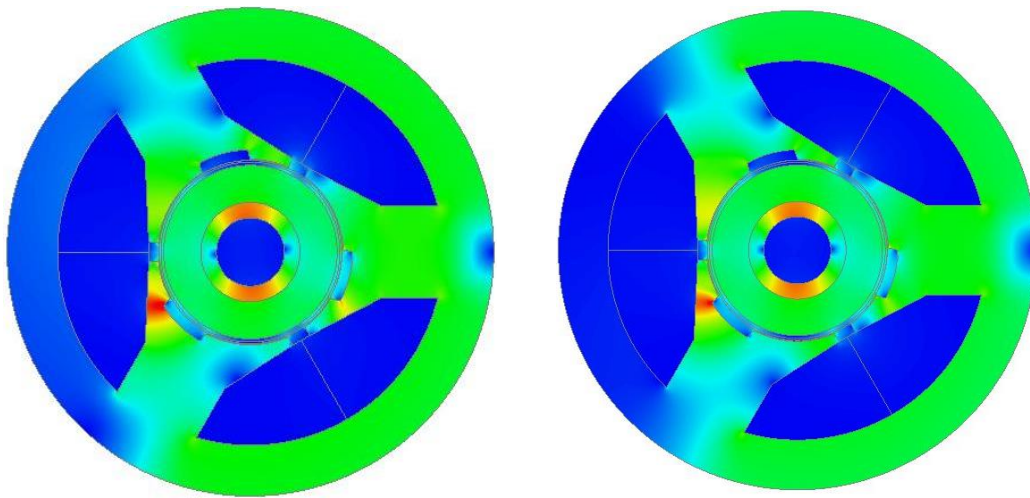
### 2.5.3 Influence of Current Angle on Machine 3

The influence of current angle on UMF is shown in Fig. 2. 25 and Fig. 2. 26.





(a) Current angle=0 Elec. Deg.



(b) Current angle=45 Elec. Deg.

(c) Current angle=85 Elec. Deg.

Fig. 2. 25 Field distribution with different current angle at 0s.

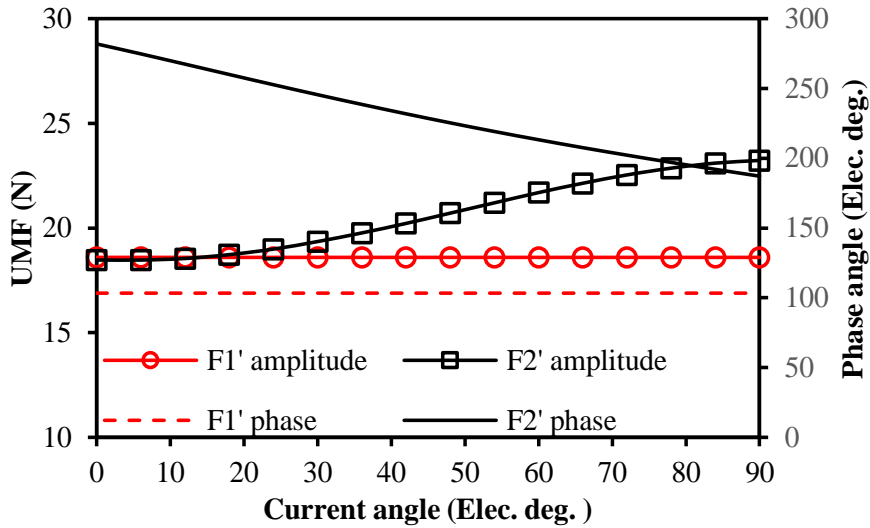


Fig. 2. 26.  $F_1'$  and  $F_2'$  with different current angle at 0s.

Different from the effect of the current amplitude, the current angle has great impact on the phase of  $F_2'$  which decreases from 270 degrees to 180 degrees almost linearly when current angle changes from 0 degree to 90 degrees. This is due to the fact that the phase of  $F_2'$  is determined by the phase of armature field as well as PM field, since the phase of PM field is not changed, the phase of  $F_2'$  is mainly decided by the phase of armature field, hence the current angle. As for the amplitude, both of  $F_1'$  and  $F_2'$  are affected, since the permeance distribution changes with the current angle as well.

## 2.6 Influence of Slot Opening Width

As one of the key design parameters, the slot opening width has significant influence on machine performance. In addition, the selection of slot opening width also depends on manufacture requirements, e.g. winding process, etc. Moreover, since the slot opening width can significantly influence the airgap permeance distribution, it can affect both no-load and on-load UMFs in 3-slot/2-pole machines. In the previous sections, the slot opening width is fixed as a constant value, i.e. 2mm. However, its value may be different in practice. As a result, the effectiveness of auxiliary slots on the maximum rated on-load UMF reduction may change with the variation of slot opening widths. Therefore, the influence of slot opening widths should be investigated, which will be detailed in this part.

### 2.6.1 Influence of Slot Opening Width on UMFs in Conventional Machines

The influence of slot opening width on UMFs in the conventional machine will be detailed at first. The range of slot opening width is chosen from 1mm to 4mm in this section, while the analysis method can be also applied on other value of the slot opening width.

The variation of the rated on-load UMF and its components, i.e.  $F_1$  and  $F_2$ , with different slot opening widths are shown in Fig. 2. 27. As can be seen, with the increase of slot opening widths, all UMFs ascend. Nevertheless, the value of  $F_2$  just rises slightly comparing with significantly increased  $F_1$ .

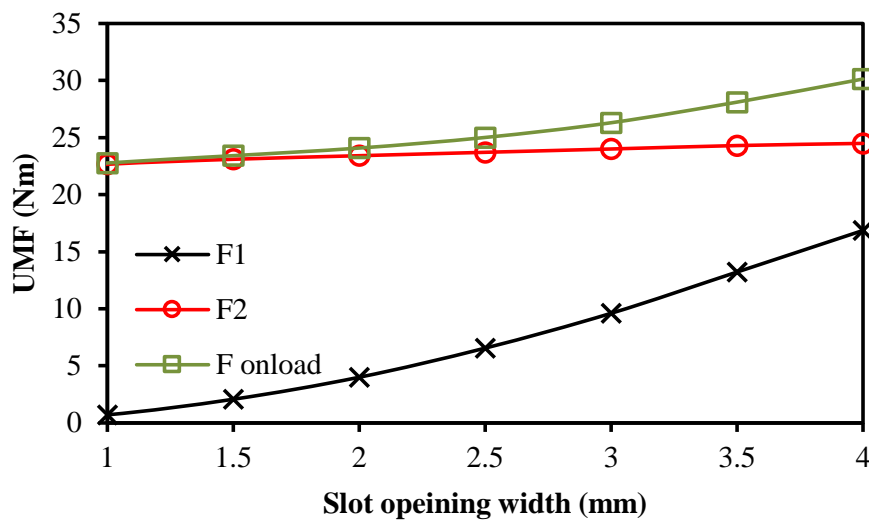
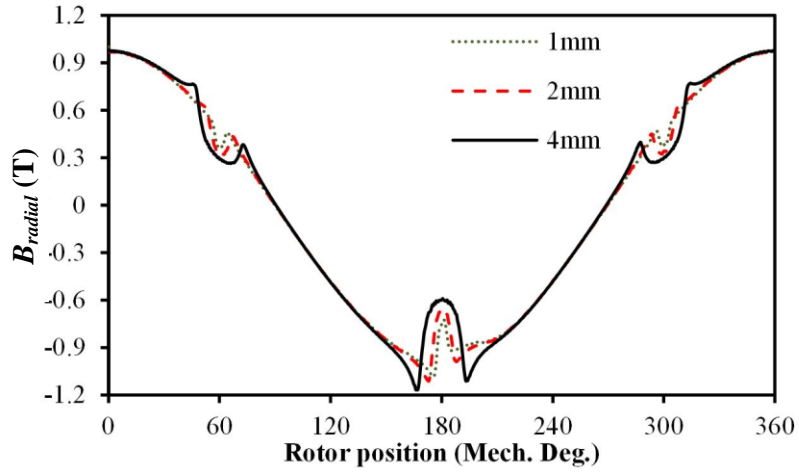


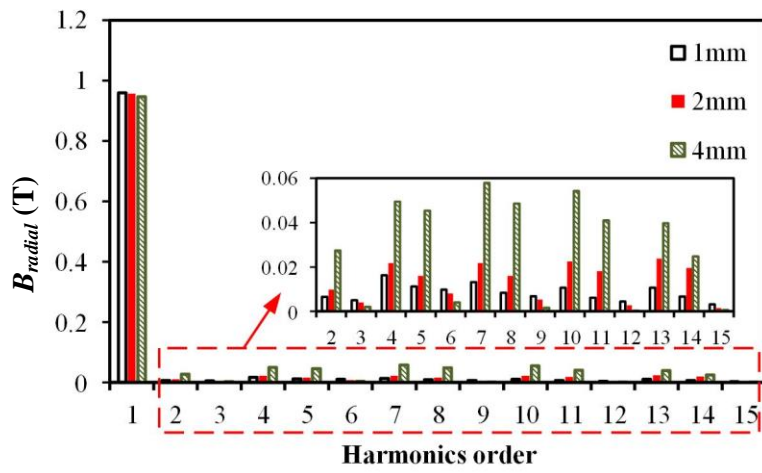
Fig. 2. 27 Variation of maximum UMFs with slot opening width at 0s.

In order to explain in more detail, the airgap flux densities of both PM and armature fields are shown in Fig. 2. 28. It should be noticed that in order to ease the comparison, only machines with 1mm, 2mm and 4mm slot opening widths are selected and studied.

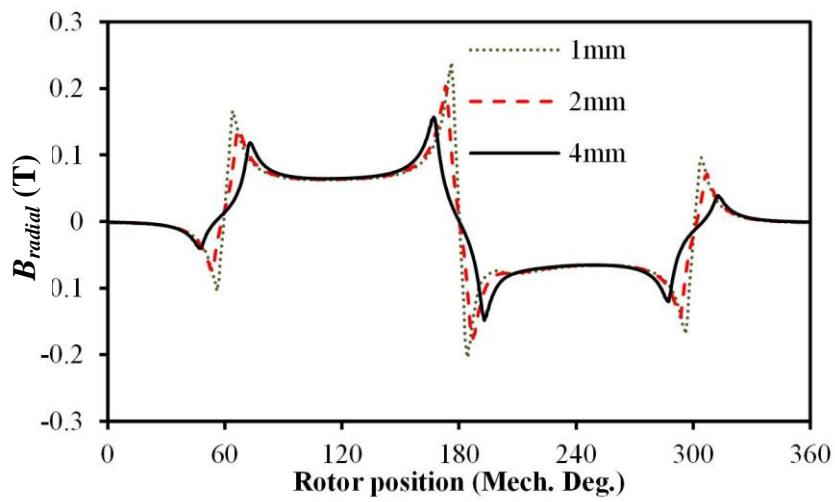
As can be seen, the fundamental PM field decreases slightly with slot opening width due to the increased equivalent airgap length. In contrast, the harmonic contents of PM field ascend, which is mainly due to the increased slotted effect. Since the increase of harmonic contents is much more significant than the decrease of the fundamental PM field, the value of  $F_1$  increases measurably.



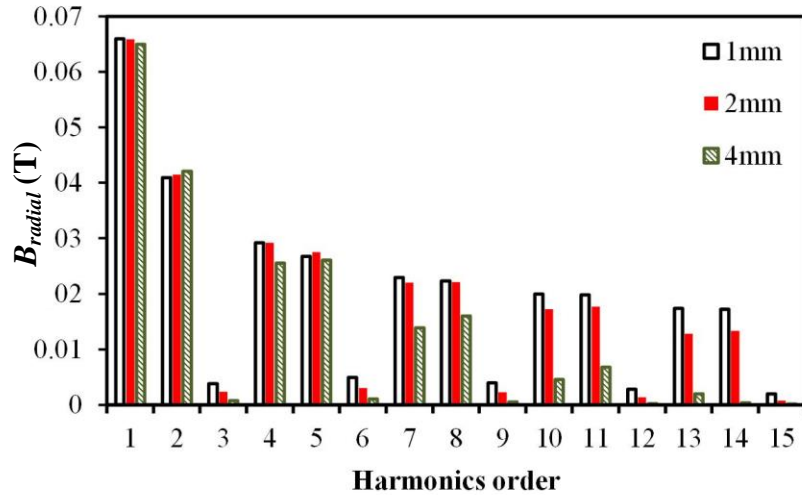
(a) PM field waveforms



(b) PM field spectra



(c) Armature field waveforms



(d) Armature field spectra

Fig. 2. 28 Variation of magnetic fields with slot opening width under rated working condition at 0s.

In contrast, the even order harmonics in armature field mainly come from the MMF harmonics due to the unbalanced winding structure. As a result, armature field harmonics are affected by the increased equivalent airgap length significantly when the slot opening width increases. Nevertheless, due to the relative large amplitude of low order armature field MMFs and permeance harmonics, the slotted effect still has relative measurable influence on low order armature spatial harmonics. Consequently, due to the cancel effect between the increased slotted effect and equivalent airgap length caused the increased slot opening width, the value of F2 just varies slightly.

### 2.6.2. Effectiveness of Different Auxiliary Slots on Rated On-Load UMF Reduction in Machines Having Different Slot Opening Widths

As shown, the slot opening width can affect the UMF in the conventional machine significantly. In this part, the effectiveness of different auxiliary slots on the maximum rated on-load UMF mitigation in machines with different slot opening widths will be detailed.

The basic stator parameters are the same as foregoing sections. The optimized stator topologies are shown in Fig. 2. 29. It should be noticed that only machines with 2mm and 4mm slot opening widths are presented. Otherwise this section will be very lengthy.

As can be seen, with the change of slot opening width, the auxiliary slots change significantly regardless the type of it.

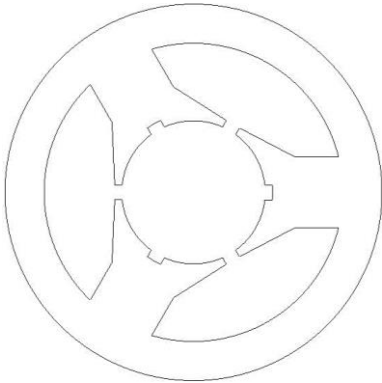
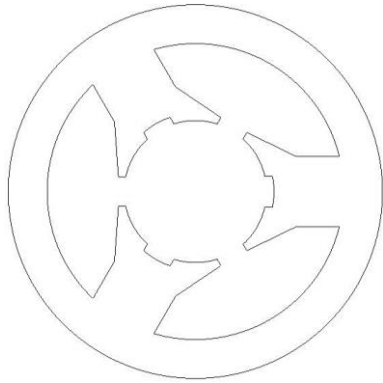
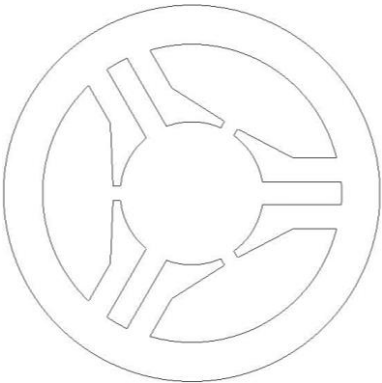
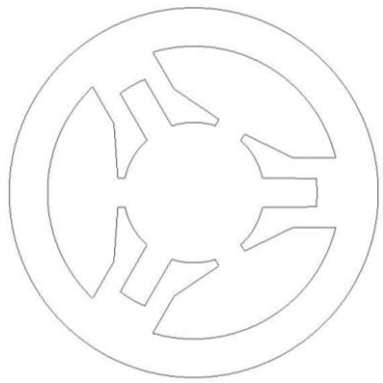
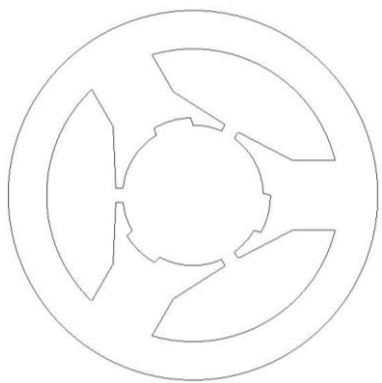
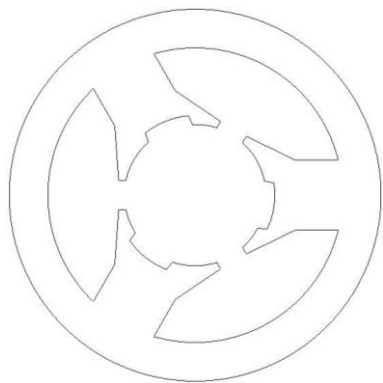
	$so=2\text{mm}$	$so=4\text{mm}$
Machine 1		
Machine 2		
Machine 3		

Fig. 2. 29 Stator cross sections of machines with different slot opening width and optimized auxiliary slots.

The variation of the maximum rated on-load UMF with slot opening width is shown in Fig. 2. 30. As can be seen, all three types of auxiliary slots can reduce the rated on-load UMF. In addition, the maximum rated on-load UMFs only fluctuate slightly

when slot opening width changes. Moreover, the Machine 3 still can offer the best performance.

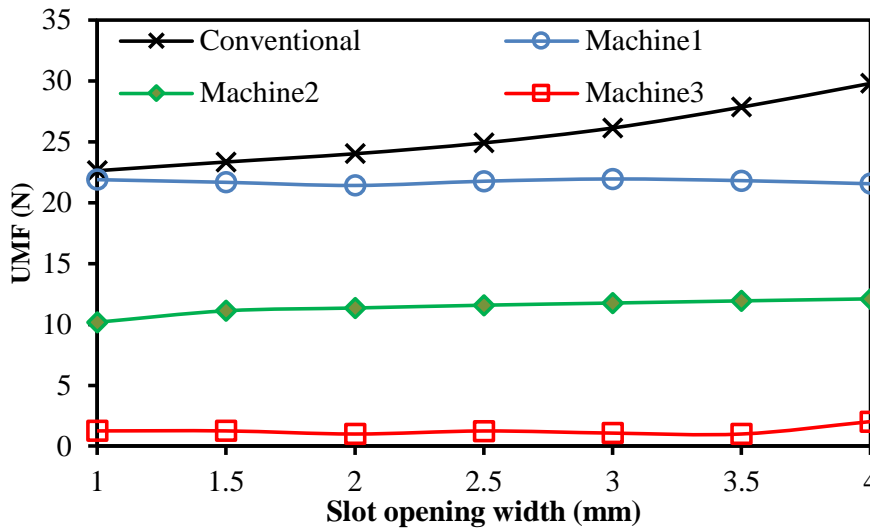
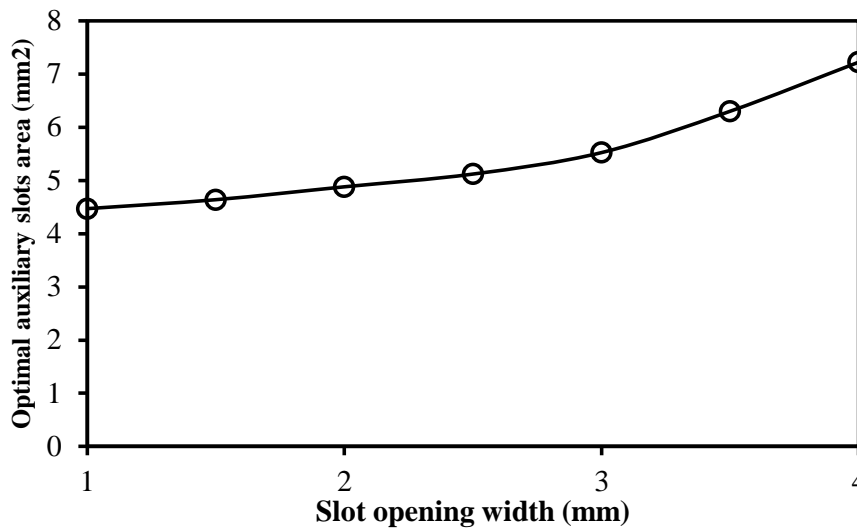
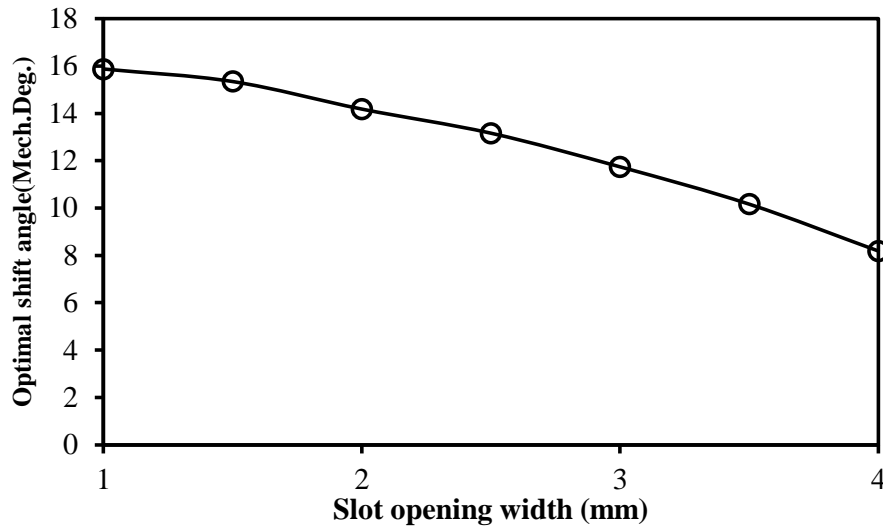


Fig. 2. 30 Variation of maximum rated on-load UMF with different slot opening width.

Due to the excellent performance of Machine 3, the influence of slot opening width on it should be emphasized. The variation of the optimal auxiliary slots parameters in Machine 3 with slot opening width are shown in Fig. 2. 31. As can be seen, its size increases with the slot opening width while the shift angle represents an opposite trend.



(a) Slot area



(b) Shift angle

Fig. 2. 31 Variation of design parameters of auxiliary slots in Machine 3 with slot opening width.

In order to explain it in more detail, the function of auxiliary slots in Machine 3 is better to be explained in another way. Due to the existence of auxiliary slots with the optimal size and position, a new UMF component can be introduced which has almost the same amplitude but opposite phase comparing with the original resultant rated on-load UMF. As a result, the maximum rated on-load UMF in the conventional machine can be significantly decreased. From this perspective, the value of  $F_1$  rises significantly due to the increase of slot opening width, and hence, the resultant rated on-load UMF. Consequently, a larger size of auxiliary slots is needed.

Nevertheless, with the increase of slot opening width,  $F_1$  acts as a more significant role in the rated on-load UMF, not only for its amplitude but also for the phase. As shown in the previous sections, since the phase difference between  $F_1$  and  $F_2$  is almost 90 degrees, and the phase of  $F_1$  is almost 0 degree. With the increase of  $F_1$ , the phase of resultant UMF becomes smaller. Consequently, the optimal shift angle for the auxiliary slots also needs to be reduced to balance the original rated on-load UMF.

## 2.7 Influence of Rotating Direction

The previous sections analyzed the machines with different types of auxiliary slots, which shows the auxiliary slots with the optimal size and position can offer the best performance in terms of the rated on-load UMF mitigation. However, the rotating



direction is fixed as clockwise in the foregoing analysis. In this section, the influence of rotating directions will be detailed.

### 2.7.1 Influence of Rotating Direction on Machine 3

The rated on-load UMFs of Machine 3 with both rotating directions are shown in Fig. 2. 32, in which “+” and “-” indicate the clockwise and anticlockwise rotating directions, respectively. The slot opening width is chosen as 2mm and the other detailed design parameters are the same as those in the previous sections.

As can be seen, Machine 3 can almost cancel out the rated on-load UMF in the clockwise rotating direction. In contrast, the rated on-load UMF is aggravated significantly when machine rotates in the opposite direction.

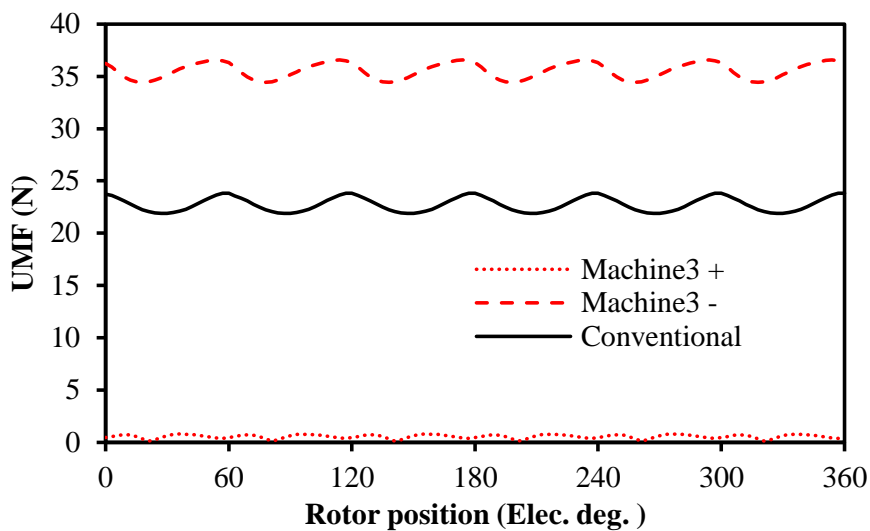
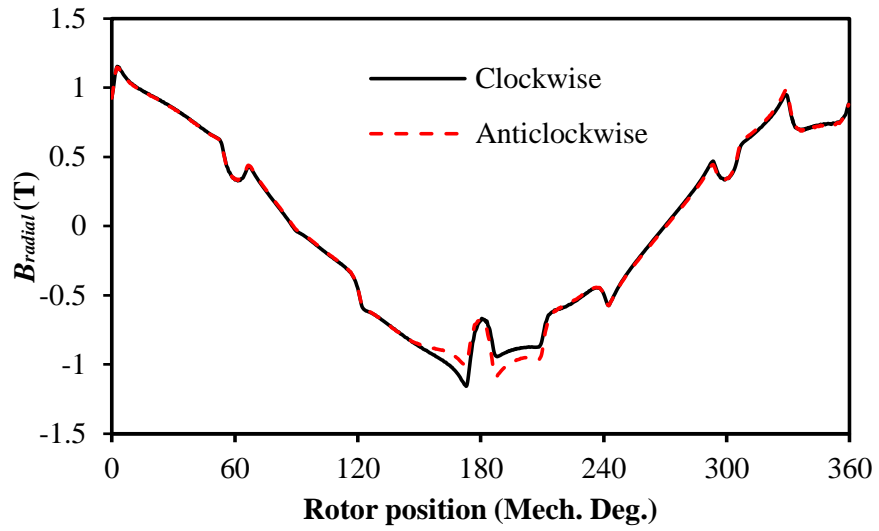


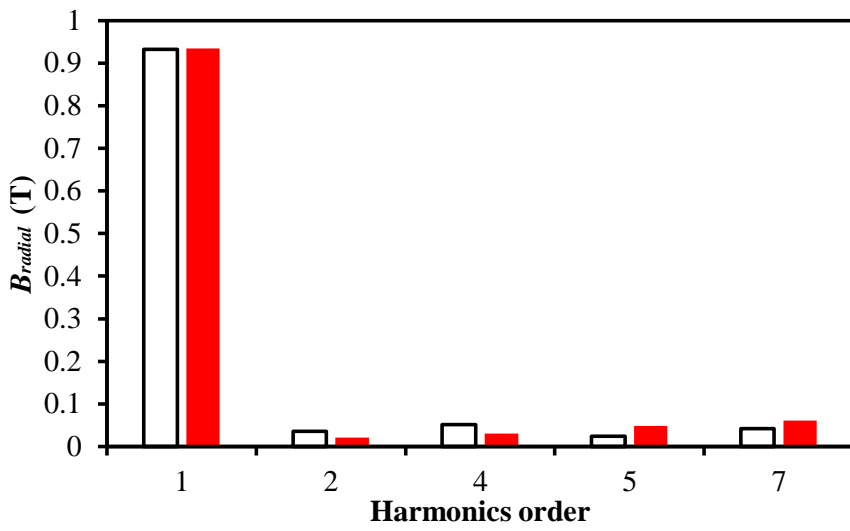
Fig. 2. 32 Comparison of rated on-load UMFs in Machine 3 with different rotating directions.

As mentioned before, since UMF essentially originates from the magnetic fields, the waveform and spectra of PM and armature fields under rated working conditions are investigated and shown in Fig. 2. 33 and Fig. 2. 34, of which both rotating directions are considered.

As can be seen, the amplitude of harmonics in both PM and armature fields just varies slightly when the rotating direction changes, which is mainly caused by airgap permeance distribution modification due to the change of stator saturation shown in Fig. 2. 35.

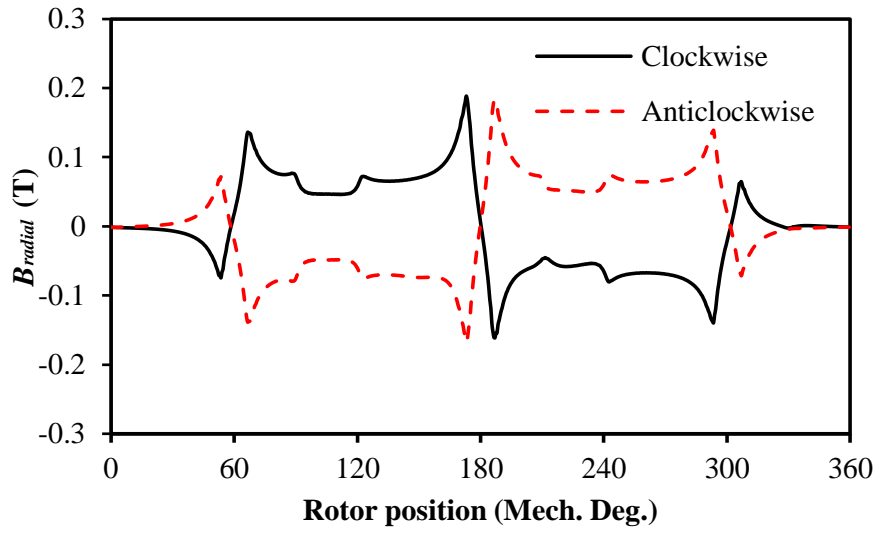


(a) Waveforms

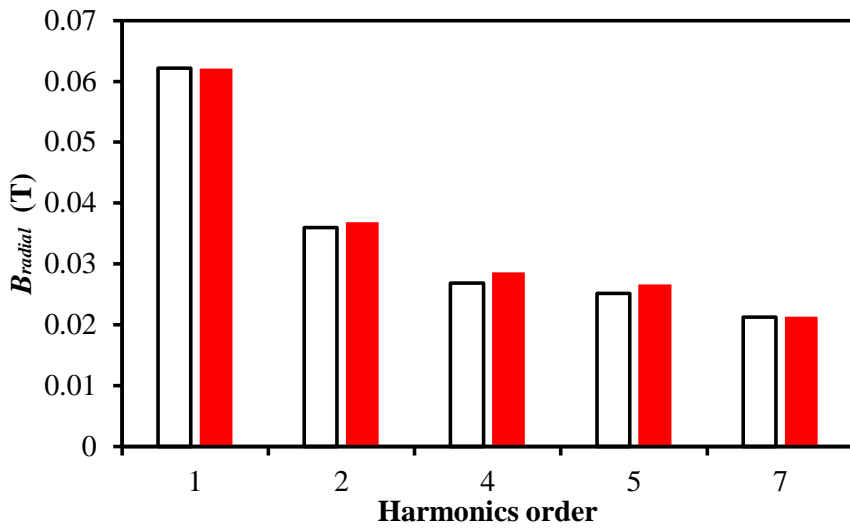


(b) Spectra

Fig. 2. 33 PM field flux density distributions in Machine 3 with different rotating directions under rated working condition at 0s.



(a) Waveforms



(b) Spectra

Fig. 2. 34. Armature field distributions in Machine 3 with different rotating directions under rated working condition at 0s.

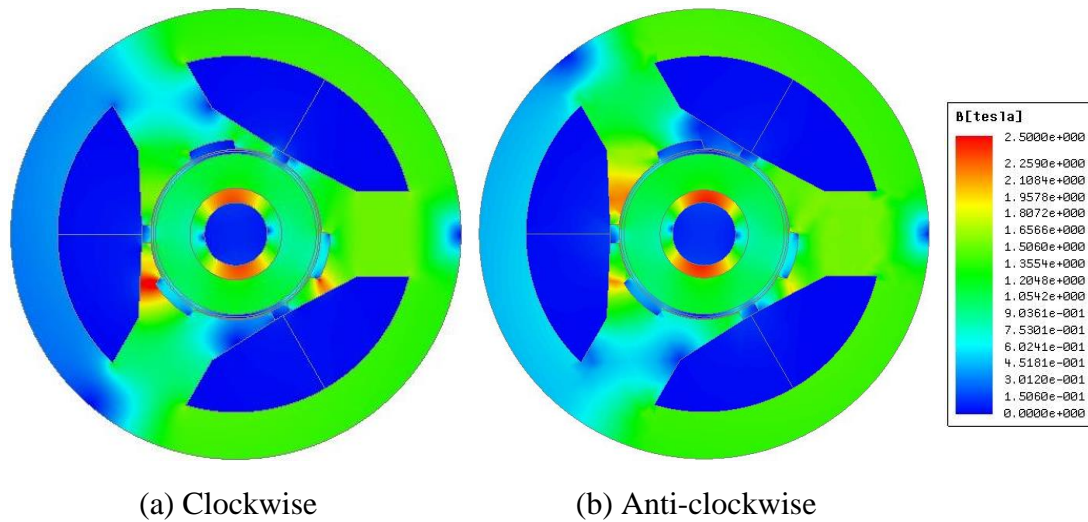
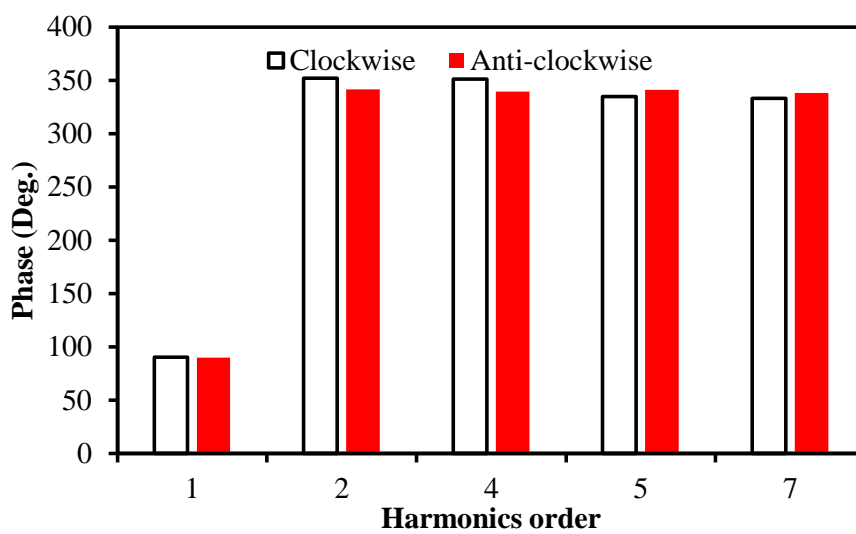


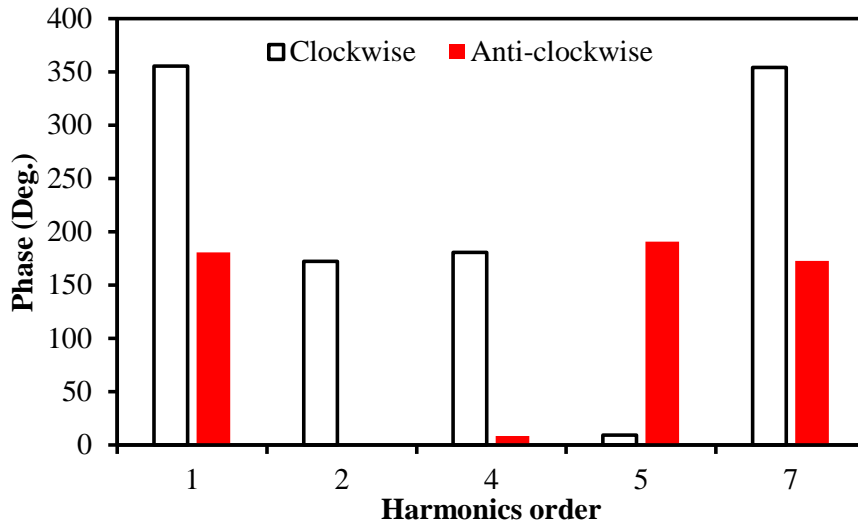
Fig. 2. 35. Rated on-load flux density distributions in Machine 3 with different rotating directions under rated working condition at 0s.

However, due to the reversed armature fields shown in Fig. 2. 34 and changed stator saturation condition shown in Fig. 2. 35, the phase of airgap flux density harmonics also varies when the rotating direction changes, especially the phase of armature field harmonics.

The phase of harmonics in Machine 3 with different rotating directions are compared in Fig. 2. 36. As shown, the armature field harmonics has almost opposite phase when the rotating direction changes, while the phase only changes slightly in PM field harmonics.



(a) PM field



(b) Armature field

Fig. 2. 36. Phase of harmonics in Machine 3 with different rotating directions under rated working condition at 0s.

Consequently, in Machine 3,  $F_1'$  changes slightly in both amplitude and phase when the rotating direction changes, while the  $F_2'$  has almost same amplitude but opposite direction. Therefore, the cancel effect between  $F_1'$  and  $F_2'$  in Machine 3 with clockwise rotating direction turns out to be additive effect when the rotating direction changes which is shown in Fig. 2. 37. As a result, the rated on-load UMF will be aggravated in Machine 3 when the rotating direction reverses.

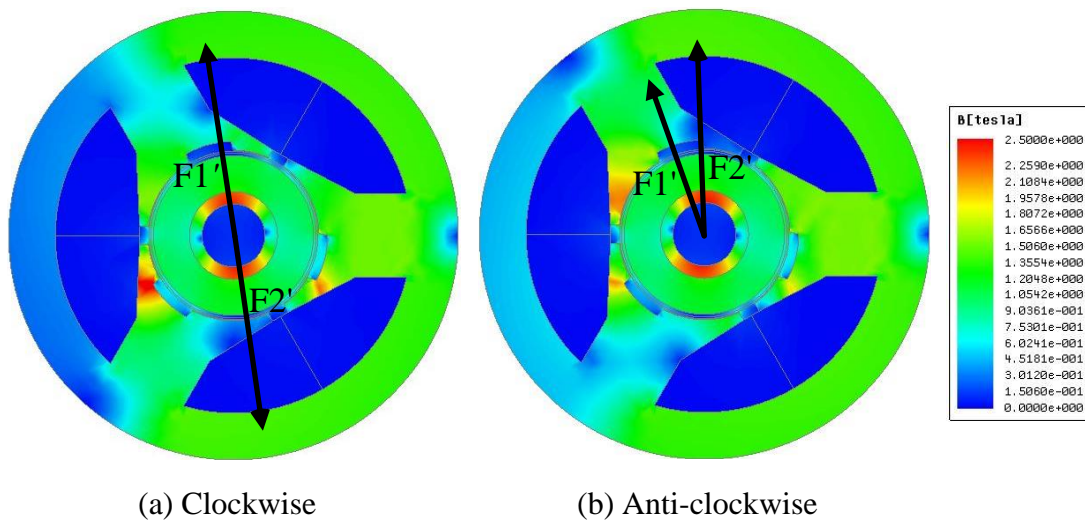


Fig. 2. 37. Directions of F1 and F2 in Machine 3 with different rotating directions under rated working condition at 0s.

### 2.7.2 Rated On-Load UMF Mitigation in Bidirectional Rotating Machines

However, both rotating directions may be required in specific applications, which indicates the auxiliary slots needs to be re-optimized in this situation. In order to ensure the auxiliary slots have the same effect on the maximum rated on-load UMF reduction when rotating direction changes, they need to be symmetrical along the middle of stator tooth.

Nevertheless, as shown in the foregoing analysis, the machine with one auxiliary slot in the middle of tooth optimized under rated working condition, i.e. Machine 2, can significantly decrease the output torque, which is very undesirable. Therefore, machines with two auxiliary slots per tooth is proposed as shown in Fig. 2. 38 which is named as Machine 4.

The global optimization and genetic algorithm are employed. The width, depth as well as position are optimized. The shift angle has the same definition comparing with former model and the optimal goal is the minimum rated on-load UMF.

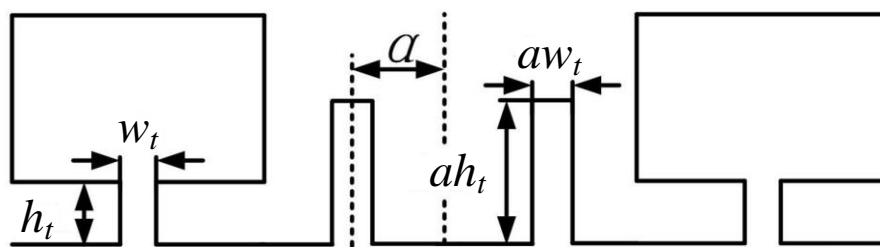


Fig. 2. 38. Auxiliary slots with optimized size and position in machine having bi-rotating directions.

The cross section of the optimized Machine 4 is shown in Fig. 2. 39, and the detailed parameters of the optimal auxiliary slots are listed in Table 2. 5. The comparison of rated on-load UMFs and torques is shown in Fig. 2. 40 and Fig. 2. 41, respectively.

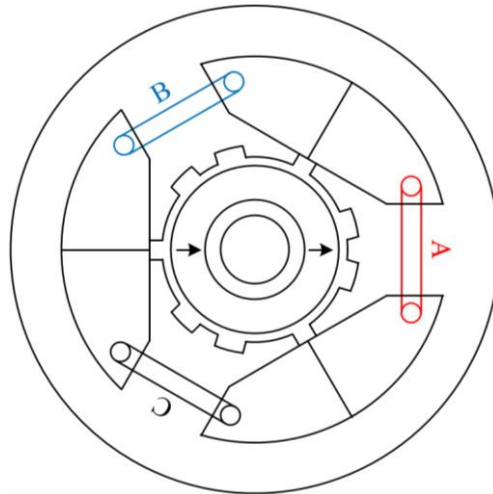


Fig. 2. 39. Cross section.

Table 2. 5

Specifications of Optimal Auxiliary Slots in Machine 4

Auxiliary slot opening height (mm)	1.18	Auxiliary slot opening width (mm)	2.93
Auxiliary slots shift angle (Deg.)	15.26		

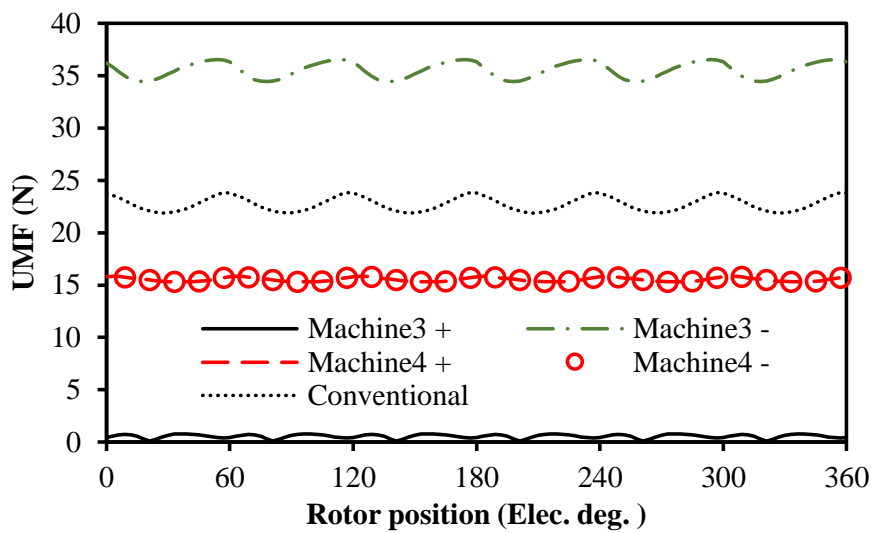


Fig. 2. 40. Variation of rated on-load UMF with rotor position.

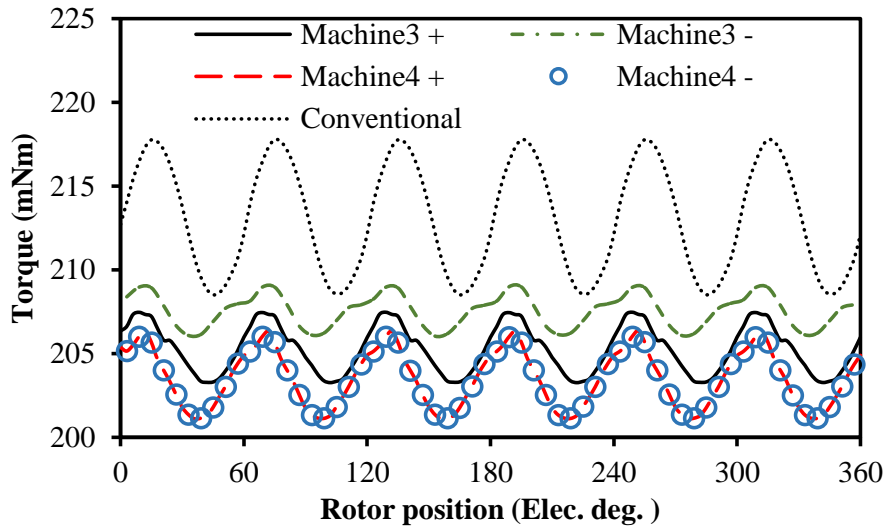


Fig. 2. 41. Variation of rated on-load output torque with rotor position.

As can be seen, the rotating direction has no influence on Machine 4, in which the maximum rated on-load UMF is decreased as much as 33%. Moreover, the torque reduction in Machine 4 is 4.47% in both directions. In contrast, the torque decreases by 4% in Machine3 with clockwise direction and 2.8% with anticlockwise direction.

However, it should be noticed that although both Machine 3 and Machine 4 use the auxiliary slots, the mechanisms descending the rated on-load UMF in these two machines are very different. In order to investigate it in more detail, the amplitude and phase of UMF components in machines with clockwise rotating direction are shown in Fig. 2. 42 and Table 2. 6, respectively.

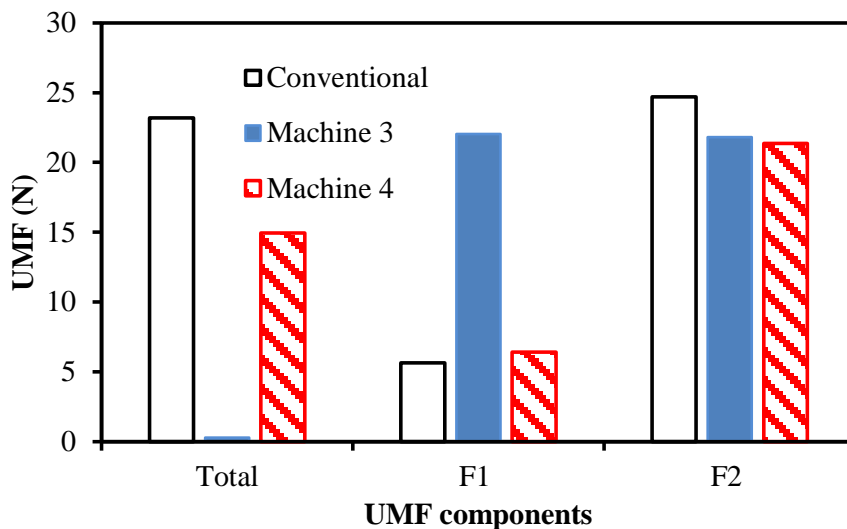


Fig. 2. 42. Amplitude of UMF components under rated working condition at 0s with clockwise rotating direction.



Table 2. 6

Phase of UMF Components Under Rated Working Condition at 0s with Clockwise Rotating Direction

	Conventional	Machine 3	Machine 4
$F_1$	23.7 degree	98.6 degree	90.5 degree
$F_2$	273.8 degree	278.2 degree	273.3 degree

As shown, the difference of  $F_2'$  among all three machines is very small in terms of both amplitude and phase, which indicates that the auxiliary slots have small influence on  $F_2'$ . The reason has been detailed in 2.3.2 already.

However, it can be seen that different from the conventional machine,  $F_1'$  has opposite direction comparing with  $F_2'$  in both Machine 3 and Machine 4, which results in measurable mitigation of rated on-load UMF. In other words, both Machine 3 and Machine 4 modify the phase of  $F_1'$  significantly.

Nevertheless, the phase change of  $F_1'$  in Machine 3 is mainly due to the modified phase of airgap permeance harmonics and partially caused by stator saturation, which has been detailed in the previous sections. Differently, due to the auxiliary slots are symmetrical along the middle of stator tooth in Machine 4, the phase of  $F_1'$  is changed by the asymmetric saturation distribution in stator only.

For the validation, the UMF vectors in both Machine 3 and Machine 4 with linear soft magnetic material and clockwise rotating direction are shown in Fig. 2. 43. The phase of  $F_1'$  is 127. 6 degree in Machine 3 but 180 degree in Machine 4. Consequently, it can be seen that the phase of  $F_1'$  is changed by auxiliary slots in Machine 3 even if when the saturation is not considered, while the phase of  $F_1'$  in Machine 4 has the same phase of the no-load UMF.

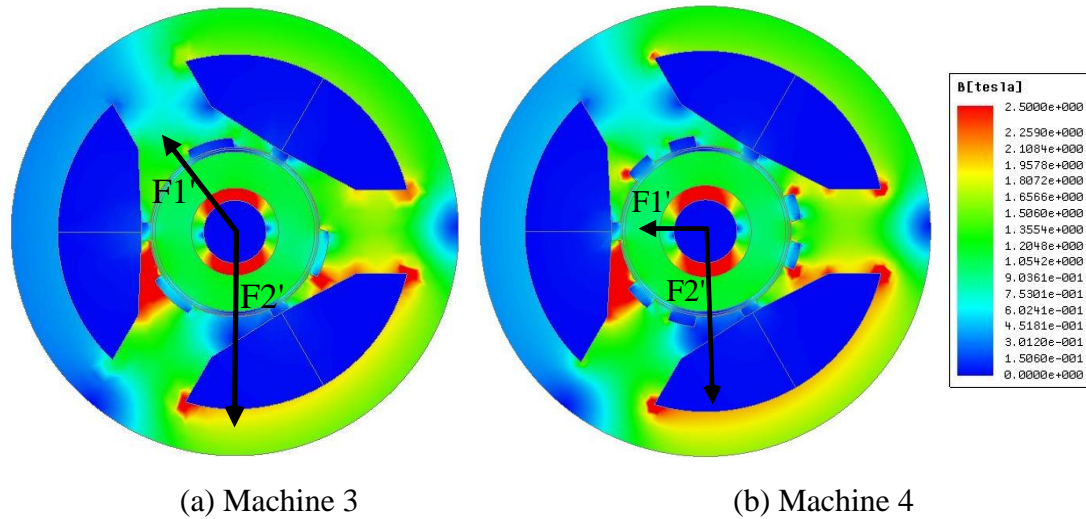


Fig. 2. 43. UMF vectors in machines with linear soft magnetic material under rated working condition under rated working condition at 0s with clockwise rotating direction.

### 2.7.3 Influence of Working Conditions

In the previous sections, a different type of auxiliary slots has been proposed for reducing rated on-load UMF in bidirectional rotating machines, and the mechanism has been investigated.

Nevertheless, it is optimized and studied under rated working condition. However, as mentioned in the previous sections, the working condition may change in practice. As a result, its influence on UMF and output torque needs to be investigated, which will be detailed in this part.

UMFs and output torques in machines with different type auxiliary slots and working conditions are shown in Fig. 2. 44 and Fig. 2. 45, respectively. Both rotating directions are considered. It should be noticed that since the rotating direction has no influence on the conventional machine and Machine 4, only the performance of these two machines with clockwise rotating direction are shown.

In terms of UMFs, Machine 4 has very similar characteristics comparing with the conventional one, but it can offer lower UMF when the current angle is small. Nevertheless, the UMF is significantly aggravated in Machine 3 in all working conditions when machine rotates anticlockwise.

As for the output torque, all machines have the similar output torque characteristics regardless of the rotating direction, which has been explained in the previous sections. Moreover, the torque reduction in Machine 3 and Machine 4 is very small under all working conditions.

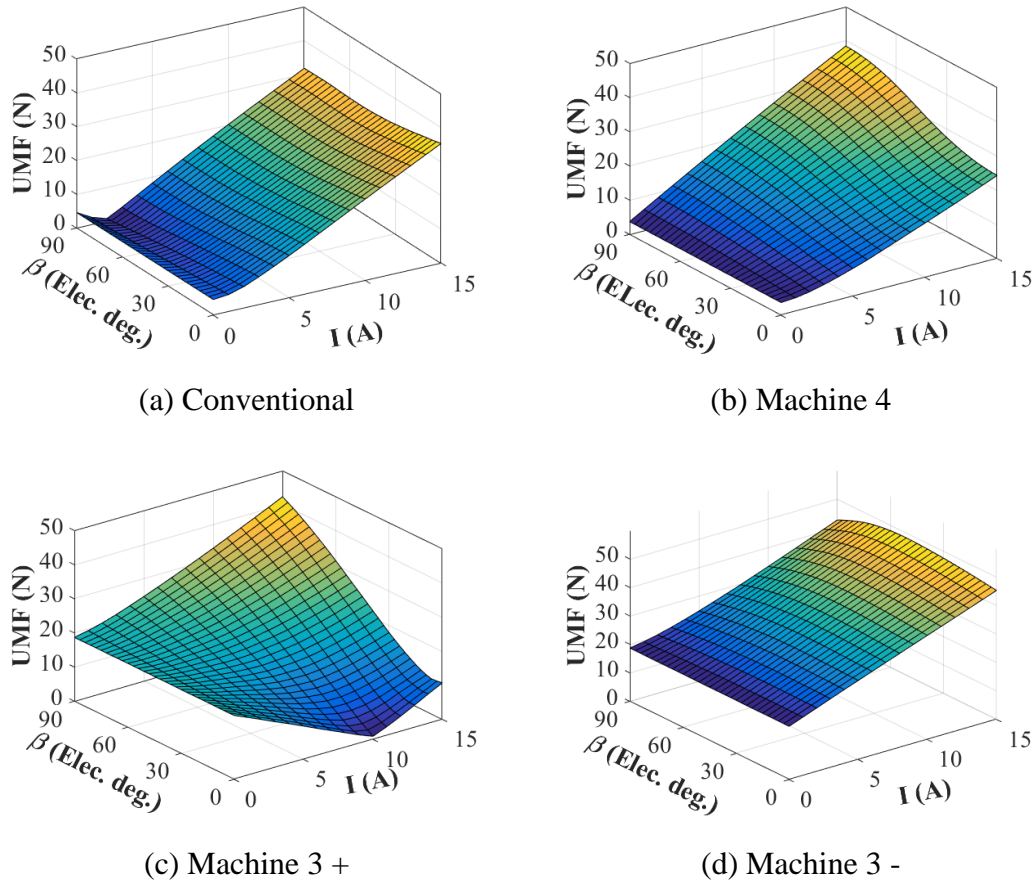


Fig. 2. 44. Variation of UMF with working conditions.

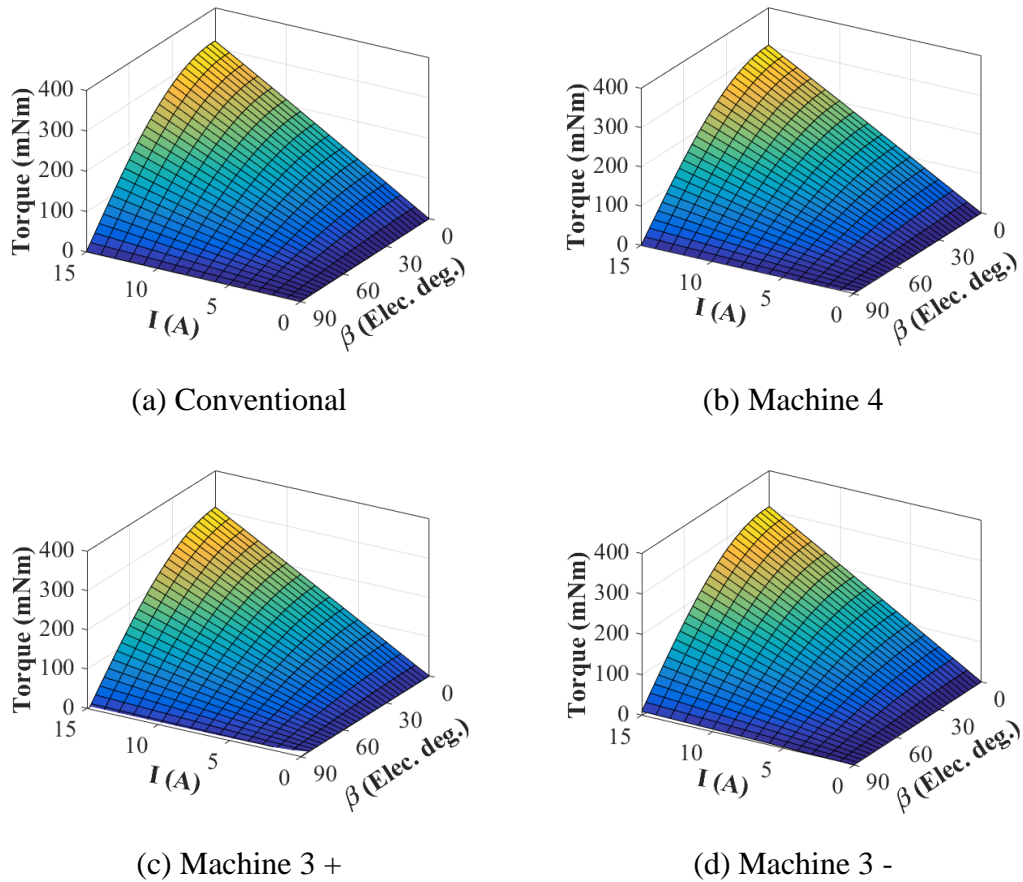
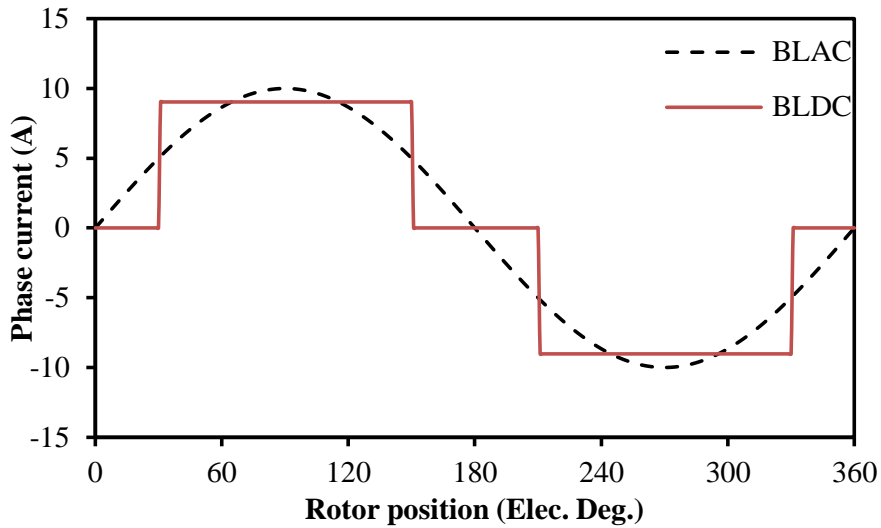


Fig. 2. 45. Variation of output torque with working conditions.

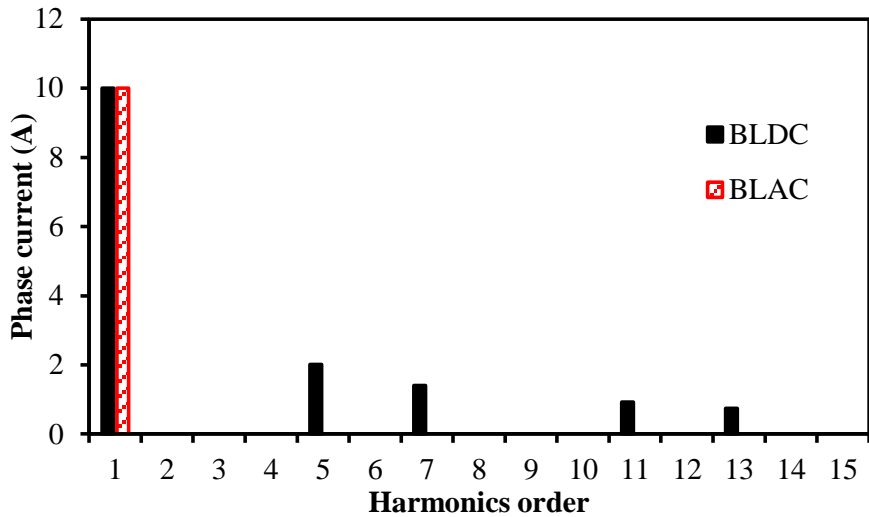
## 2.8 Influence of Drive Mode

In the previous sections, the brushless AC (BLAC) drive mode is used, which indicates the time harmonics has not been considered. However, in practice, the brushless DC (BLDC) drive mode is usually selected for ultra-high speed machines. As shown in literatures, the time harmonics caused by BLDC drive mode can have significant influence on the rated on-load UMF. Consequently, the influence of drive mode on the rated on-load UMF reduction will be investigated in detail in this section.

The comparison of input currents with different drive modes is shown in Fig. 2. 46. It should be noticed that the fundamental current is kept as the same in these two drive modes, which results in lower peak current value in BLDC machines.



(a) Waveforms



(b) Spectra

Fig. 2. 46. Comparison of current waveforms with different drive modes.

As can be seen, there are abundant time harmonics in BLDC machines, which can result in additional UMF and torque ripple. In addition, different drive modes also affect the magnet eddy current loss significantly which will be detailed in next chapter.

The variations of rated on-load UMFs in machines with different drive modes are shown in Fig. 2. 47. As shown, the shape of rated on-load UMF is almost circular when BLAC drive mode is used, the slightly deformation is mainly due to the local saturation.

Nevertheless, in the BLDC machine, the force locus is affected by the time harmonics measurably, which has relative irregular shape.

Since the time harmonics in BLDC drive mode leads to additional UMF and affects the stator saturation, it may influence the effectiveness of auxiliary slots. As a result, the auxiliary slots have to be re-optimized when BLDC drive mode is used. It should be noticed that the Machine 3 is selected here due to its excellent performance, while the method can be also applied to any other type of auxiliary slots.

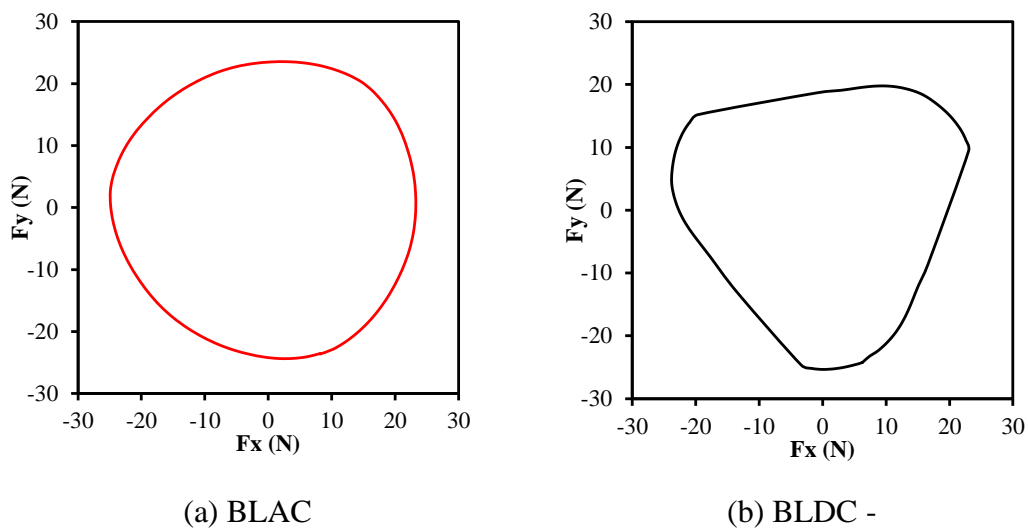


Fig. 2. 47. Loci of rated on-load UMFs in machines having different drive modes.

The detailed design parameters of optimal auxiliary slots in Machine 3 with different drive mode are listed in Table 2. 7.

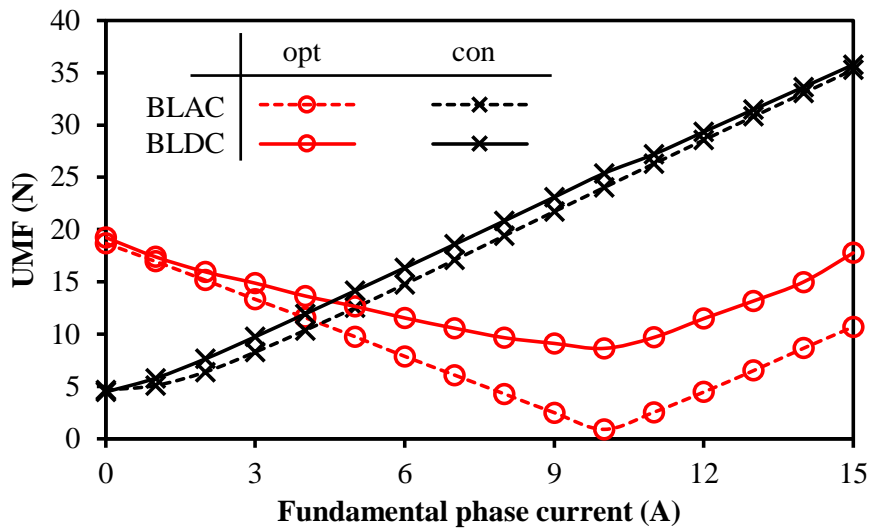
Table 2. 7

Size Comparison of The Optimal Auxiliary Slot in Machines Having Different Drive Mode

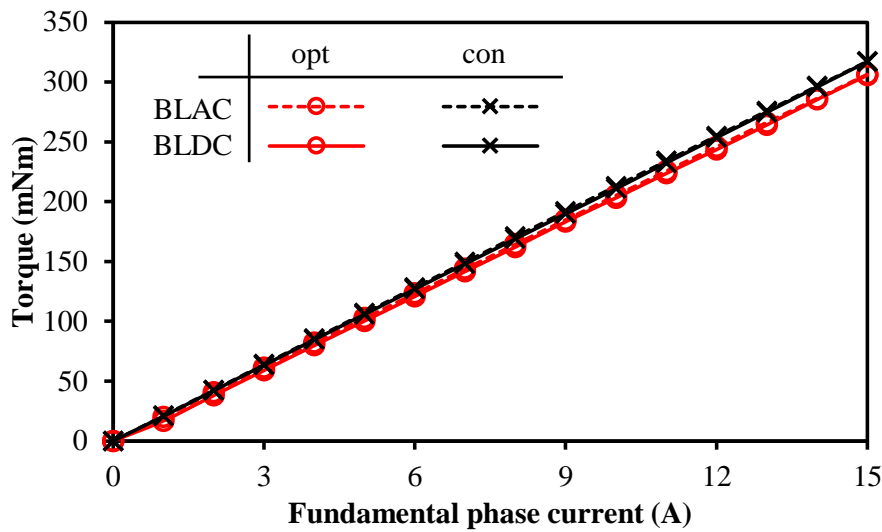
	BLDC	BLAC
Auxiliary slots width (mm)	4.72	4.98
Auxiliary slots height (mm)	1.15	0.98
Shift angle (Mech. Deg.)	13.21	14.18

The variations of UMFs and output torques in Machine 3 with different drive modes are shown in Fig. 2. 48. As can be seen, the maximum rated on-load UMF can be reduced as much as 65.9% in Machine 3 with BLDC drive mode, which indicates that

the Machine 3 can also offer good performance as for rated on-load UMF mitigation in BLDC machines.



(a) Maximum on-load UMF



(b) Average torque

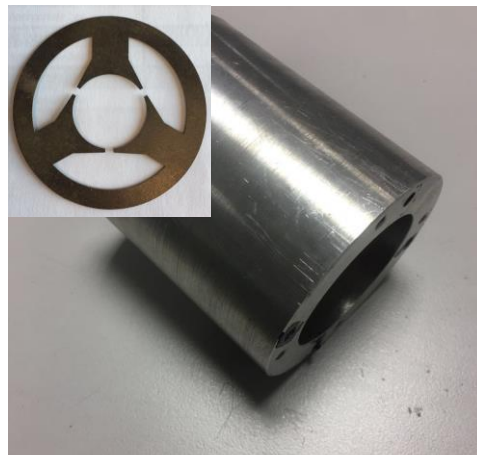
Fig. 2. 48. Variation of machine performance with fundamental phase input current.

In terms of output torque, its value decreases when auxiliary slots are introduced, which is due to the increased equivalent airgap length. Nevertheless, since the size of auxiliary slots is relative small, the reduction of output torque is slight regardless of the drive mode.

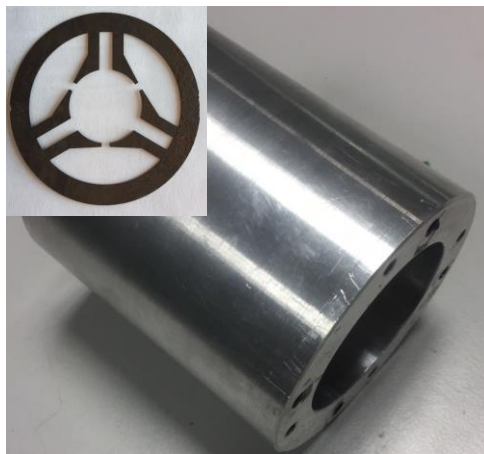
## 2.9 Experimental Validation

### 2.9.1 Prototype Machines and Test Rig

To validate the previous numerical analyses, three prototype machines are built, i.e., the conventional machine, Machine 2 and Machine 3. All three prototype machines as well as the test rig are designed and built by myself. Meanwhile, the Department of Electronic and Electrical Engineering of the University of Sheffield provided invaluable help in terms of the manufacture of prototype machines. The rated current is selected as 10A and the current angle is chosen as zero electrical degree. The detailed main design parameters are listed in previous sections. It should be noticed that the Machine 1 has not been built since it has very similar electromagnetic performance comparing with the conventional machine. The photos of three prototype machines are shown in Fig. 2. 49. All machines share the same rotor, in which the magnetic ring is used.



(a) Conventional machine



(b) Machine 2



(c) Machine 3





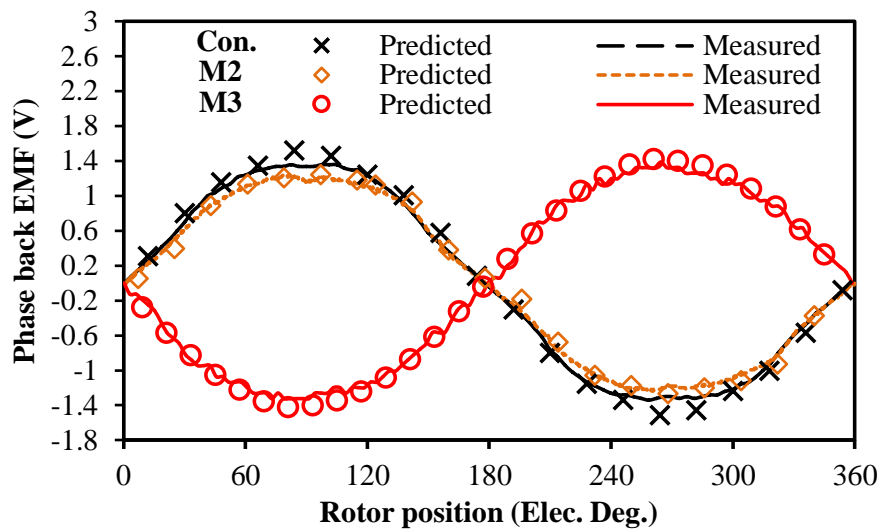
(d) Rotor

Fig. 2. 49 Stators and rotor for the prototype 3-slot/2-pole machines.

The back EMFs and static torques are tested at first and the UMF is also carried out for validation.

### 2.9.2 Back EMF Waveforms

The measured phase back EMFs with 1000 r/min are shown in Fig. 2. 50 which have excellent agreements comparing with the predicted values. The slight difference is mainly due to the manufacture error as well as the end effect. Moreover, it is evident that the conventional machine has the highest phase back EMF, while the difference between Machine 3 and the conventional machine is very small, the slight reduction is due to the increased equivalent airgap length caused by the auxiliary slots.



(a) Waveforms

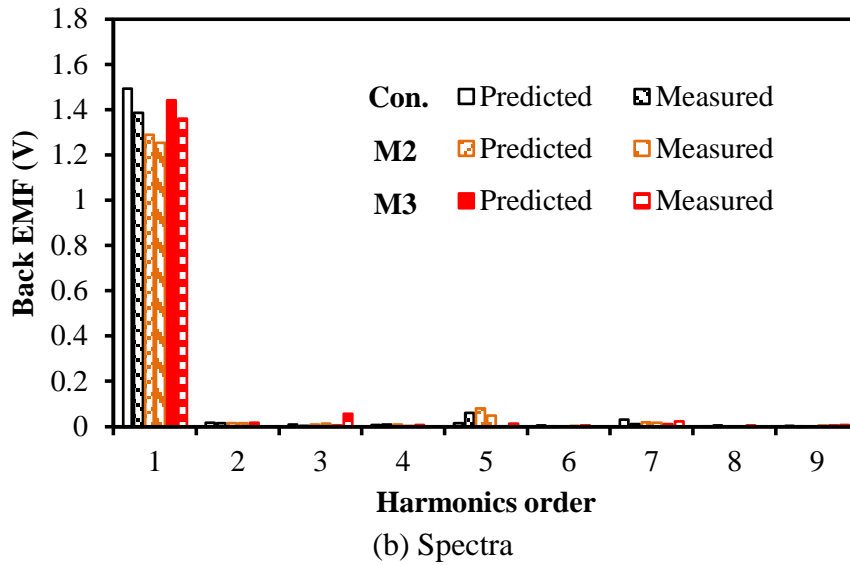
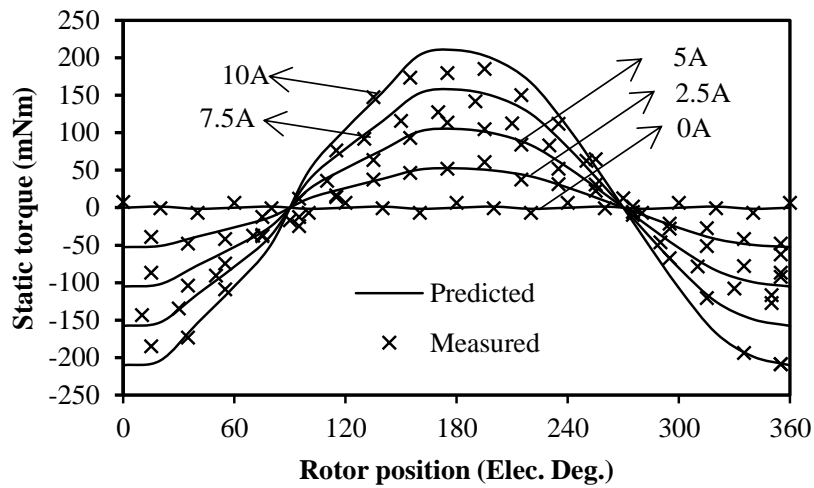


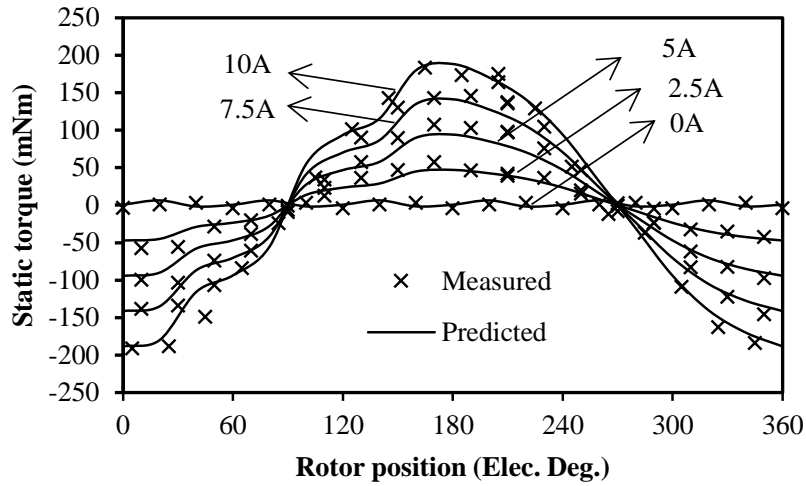
Fig. 2. 50 Comparison of FE-predicted and measured back EMFs at 1000r/min.

### 2.9.3 Static Torque Waveforms

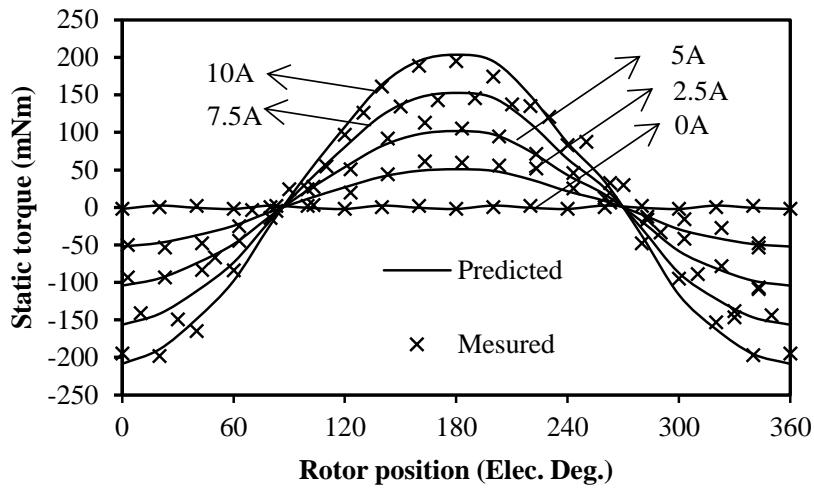
In addition, the predicted and measured static torques with different rotor positions and currents are compared in Fig. 2. 51. Good agreements can be observed, while there is still slight error which is due to the tolerance in manufacturing and the end effect. In addition, the test rig may also have influence on the measured value since the static torque is small and relative sensitive to the test environment.



(a) Conventional machine



(b) Machine 2



(c) Machine 3

Fig. 2. 51 Comparison of FE-predicted and measured static torques with different rotor positions and q-axis currents.

### 2.9.4 UMF waveforms

The UMFs are also tested. It should be noticed that it is very complicated to measure the variation of the UMF with different rotor positions. Instead, the UMF with one fixed rotor position is tested. As for the fixed rotor position, it is chosen as the position under zero d-axis current control for all machines, which means the North Pole is always aligned with the Phase A.

It should be mentioned that the phase of maximum UMF changes with the input current, which means it is very hard to measure it directly even if the rotor is kept as the same position. However, it is possible to measure both the vertical and horizontal UMF

components, and the resultant UMF can be obtained and observed by using the interpolation method. As a result, the special end cap needs to be used which is shown in Fig. 2. 52, the shaft hole is deeper as much as 0.5mm for one side in the special end cap. By this means, the shaft can move from the normal position to an eccentric position.

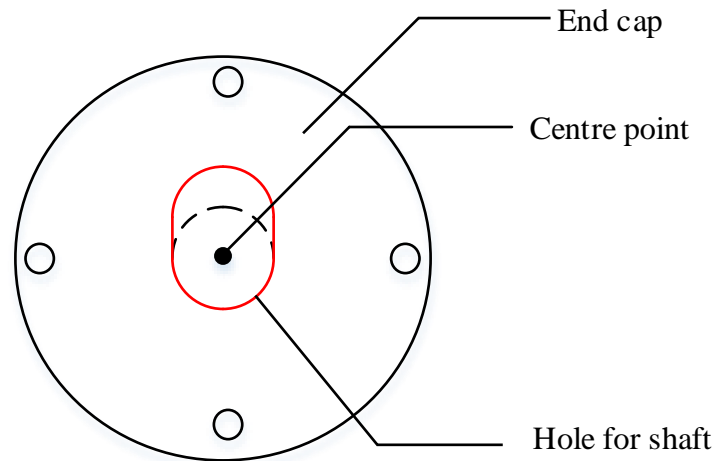
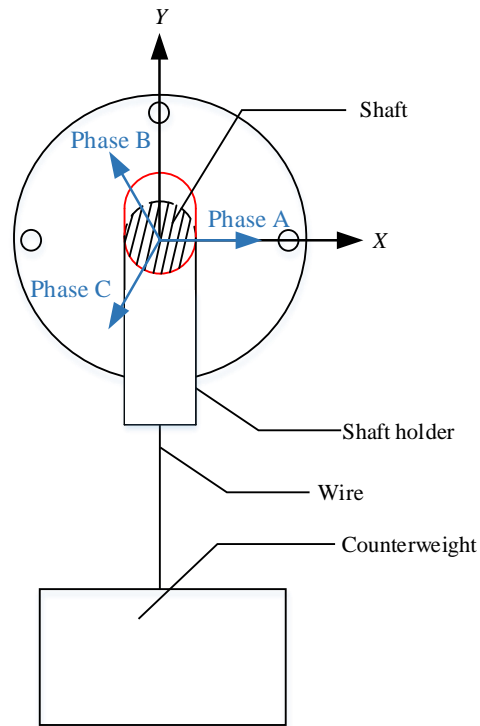


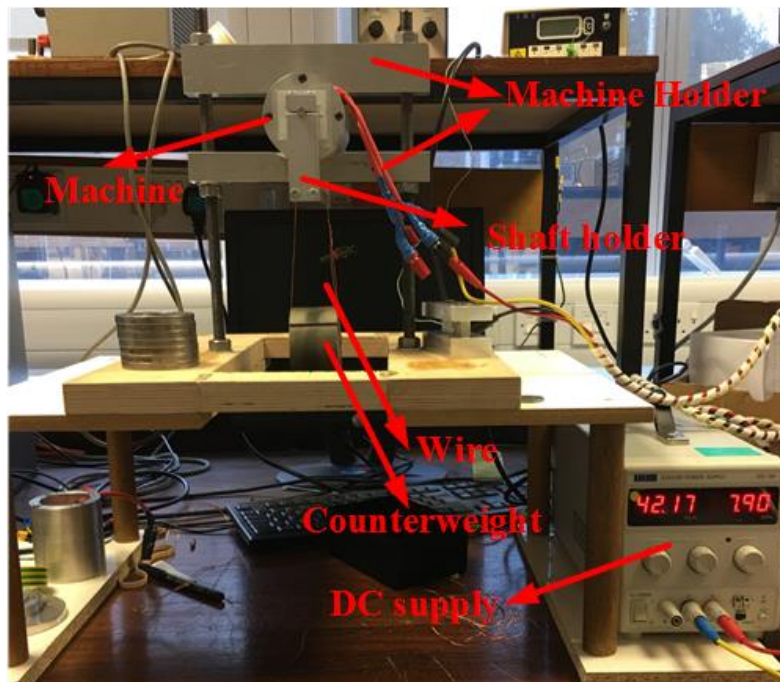
Fig. 2. 52 Special end caps for UMF test.

The whole test rig is shown in Fig. 2. 53. As can be seen, the eccentric hole is upwards and a wire is used to connect the shaft holder and the counterweight. The windings in all three machines are excited with  $I_A = 0$  and  $I_B = -I_C = -\frac{\sqrt{3}}{2}I_{DC}$  for a q-axis current. When the gravity of the counterweight, rotor and shaft holder is balanced with the UMF in vertical direction, the shaft will be at normal position and any small force upwards will stabilize the rotor in the eccentric position.

It should be noticed that since the UMFs have both vertical and horizontal components and their values could be positive and negative. As a result, the displacement of stator depends on the direction of the UMF components needed to be tested. The stator positions with different UMF components are listed in Table 2. 8. In terms of the definition of UMF directions, the initial position of machine is located as shown in Fig. 2. 53, which means  $F_x$  has the same phase with Phase A, and  $F_y$  is located in a direction of  $F_x$  counter clockwise ninety degrees.



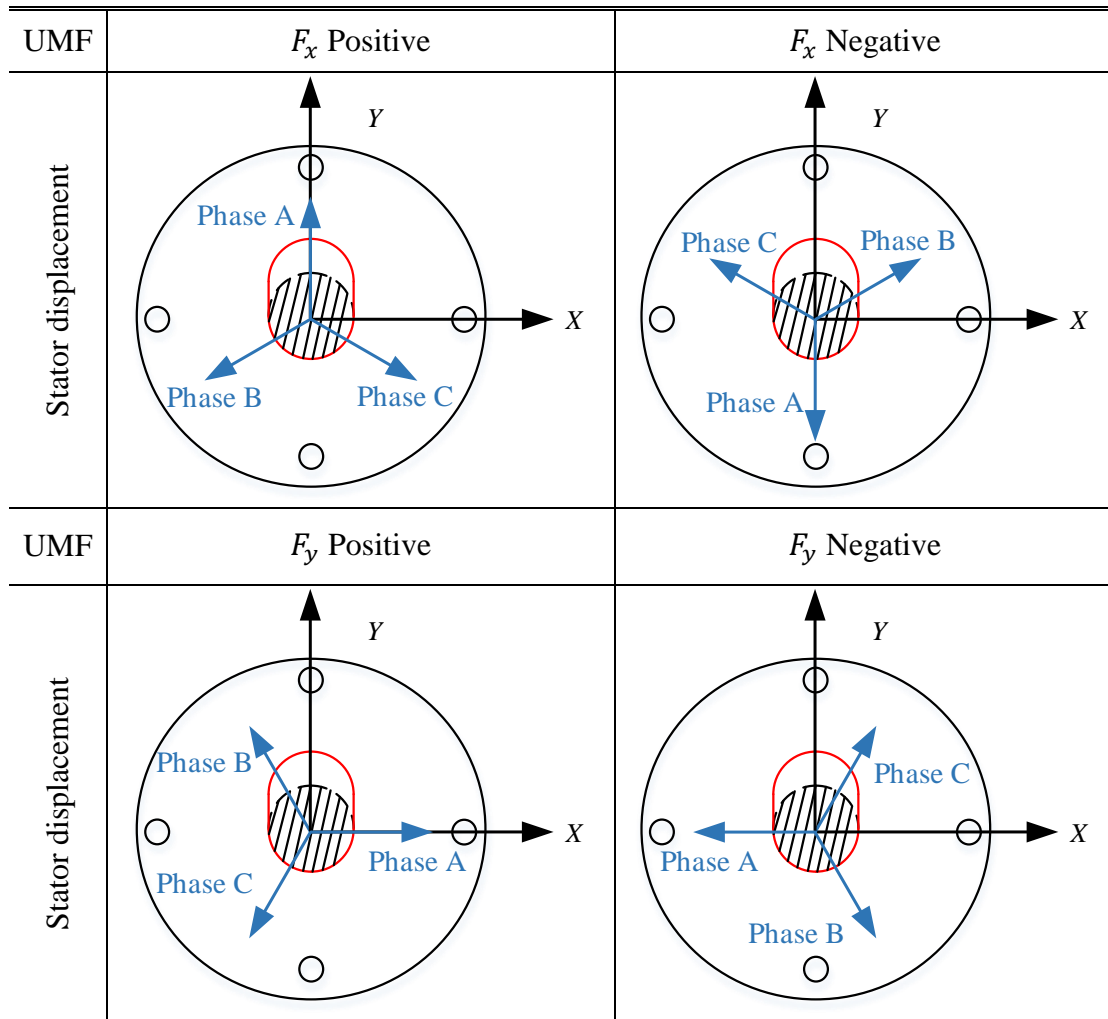
(a) Designed



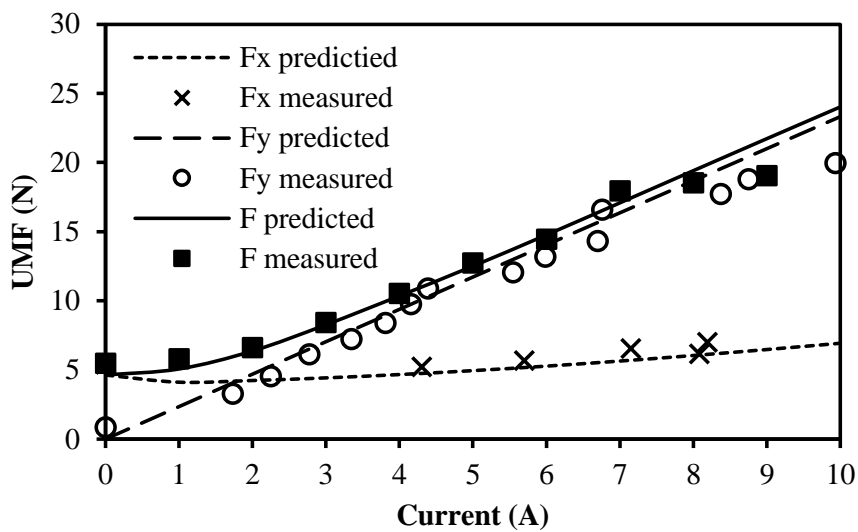
(b) Rig

Fig. 2. 53 Test rig UMF.

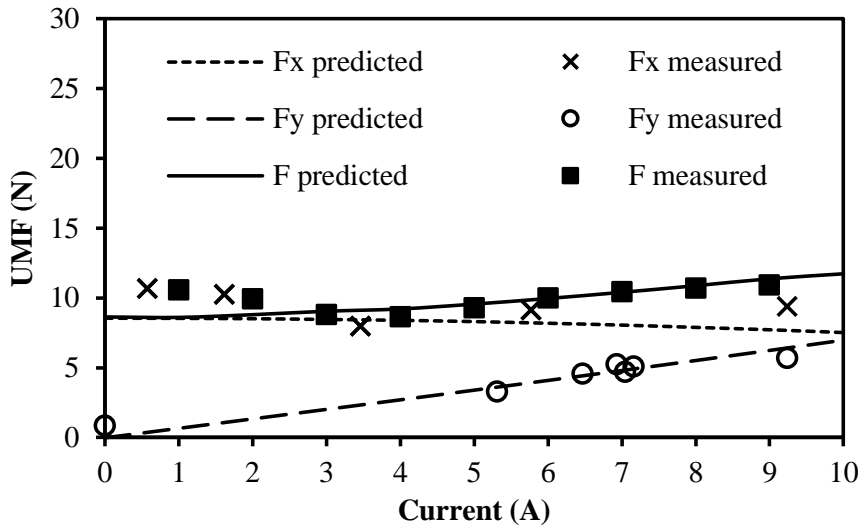
Table 2. 8  
Stator Displacement with Different UMFs Needed to Be Tested



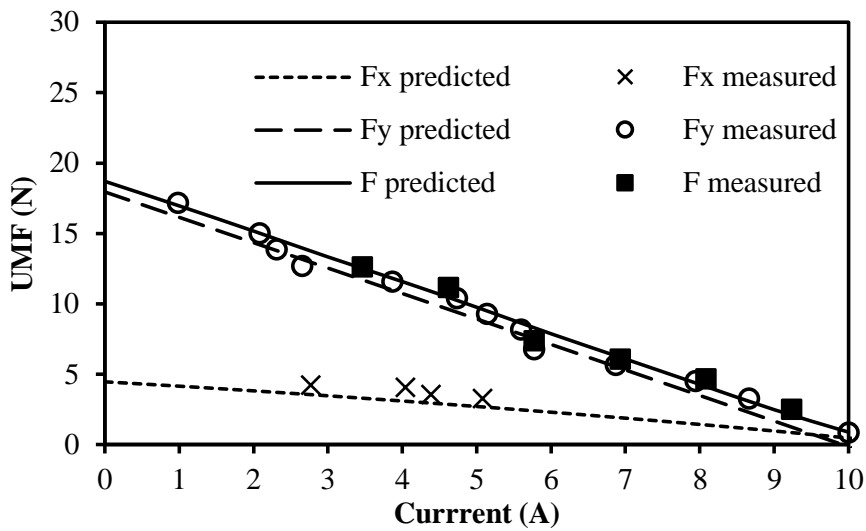
The comparison of predicted and measured UMFs are shown in Fig. 2. 54.



(a) Conventional machine



(b) Machine 2



(c) Machine 3

Fig. 2. 54 Comparison of FE-predicted and measured UMF at specific rotor positions

$$(I_A = 0A, \text{ and } I_B = -I_C = -\frac{\sqrt{3}}{2} I_{DC}).$$

Both the horizontal and vertical UMF components are tested. However, since the mass of the counterweight is discrete, the resultant UMF is obtained by using interpolation method. As shown, the difference between predicted and measured values are small. The slight error may be caused by the frictional force, misalignment between the North Pole and phase A as well as the manufacture tolerance.

The experimental results also show that the Machine 3 has the lowest maximum rated on-load UMF while the conventional machine has the highest one.

## 2.10 Summary

This chapter focuses on the rated on-load UMF reduction in 3-slot/2-pole high speed machines by using auxiliary slots. The characteristics of UMFs in the conventional machine is studied at first with the aid of frozen permeability method. Then, three different types of auxiliary slots are proposed for mitigating the rated on-load UMF. It shows that Machine 1 can almost eliminate the no-load UMF, but has very limited influence on the rated on-load UMF. Machine 2 can effectively reduce the rated on-load UMF but it also sacrifices significant amount of output torque. In contrast, Machine 3 can almost eliminate the rated on-load UMF and the reduction of output torque is very slight. However, all types of auxiliary slots can be more effective only for one specific load condition. In addition, the performance of machines with different type of auxiliary slots have been compared and the influence of several design factors, e.g. slot opening width, rotating direction and drive mode, has been detailed. Finally, several prototype machines have been built and tested. All measured results validate the analyses and predictions.



# **CHAPTER 3**

## **MAGNET EDDY CURRENT LOSS REDUCTION IN HIGH SPEED PM MACHINES BY USING AUXILIARY SLOTS**

Magnet eddy current loss is very important for any type of permanent magnet machines, especially for the high-speed one. Since it increases significantly with the rotating speed and has a great effect on the magnet temperature, and hence, the electromagnetic performance and irreversible demagnetization. In this chapter, the auxiliary slots with optimized size and position are used to reduce the magnet eddy current loss. By this means, the asynchronous spatial harmonics caused by the armature reaction and the conventional slots can be partially decreased by the harmonics produced by the introduced auxiliary slots. It is proved that the rated on-load magnet eddy current loss can be reduced as much as 81.5% by this method while the rated on-load torque is only decreased by 4.8% in the prototype 3-slot/2-pole machine with BLAC drive mode. In addition, it shows that the proposed method could offer better performance in a machine with relative larger airgap length and it is also effective for other slot/pole combinations. Moreover, the influence of different drive mode is also investigated.

This chapter was published on International Conference on Electrical Machines and Drives (IEMDC) 2017, and Transactions on Industry Applications, which are referred as [MAJ17c] and [MAJ18a] listed in the references.

### **3.1 Introduction**

The interest of high speed permanent magnet (HSPM) machine has grown significantly recently due to its high efficiency, high power density, as well as small size [REF10] [GER14] [BOR08] [ZHA15b] [EWA09] [BIA04] [BAI09] [LOV04]. However, as a consequence of asynchronously rotating airgap flux density harmonics, the magnet eddy current loss, which is caused by the spatial harmonics as well as the time harmonics, has significant influence on the machine performance [ZHU06]. This part of loss is much more important for high speed machines since it increases with rotating speed significantly, and affects the temperature of magnet, and hence, the output torque, the efficiency as well as the potentially irreversible demagnetization of permanent magnets.

In terms of spatial harmonics reduction, many different methods are proposed in the last few decades. Winding optimization is one of the most effective ways since a proper winding design can reduce the MMF harmonics of armature field effectively [MER15] [SPA15] [TOD04] [XUE12]. However, this method might lead to low winding factor so that the copper loss will be increased to obtain the same output torque. Moreover, the length of end winding is also increased when the winding is overlapped. As a result, the shaft natural frequency could be decreased, which may cause mechanical problem when machine operates under high speed conditions [EDE02].

Another method is using a relatively large air-gap, which is also desirable for high speed machines in terms of mechanical and aerodynamic considerations [TAK94]. Since the high order spatial harmonics decay very quickly with the airgap, the large air-gap can filter most of them. However, this method is less effective for low order spatial harmonics and the output torque is also reduced significantly. Segmentation is another choice [BEL13] [MIR10] [YAM09] [VEE97] [HUA10] [MAR14]. Nevertheless, both these two methods are characterized as complicated manufacturing process as well as high cost [BEL14].

In addition, optimization of rotor shapes can also offer good performance. [CHA10] and [CHA15] present two different rotor shapes for magnet eddy current loss reduction. However, both of them are designed for an IPM machine, and there might be a mechanical problem if they are employed for a SPM machine due to the bending effect and edge effect appearing on the edge of magnets [BIN06]. In contrast, stator structure optimization is more suitable for high speed SPM machines since the geometry of the rotor will not be modified. [BEL14] shows that slot openings with optimized size and position can reduce magnet eddy current loss. However, the reduction is only as much as 15%. In addition, inserting auxiliary slots in the middle of stator teeth can reduce the no-load magnet eddy current loss dramatically [ZHA07]. Nevertheless, the influence of armature field is not considered in this method. Consequently, it has very limited influence under rated on-load condition.

This chapter focuses on rated average on-load magnet eddy current loss reduction by using auxiliary slots. Both size and position of auxiliary slots are optimized under rated working condition. By this method, the asynchronous harmonics produced by armature field and conventional slots can be partially compensated by the harmonics produced

by auxiliary slots. The 3-slot/2-pole machine with concentrated windings is chosen as the prototype machine and investigated at first due to its simple structure. Then the influences of airgap lengths, slot/pole number combinations and drive mode are studied as well. Finally, some experiment results are carried out for validation.

### **3.2 Field Analysis in 3-slot/2-pole Permanent Magnet Machines**

In order to understand the source of asynchronous spatial harmonics in 3-slot/2-pole machine, the air-gap magnetic field analysis is very necessary. In this section, the air-gap flux density is calculated by a simple MMF-permeance model which has several assumptions.

- 1) The saturation of stator lamination is not considered. In addition, since this model is only for explaining the working mechanism of the proposed method instead of giving the accurate solution, the tangential flux component is neglected as well.
- 2) The relative recoil permeability of PM is the same as air.
- 3) Negligible eddy current reaction.
- 4) The flux leakage and end effect are neglected.

#### **3.2.1 Prototype**

The prototype machine is introduced at first. A 3-slot/2-pole conventional PM machine with concentrated winding is selected as the prototype machine, of which the cross section is the same as the machine shown in Fig. 2. 1, and its detailed parameters are listed in Table 3. 1. It should be noticed that in order to ease the investigation, the thickness of sleeve is also included in the airgap length which will not be calculated and presented separately. In the prototype machine, the concentrated winding and a 2-pole PM ring are employed. In addition, the BLAC drive mode is used at first due to its simplicity, while the influence of different drive mode will be investigated in later sections.

Table 3. 1  
Basic Parameters Of 3-Slot/2-Pole Prototype Machine

Slot number	3	Shaft diameter (mm)	7
Pole number	2	Magnet thickness (mm)	4
Stator outer diameter (mm)	50	Axial length (mm)	30
Stator inner diameter (mm)	19.8	Magnet remanence (T)	1.2
Stator yoke height (mm)	5.2	Rated current (A)	10
Slot opening (mm)	2	Current angle (Elec. Deg.)	0
Air-gap length (mm)	0.6	Rated speed (rpm)	60000
Rotor outer diameter (mm)	17.8	Number of turns per phase	32

### 3.2.2 Open Circuit Air Gap Flux Density

The MMF distribution of the PM field could be expressed as:

$$F_{PM}(\theta, t) = F_{PM} \cdot \cos(\theta - \omega t) \quad (3.1)$$

where  $F_{PM}$  is the amplitude of PM field MMF,  $\theta$  indicates the rotor position in mechanical degrees and  $\omega$  is the electrical angular velocity. Since the diametric magnetization is used in the prototype machine, there is no harmonics in PM MMF distributions.

The airgap permeance distribution accounting for conventional stator slots is shown in Fig. 3. 1 and it can be decomposed into a series of Fourier series as:

$$P(\theta) = P_0 + P_{kN_s} \sum_{k=1}^{\infty} \cos(kN_s(\theta - \theta_0)) \quad (3.2)$$

where  $P_0$  and  $P_{kN_s}$  are the coefficients of DC and harmonics components of permeance,  $k$  is the index of each harmonic,  $N_s$  is the number of stator tooth and  $\theta_0$  indicates the phase difference.

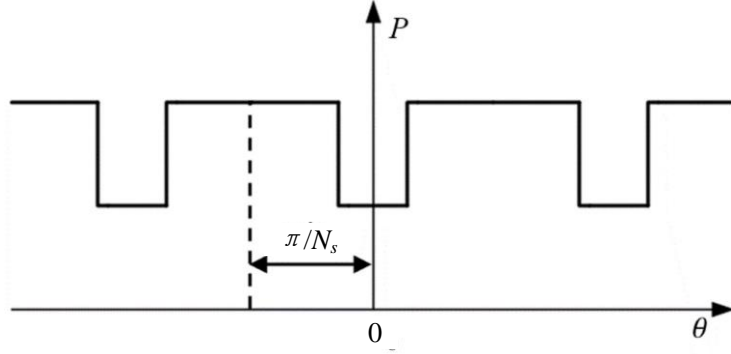


Fig. 3. 1Airgap permeability distributions accounting for stator slots.

As a result, the open-circuit airgap flux density could be calculated by multiplying the MMF of PM field as well as airgap permeance distributions.

$$\begin{cases}
 B_{PM}(\theta, t) = F_{PM}(\theta, t) \cdot P(\theta) \\
 = P_0 F_{PM} \cdot \cos(\theta - \omega t) + \frac{1}{2} F_{PM} P_{kN_s} \sum_{k=1}^{\infty} (\cos A + \cos B) \\
 A = (kN_s + 1)\theta - kN_s\theta_0 - \omega t \\
 B = (kN_s - 1)\theta - kN_s\theta_0 + \omega t
 \end{cases} \quad (3.3)$$

However, when the rotor is regarded as fixed when the motor is running, the speed of harmonics has to be changed, and the modified speed represents the relative speed between rotor and asynchronous harmonics.

$$\begin{cases}
 B_{PM}(\theta, t) = F_{PM}(\theta, t) \cdot P(\theta) \\
 = P_0 F_{PM} \cdot \cos(\theta) + \frac{1}{2} F_{PM} P_{kN_s} \sum_{k=1}^{\infty} (\cos A' + \cos B') \\
 A' = (kN_s + 1)\theta - kN_s\theta_0 + kN_s\omega t \\
 B' = (kN_s - 1)\theta - kN_s\theta_0 - kN_s\omega t
 \end{cases} \quad (3.4)$$

It is found that the  $(kN_s+1)$ th and  $(kN_s-1)$ th spatial harmonics have the same relative rotating speed comparing with the rotor, which means both of the  $(kN_s+1)$ th and  $(kN_s-1)$ th spatial harmonics contribute to the  $kN_s$ th time harmonics for the rotor.

### 3.2.3 Armature Reaction Air-Gap Flux Density

Fig. 3. 2 shows the MMF distribution of armature field when  $I_A = 0A$ , and  $I_B = -I_C = -\frac{\sqrt{3}}{2}I_{source}$ , where  $I_A$ ,  $I_B$ ,  $I_C$  and  $I_{source}$  indicate the current for phase A, B, C and the

current source. It should be noticed that measurable even order armature MMF harmonics exist in a 3-slot/2-pole machine, which is mainly due to the diametrically asymmetric disposition of the stator slots and coils [WAN14].

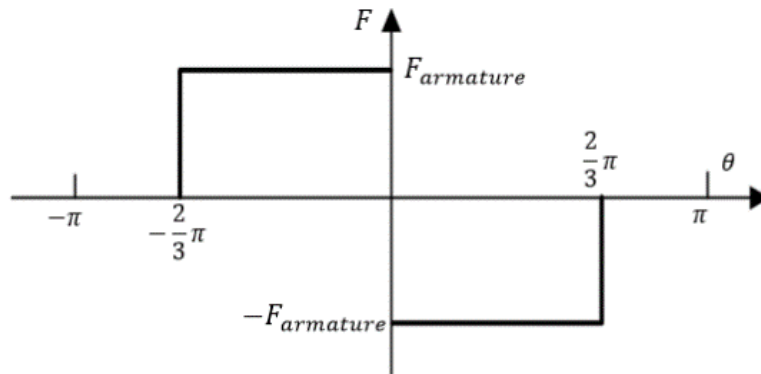


Fig. 3. 2 Air-gap MMF generated by armature field in 3-slot/2-pole SPM machine

$$(I_A = 0A, \text{ and } I_B = -I_C = -\frac{\sqrt{3}}{2}I_{source}).$$

The MMF of 3 phases can be expressed as:

$$\begin{cases} F_a = \sum_{q=1}^{\infty} [F_q \cdot \sin(q\theta)] \cdot \sin(\omega t) \\ F_b = \sum_{q=1}^{\infty} [F_q \cdot \sin\left(q\left(\theta - \frac{2\pi}{3}\right)\right)] \cdot \sin\left(\omega t - \frac{2\pi}{3}\right) \\ F_c = \sum_{q=1}^{\infty} [F_q \cdot \sin\left(q\left(\theta + \frac{2\pi}{3}\right)\right)] \cdot \sin\left(\omega t + \frac{2\pi}{3}\right) \end{cases} \quad (3.5)$$

The Fourier series expression of air-gap armature MMF can be calculated as a sum of 3 phases:

$$\begin{cases} F_{ABC}(\theta, t) = \frac{3}{2} \sum_{q=1}^{\infty} [F_q \cdot \sin(\xi)] \\ \xi = \begin{cases} (n\theta + m\omega t) \cdot -m, n \neq 3r \\ 0, n = 3r \end{cases} \\ m = \begin{cases} -1, n = 3i - 2 \\ 1, n = 3i - 1 \end{cases} \end{cases} \quad (3.6)$$

where  $\omega$  is the electrical speed,  $n$  represents the harmonics order,  $m$  indicates that the harmonic has the same rotating direction comparing with fundamental harmonics, and  $i$  is any positive integer.

The armature air-gap flux density is the product of armature MMF and air-gap permeance:

$$B_{ABC}(\theta, t) = F_{ABC}(\theta, t) \cdot P(\theta) \\ = \underbrace{\frac{3}{2} P_0 \sum_{q=1}^{\infty} [F_q \cdot \sin(\xi)]}_{\text{MMF harmonics}} + \underbrace{\frac{3}{4} F_q P_{kn_r} \sum_{q=1}^{\infty} \sum_{k=1}^{\infty} [\sin C + \sin D]}_{\text{MMF-slot harmonics}} \quad (3.7)$$

$$\begin{cases} C = \xi + kN_s(\theta - \theta_0) \\ D = \xi - kN_s(\theta - \theta_0) \end{cases} \quad (3.8)$$

$$\begin{cases} C = (kN_s - pq) \cdot \theta - \omega t - kN_s \theta_0 \\ D = -(kN_s + pq) \cdot \theta - \omega t + kN_s \theta_0 \end{cases} \quad (3.9)$$

where MMF harmonics represent the air-gap flux density harmonics caused by non-sinusoidal armature MMF only, and MMF-slot harmonics indicate the spatial harmonics caused by the interaction of armature MMF harmonics and the permeance variation caused by slots.

If the rotor is regarded as fixed, the harmonics will be modified as

$$B_{ABC}(\theta, t) = F_{ABC}(\theta, t) \cdot P(\theta) \\ = \underbrace{\frac{3}{2} P_0 \sum_{q=1}^{\infty} [F_q \cdot \sin(\xi')]}_{\text{MMF harmonics}} + \underbrace{\frac{3}{4} F_q P_{kN_s} \sum_{q=1}^{\infty} \sum_{k=1}^{\infty} [\sin C' + \sin D']}_{\text{MMF-slot harmonics}} \quad (3.10)$$

$$\xi' = \begin{cases} -pq\theta - (pq+1) \cdot \omega t, q \neq 3r \\ 0, q = 3r \end{cases} \quad (3.11)$$

$$\begin{cases} C' = (kN_s - pq) \cdot \theta + (kN_s - pq - 1) \omega t - kN_s \theta_0 \\ D' = -(kN_s + pq) \cdot \theta - (kN_s + pq + 1) \omega t + kN_s \theta_0 \end{cases} \quad (3.12)$$

### 3.2.4 Resultant Air-Gap Flux Density

It is found that the modified harmonics of  $B_{ABC}$  have the same characteristics compared with  $B_{PM}$ , which means the same order harmonic in  $B_{ABC}$  and  $B_{PM}$  have the same frequency as well as rotating direction, and the only difference between them is the amplitude and the phase angle. Hence, the resultant air-gap flux density can be calculated as

$$\begin{aligned} B_{\text{resultant}} &= B_{PM} + B_{ABC} \\ &= \sum_{j=1,4,7,\dots} B_j \cdot \sin(j\theta - \omega t + \theta_j) + \sum_{k=2,5,8} B_k \cdot \sin(k\theta + \omega t + \theta_k) \end{aligned} \quad (3.13)$$

where  $j, k$  are the harmonic indices;  $B_j, B_k$  are the Fourier coefficients of the  $j$ th,  $k$ th harmonics, while  $\theta_j, \theta_k$  represent the corresponding phases.

### 3.3 Effect of Auxiliary Slots on Magnet Eddy Current Loss

The effect of auxiliary slots mainly reflects on the modification of air-gap permeance distribution. Fig. 3. 3 shows the permeance model accounting for both conventional and auxiliary slots.

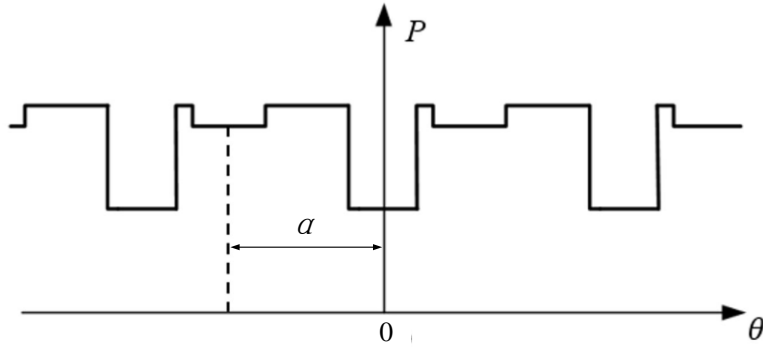


Fig. 3. 3 Air-gap permeance distribution accounting for conventional stator slots and auxiliary slots.

As can be seen, the auxiliary slots have similar effect on permeance modification comparing with the conventional slots. According to (3.1) - (3.10), the harmonics produced by auxiliary slots can be also presented in a similar form:



$$\begin{aligned}
B_{har,aux} &= B_{PM,har,aux} + B_{ABC,har,aux} \\
&= \sum_{j=4,7,11\dots} B_j' \cdot \sin(j\theta - \omega t + \theta_j') + \sum_{k=2,5,8} B_k' \cdot \sin(k\theta + \omega t + \theta_k')
\end{aligned} \tag{3.14}$$

where  $B_{har,aux}$ ,  $B_{PM,har,aux}$  and  $B_{ABC,har,aux}$  are the total field harmonics, PM field harmonics as well as MMF-slot harmonics caused by auxiliary slots;  $B_j'$ ,  $B_k'$  are the Fourier coefficients of the  $j$ th,  $k$ th harmonics, while  $\theta_j'$ ,  $\theta_k'$  represent the corresponding phases.

Since the auxiliary slots affect the air-gap permeance distribution similarly comparing with the conventional slot openings, the harmonics produced by auxiliary slots have the same rotating speed and direction as the harmonics in the conventional machine. Meanwhile, with changing the size and position of auxiliary slots, the amplitude and phase of harmonics produced by auxiliary slots can be also modified. Therefore, it is possible to use these harmonics to partially decrease the asynchronous harmonics in the conventional machines so that the magnet eddy current loss can be reduced. Consequently, both optimal size and position of auxiliary slots are required so that the air-gap flux density harmonics produced by them can have the same amplitude but opposite direction comparing with the original asynchronous spatial harmonics.

The FE method is employed for global optimization and the magnet eddy current loss calculation. The goal of the optimization is the minimum average magnet eddy current loss under rated working condition, and the genetic algorithm is employed in the optimization process. The optimized parameters are height which may be known as depth, width as well as position of auxiliary slots. As stated in Chapter 2, the large torque reduction is undesirable. Consequently, only the candidates having torque reduction smaller than 5% will be considered, and qualified candidate with the minimum rated average magnet eddy current loss will be chosen as the optimal one.

The comparison of topologies of the conventional and proposed machines are shown in Fig. 3. 4, and the detailed parameters of the optimal auxiliary slots are listed in Table 3.

2

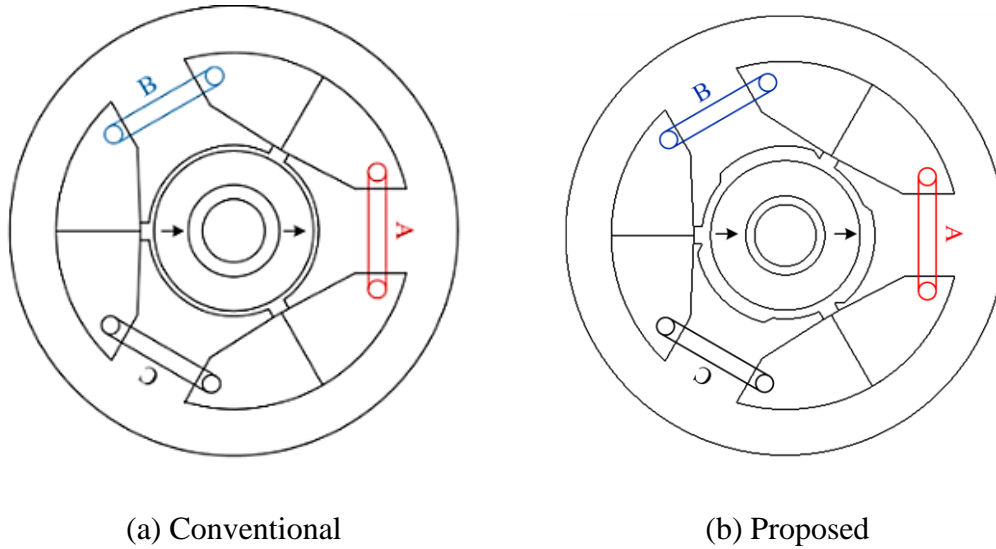


Fig. 3. 4 Cross sections of machine without and with auxiliary slots.

Table 3. 2  
Design parameters of the optimal auxiliary slots

Auxiliary slots height (mm)	0.549
Auxiliary slots Width (mm)	9.540
Auxiliary slots Shift angle (Deg.)	16.384

The magnet eddy current loss is compared in Fig. 3. 5 which can be divided into two different regions. The loss in the region A is lower in the conventional machine, while the opposite trend can be observed in the region B. As can be seen, the magnet eddy current loss under rated working condition, i.e. the current equals to 10A and current angle is zero, is reduced by 81.5% in the proposed machine, which shows the great effectiveness of this method.

In order to validate the proposed method further, the 3D FE results are carried out and compared in Fig. 3. 6 and Table 3. 3Table 3. 1. As shown, the 3D results also confirm the effectiveness of the proposed method. The slight reduction of magnet eddy current loss in 3D FE results is mainly due to the flux leakage in the end part of machines.

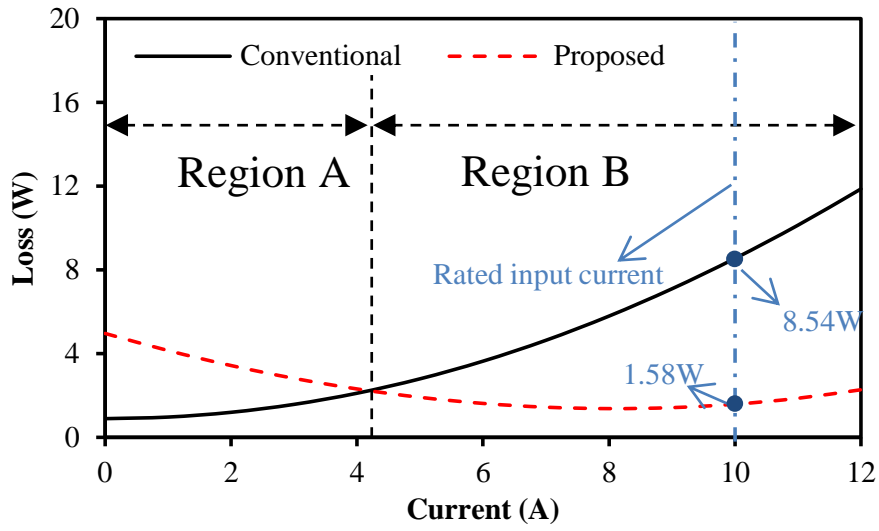
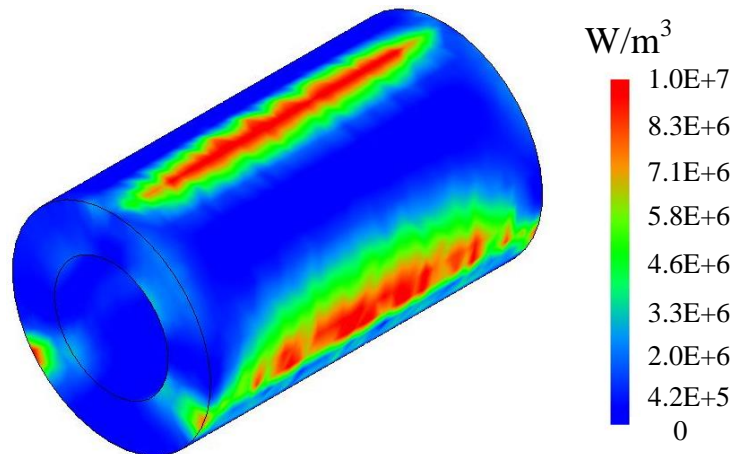
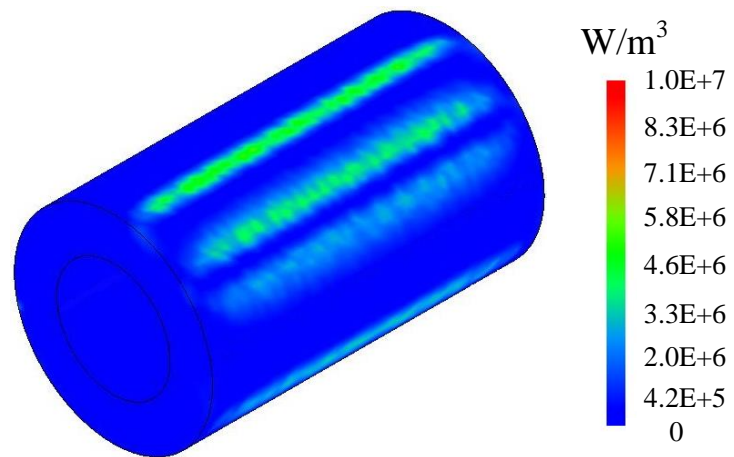


Fig. 3. 5. Average magnet eddy current loss with different currents.



(a) Conventional



(b) Proposed

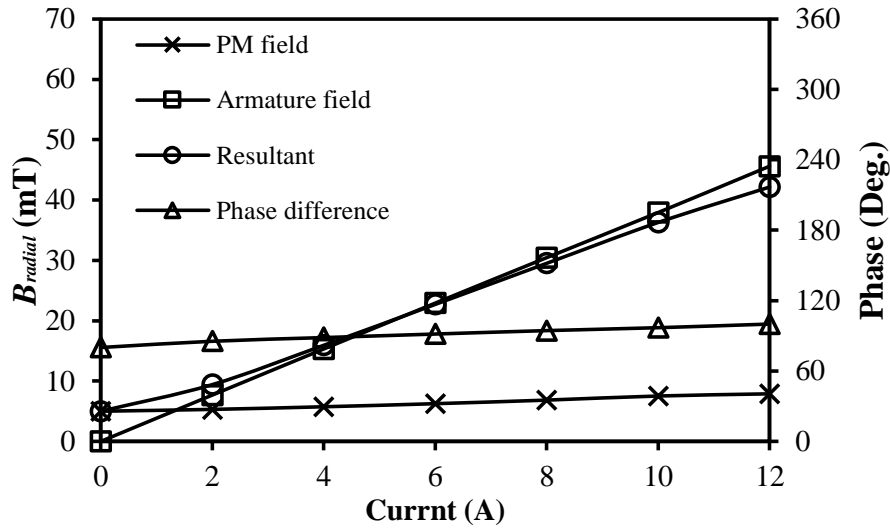
Fig. 3. 6 Magnet eddy current loss distribution under rated working condition at 0s.

Table 3. 3  
Comparison of Magnet Eddy Current Loss

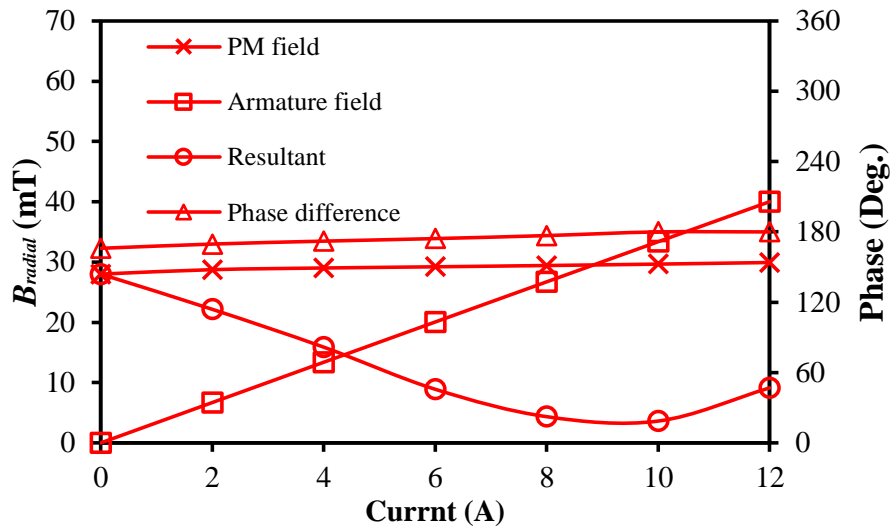
	Conventional	Proposed
2D Prediction (W)	8.54	1.58
3D Prediction (W)	7.02	1.23

In order to investigate in details, the spatial harmonics are analysed and shown in Fig. 3. 7, in which the representative harmonic, i.e. the 2nd spatial harmonic, is selected, while the analysis method can be applied on any other spatial harmonics. In the figure, the first three legends indicate the amplitude of the 2nd order flux density harmonics which are corresponded with the left y-axis, and the last legend indicates the phase difference of the 2nd flux density harmonics between PM and armature fields which are corresponded with the right y-axis.

As can be seen, the phase difference between the 2nd harmonics in armature and PM fields are about 180 degrees in the proposed machine, which results in a cancelling effect. However, the amplitude of the 2nd harmonic produced by armature reaction is proportional to the input current. Consequently, the cancelling effect is not significant when the input current is low, and the magnet eddy current loss is increased due to the enhanced asynchronous harmonics in PM field due to the increased slotted effect. In contrast, the cancelling effect becomes much more significant when the current is higher. Therefore, the magnet eddy current loss is reduced significantly. As for the conventional machine, the phase difference between the 2nd harmonics in PM and armature fields is about 90 degrees. As a result, there is almost no cancelling effect and the harmonics in these two fields nearly add with each other over the whole current interval.



(a) Conventional



(b) Proposed

Fig. 3. 7 Variation of the 2nd order flux density harmonic with different current values at 0s.

In order to verify that the magnet eddy current loss reduction is due to the spatial harmonics reduction, the comparison of magnet eddy current density distributions is shown in Fig. 3. 8, where  $H_{PM}$  is the distance between the radial position of magnet and the central of shaft. The 8.9 mm indicates the outer surface of magnet and 5.1 mm denotes the location of magnet very close to the shaft. It is worth noting that the magnet eddy current density distribution is used instead of flux density distribution. This is due to the fact that the magnet eddy current density distribution considers both amplitude

and frequency of spatial harmonics, while the flux density distribution only takes the amplitude of harmonics into account.

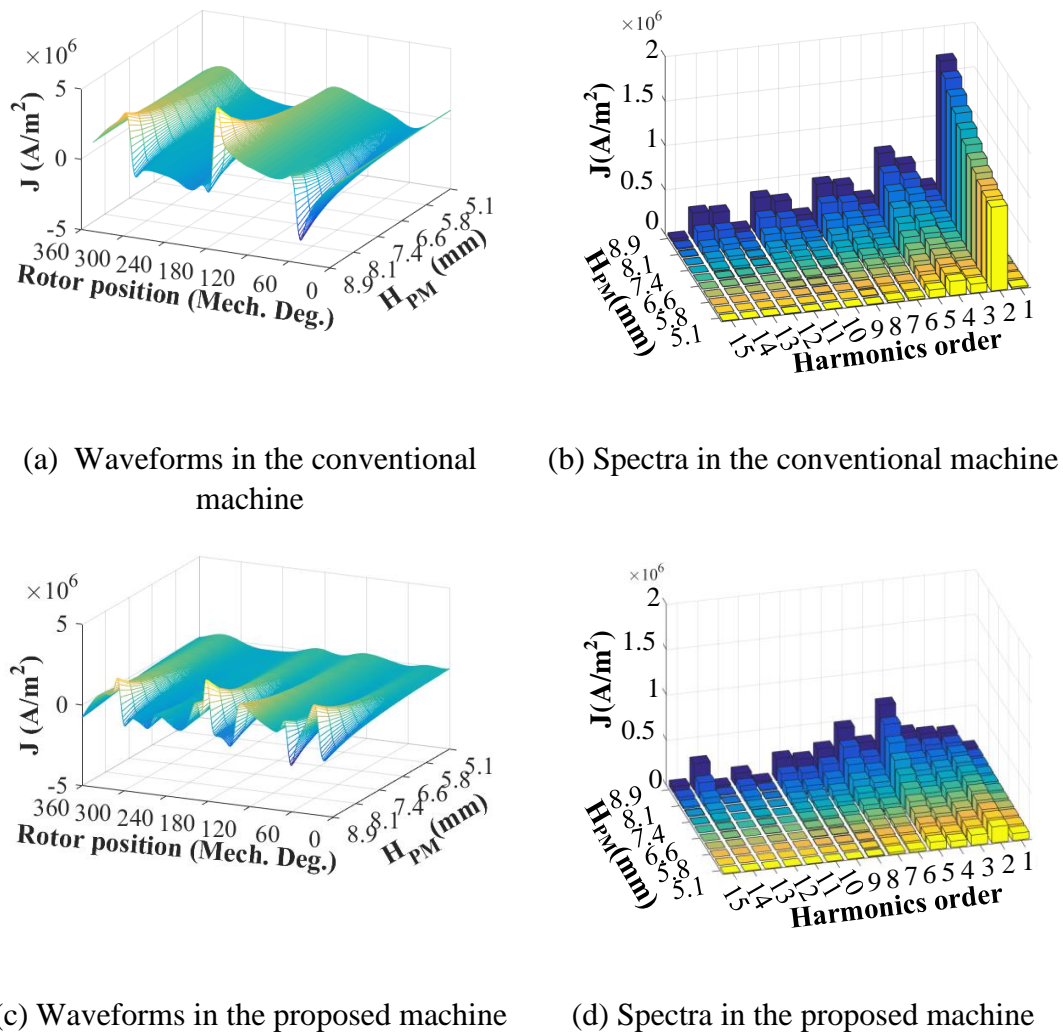


Fig. 3. 8 Comparison of rated on-load magnet eddy current density distribution at 0s.

As can be seen, the magnet eddy current loss in the conventional machine is mainly caused by low order harmonics, i.e. the 2nd, 4th and 5th harmonics. However, these harmonics are decreased significantly when the optimal auxiliary slots are added, especially the 2nd harmonic. As a result, the magnet eddy current loss is reduced significantly.

The variation of harmonics also reflects on the magnet eddy current loss distributions as shown in Fig. 3. 9.

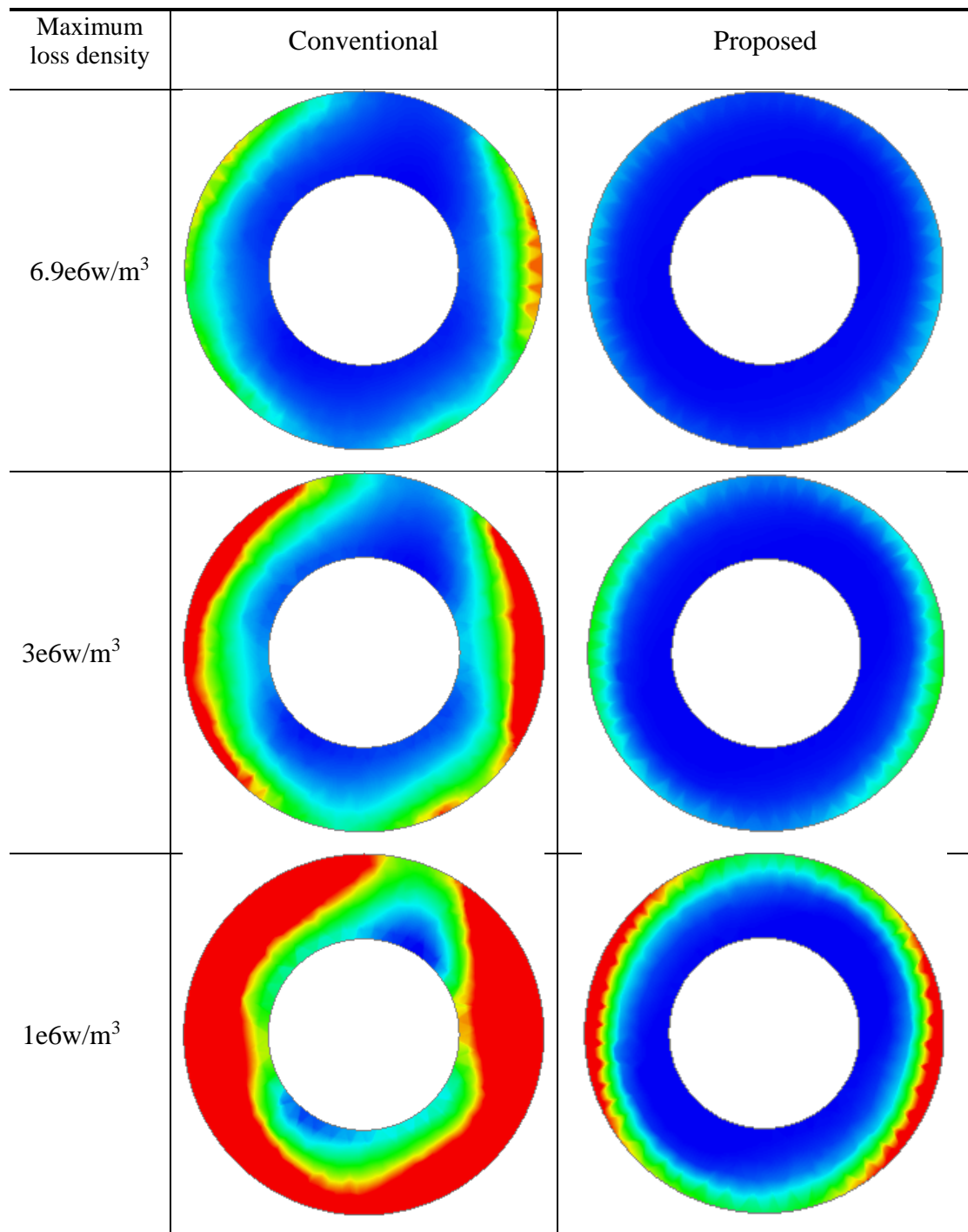


Fig. 3. 9. Rated on-load magnet eddy current Loss distribution at 0s.

Three different maximum loss densities are used and listed in the left column of Fig. 3.9. With decreasing of the maximum loss density, more rotor area turns to be warmer, since all the rotor area with loss density higher than the maximum value will turn to be red. By this way, the loss distribution can be observed more clearly. Comparing with the conventional machine, the magnet eddy current loss of the proposed machine concentrates on the surface of magnet material, since the low order harmonics can

penetrate the air-gap and get into the magnet deeply [BAI09], and hence produce most of the magnet loss in the conventional machine. However, with the significant reduction of low order spatial harmonics, the loss in proposed machine is mainly caused by the high order spatial harmonics. Consequently, the loss concentrates more on the surface of magnet.

Although the harmonics reduction can be used for explaining why the proposed method works, the physical reason of magnet eddy current loss is due to the variation of flux density of magnet. Therefore, the direct observation of flux density variation of magnet is also necessary. By way of example, one point is chosen on the middle of North Pole shown in Fig. 3. 10, and its flux densities with different rotor positions are shown in Fig. 3. 11.

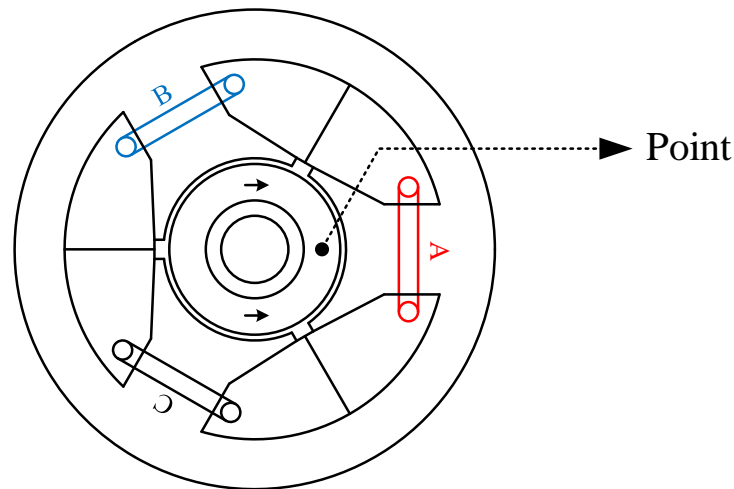


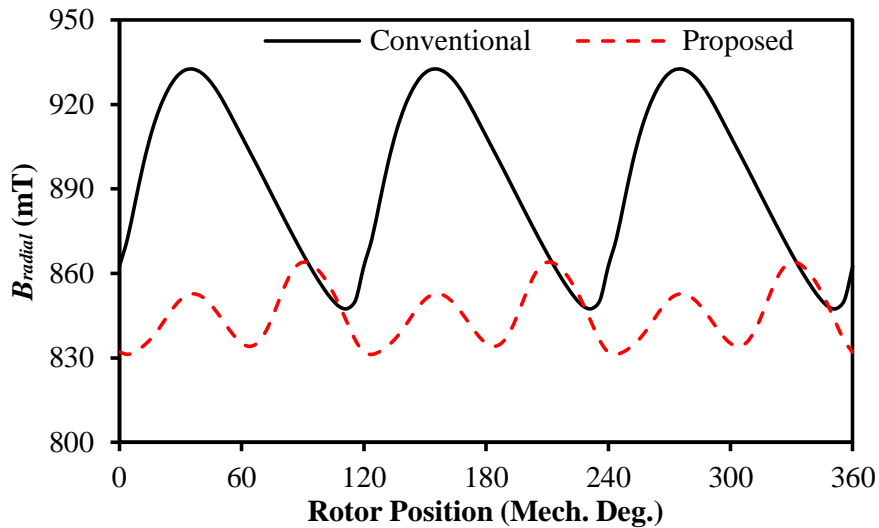
Fig. 3. 10. Point in the middle of North Pole of magnet.

As can be seen, the main time harmonics on the point is 3rd harmonics, according to the (3.2) - (3.9), the 3rd time harmonic are produced by the 2nd and 4th spatial harmonics, which is consistent with the observation of Fig. 3.8, and the reduction of the 2nd and 4th spatial harmonics also reflects on the decreasing of the 3rd time harmonic shown in Fig. 3.11.

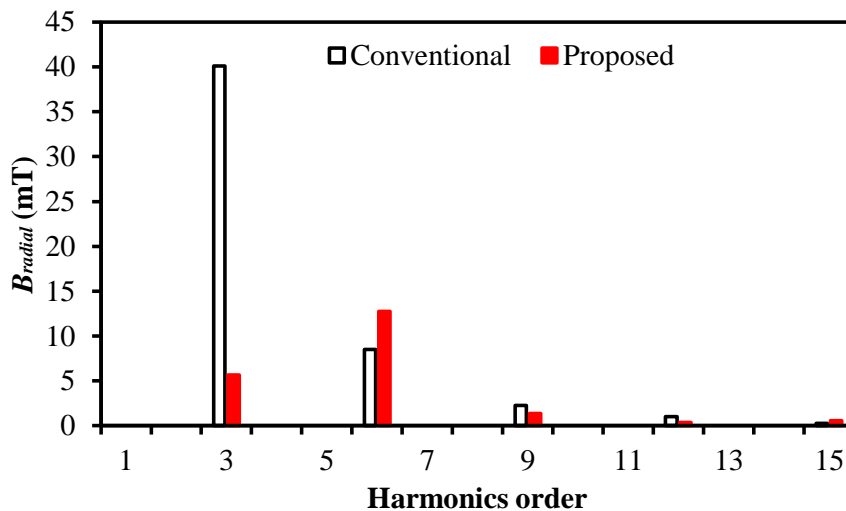
Moreover, Fig. 3. 12 shows the magnetic field distributions in the conventional and proposed machines under rated working condition. By way of example, three rotor positions are chosen. It can be seen that in the conventional machine, the flux density at the chosen point reaches a relative high value at zero electrical degree, which is due to fact that the current is zero for phase A. Consequently, there will be an adding



magnetism effect for the North Pole in this situation. In contrast, armature field in the proposed machine is reduced when rotor position equals to zero electrical degrees, which is due to the increased air-gap length caused by auxiliary slots. Therefore, the adding magnetism effect is also reduced, which results in small flux density variation. Since the auxiliary slots have similar effect on the other rotor positions, they will not be explained here.

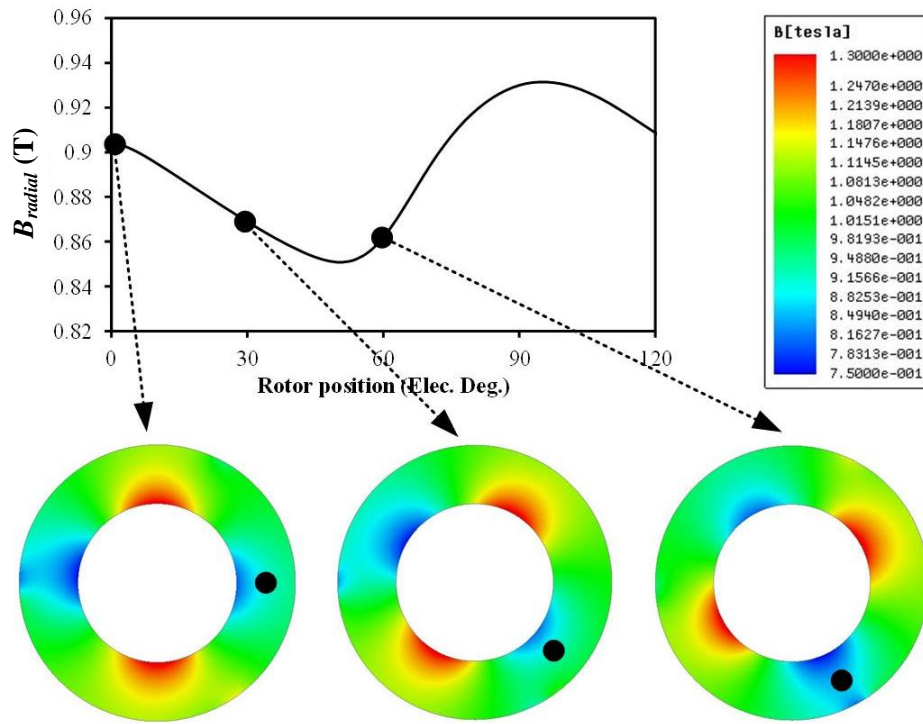


(a) Waveforms

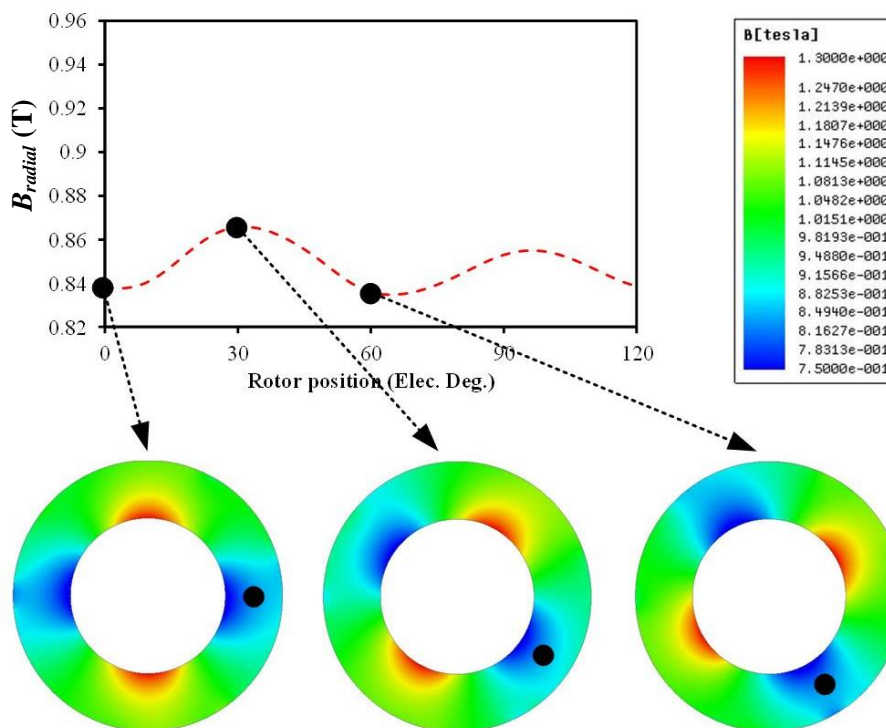


(b) Spectra

Fig. 3. 11. Flux density variation at chosen point under rated working condition.



(a) Conventional



(b) Proposed

Fig. 3. 12. Comparison of rated on-load magnet magnetic field.

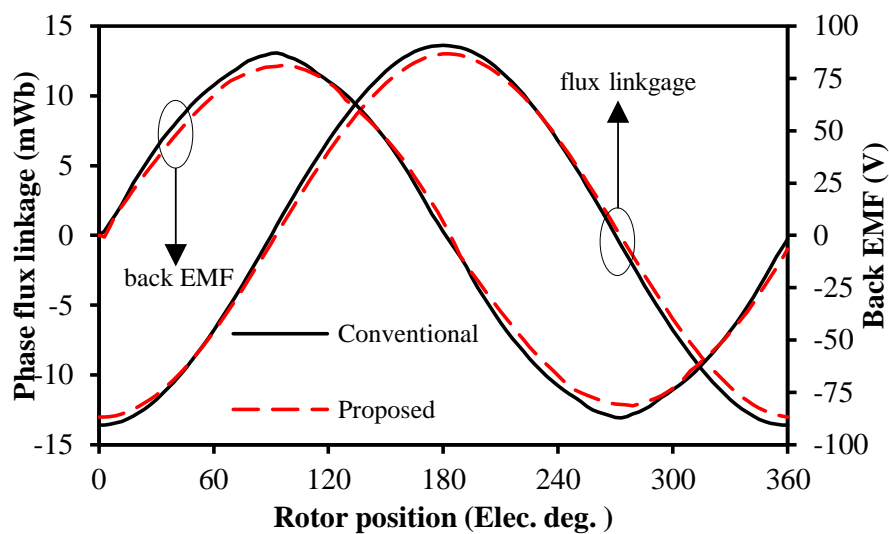
### 3.4 Machine Performance

In previous sections, the mechanism and the effectiveness of auxiliary slots with the optimal size and position on rated average on-load magnet eddy current loss reduction have been explained and investigated. In this section, the electromagnetic performance of the proposed machine is evaluated and compared with the conventional one.

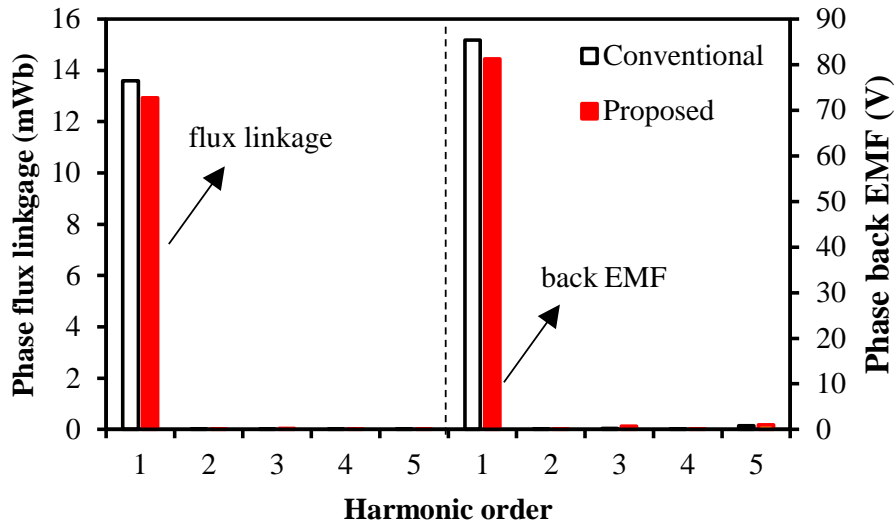
#### 3.4.1 Flux Linkage and Back EMF

Fig. 3. 13 compares the open-circuit phase flux linkage. It can be seen that the difference is very small and the slight reduction in the proposed machine is mainly due to the increased equivalent air-gap length caused by auxiliary slots.

The phase back EMFs are also compared in Fig. 3. 13. Since the back EMF is proportional to the phase flux linkage. The impact of auxiliary slots on phase flux linkages is also reflected on the phase back EMFs that the fundamental is reduced slightly. The spectra shows that the harmonics contents in these two machines are very low, which means the auxiliary slots do not introduce extra back EMF harmonics.



(a) Waveforms



(b) Spectra

Fig. 3.13 Phase flux linkage and back EMF comparison.

### 3.4.2 Torque Characteristics

The cogging torques are compared under no-load condition in Fig. 3.14. It can be seen that cogging torques in these two machines have different amplitude as well as phase, which is caused by the shifted auxiliary slots. Moreover, the difference between cogging torques in these two machines is very small, which means the auxiliary slots do not increase the cogging torque significantly.

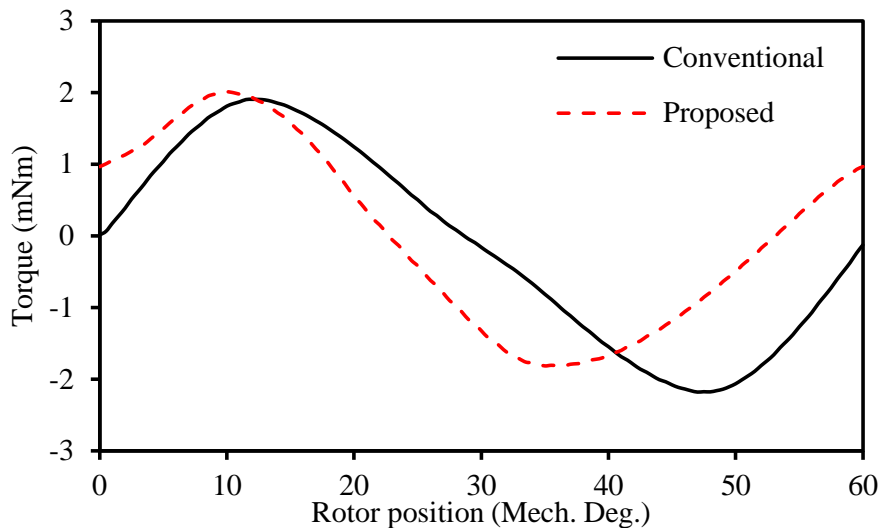


Fig. 3.14. Cogging torque comparison under no-load condition.

The rated on-load torque of these two machines are shown in Fig. 3.15. As shown, the output torque of the proposed machine is only reduced slightly, by 4.8%, which is also

caused by the increased equivalent air-gap length. In terms of the torque ripple, both these two machines have very low torque ripple since the cogging torque and back EMF harmonics in these two machines with the diametric PM magnetization are very low.

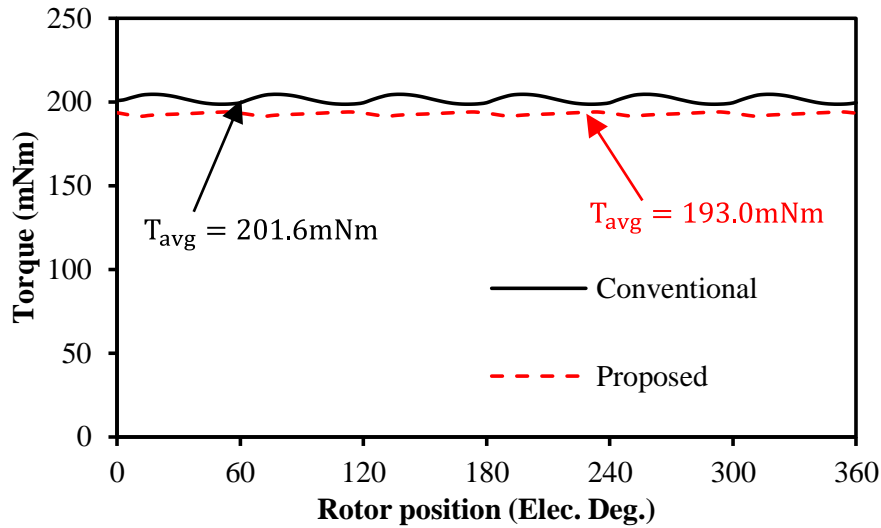


Fig. 3. 15. Rated on-load torque comparison.

### 3.5 Effect of Working Condition

Previous sections focus on the performance evaluation under the rated working condition. However, the working conditions may change in practice as illustrated in Chapter 2. Therefore, the investigation of the effect of working conditions is very necessary.

Fig. 3. 16 shows the variations of magnet eddy current loss and on-load average torque with different working conditions. It is found that the loss in the conventional machine increases with current amplitude and the current angle has small influence on its value. In contrast, as for the proposed machine, the minimum average magnet eddy current loss occurs around the rated working condition, and the maximum loss occurs when the d-axis current reaches the maximum value. In addition, the proposed machine has almost the same output torque comparing with the conventional one under all working conditions, the slight reduction of torque is due to the increased equivalent air-gap caused by auxiliary slots.

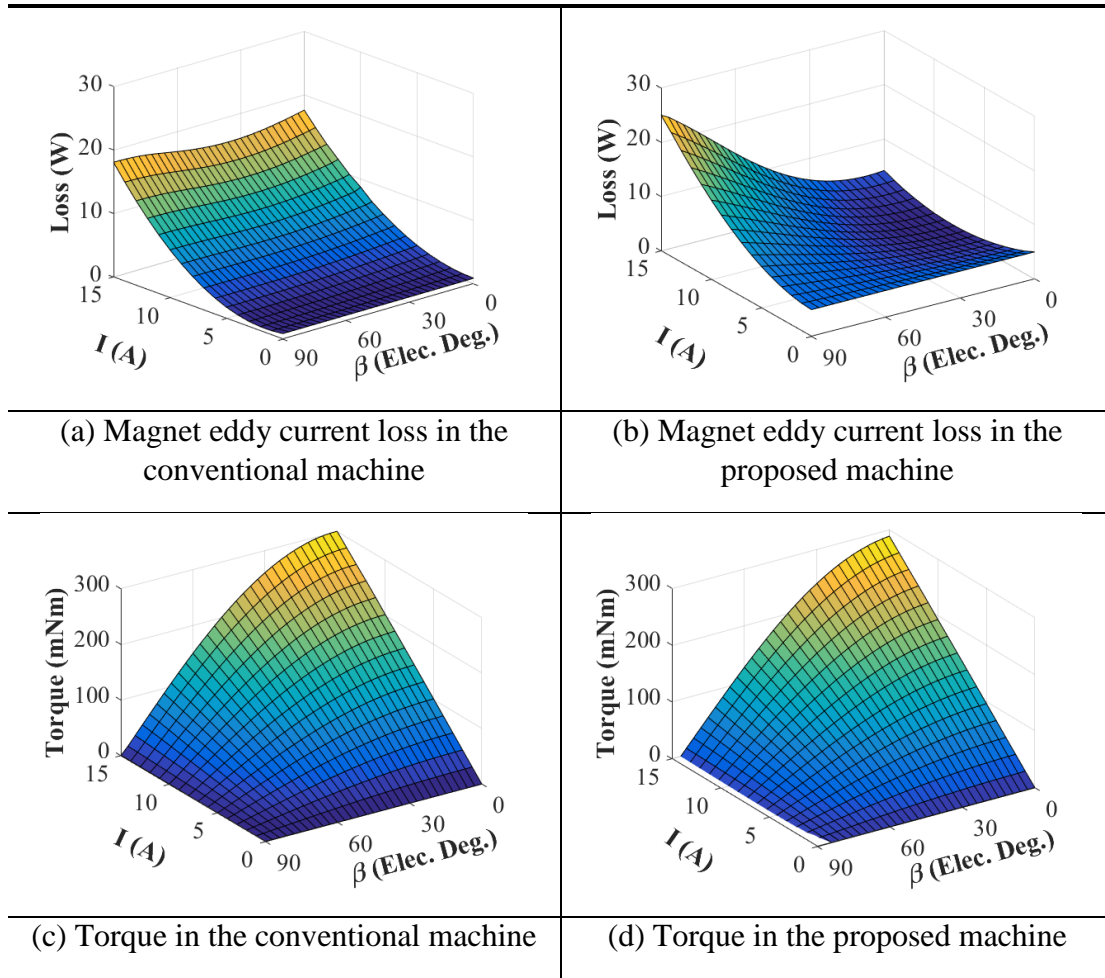


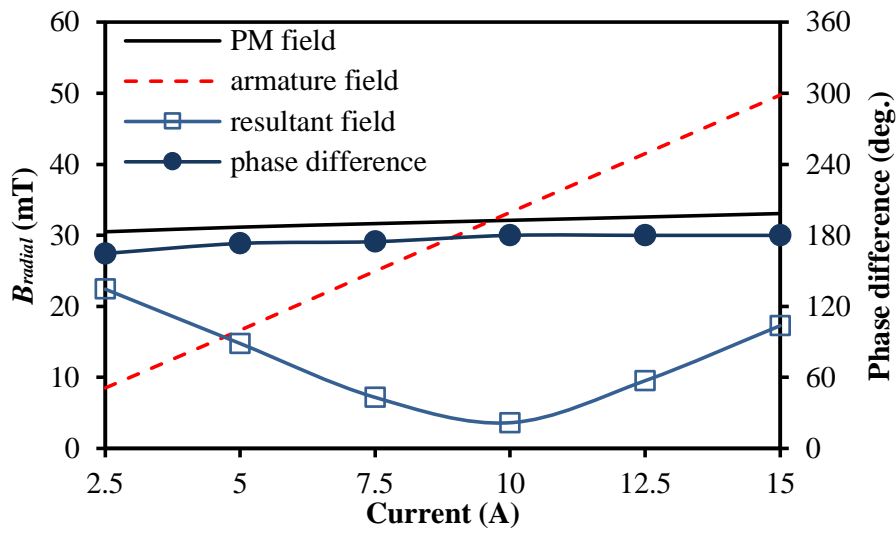
Fig. 3. 16. Performance of machines under different working conditions.

In order to investigate this phenomenon in more details, the air-gap flux density harmonics with different working conditions are simulated by frozen permeability method. By way of example, amplitude and phase of the 2nd and the 4th harmonics with different input current and current angle are shown in Fig. 3. 17 and Fig. 3. 18, respectively. It should be noticed that the current angle is fixed as zero in Fig. 3. 17, and the current amplitude is fixed as 10A in Fig. 3. 18.

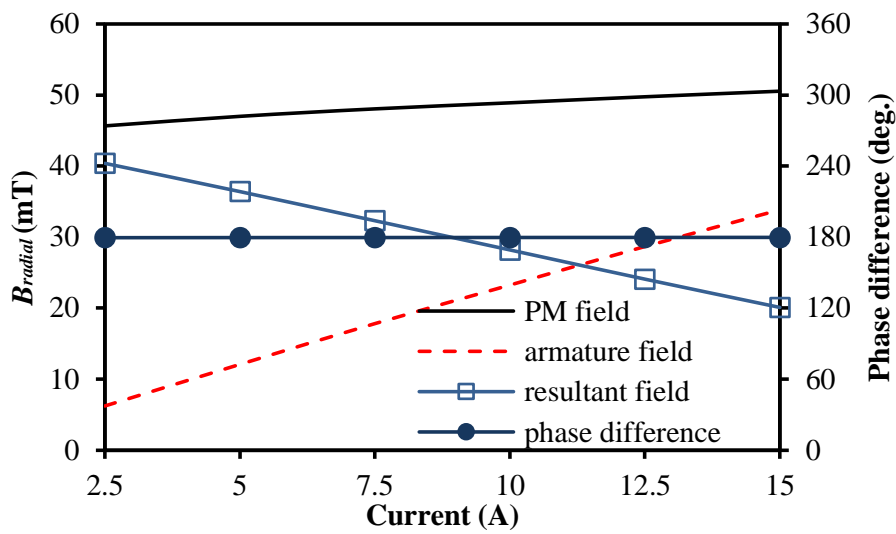
It should be mentioned that the other harmonics also have minor effect on the loss. Hence, the amplitudes of 2nd and 4th harmonics of the optimized machine may not be zero under rated working condition. Moreover, although there are only two harmonics analysed here, but the principle can be also applied to any other harmonics.

As can be seen, the effect of current amplitude mainly reflects on the variation of harmonics amplitude caused by armature reaction, while the phase difference between the harmonics produced by PM field and armature field is almost kept as the same. In

contrast, when the current angle changes, the phase difference varies dramatically while the amplitude of harmonics are just affected slightly.

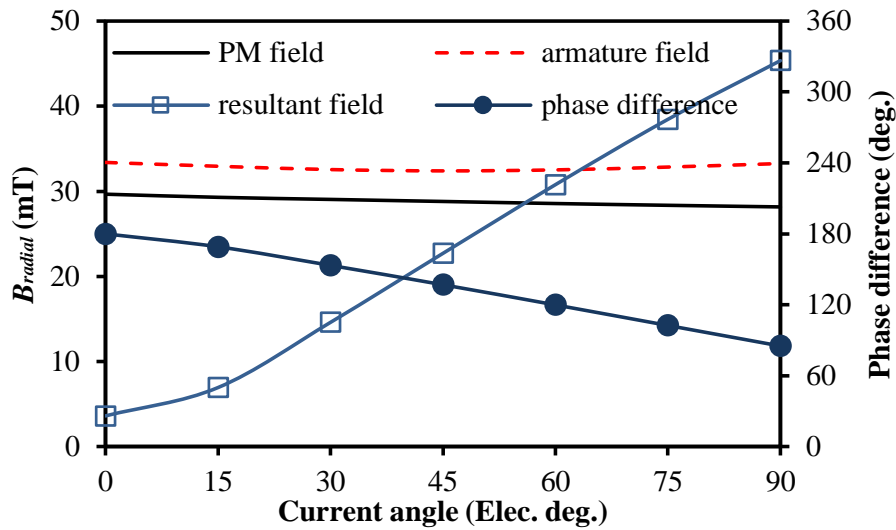


(a) The second harmonic

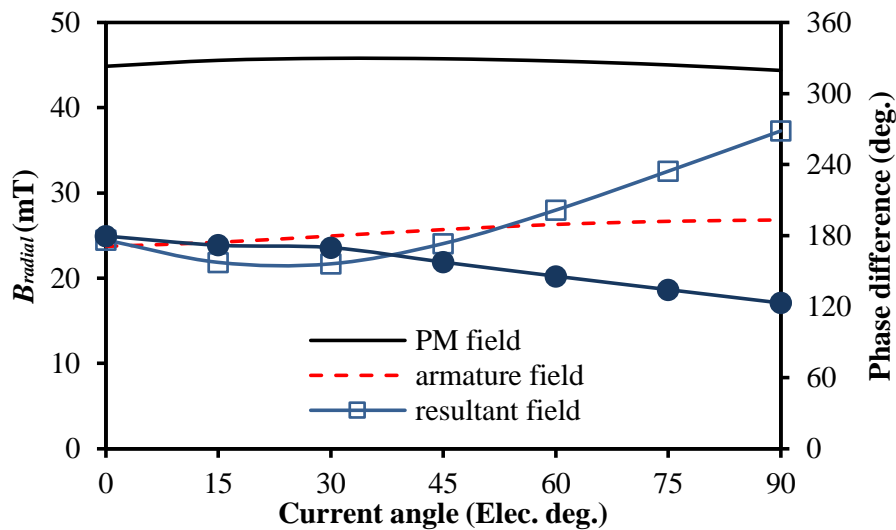


(b) The fourth harmonic

Fig. 3. 17. Variation of harmonics in the proposed machine with different current amplitude at 0s.



(a) The second harmonic



(b) The fourth harmonic

Fig. 3. 18. Variation of harmonics in the proposed machine with different current angle at 0s.

### 3.6 Influence of Airgap Length

The previous sections focus on the machines with fixed airgap length. However, the airgap length could be different depending on the rotating speed, materials of sleeve and magnet, etc. Therefore, the influence of airgap length needs to be investigated as well.

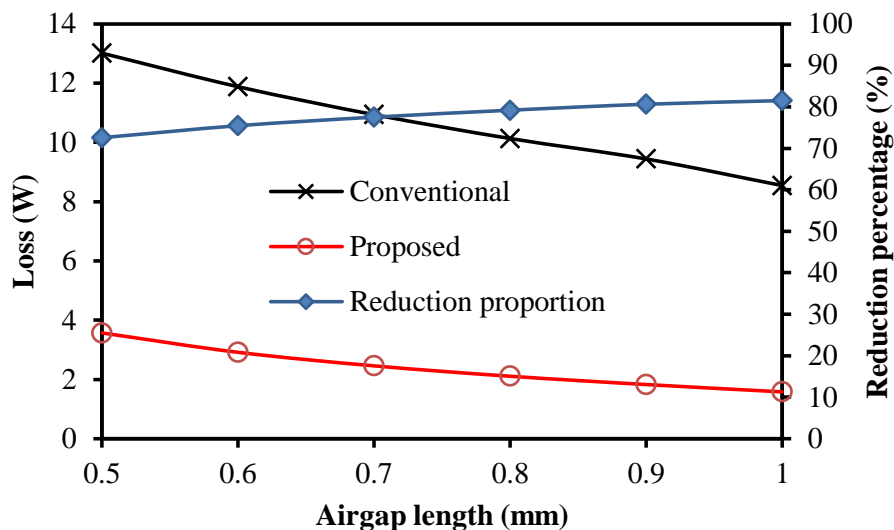
Since this thesis mainly focuses on the magnet eddy current loss, in order to make fair comparison, the rotor structure and the rotating speed will be kept as the same while



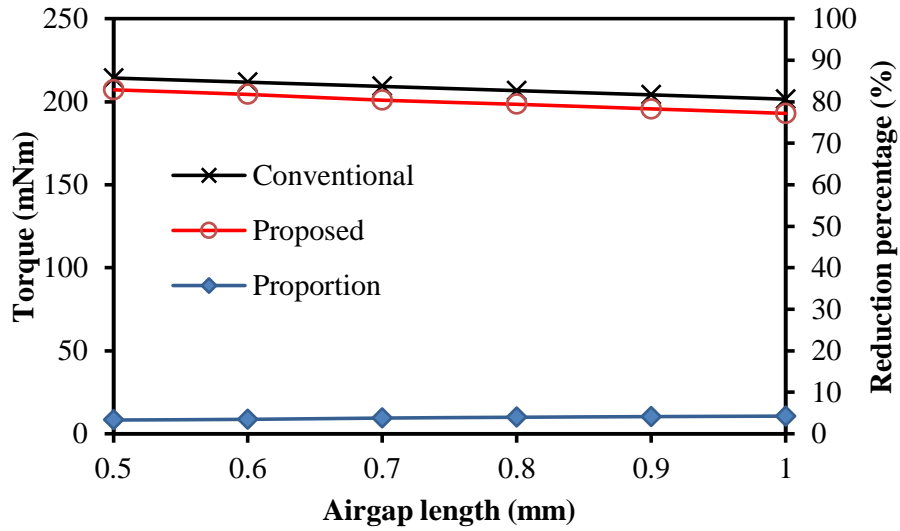
the inner diameter of stator will shrink slightly with airgap lengths. The minimum airgap length is chosen as 0.5mm while the maximum value is 1mm. It is assumed that the mechanical requirement could be met in all situations, since the performance of loss is emphasized.

The auxiliary slots have been optimized with different airgap lengths individually. The rated average on-load magnet eddy current loss and torque with different airgap length are shown in Fig. 3. 19.

It can be seen that the magnet eddy current loss decreases in both conventional and proposed machines when airgap length increases, and it shows that the proposed method could significantly reduce the loss in all different airgap lengths. Moreover, the reduction proportion has also been calculated which is defined as the reduced value over the value in the conventional machine. It can be seen that the reduction proportion of magnet eddy current loss increases with the airgap length from 72.5% to 81.4%, which means the proposed method could offer better performance in terms of the loss reduction in machines having larger airgap length. As for the rated on-load torque, it can be seen that its value decreases with airgap length in both machines, and the difference between the conventional and proposed machines is insensitive to the airgap lengths, of which the variation is smaller than 1%.



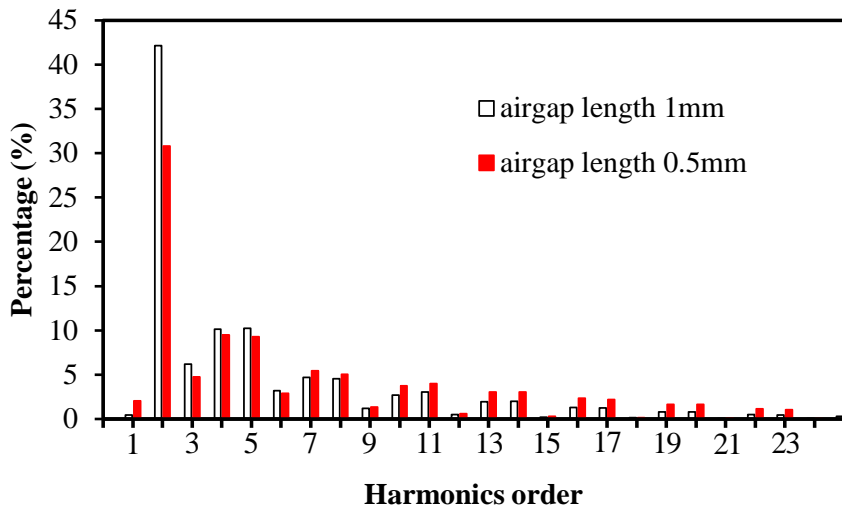
(a) Rated on-load magnet eddy current loss



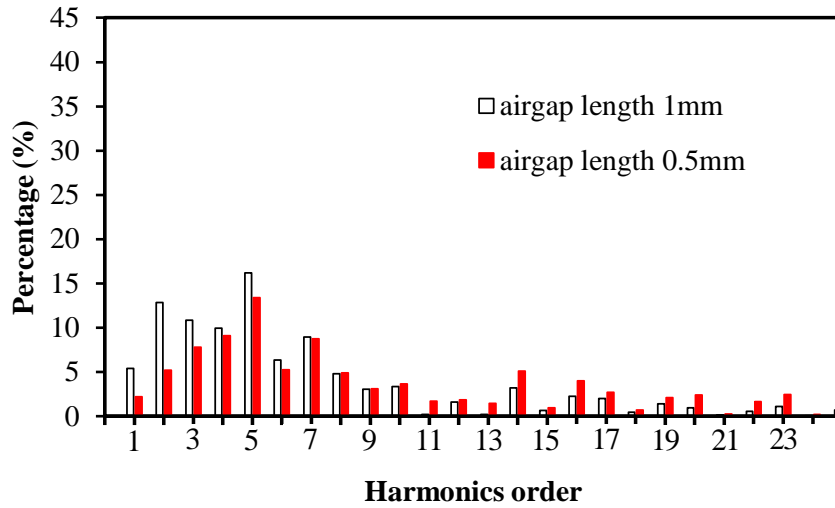
(b) Rated on-load average torque.

Fig. 3. 19. Machine performances with different airgap lengths.

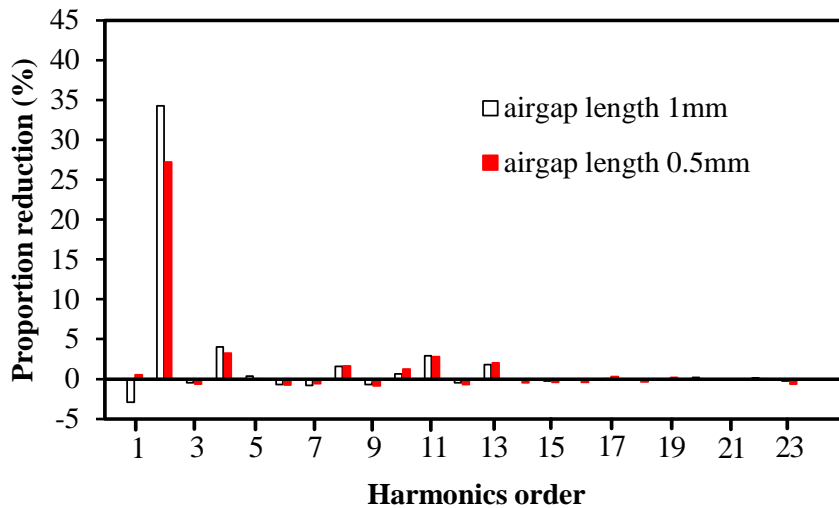
The influence of auxiliary slots on the magnet eddy current loss in machines having different airgap lengths mainly depends on the current density harmonic contents on the magnet. The comparison of current densities is shown in Fig. 3. 20. The proportion of the current density harmonics on the PM in the conventional and the proposed machines with 0.5mm and 1mm airgap lengths are compared, and the reduction due to the auxiliary slots is also shown.



(a) Conventional



(b) Proposed



(c) Harmonic reduction by auxiliary slots

Fig. 3. 20. Harmonic percentage of current density on the PM with different airgap length under rated working condition at 0s.

As can be seen, the low order harmonics have larger percentage in the machine with 1mm airgap length, hence more contribution to the loss, especially the 2nd harmonic. This is due to the fact that the high order harmonics have relatively smaller skin depth and the larger airgap length could filter out part of them. As a result, the higher order harmonics have more influence on the loss in machines with smaller airgap length comparing with the larger one.

However, the proposed method can only decrease part of the spatial harmonics content, which indicates that the machine having relative narrow spatial harmonics spectra can benefit more from the proposed method as shown in Fig. 3. 20 (c). Consequently, the machines with larger airgap length could benefit more in terms of the magnet loss reduction from the proposed method.

### 3.7 Influence of Drive Mode

In the previous sections, the BLAC drive mode is used which indicates the time harmonics are not considered. Nevertheless, the BLDC drive mode is a very competitive candidate, especially for ultra-high speed machines. Consequently, the effectiveness of the proposed method on the magnet eddy current loss reduction in BLDC machines will be detailed in this part.

The comparison of input currents with different drive modes is shown in Chapter 2. As can be seen, there are abundant time harmonics when the BLDC drive mode is used, which can significantly aggravate the magnet eddy current loss. The comparison of the rated on-load magnet eddy current loss in the conventional machine is shown in Fig. 3. 21. The magnet eddy current loss is much more significant when the BLDC drive mode is employed. The average value of this part of loss is 19.1W in machines with BLDC, which is 2.24 times that of the magnet eddy current loss in BLAC machines.

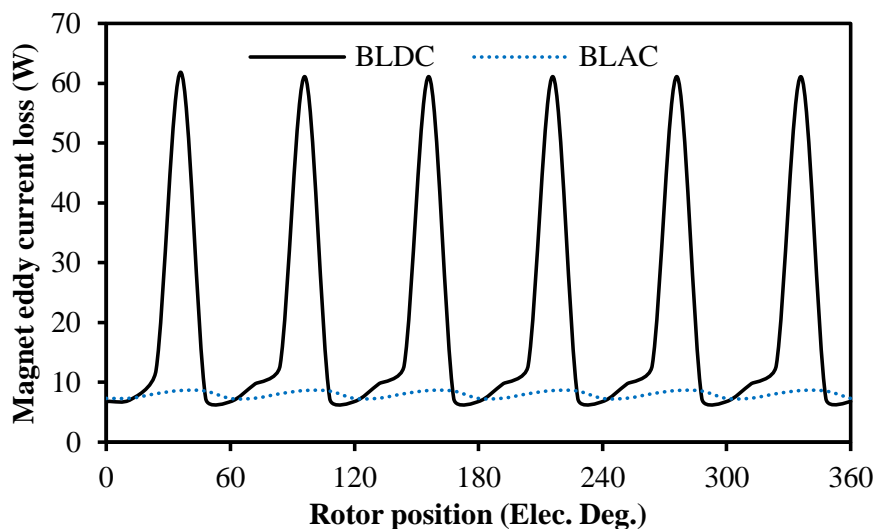


Fig. 3. 21. Comparison of rated on-load magnet eddy current loss in the conventional machine.

Due to the change of drive mode, the auxiliary slots also need to be re-optimized. The comparison of stator structures in the conventional and the proposed BLDC machines is shown in Fig. 3. 22. In addition, the detailed design parameters are listed in Table 3. 4.

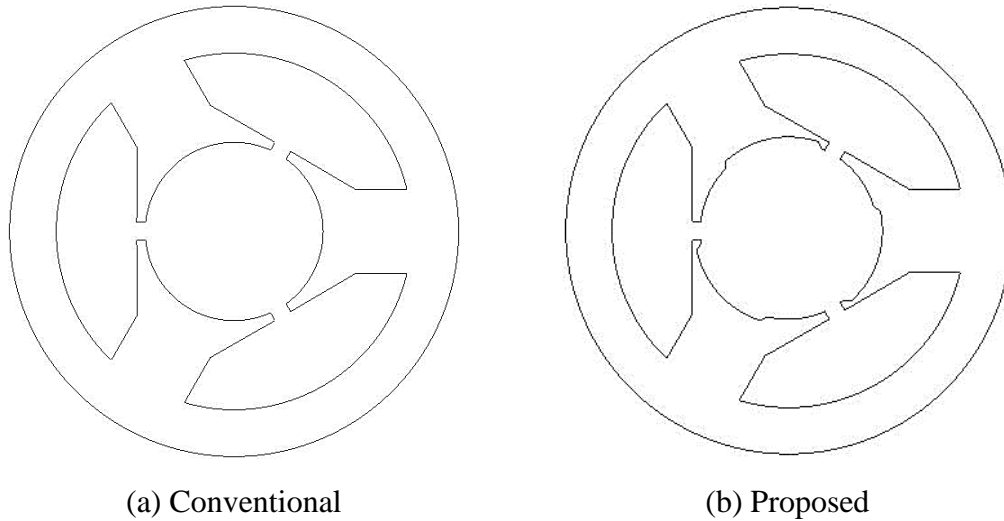


Fig. 3. 22 Comparison of stator structures in the conventional and proposed machines having BLDC drive mode.

Table 3. 4

Design Parameters of Optimal Auxiliary Slots

Auxiliary slots height (mm)	0.623
Auxiliary slots width (mm)	9.167
Auxiliary slots shift angle (Deg.)	17.912

The variations of average on-load magnet eddy current loss and output torque with different input current are shown in Fig. 3. 23 and Fig. 3. 24, respectively.

As can be seen, the proposed method can still reasonably mitigate the rated on-load magnet eddy current loss when the BLDC drive mode is used, the reduction is as much as 38.7%. In addition, it shows that the proposed machine has relative lower output torque, which is caused by the increased equivalent airgap length as illustrated previously. Nevertheless, the reduction of torque is very slight.

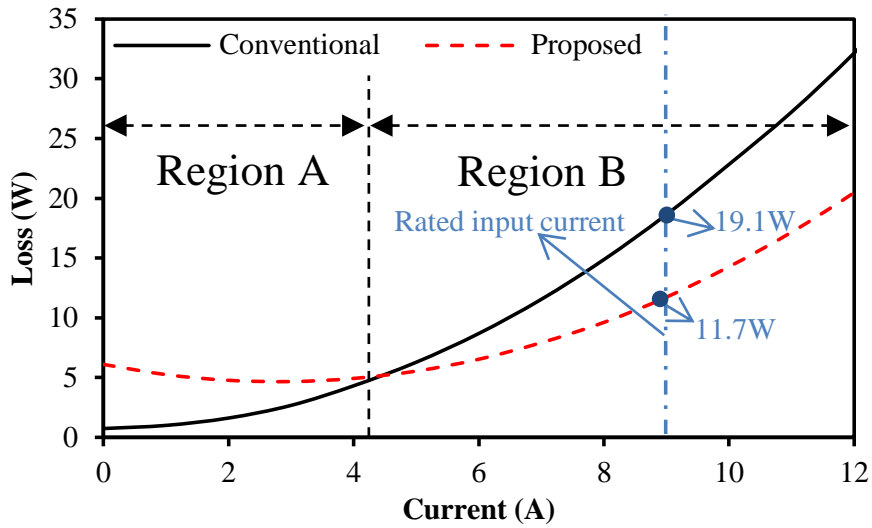


Fig. 3. 23. Comparison of average magnet eddy current loss with different input current.

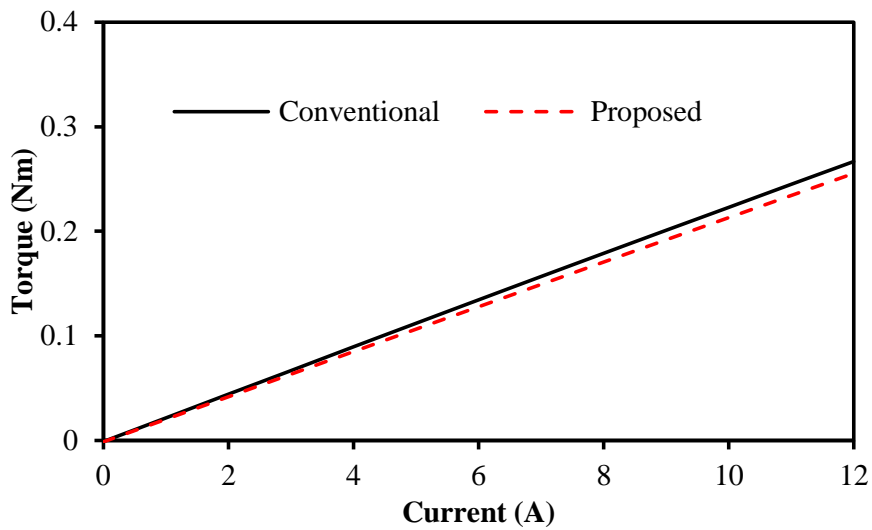
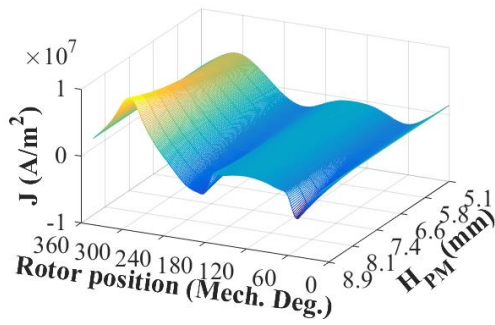
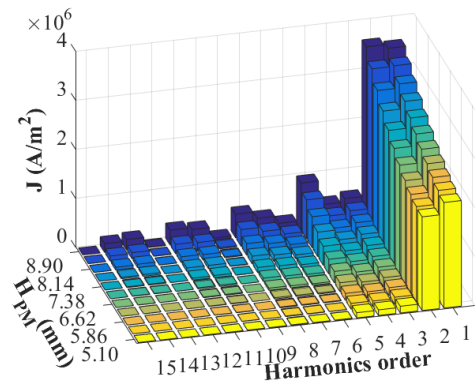


Fig. 3. 24 Comparison of average output torque with different input current.

As can be seen, the proposed method can still reduce the magnet eddy current loss when the BLDC drive mode is used, but it is not as effective as in machines with BLAC drive mode. In order to show more details, the magnet eddy current density in the conventional and proposed machines under BLDC drive mode are shown in Fig. 3. 25 and Fig. 3. 26, respectively.

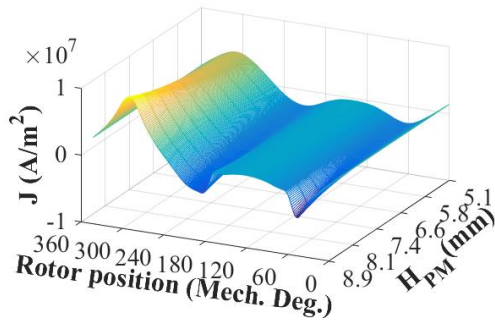


(a) Waveforms

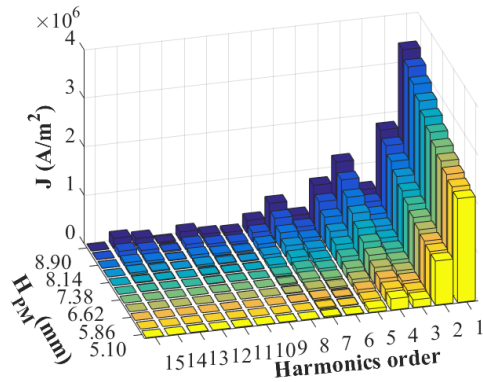


(b) Spectra

Fig. 3. 25 Magnet eddy current density distribution in the conventional machine.



(a) Waveforms



(b) Spectra

Fig. 3. 26 Magnet eddy current density distribution in the proposed machine.

It should be noticed that the time is chosen as 1/10 electrical period, instead of 0s. This is due to the fact that the magnet eddy current loss fluctuates significantly in BLDC machines, and it has almost the same loss value at the initial position comparing with the BLAC machine which has been illustrated in Fig. 3. 21. To show the characteristics of magnet eddy current loss in a BLDC machine more clearly, the 36 electrical degree rotor position is selected.

As shown, different from the magnet eddy current loss in BLAC machines, the fundamental field also contributes to the magnet eddy current loss significantly in BLDC machines, which is mainly due to the abundant time harmonics. Since the

proposed method is mainly for reducing the unwanted special harmonics, it has almost negligible impact on the time harmonics. Consequently, the contribution of fundamental field to magnet eddy current loss is kept almost as the same even when the optimal auxiliary slots are introduced. As a result, the proposed method can offer excellent in BLAC machines but it is less effective when BLDC drive mode is used.

### 3.8 Influence of Slot/Pole Number Combinations

The previous sections investigated the influence of auxiliary slots on the magnet eddy current loss in a 3-slot/2-pole machine. Nevertheless, other slot/pole number combinations could be also applied to high speed permanent magnet machines. The feasibility of the proposed method on 6-slot/2-pole machines is studied in this section. Both full pitch and tooth-coil windings are taken into account.

The conventional 6-slot/2-pole machines are shown in Fig. 3. 27 and the detailed parameters are shown in Table 3. 5.

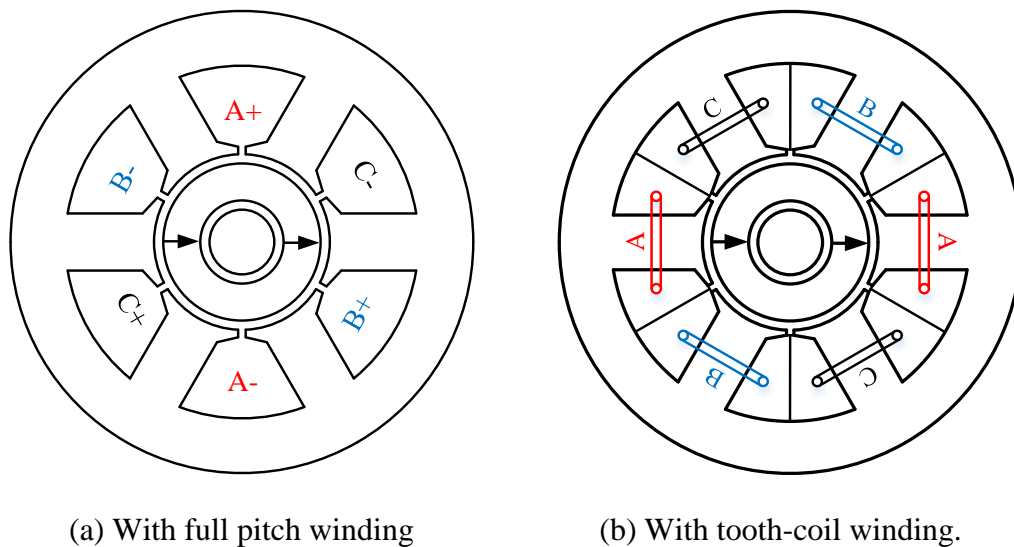


Fig. 3. 27 Cross sections of conventional 6-slot/2-pole machines.



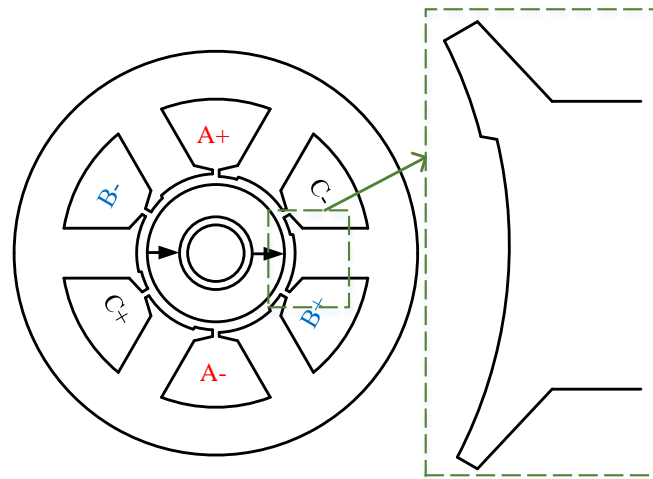
Table 3. 5  
Basic Parameters of 6-Slot Machines

Parameters	Full pitch winding	tooth-coil winding
Stator tooth width (mm)	5.93	5.63
Stator yoke height (mm)	3.09	2.96
Slot opening (mm)	0.41	0.41
Tooth tip height (mm)	0.82	0.55

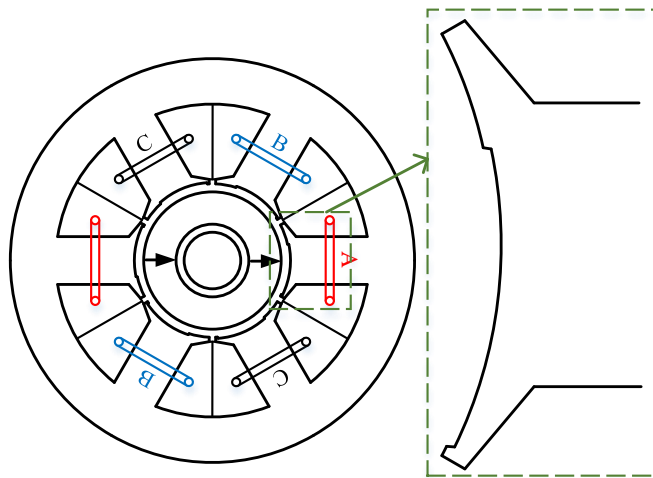
It should be mentioned that these two machines share the same rotor which has the same parameters listed in previous sections, but the stators have been optimized for the maximum rated on-load torque individually due to the different winding configurations. In addition, the input current is fixed as 10A for both machines during the optimization and the current angle is kept as zero degree, which means the output torques of machines with different winding structures should be also different.

In terms of auxiliary slots, the size and position are optimized for the minimum average magnet eddy current loss in both 6-slot machines separately. The optimized machine topologies are shown in Fig. 3. 28, and the detailed optimal auxiliary slots parameters are listed in Table 3. 6.

The comparison of average magnet eddy current losses with different input current is shown in Fig. 3. 29. As can be seen, the auxiliary slots can significantly reduce the rated average magnet eddy current loss in both 6-slot machines. The reductions in machines with full pitch and tooth-coil windings are as much as 82.4% and 78.7% under the rated working condition, respectively. Moreover, the machine having tooth-coil winding has lower magnet eddy current comparing with the machine with full pitch winding, which benefits from the lower armature field spatial harmonics caused by the lower winding factor. The total winding factor for the prototype machine with full pitch winding is 1 for all harmonics, while it is 0.5 for all harmonics in the prototype machine with tooth-coil winding.



(a) With full pitch winding



(b) with tooth-coil winding.

Fig. 3. 28. Cross sections of 6-slot/2-pole machines with optimal auxiliary slots.

Table 3. 6  
Basic Parameters of Optimal Auxiliary Slots in 6-Slot Machine

Parameters	Full pitch winding	Tooth-coil winding
Height (mm)	0.27	0.13
Width (mm)	6.83	5.86
Shift angle (Deg.)	6.51	7.74

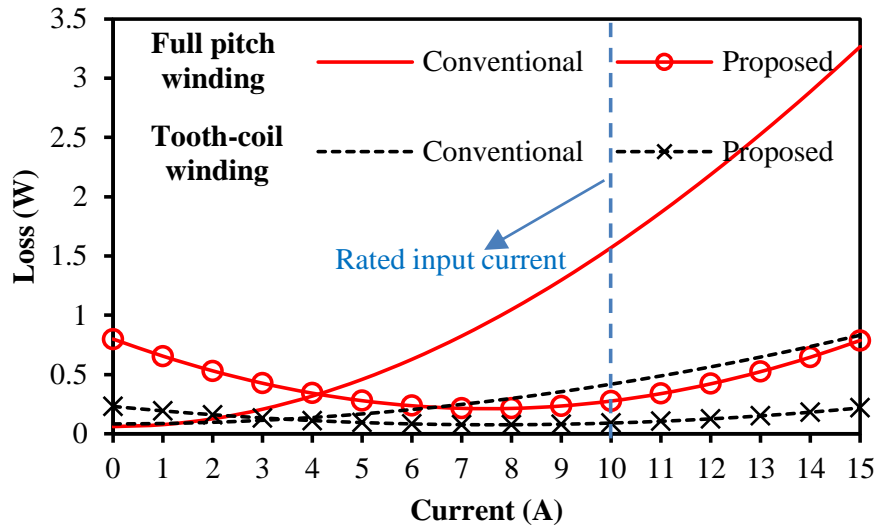
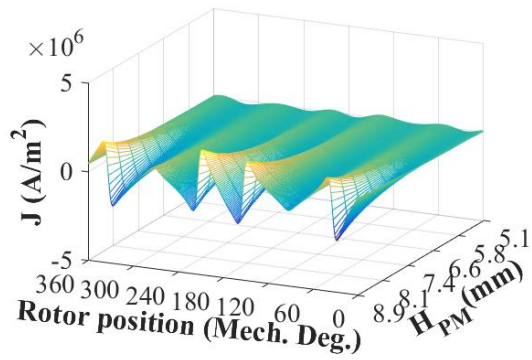
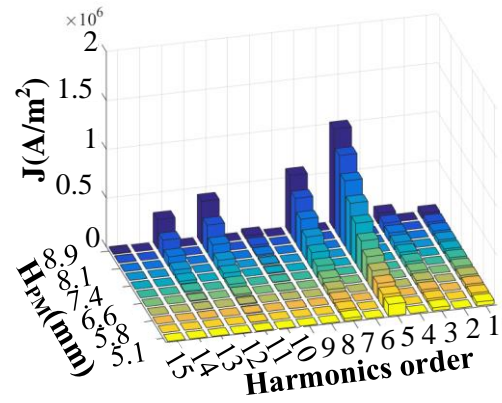


Fig. 3. 29. Magnet eddy current loss of 6-slot/2-pole machines with different currents.

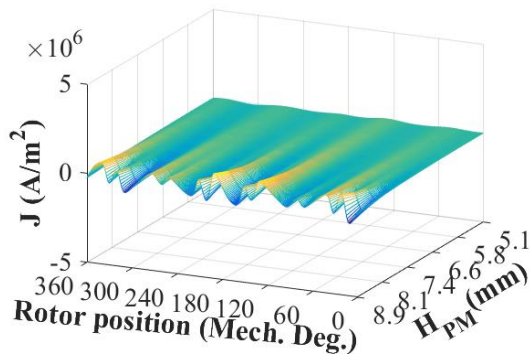
The current density with different magnet thicknesses and rotor positions are shown in Fig. 3. 30 and Fig. 3. 31. As shown, the magnet eddy current loss in 6-slot machines mainly comes from the 5th, 7th, 11th, and 13th spatial harmonics, and the auxiliary slots could reduce these harmonics significantly, which results in much lower magnet eddy current loss.



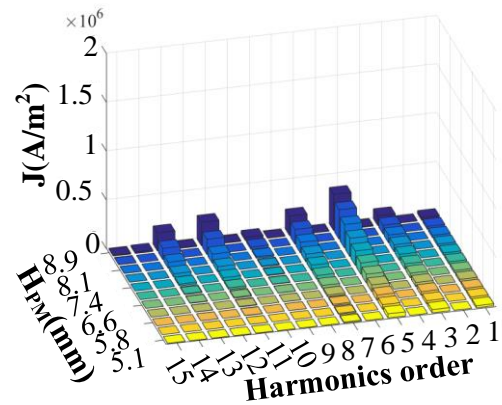
(a) Waveforms of the conventional machine



(b) Spectra of the conventional machine

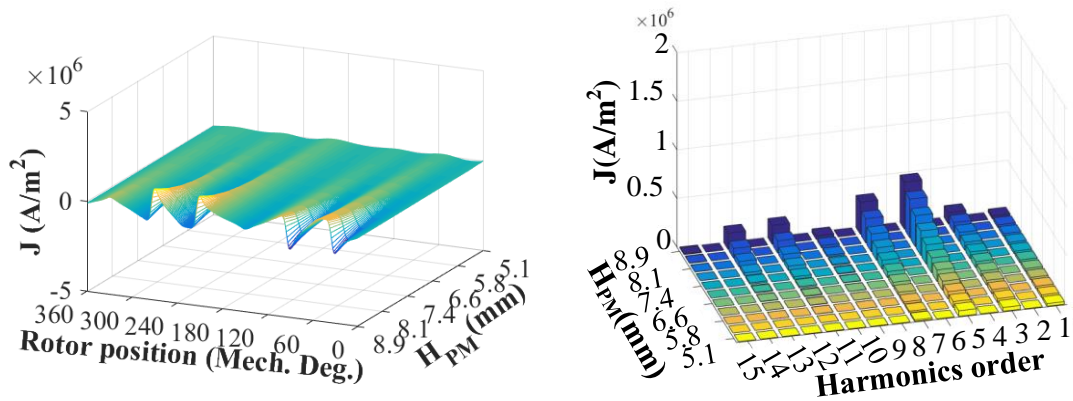


(c) Waveform of the optimal machine



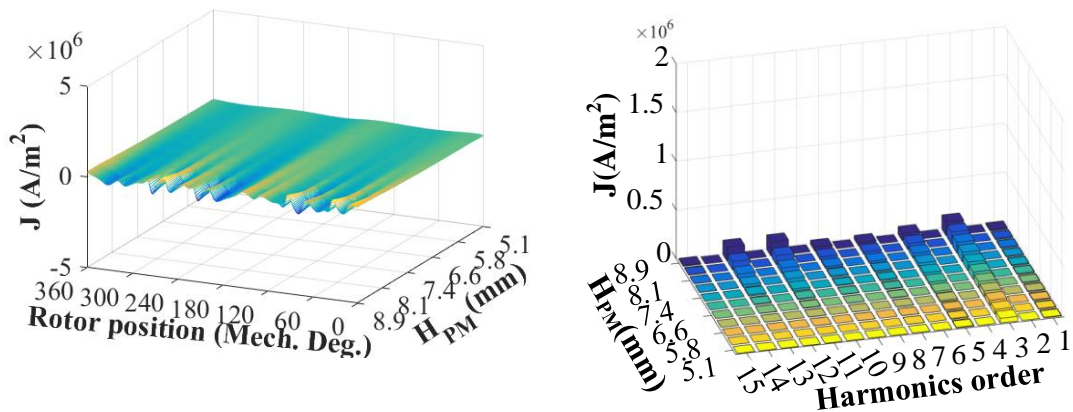
(d) Spectra of the optimal machine

Fig. 3. 30. Comparison of current density distributions of 6-slot/2-pole machine with full pitch winding under rated working condition at 0s.



(a) Waveforms of the conventional machine

(b) Spectra of the conventional machine



(c) Waveform of the optimal machine

(d) Spectra of the optimal machine

Fig. 3. 31. Comparison of current density distributions of 6-slot/2-pole machine with tooth-coil winding under rated working condition at 0s.

However, the lower winding factor in machine with tooth-coil winding also results in lower output torque. The comparison of rated on-load torque is shown in Fig. 3. 32. As can be seen, the torque of the machine with full pitch winding is almost twice comparing with the machine having tooth-coil winding.

In terms of the torque reduction due to the auxiliary slots, the torque decreases by 1.2% in the machine with tooth-coil winding but 2.6% in machine with full pitch winding. As can be seen, the auxiliary slots have less influence on the torque in the machine with tooth-coil winding. This is due to the spatial harmonics in this machine is relatively low,

which means the smaller size auxiliary slots are required to compensate the spatial harmonics. As a result, the increased equivalent airgap length due to auxiliary slots is smaller in machine with tooth-coil winding.

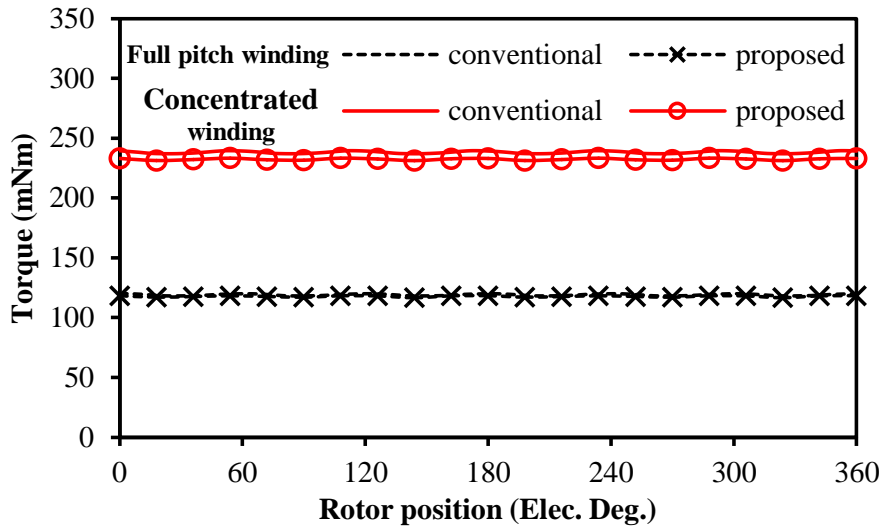
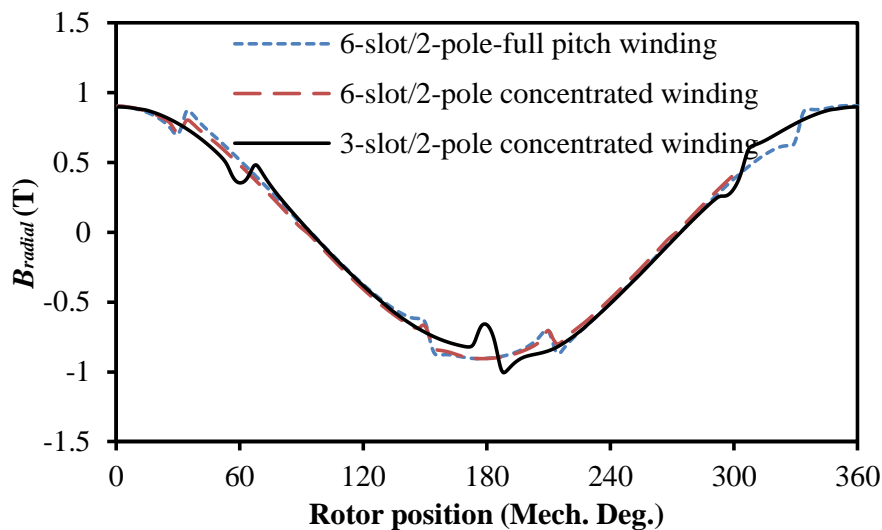
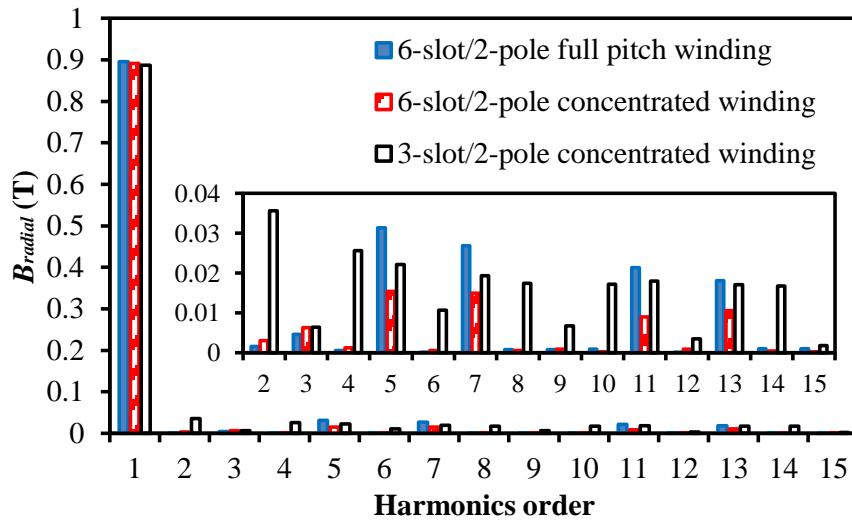


Fig. 3. 32. Rated on-load torque of 6-slot/2-pole machines with different currents.

In contrast, the torque reduction in the 3-slot machines is 4.8%, which is much higher than that in 6-slot machines, since the spatial harmonics content in 3-slot machines are much higher due to asymmetric windings. The rated on-load airgap flux densities at 0s are shown in Fig. 3. 33, and the comparison of total harmonic distortion (THD) is listed in Table 3. 7.



(a) Waveforms



(b) Spectra

Fig. 3.33 Rated on-load airgap flux density comparison in the conventional machines.

Table 3.7

THD in Conventional Machines with Different Slot/Pole Number Combinations and Winding Configurations

3-slot/2-pole tooth-coil winding	7.56%
6-slot/2-pole full pitch winding	5.61%
6-slot/2-pole tooth-coil winding	2.98%

It can be seen that the abundant even low order spatial harmonics due to asymmetric windings result in higher spatial harmonics, and hence, higher THD, which means larger auxiliary slots are required in 3-slot machines. Consequently, the torque reduction is higher in 3-slot machines.

### 3.5 Experimental Validation

In order to validate the numerically predicted results, the experiments for back EMFs and static torques are carried out. The pictures of conventional and proposed machines are shown in Fig. 3.34. Both conventional and proposed 3-slot/2-pole machines have been built with the airgap length of 0.6mm.

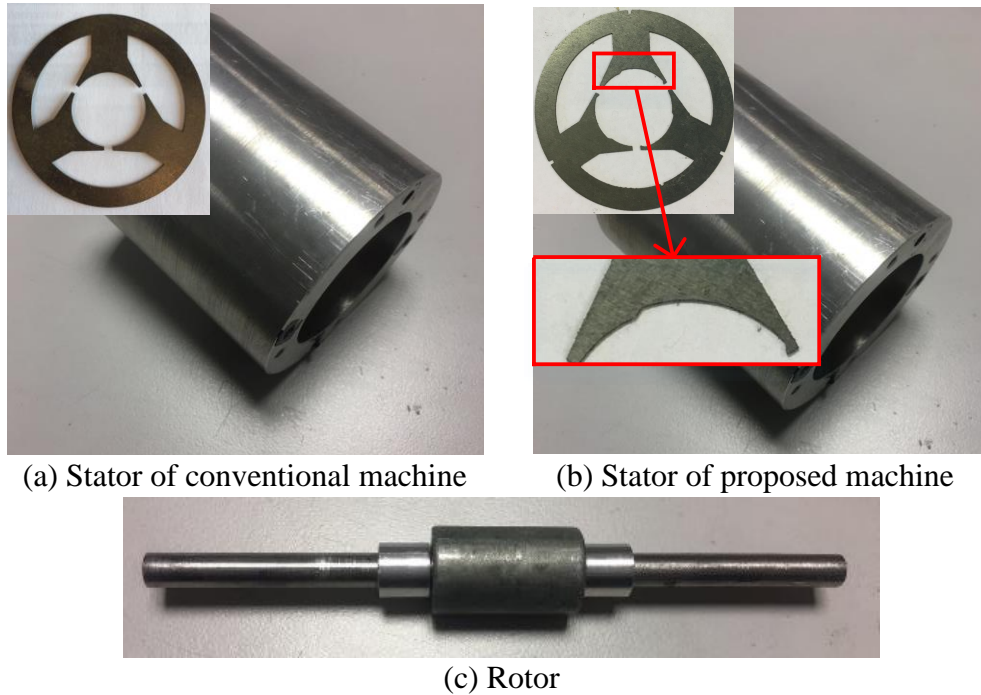


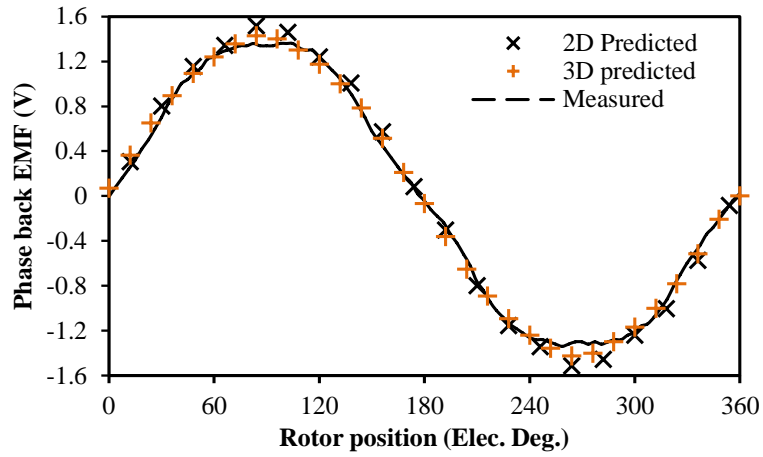
Fig. 3. 34 Photos of 3-slot/2-pole prototype machines.

It should be noticed that due to the small size, low output torque and high rotating speed, the total loss and each loss component are very hard to be measured accurately. Nevertheless, several main electromagnetic performances, i.e. the open-circuit back EMF and static torque, are tested to verify the correctness of the FE results.

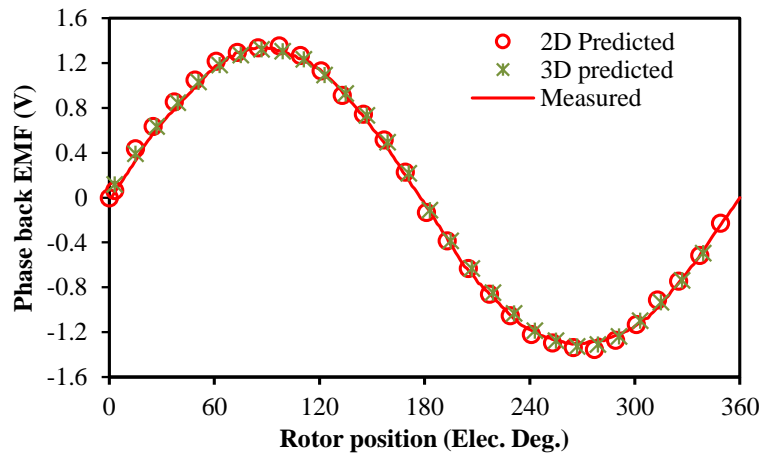
The open-circuit back-EMFs at 1000r/min are measured and compared with 2D and 3D FE predicted results in Fig. 3. 35. It can be seen that the great agreement is observed. In addition, the 3D simulation results are closer to the test results, since it has taken the end effect into consideration. The slight difference is mainly due to the manufacturing error, etc. Moreover, the difference between the conventional and the proposed machines is small which means the auxiliary slots have slight influence on the back EMF.

In addition, the static torque of both machines are measured, which is defined as the torque with fixed input current as  $I_q = 10$  A. The variation of rated static torque with different rotor position is shown in Fig. 3. 36(a) and the maximum torque with different input current is shown in Fig. 3. 36 (b). It can be seen that the difference between the predicted and measured values is very small, and it shows the conventional machine has slightly higher output torque comparing with the proposed one.

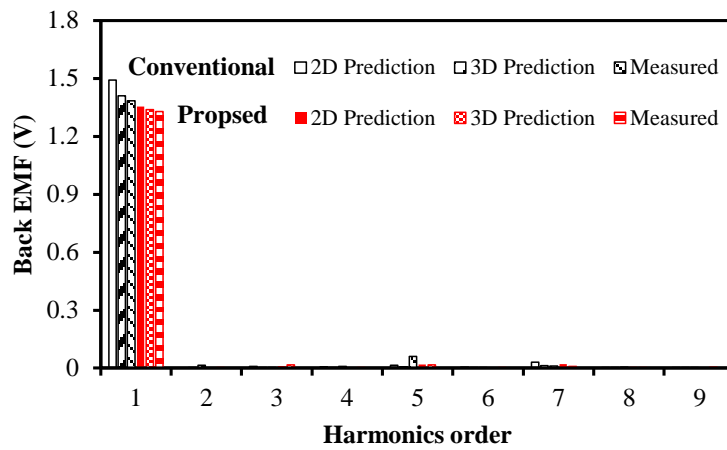




(a) Waveforms of the conventional machine.

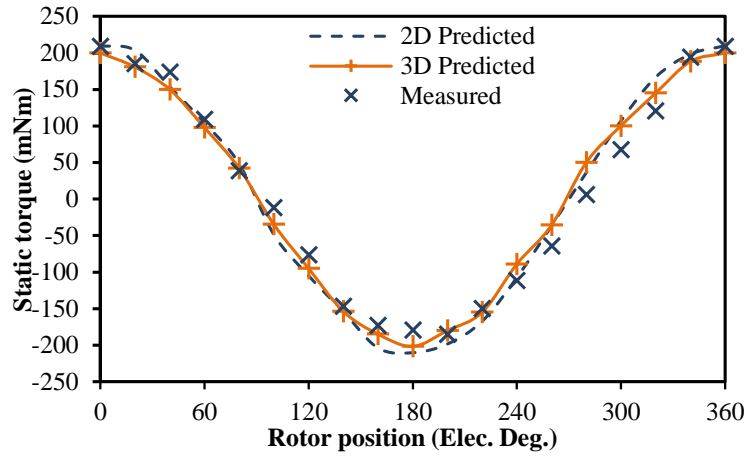


(b) Waveforms of the proposed machine

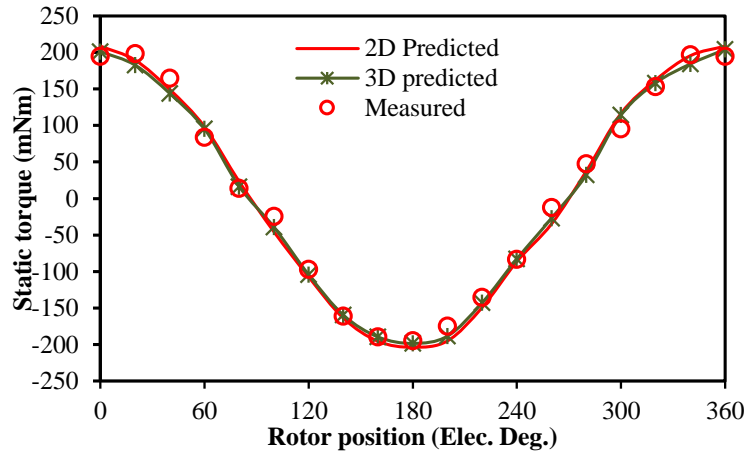


(c) Spectra.

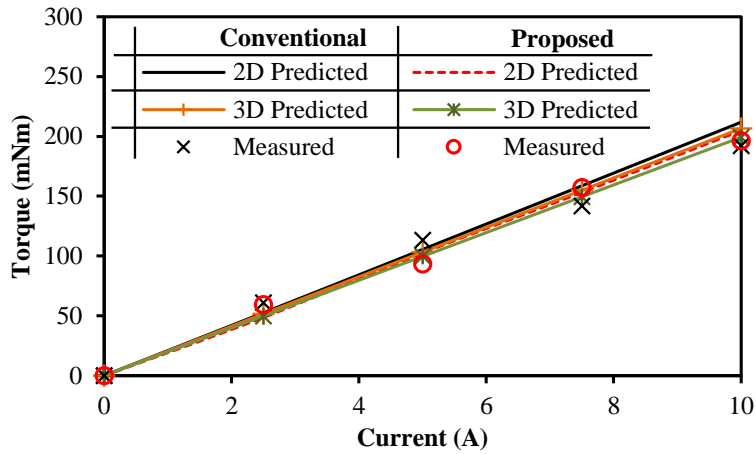
Fig. 3.35 Comparison of FE-predicted and measured back EMFs at 1000r/min.



(a) Torque in the conventional machine with different rotor positions and  $I_q = 10$  A.



(b) Torque in the proposed machine with different rotor positions and  $I_q = 10$  A.



(c) Maximum on-load torque with different  $I_q$ .

Fig. 3. 36. Comparison of FE-predicted and measured static torques with different rotor positions and q-axis currents.

### 3.6 Summary

The rated on-load magnet eddy current loss reduction in high speed machines is investigated in this chapter. A 3-slot/2-pole BLAC machine is selected as the prototype machine at first, and its airgap flux density distribution is studied by a simple MMF-permeance analytical model. Then, the method using auxiliary slots with optimal size and position is proposed. It shows this method can significantly reduce the rated on-load magnet eddy current loss, which is mainly due to the reduction of asynchronous spatial harmonics. Although the proposed method can result in torque reduction, the decrease is very slight. Moreover, the influence of working conditions is studied, which indicates that the proposed method can be more effective only for one specific load condition. In addition, the influence of other design parameters, e.g. airgap lengths, slot/pole number combinations and drive modes, is also investigated. It is proved that the machine with larger airgap length can benefit more from the proposed method, and this method can also offer excellent performance in 6-slot high speed PM machines. However, the proposed method is less effective in machines with BLDC drive mode, since the abundant time harmonics caused by BLDC drive mode aggravate the magnet eddy current loss significantly, and the proposed method has negligible influence on the time harmonics. Finally, two prototype machines are built and tested. Although the magnet eddy current loss is very hard to be measured, several other main electromagnetic performances, e.g. the back EMF and the static torque, are tested to validate the analyses and predictions.

In addition, it should be noticed that although the auxiliary slots with the optimal size and position are used for reducing both the rated average magnet eddy current loss and the maximum rated on-load UMF, it is necessary to illustrate the influence of the proposed method on different parasitic effects separately.

Since the proposed method has different working mechanisms on the rated average magnet eddy current loss and the maximum rated on-load UMF reduction. Although both these two parasitic effects essentially origin from the unwanted spatial harmonics and the field analysis is employed in both chapters. The contribution of each spatial harmonics to the magnet eddy current loss has additive effect. As a result, all spatial harmonics need to be cancelled out ideally so that the magnet eddy current loss can be eliminated. Therefore, the working mechanism of the proposed method on magnet eddy

current loss reduction is better to be illustrated from the harmonics reduction perspective. In contrast, UMF components caused by different spatial harmonics can be treated as several vectors, and the aim of the proposed method is to make the sum of these vectors to be zero instead of eliminating all of them. Consequently, the effectiveness of the proposed method as for the UMF reduction is better to be explained from the vector cancelling perspective.

# **CHAPTER 4**

## **INFLUENCE OF MAGNET THICKNESS ON ELECTROMAGNETIC PERFORMANCE OF HIGH SPEED PM MACHINES**

As one of the key design parameters, the magnet thickness has significant influence on the electromagnetic performance in high speed machines. Consequently, its effect will be comprehensively investigated in this chapter. The investigation is carried out based on a conventional 3-slot/2-pole high speed machine. To make the comparison fair enough, the rated output torque and the rotating speed are fixed when the magnet thickness varies. It is found that the relatively thick magnet can not only affect the electromagnetic performances such as flux linkage, back EMF, inductance and demagnetisation, but also significantly reduce parasitic effects, e.g. on-load magnet eddy current loss as well as on-load UMF, as confirmed by finite element analyses, albeit with some experiments.

### **4.1 Introduction**

In terms of machine types of high speed permanent magnet machines, although both SPM and IPM machines can be used, the SPM machines are more suitable for the ultra-high speed situation due to the mechanical consideration [BIN06].

As for high speed SPM machines, [BIA05] gives the general design considerations including the stator structure, rotor loss, mechanical constrain and PM demagnetization. [BIN06] compares the mechanical performance of several different rotor structures, i.e. surface-mounted magnet rotors with and without inter-pole gap and the buried magnet rotor. It shows that the surface-mounted magnet rotor without inter-pole gap can offer the best mechanical performance under the high speed situation. [BOR10] investigates the rotor stress and the critical speed for a ring PM rotor, [CHE14] studies the stress of a solid cylinder rotor, and the mechanical performance of these two different rotor structures is compared in [XIA16] which shows the ring PM rotor with carbon fibre sleeve is more favourable when the speed is not too high, while the metallic sleeve is more suitable for ultra-high speed situation due to its higher rigidity. The influence of different magnetizations is investigated in [PHY12], [MYE00] and [MYE01]. It is

found that the Halbach magnetization is more suitable for high speed machines since it can result in the lowest electromagnetic loss.

Nevertheless, the influence of magnet thickness on the electromagnetic performance of small high speed machines has not been studied comprehensively. In order to fill this gap, it will be studied in this chapter in details. It shows that the magnet thickness has great influence on back EMF, flux linkage as well as inductance. Moreover, the relatively thick magnet in high speed machines could effectively reduce on-load magnet eddy current loss as well as on-load UMF. In addition, it could offer better demagnetization performance. Nevertheless, the thick magnet has relative low magnet usage efficiency.

In the prototype machines employed in this chapter, the equivalent airgap length which contains actual airgap length and sleeve thickness is designed as a relative large value, i.e. 1.2mm. In addition, a high strength sleeve should be used due to mechanical consideration. The mechanical stress calculation and the optimal sleeve length is presented in Appendix IV. It should be noticed that in Appendix IV, the rotor core is removed, which indicates that the optimal sleeve thickness presented in Appendix IV should be thicker than the value used in this chapter. Nevertheless, since the split ratio of prototype machines in this chapter is 0.36, the maximum sleeve thickness required in theory is smaller than 0.5mm even according to the calculation of Appendix IV, which is much smaller comparing with the equivalent airgap length. Therefore, there should not be mechanical problem for the prototype machines in this chapter. In addition, since the sleeve can be treated as the equivalent airgap length for electromagnetic fields, in order to make the model structure clearer and simpler, the sleeve will not be presented in the models in this chapter. Moreover, the magnetic ring is used, which is due to its simple structure as well as easy manufacture process.

This chapter is organized as follows, the detailed design parameters of the prototype machine is introduced in Section 4.2, and so does the variation of rated input phase current with different magnet thickness. Then, the effect of magnet thickness on both PM and armature fields is investigated in Section 4.3. In Section 4.4, the influence of the magnet thickness on main electromagnetic performances of high speed machine is investigated. Finally, some experimental results are carried out to validate the FE analysis results and predictions in Section 4.5.

## 4.2 Prototype Machines

The investigation of this chapter is based on a conventional 3-slot/2-pole machine. The tooth-coil concentrated winding and the diametric magnetization are employed. The cross section is the same as the machine shown in Fig. 2. 1, and the detailed parameters are listed in Table 4.1.

It is worth noting that the rated output torque is fixed in later investigations. Otherwise, the thicker magnets always result in higher output torque if the input current is fixed. Consequently, the comparison of machines with different magnet thickness would be unfair. The rated average output torque is fixed as 100mNm and the rotating speed is kept as 60000rpm. The variation of input current amplitude with magnet thickness is shown in Fig. 4. 1, which shows the input current decreases with magnet thickness significantly. It should be noticed that the 120° brushless DC (BLDC) operation mode is used, and the ideal rectangular phase current is employed to evaluate the on-load characteristics.

Table 4. 1  
Basic Parameters of Machine

Slot number	3	Shaft diameter (mm)	5
Pole number	2	Rotor outer diameter (mm)	15.6
Stator outer diameter (mm)	50	Axial length (mm)	12
Stator inner diameter (mm)	18	Magnet remanence (T)	1.2
Stator yoke height (mm)	5.2	Current angle (Elec. Deg.)	0
Slot opening (mm)	2	Rated speed (rpm)	60000
Air-gap length (mm)	1.2	Number of turns per phase	45

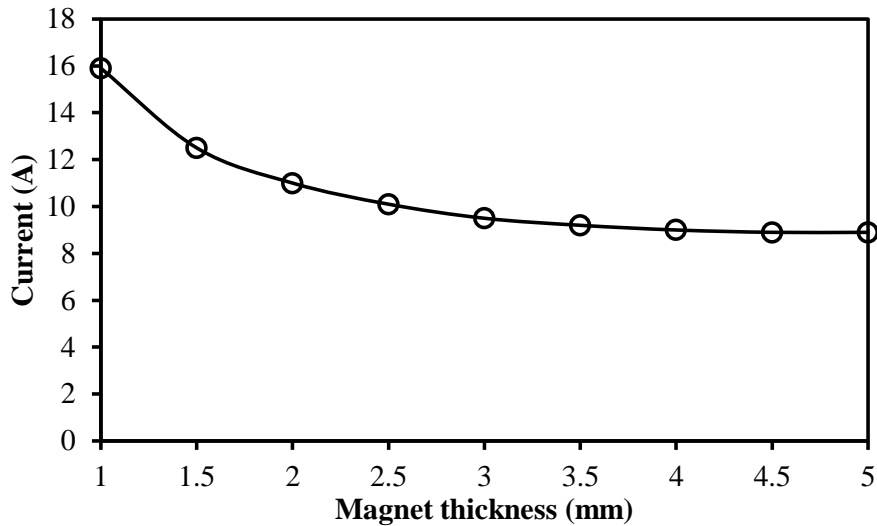


Fig. 4. 1 Variation of input current with different magnet thickness.

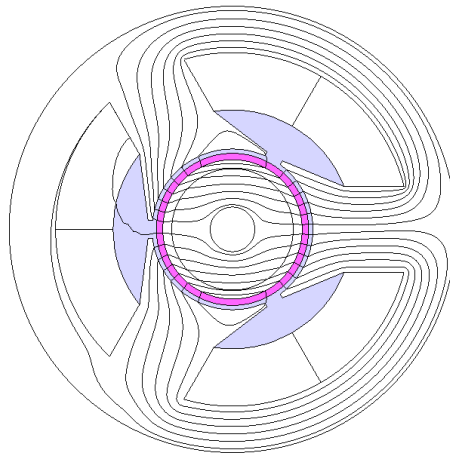
### 4.3 Effect of Magnet Thickness on Magnetic Fields

Since the electromagnetic performance highly depends on the magnetic field distribution, it is necessary to analyse the effect of magnet thickness on magnetic fields firstly. In this section, both radial and tangential components of PM and armature fields are investigated under the rated on-load condition. It is worth noting that both PM and armature fields are affected by saturation significantly. Therefore, the frozen permeability method [CHU13] is used here to separate these two fields precisely.

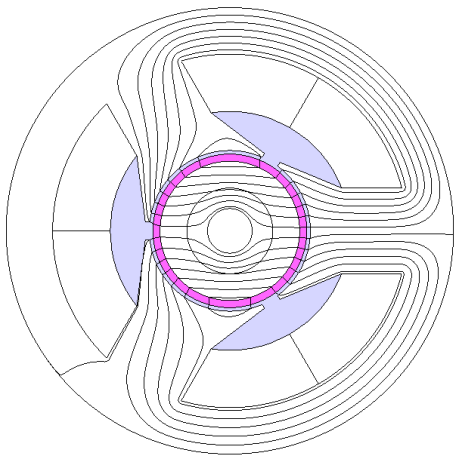
In order to show the influence of magnet thickness more clearly, three different magnet thicknesses, i.e. 1mm, 3mm and 5mm, are selected.

The PM fields are studied firstly as shown in Fig. 4. 2 and Fig. 4. 3, respectively. As can be seen, both radial and tangential PM fields increase with magnet thickness due to the increased MMF. However, different behaviour can be observed in armature fields which are shown in Fig. 4. 4 and Fig. 4. 5. Since the sleeve and magnet act as equivalent air-gap for armature fields and the rated input phase current decreases with magnet thickness in order to keep the same output torque, all components in armature fields decrease with magnet thickness.

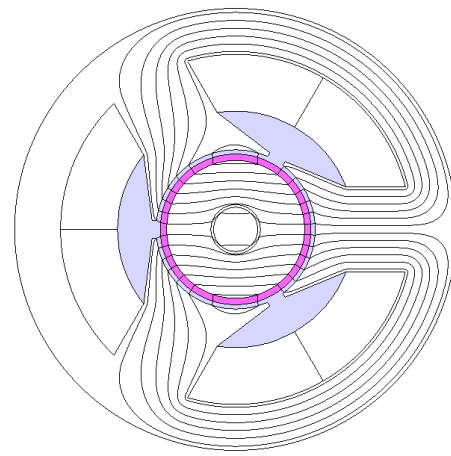




(a) PM thickness=1mm

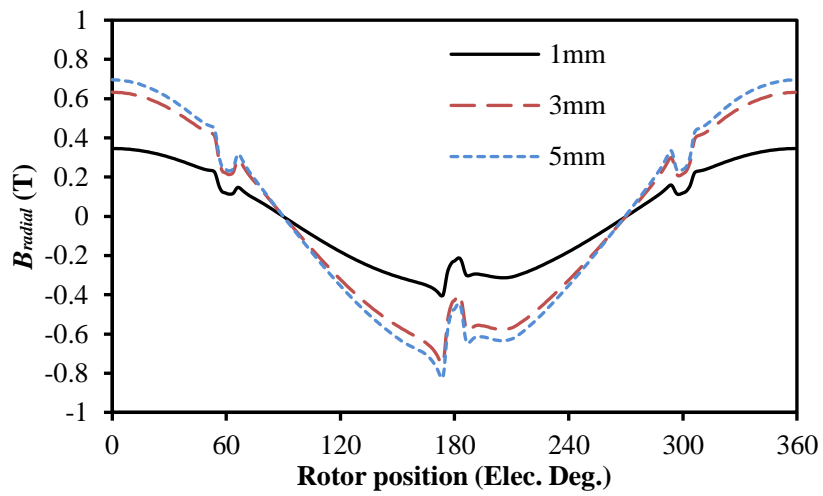


(b) PM thickness=3mm

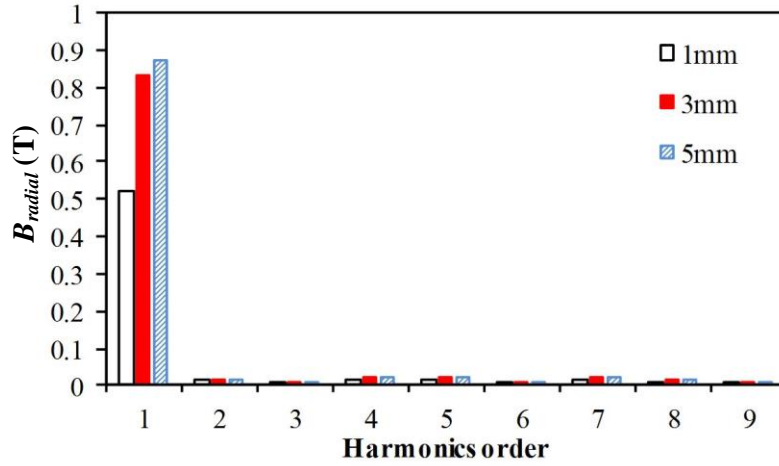


(c) PM thickness=5mm

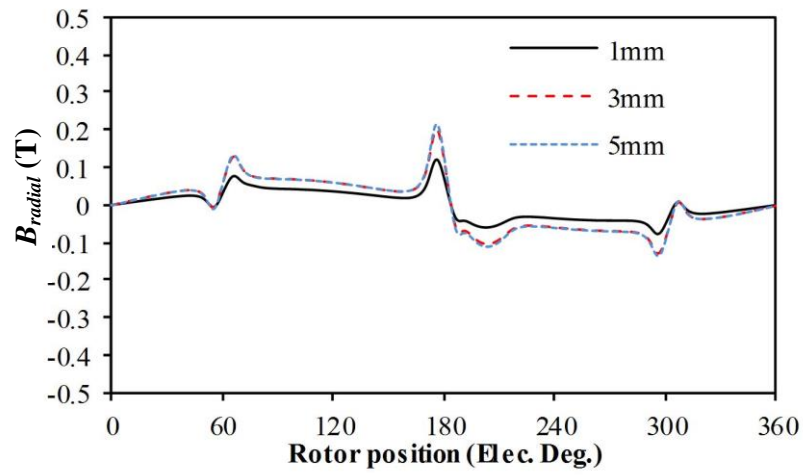
Fig. 4. 2 PM field distributions of 3-slot/2-pole PM machines with different magnet thickness at 0s.



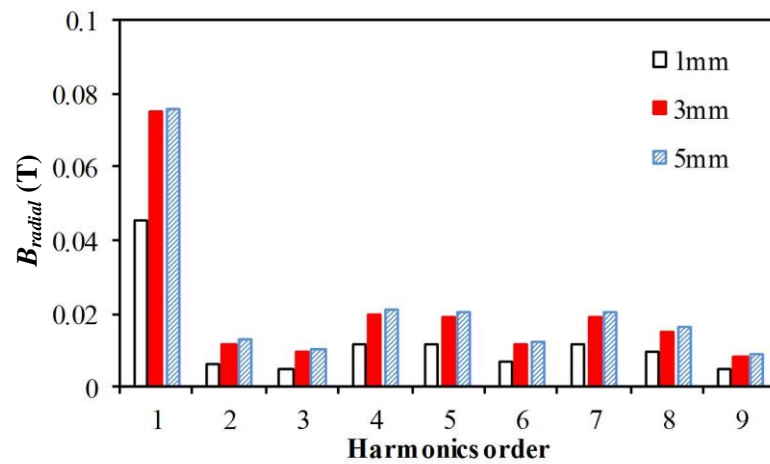
(a) Radial field waveforms



(b) Radial field spectra

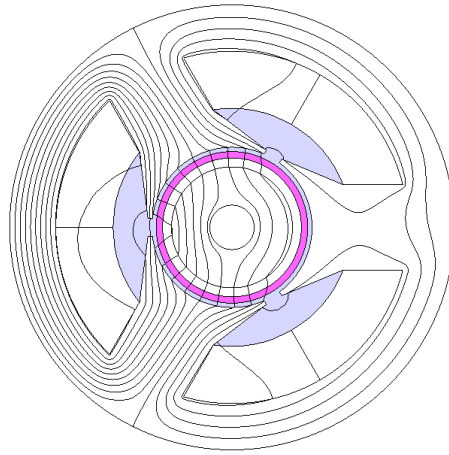


(c) Tangential field waveforms

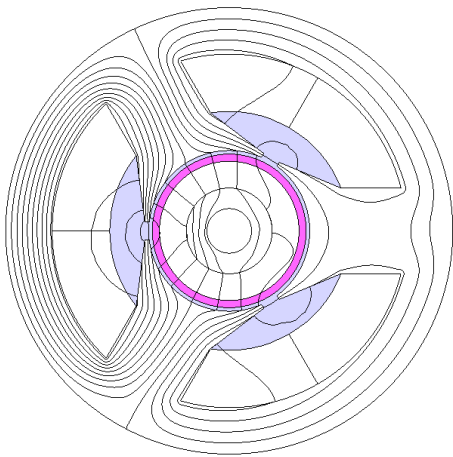


(d) Tangential field spectra

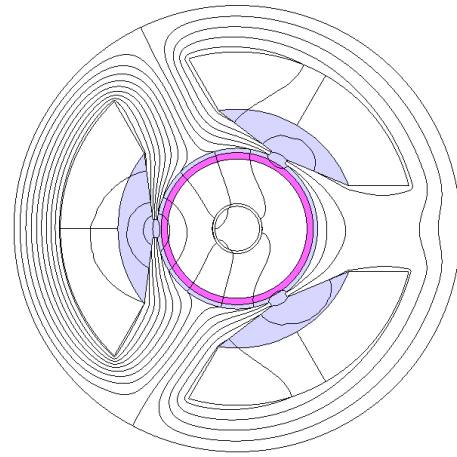
Fig. 4. 3 PM field distributions at 0s.



(a) PM thickness=1mm

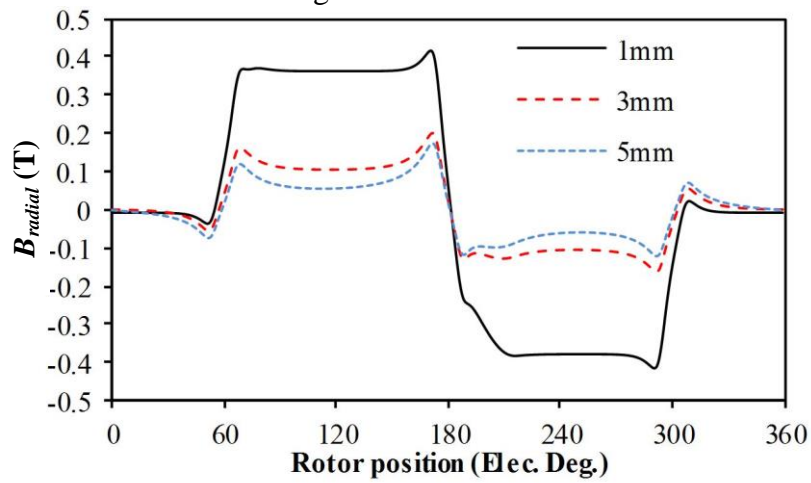


(b) PM thickness=3mm

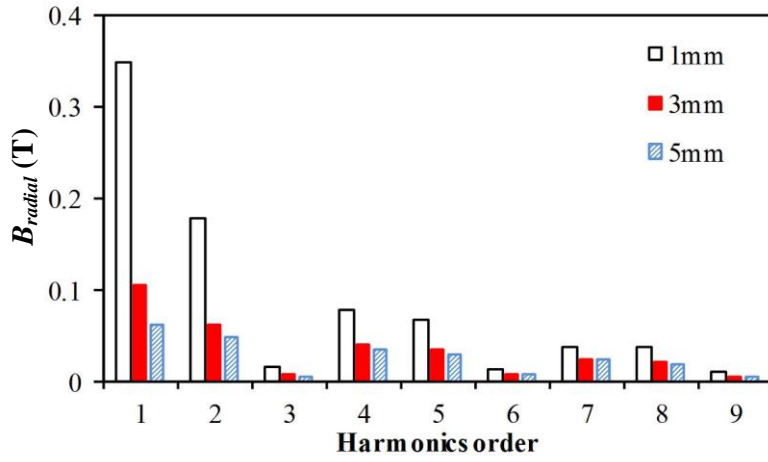


(c) PM thickness=5mm

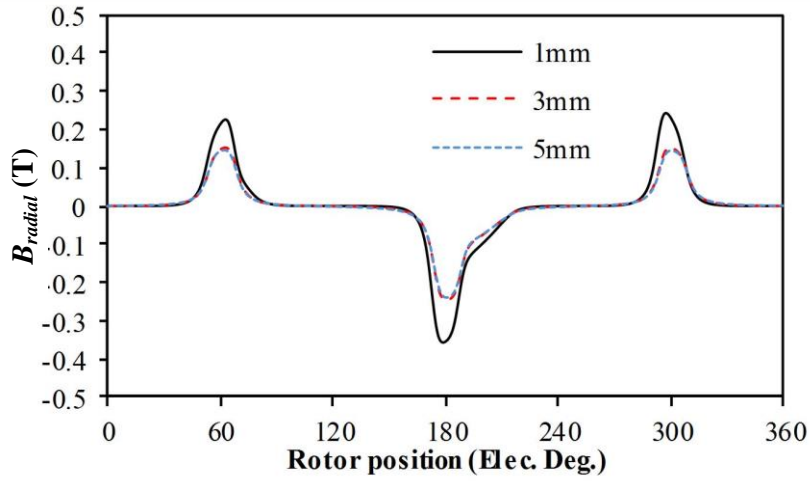
Fig. 4. 4. Armature field distributions of 3-slot/2-pole PM machines with different magnet thickness at 0s.



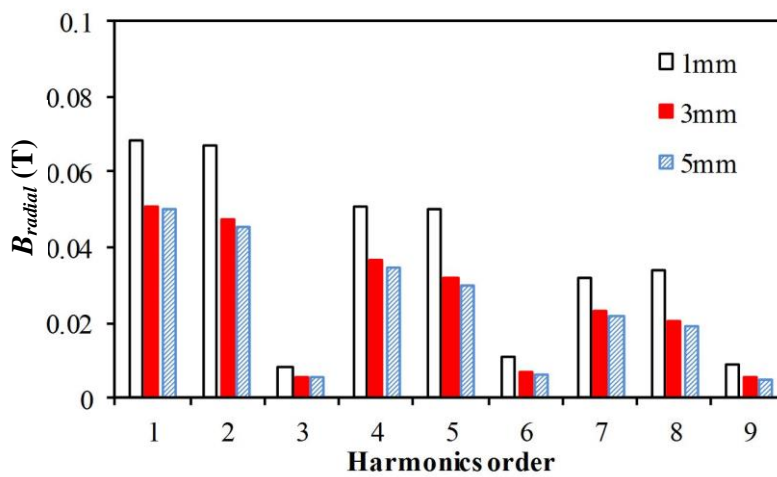
(a) Radial field waveforms



(b) Radial field spectra



(c) Tangential field waveforms



(d) Tangential field spectra

Fig. 4. 5. Armature field distributions at 0s.

Nevertheless, it can be seen that the radial and tangential PM fields vary with almost the same ratio when magnet thickness changes. In contrast, the radial component of armature fields is much sensitive to the variation of magnet thickness comparing with the tangential component. This is due to the fact that the enhanced flux leakage caused by the increased equivalent air-gap length also contributes to tangential component of armature fields. Therefore, there is a cancelling effect between decreased MMF of armature fields and increased flux leakage. Consequently, the radial armature field decreases further comparing with the tangential one, and their difference decreases with magnet thickness significantly.

As for the proportion of harmonics content, it is much higher in armature fields comparing with PM fields. This can be explained by two reasons, the first one is that the MMF in armature fields has a lot of harmonics while the fundamental component in the MMF of PM fields is dominant. Secondly, relative small slot opening is adopted in the prototype machine. Consequently, the harmonics caused by slotting effect are measurably small.

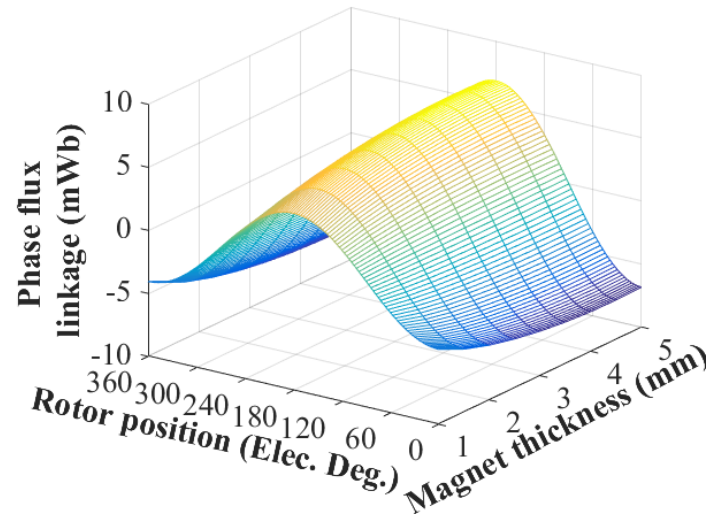
#### **4.4 Effect of Magnet Thickness on Machine Performance**

In this section, the influence of magnet thickness on the electromagnetic performance will be investigated comprehensively. Its effect on phase flux linkage, phase back EMF, unbalanced magnetic force, loss, demagnetization as well as economic issue will be studied.

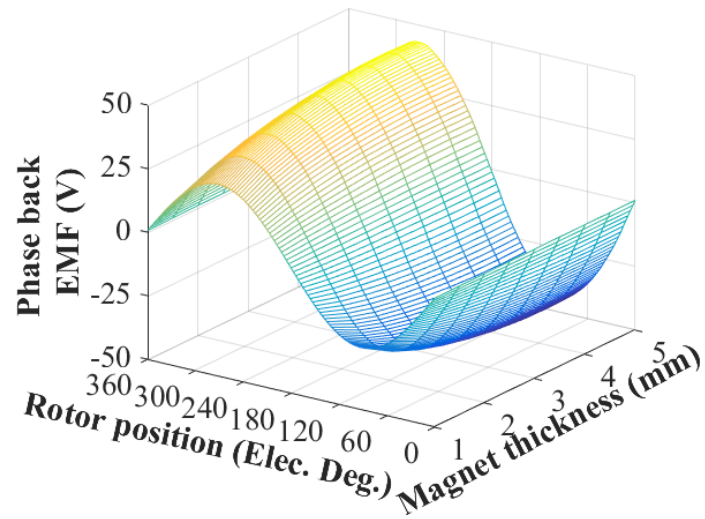
##### **4.4.1 Phase Flux Linkage and Phase Back EMF**

The flux linkage and the back EMF are critical for all machines, especially for high speed machines. Since the high value of back EMF may make the terminal voltage exceed the DC voltage limitation when the rotating speed is very high.

The waveforms of the open circuit phase flux linkage and the back EMF with different magnet thickness are shown in Fig. 4. 6. Moreover, the fundamental and total harmonic distortion (THD) are shown in Fig. 4. 7.

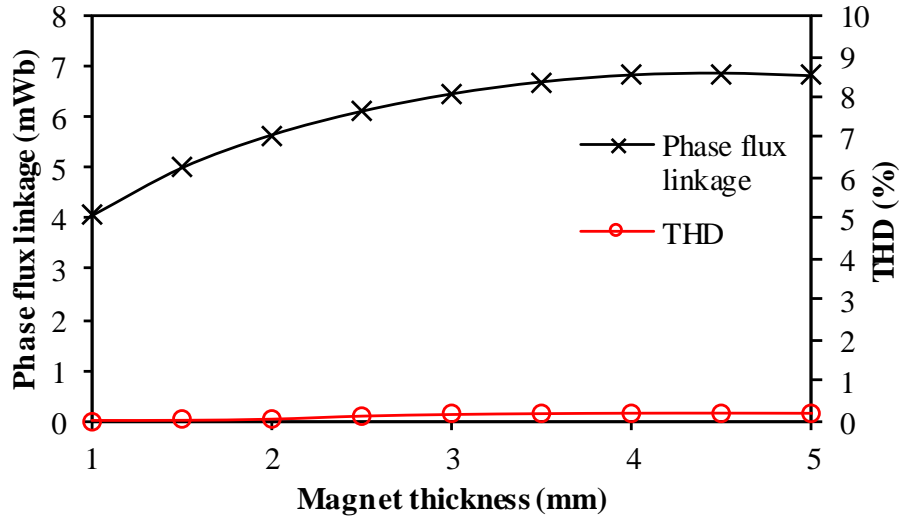


(a) Phase flux linkage

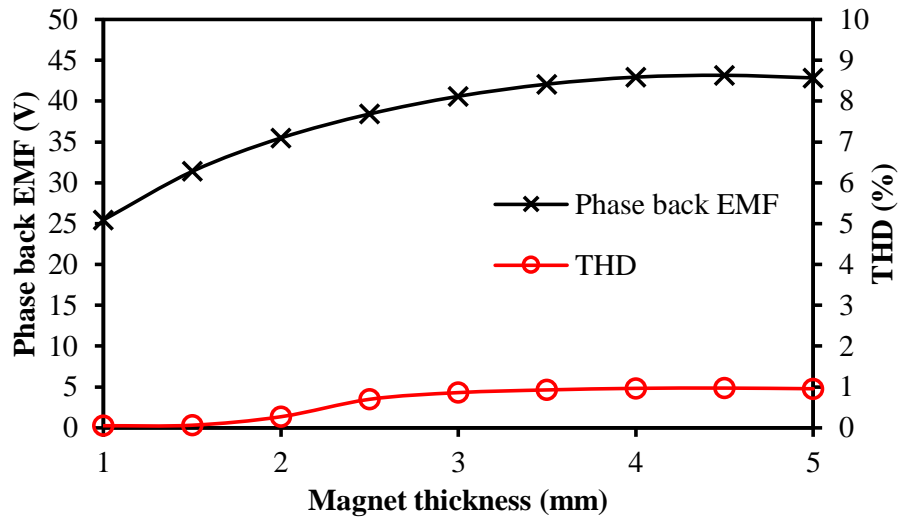


(b) Phase back EMF

Fig. 4. 6. Variation of phase flux linkage and phase back EMF with different magnet thickness.



(a) Phase flux linkage



(b) Phase back EMF

Fig. 4. 7. Variation of fundamentals value and THDs of flux phase flux linkage and phase back EMF with different magnet thickness.

As shown, the fundamental flux linkage and back EMF increase with magnet thickness rapidly when the magnet is thin. In contrast, the increase is almost negligible when the magnet is thicker than 3.5mm.

In terms of the harmonic content, the THD is calculated by:

$$THD = \sum_{i=2} \sqrt{V_i^2} / V_1 \quad (4.1)$$

where  $i$  indicates the harmonic order,  $V$  indicates its amplitude, and  $V_1$  is the amplitude of the fundamental component.

As can be seen, the THDs of the flux linkage and the back EMF increase with magnet thickness. However, their values remain at very low level, which is mainly due to the diametric magnetization of PM as well as relatively small slot opening.

#### 4.4.2 On-load Torque Characteristics

The variation of torque with different magnet thickness and phase current amplitude is shown in Fig. 4. 8. A relatively large current range is chosen to observe the overload capability of machines.

As shown, the higher phase current and thicker magnet always result in higher output torque due to higher electric and magnetic loadings. Moreover, the variation of torque gradient with different magnet thickness and current is also calculated to evaluate the overload capability, which is shown in Fig. 4. 9.

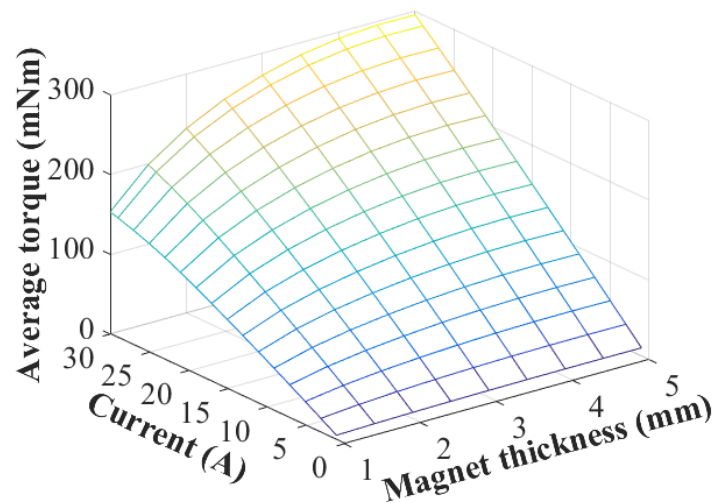


Fig. 4. 8 Variation of torque with different magnet thickness and phase current.



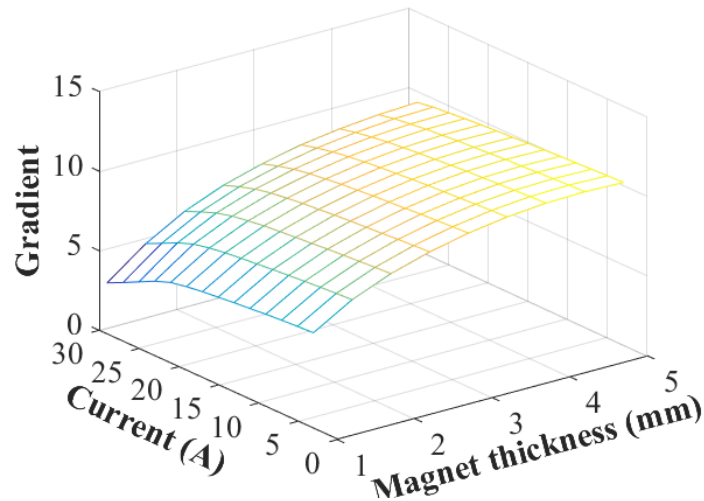


Fig. 4. 9 Variation of torque gradient with different magnet thickness and phase current.

It could be seen that the machine with thinner magnet has larger gradient decrease when the phase current increases, which indicates that the machine having thicker magnet also could provide better overload performance. Since the machine with thinner magnet has relative smaller equivalent airgap length for armature field. Therefore, the large phase current could result in more serious saturation due to the stronger armature field. Although the machine having thicker magnet has stronger PM field, while its influence is weaker than the increased armature field when the phase current is large and the equivalent airgap length is small.

#### 4.4.3 Unbalanced Magnetic Force

The UMF is also critical for high speed machines. Since it may cause extra noise and vibration, and significantly reduce the life of bearings. The UMF occurs in 3-slot/2-pole machine even if there is no manufacture tolerance, e.g. rotor eccentricity, which is mainly due to the asymmetric stator topology and unbalanced winding configurations as illustrated in previous chapters.

The variation of maximum rated on-load UMF with different magnet thickness is shown in Fig. 4. 10.

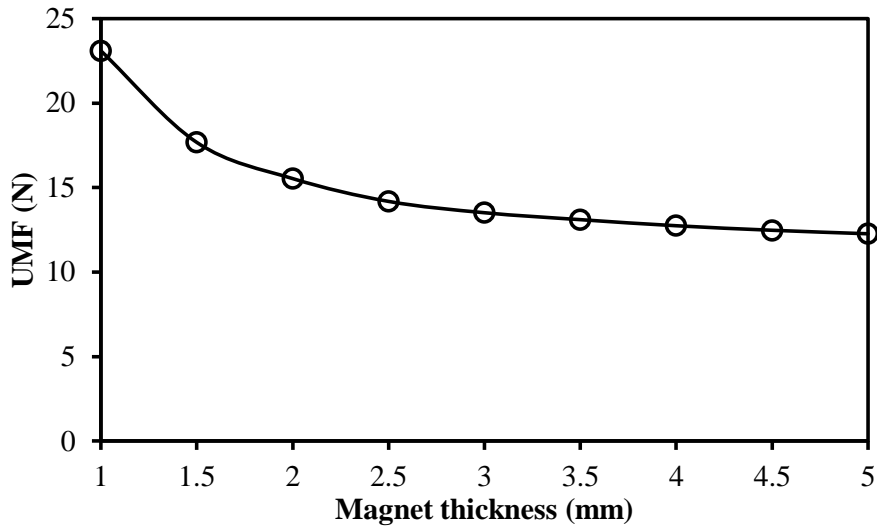


Fig. 4. 10 Variation of maximum rated on-load UMF with different magnet thickness.

It can be seen that the maximum rated on-load UMF decreases considerably (more than 40%) when the magnet thickness increases from 1mm to 5mm. In order to investigate in more details, the rated on-load UMF has to be separated according to difference sources. The variations of UMF components with magnet thickness are shown in Fig. 4. 11, in which  $F_1$  and  $F_3$  indicate the UMFs due to PM and armature fields self-interaction, and  $F_2$  is the UMF due to the mutual-interaction between these two fields.

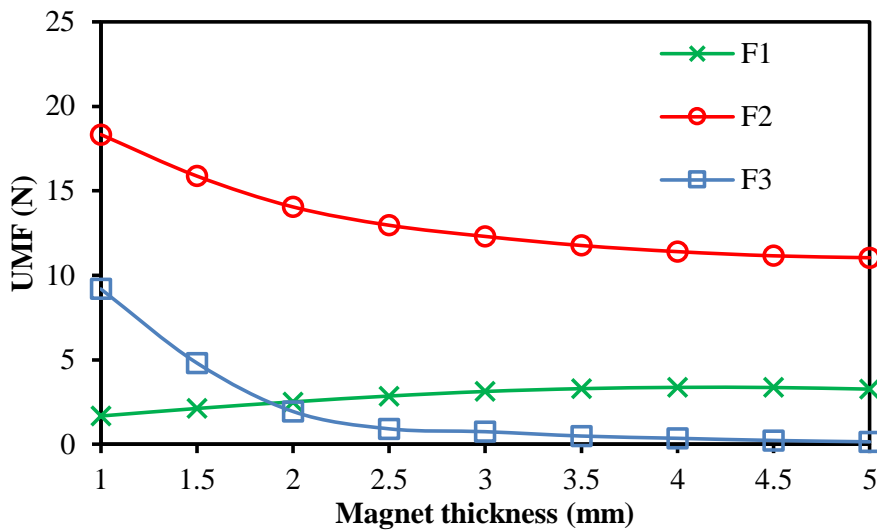


Fig. 4. 11. Variation of UMF components with different magnet thickness under rated working condition at 0s.

It should be mentioned that the amplitude of UMF varies with rotor positions due to the variation of field distributions. In order to ease the investigation and make the fair

comparison, the 0 degree rotor position is chosen, which indicates the North Pole aligns with the phase A. Nevertheless, this method can be also applied to any other rotor positions.

It is found that  $F_1$  increases with magnet thickness due to the enhanced PM fields. In contrast,  $F_3$  decays very quickly with magnet thickness caused by the significantly reduced armature fields. Consequently,  $F_3$  has significant influence on the resultant on-load UMF when the magnet is very thin, while its influence can be almost neglected when the magnet becomes thick. As for  $F_2$ , its value is measurable over whole interval but decreases significantly with magnet thickness.

Since  $F_2$  almost dominates the resultant UMF, it should be emphasized. The radial and tangential components of  $F_2$  are separated by frozen permeability method [CHU13] and shown in Fig. 4. 12 represented by  $F_{2r}$  and  $F_{2t}$ , respectively.

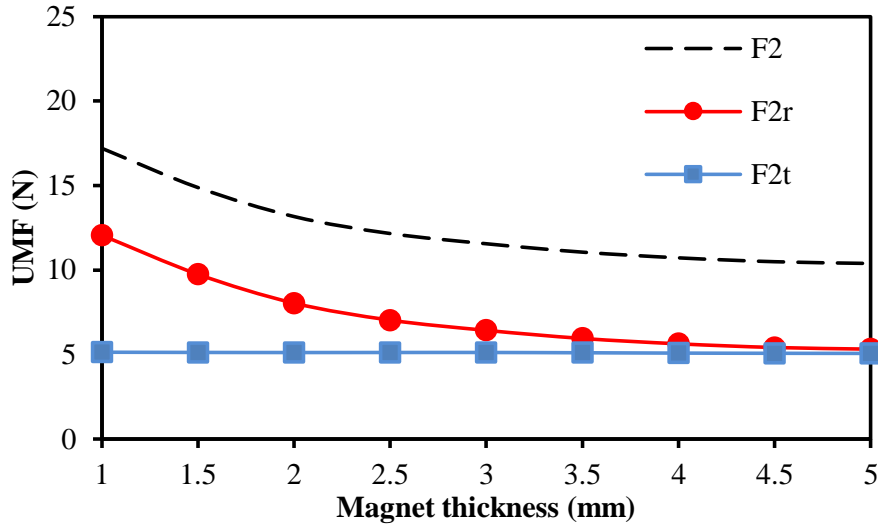


Fig. 4. 12. Decomposition of  $F_3$  with different magnet thickness under rated working condition at 0s.

As can be seen, an additive effect between these two components can be observed due to the slot/pole combination [WUL10]. However,  $F_{2r}$  decreases with magnet thickness significantly while  $F_{2t}$  is almost constant. In order to investigate its reason in more details,  $F_{2r}$  and  $F_{2t}$  need to be decomposed further according to:

$$\sigma_2 = \overbrace{(B_{mr} \cdot B_{ar}) / \mu_0}^{\sigma_{2,1}} - \overbrace{(B_{mt} \cdot B_{at}) / \mu_0}^{\sigma_{2,2}} \quad (4.2)$$

$$\tau_2 = \overbrace{B_{mr} \cdot B_{at} / \mu_0}^{\tau_{2,1}} + \overbrace{B_{ar} \cdot B_{mt} / \mu_0}^{\tau_{2,2}} \quad (4.3)$$

The UMFs caused by stress components shown in (2.2)-(2.3) with magnet thickness are shown in Fig. 4. 13, in which  $F_{2r1}$ ,  $F_{2r2}$ ,  $F_{2t1}$  and  $F_{2t2}$  are the UMFs caused by  $\sigma_{2,1}$ ,  $\sigma_{2,2}$ ,  $\tau_{2,1}$  and  $\tau_{2,2}$ , respectively.

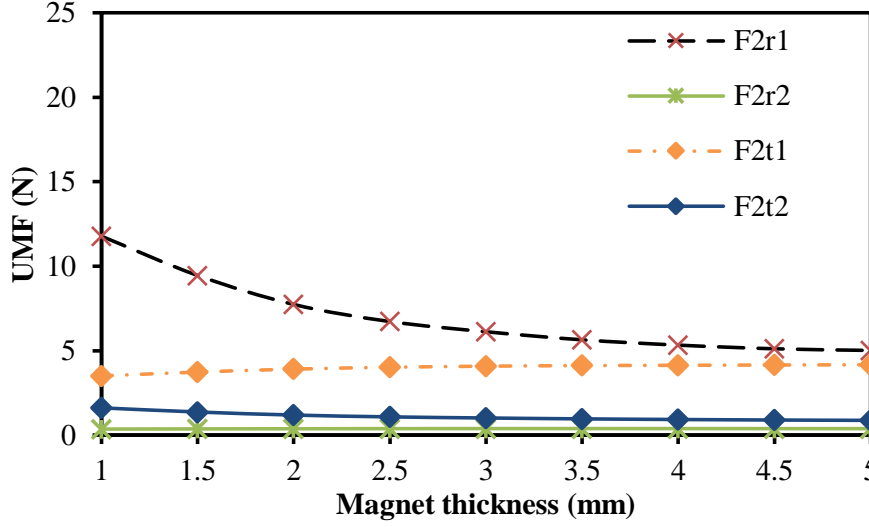


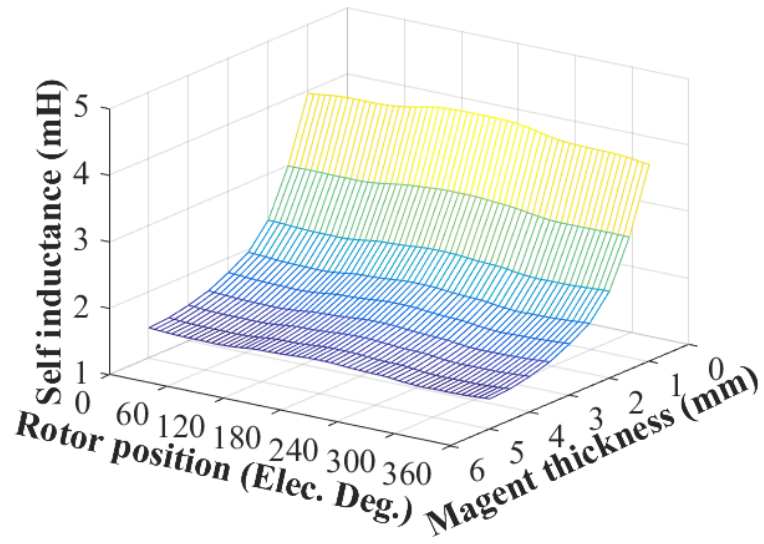
Fig. 4. 13. Variation of F3 components with different magnet thickness under rated working condition at 0s.

As can be seen,  $F_{2r1}$  and  $F_{2t1}$  dominate the values of  $F_{2r}$  and  $F_{2t}$ . In contrast,  $F_{2r2}$  and  $F_{2t2}$  have negligible influence. In terms of  $F_{2r1}$ , it depends on the radial components of both PM and armature fields. Since the reduction of armature radial field is much more significant than the enhancement of radial PM field,  $F_{2r1}$  presents a measurable reduction when magnet thickness increases. In contrast,  $F_{2t1}$  results from the radial PM field and the tangential component of armature field. Although both radial and tangential armature fields decrease with magnet thickness, the tangential field is more insensitive to the variation of magnet thickness as explained in Section 4.3. As a result, the variation of  $F_{2t1}$  is very small which can be almost neglected.

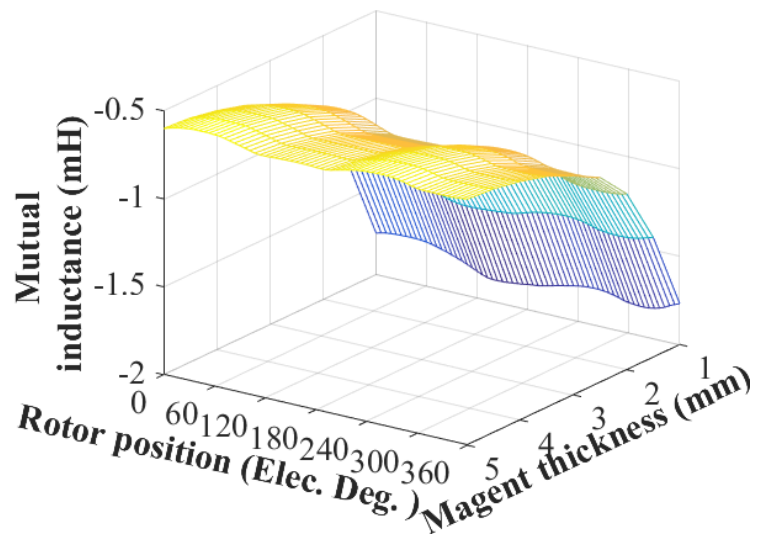
In addition, it should be noticed that according to (4.2)-(4.3), the difference between  $F_{2r1}$  and  $F_{2t1}$  depends on the difference between radial and tangential armature fields. As shown in Fig. 4. 5, the values of radial and tangential armature fields become closer to each other when magnet thickness increases. Consequently, the difference between  $F_{2r1}$  and  $F_{2t1}$  decreases with magnet thickness.

#### 4.4.4 Self and Mutual Inductances

The variations of self and mutual inductances with different rotor position and magnet thickness are shown in Fig. 4. 14. In addition, the variation of average inductances with magnet thickness is shown in Fig. 4. 15.



(a) Self inductance



(b) Mutual inductance

Fig. 4. 14 Variation of self and mutual inductance with different magnet thickness and rotor position.

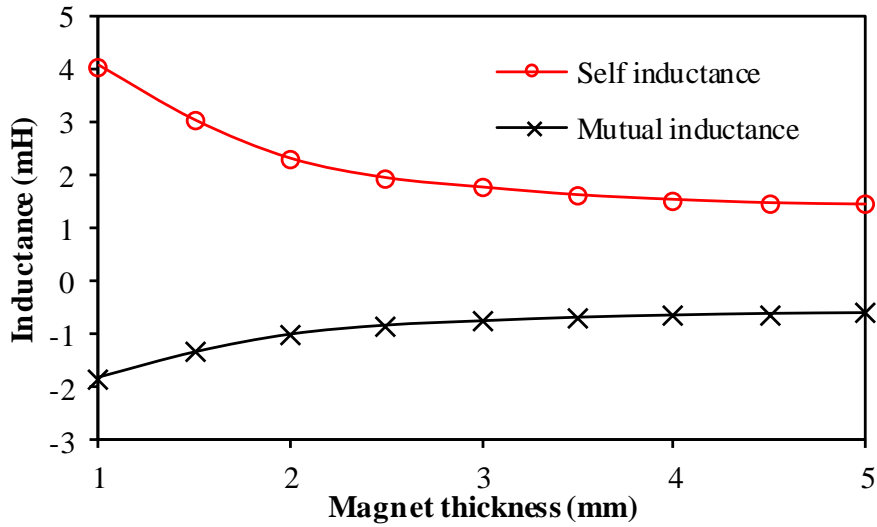


Fig. 4. 15. Variation of average self and mutual inductance with magnet thickness and rotor position.

As can be seen, both self and mutual inductances decrease with magnet thickness rapidly at first but slowly when the magnet is thick enough. The decrease is mainly due to the rise of equivalent airgap length for the armature field, and hence, the reduction of armature reaction. In addition, the inductances vary slightly with different rotor positions due to localized saturation in the stator tooth [LIG14].

#### 4.4.5 Stator Iron Loss and Magnet Eddy Current Loss

In high speed machines, the stator iron loss and magnet eddy current loss are very critical, since their values are much more significant comparing with low speed machines due to the high rotating frequency. Consequently, these loss components have more measurable influence and they should be investigated as well.

The variations of average no-load and on-load magnet eddy current losses with different magnet thickness are shown in Fig. 4. 16. As can be seen, the no-load magnet eddy current loss increases with magnet thickness due the increased magnet volume and harmonics content in PM field. However, its value is negligible in all cases, which is due to the diametric magnetization and small slot opening, and hence, low spatial harmonics caused by slotting effect.

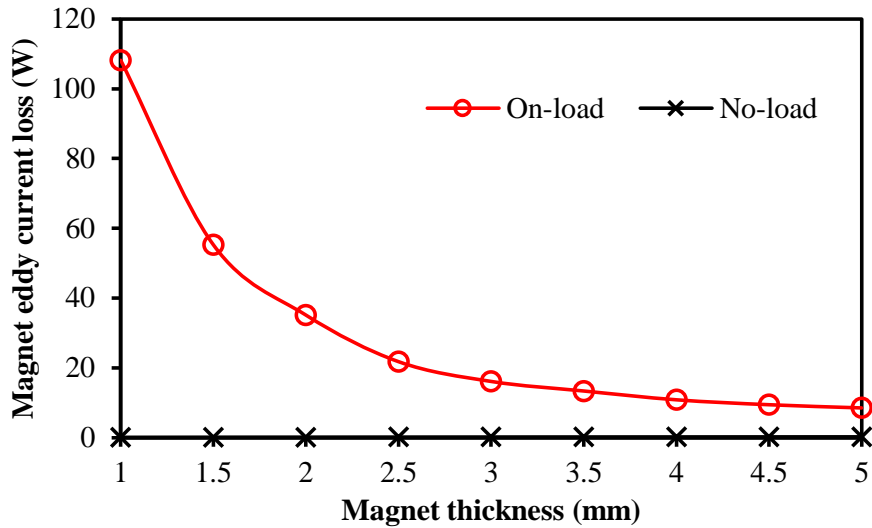


Fig. 4. 16. Variation of average magnet eddy current loss with magnet thickness.

In contrast, the average rated on-load magnet eddy current loss is much higher, while it decreases with magnet thickness significantly. The variation of average rated on-load magnet eddy current loss with different rotor position is shown in Fig. 4. 17. In order to ease the comparison, the machines with 1mm, 3mm and 5mm magnets are chosen. As shown, the magnet eddy current loss fluctuates significantly with different rotor positions, which is caused by the abundant time harmonics.

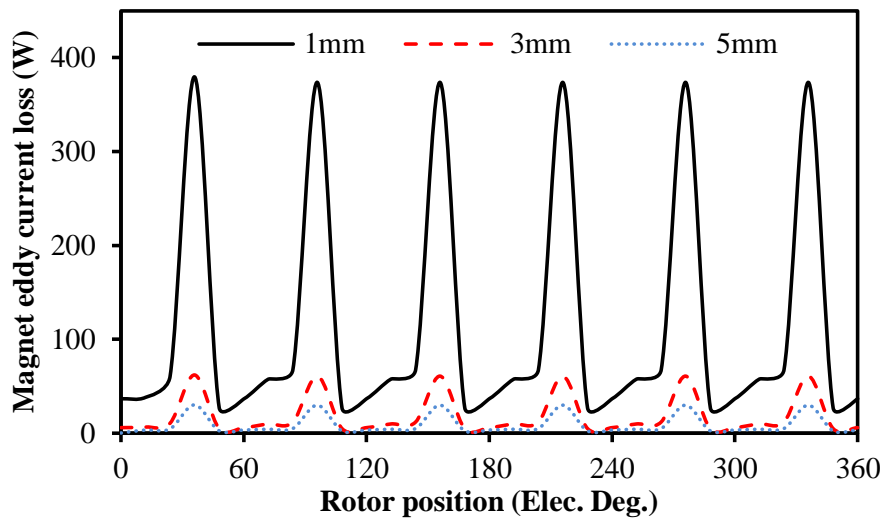


Fig. 4. 17. Variation of average rated on-load magnet eddy current loss with different rotor position.

A circle on the magnet surface is selected which is shown in Fig. 4. 18 and the eddy current density distribution along this circle is calculated as shown in Fig. 4. 19. It should be noted that the magnet eddy current density changes with rotor positions, and

the 36 electrical degree rotor position is chosen in Fig. 4. 19. The detailed reason has been explained in Chapter 3 in details.

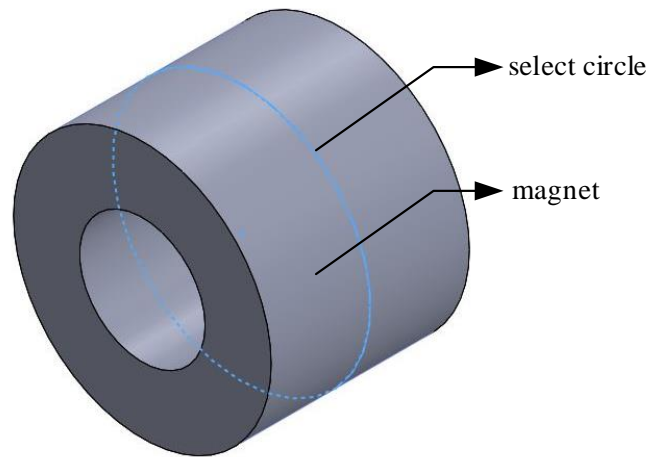
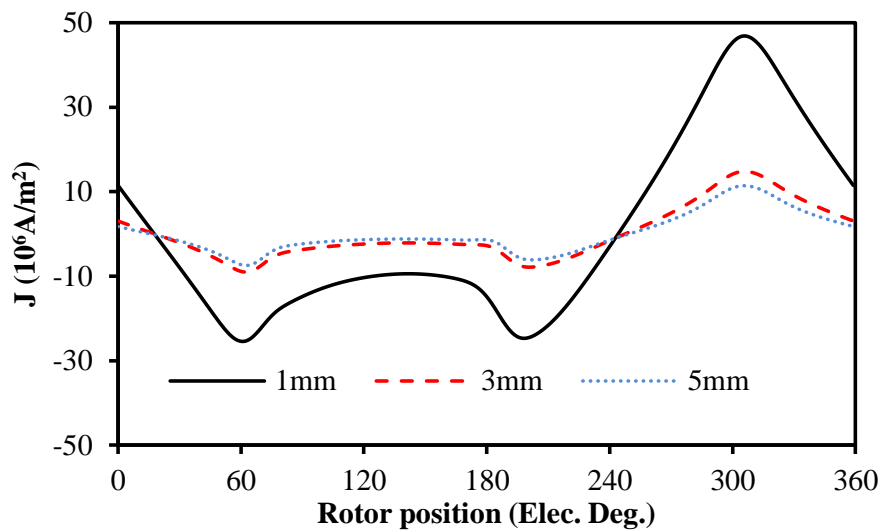


Fig. 4. 18 Illustration of selected circle on surface of magnet.

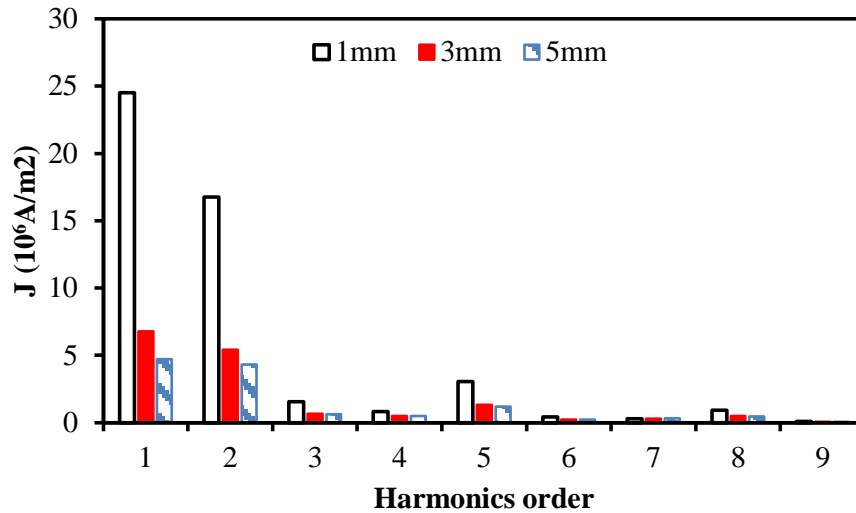
It can be seen that the most of magnet eddy current loss results from the low order harmonics. Moreover, there is also fundamental component in the current density distribution, which indicates that part of the loss results from the time harmonics due to the BLDC drive.

As for the source of the low order spatial harmonics, most of them result from the armature fields as shown in Fig. 4. 4 and Fig. 4. 5. Consequently, the decreased armature fields caused by the increased magnet thickness is the main reason of the reduced magnet eddy current loss.



(a) Waveforms





(b) Spectra

Fig. 4. 19 Comparison of eddy current densities of machines with different magnet thickness.

However, it should be noticed that both the increased equivalent airgap length and the decreased phase current could descend the armature fields. In order to evaluate their contributions separately, the variation of average rated on-load magnet eddy current losses with different magnet thickness and input phase current are calculated and shown in Fig. 4. 20. The maximum and minimum currents are selected as the rated currents of machines with 1mm and 5mm magnets, respectively. As shown, both these two factors could reduce the magnet eddy current loss and they have almost equivalent influence.

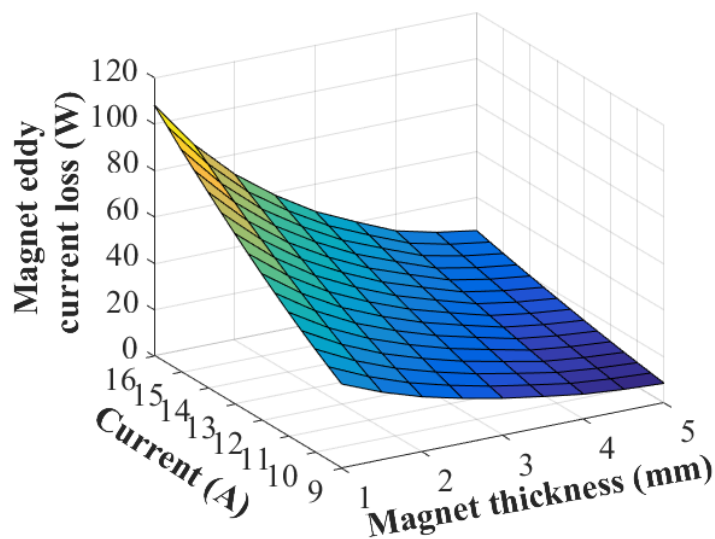


Fig. 4. 20. Variation of magnet eddy current loss with different magnet thickness and phase current.

The variation of average rated on-load stator iron loss with different magnet thickness is shown in Fig. 4. 21. As can be seen, the loss decreases rapidly at first but reaches a steady state when the magnet is thick enough.

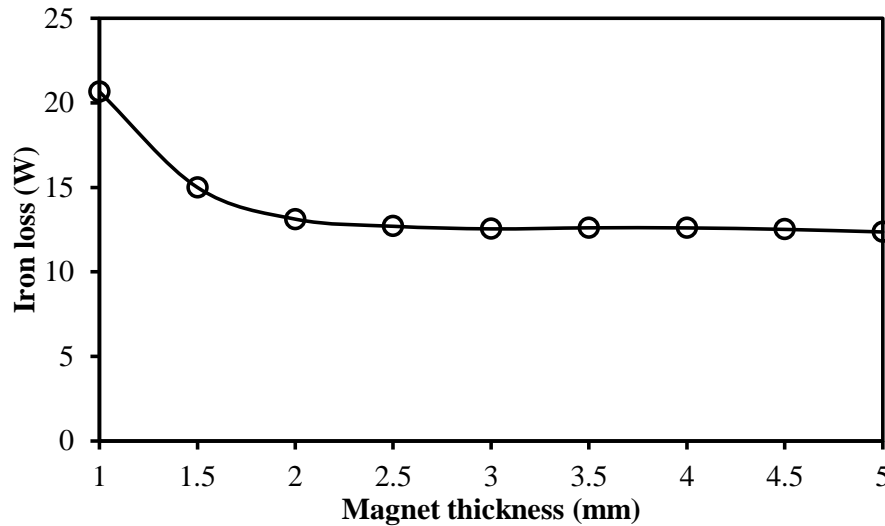


Fig. 4. 21. Variation of stator iron loss with different magnet thickness.

Different from the magnet eddy current loss, both PM and armature fields could result in significant flux density variation in stator laminations, and hence, contribution to stator iron loss. Consequently, the change of stator iron loss is mainly due to different influence of magnet thickness on the armature and PM fields. The armature field decreases with the magnet thickness rapidly at first but slowly when the magnet is relative thick. In contrast, the magnet thickness has almost opposite effect on the PM field. Nevertheless, comparing with radial armature field, the radial PM field is more insensitive to the magnet thickness as shown in Section 4.3. As a result, the stator iron loss decreases with magnet thickness at first due to the significantly reduced armature reaction, while the cancelling effect between the increased PM field and decreased armature field makes the variation of iron loss is not very significant when the magnet is relative thick.

#### 4.4.6 Demagnetization

Due to the high rotor loss caused by high rotating frequency as well as BLDC drive mode, the PM material may suffer from high temperature. In addition, since the output torque of high speed PM machines is relative low, any small load variation may introduce d-axis current caused by the modified current angle. As a result, the

demagnetization is a very critical problem for high speed PM machines which will be investigated in this part.

The worst case is chosen here where  $I_d = -I_{phase}$  and the temperature of PM material is selected as 100°C. The B-H curves of PM under different temperatures are shown in Fig. 4. 22. As can be seen, the knee point increases with temperature significantly which is about 0.4T when the PM temperature is 100°C.

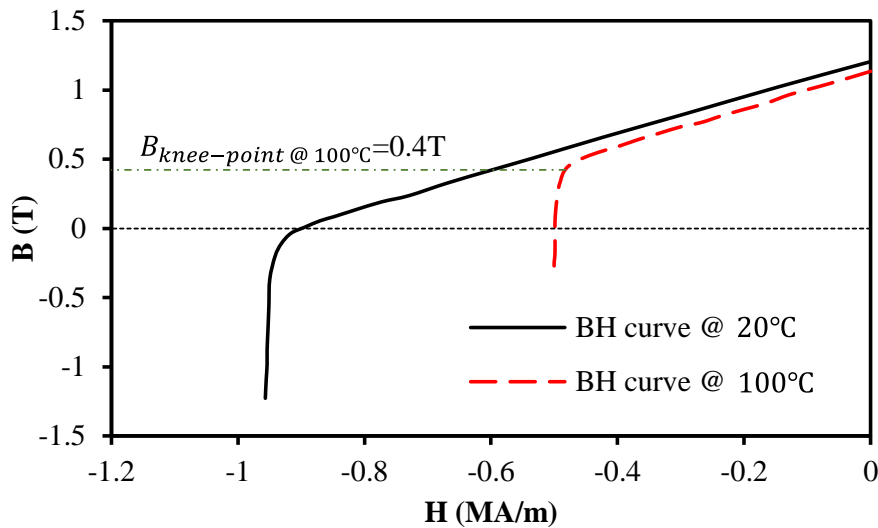


Fig. 4. 22. B-H curves of NdFeB35 with different temperature.

The field distributions along magnetization direction of machines with different magnet thickness are shown in Fig. 4. 23, where the maximum flux density is 0.4T.

Consequently, any area having the flux density lower than this value is demagnetized. It can be seen that the demagnetization area decreases with magnet thickness significantly, and there is almost no demagnetization when the magnet thickness is 2mm.

This is mainly due to two reasons. The first one is the amplitude of input current decreases with magnet thickness significantly, which is shown in Fig. 4.2. Secondly, the equivalent airgap for armature field increases with magnet thickness as well. As a result, a relative thicker magnet is more suitable for high speed PM due to the favourable demagnetization performance.

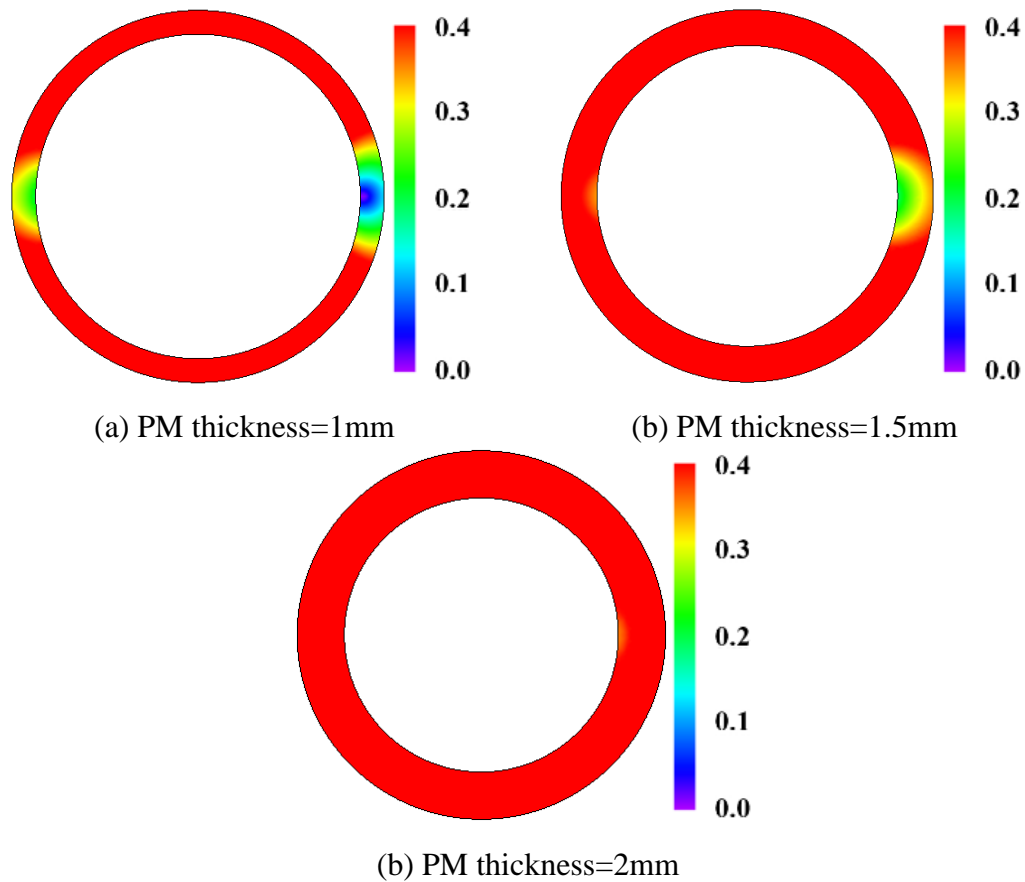


Fig. 4. 23. Field distributions of machines with different magnet thickness under fault working condition.

#### 4.4.7 Economic Issue

In addition to the characteristics mentioned above, the cost issue is also very critical to machines, especially for industry applications. Therefore, it will also be investigated here so that the comparison could be more comprehensive.

Since the machines share the same stator structure, the only difference is the rotor part. As the permanent magnet material (NdFeB) is far more expensive comparing with the laminations and copper, the magnet usage efficiency (ratio of average torque to magnet cost) is employed here instead of the efficiency of total cost of machine to make the comparison more pertinent. According to [HUA15], the price for NdFeB PM is chosen as 150 USD/kg.

The variation of magnet usage efficiency with different magnet thickness and phase current is shown in Fig. 4. 24. As shown, the larger phase current could result in higher efficiency. This is due to the enhancement of the armature field, and hence, the increase of the output torque. However, it should be noticed that the selection of current is

limited by the maximum copper loss. In addition, thanks to the smaller equivalent airgap length for armature field as well as lower volume of magnet material, the machines with thinner magnet also could provide higher magnet usage efficiency.

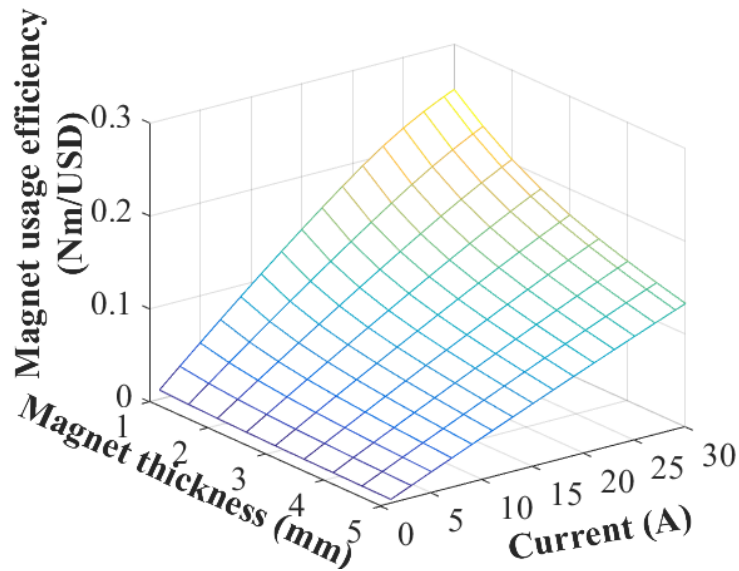


Fig. 4. 24. Magnet usage efficiency with different magnet thickness and phase current.

Moreover, the variation of magnet usage efficiency with different magnet thickness under rated working condition is shown in Fig. 4. 25.

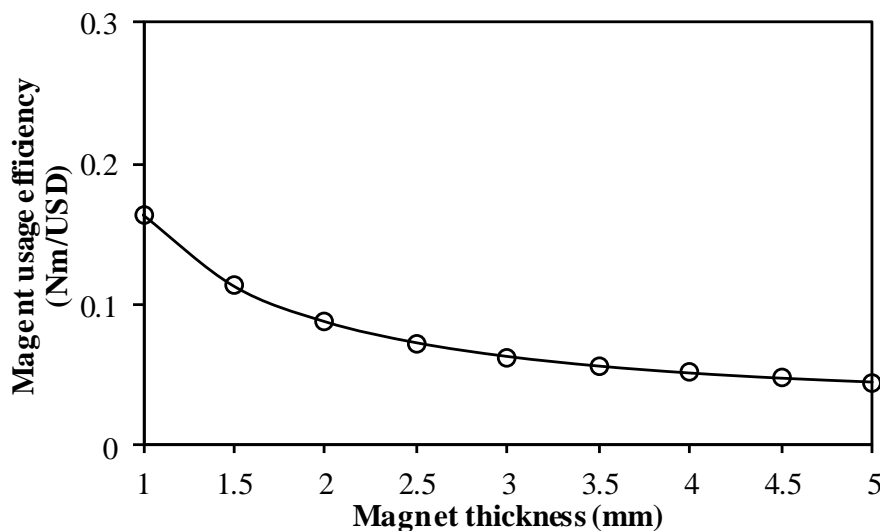


Fig. 4. 25. Variation of magnet usage efficiency with different magnet thickness under rated output torque.

It can be seen that the efficiency decreases with the magnet thickness rapidly at first, but then relatively slower when the magnet is thick enough. As a result, the trade-off

between the magnet usage efficiency and other performances, e.g. magnet eddy current loss, demagnetization, etc., should be balanced in practice.

#### 4.5 Experimental Validation

The experiments are carried out to verify the numeric analysis results. For simplicity, two machines with the same structure but different magnet thicknesses, i.e. 2mm and 4mm, are built and tested. The key design parameters are the same as shown in Section 4.2, and the main components are shown in Fig. 4. 26.

As can be seen, the prototype machine consist of four different parts: a single end support frame, a 3-slot stator, a fan housing and a rotor. It should be noticed that the single end supporting frame is used here. Although this structure may make the machine easier to suffer from the eccentricity due to the UMF, while the value of UMF in the prototype machine is small, which means the deformation of rotor due to UMF could be neglected.



(a) Frame



(b) Stator



(c) Fan housing



(d) Shaft, bearing and fan



(e) Rotor with 2mm magnet

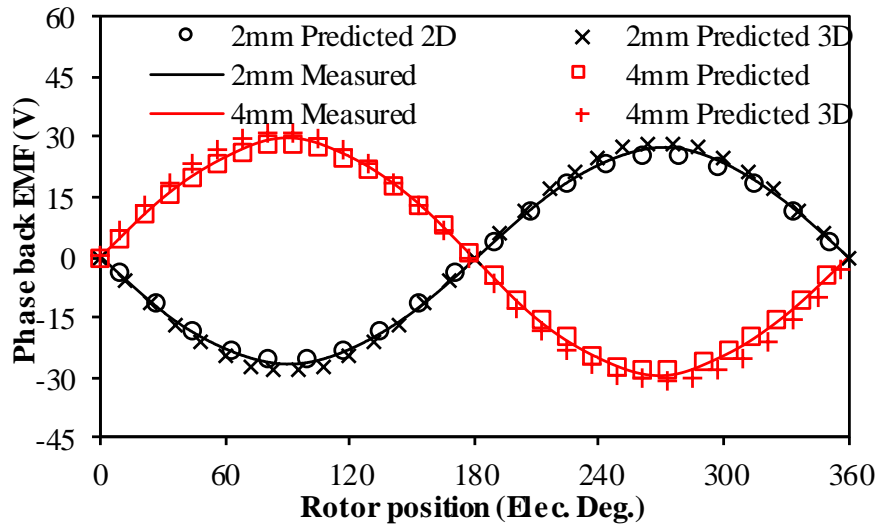


(f) Rotor with 4mm magnet

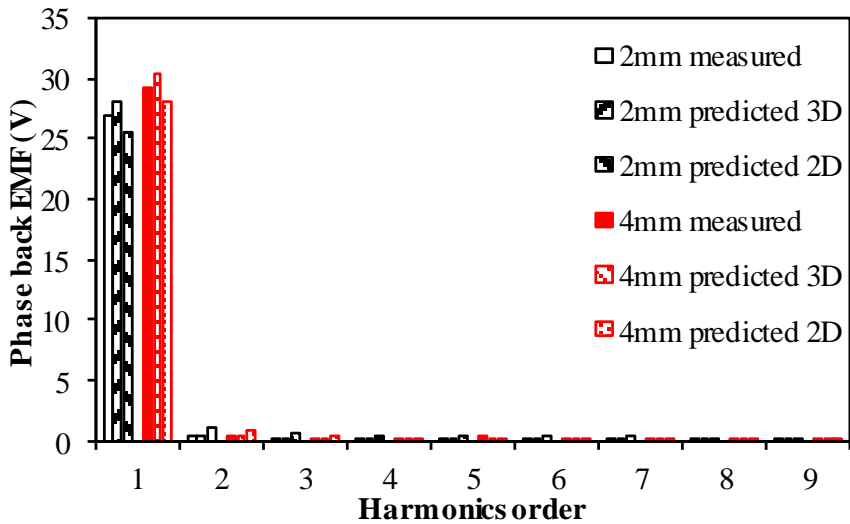
Fig. 4. 26. Photos of prototype machines with different magnet thickness.

The phase back EMF is tested at first. The waveforms and spectra of back EMF are shown in Fig. 4. 27. Moreover, the comparison of back EMF constant is shown in Table 4. 2. The motors are driven by using the same BLDC driver to the maximum speed at first, then the current supply is cut down so that the open-circuit back EMF under the high speed condition can be measured. It should be noticed that the maximum speed is different for machines having different magnet thicknesses. Since the magnet thickness affects the back EMF constant significantly and the DC voltage limitation is the same for all prototype machines, which means the machine having thicker magnet should have higher back EMF constant, and hence, lower maximum rotating speed. The maximum rotating speeds for machines with 2mm and 4mm magnets are 42.6 krpm and 37.8 krpm, respectively.

As shown, good agreement can be achieved between the measured and 3-D FE predicted results. However, the 2-D predicted values are lower than the measured results, since the magnet axial length is chosen as 14mm to utilize the end part in practice, while the length of stator laminations is 12mm. The differences of machines having 2mm and 4mm magnets are 5.9% and 3.9% between the measured and 3-D FE predicted results, respectively. The slight error is mainly due to the manufacture tolerance. In addition, it can be seen that the machine with 4mm magnet has higher back EMF constant, which is consistent with the FE predicted result.



(a) Waveforms



(b) Spectra

Fig. 4. 27. Variation of FE-predicted and measured phase back EMF waveforms and spectra.

Table 4. 2

Back EMF Constant Comparison			
Magnet thickness	Measured	2D FEA	3D FEA
2mm	$6.42 \times 10^{-4}$	$5.98 \times 10^{-4}$	$6.80 \times 10^{-4}$
4mm	$7.75 \times 10^{-4}$	$7.42 \times 10^{-4}$	$8.05 \times 10^{-4}$

\* The unit is V/rpm for back EMF constant.



The variation of static torque with different  $I_q$  is also tested which is shown in Fig. 4. 28. During the test, the rotor position is chosen as the situation where the North Pole is aligned with Phase A. As can be seen, the error between the 3-D FE predicted results and measured values is very small.

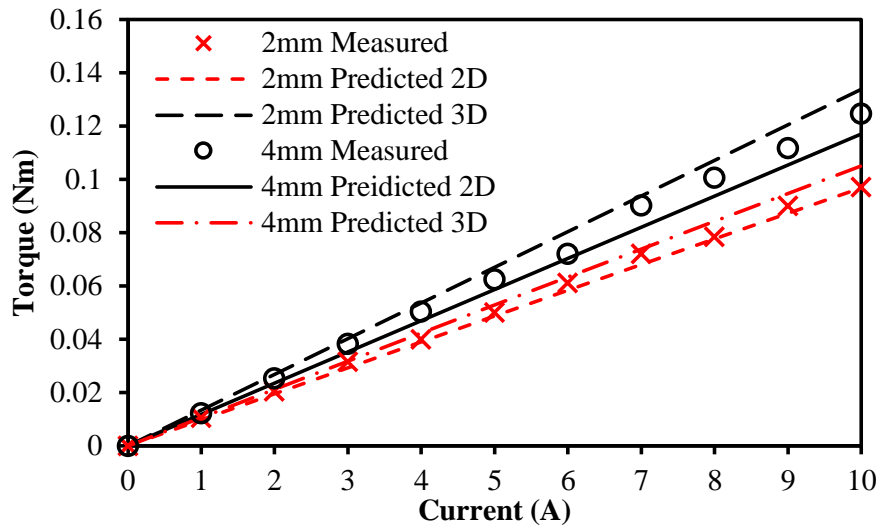


Fig. 4. 28 Comparison of FE-predicted and measured static torques with different q-axis currents.

Moreover, the on-load current waveforms are also tested. The photo of test rig is shown in Fig. 4. 29 and the measured current waveforms are shown in Fig. 4. 30.

As for the current waveforms, it can be seen that the machine with 2mm magnet has higher current amplitude, which is due to the higher rotating speed, and hence, the higher output power. The speed is 42.6 krpm for the machine with 2mm magnet while 37.8 krpm for the machine 4mm magnet. In addition, the current waveform is different from an ideal rectangular one, which is mainly caused by the commutation and the inductance.

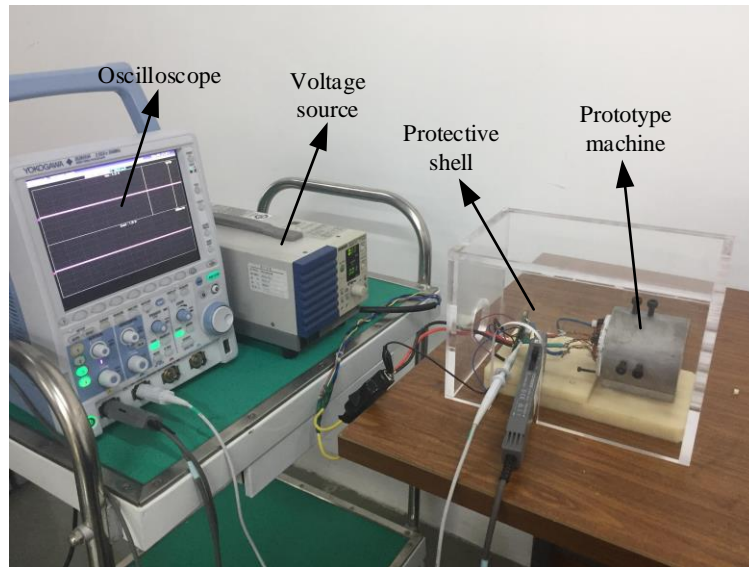


Fig. 4. 29. Current waveform test rig.

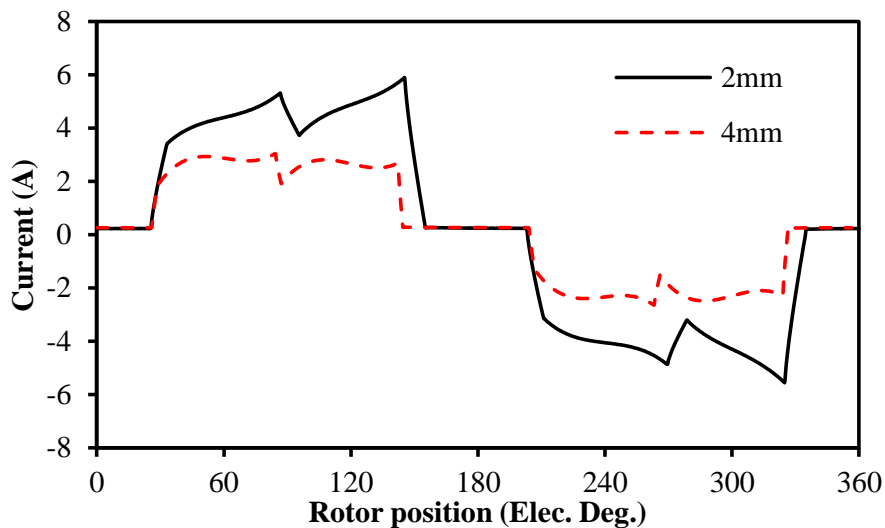


Fig. 4. 30. Measured phase current waveforms of the prototype machines with different magnet thicknesses.

#### 4.6 Summary

In this chapter, the influence of magnet thickness on the performance of high speed machines is investigated comprehensively. It is found that the increasing magnet thickness enhances the phase flux linkage, phase back EMF, demagnetization performance and over load capability. Moreover, the relative thick magnet can effectively reduce the maximum rated on-load UMF, which is investigated in depth by FE and an analytical model based on the Maxwell stress tensor. In addition, the variation of magnet thickness also affects the magnet eddy current significantly. It

shows the relative thick magnet can also result in lower magnet eddy current loss, which is caused by decreased armature fields and increased equivalent airgap length.

# **CHAPTER 5**

## **OPTIMIZATION OF SPLIT RATIO IN SMALL HIGH SPEED PM MACHINES CONSIDERING DIFFERENT LOSS LIMITATIONS**

As one of the key design parameters, the split ratio is very critical for all machines. In this chapter, the optimal split ratio in small high speed PM machines will be investigated comprehensively. Different loss limitations based on the thermal consideration are taken into account. In addition, the influence of several key design parameters are investigated as well.

### **5.1 Introduction**

As one of the most important design parameters, the split ratio, which is defined as the ratio between the outer rotor and stator diameters, has significant influence on the machine performance [CUI15].

There are many discussions about the optimal split ratio of PM machines. [HEM87] shows there is an optimal split ratio for the minimum copper loss, and it affects the magnetic circuit significantly. [PAN06] investigates the optimal split ratio for both brushless AC and DC motors having either overlapping or non-overlapping windings. The influence of detailed design parameters, e.g. tooth tip height, end winding, etc., are also taken into account. The analytical models for the optimal split ratio of machines having inner and outer rotors are derived in [SHE11] [CHU12], and [WUL09] investigates the optimal split ratio in fractional slot interior permanent magnet machines. In [REI13], the split ratio is optimized by considering both global and local thermal limitations, which constrains the total copper loss and the maximum allowed current density simultaneously. In [JAN11] and [PRI16], the thermal limitation is considered more accurately by using a lumped-parameter thermal network (LPTN) model, which considers both copper and iron losses.

Previous literatures mainly focus on low speed machines. In contrast, [EDE01] [ZHU97] investigates the optimal split ratio in high speed permanent magnet brushless DC motors. The influences of iron loss, copper loss and airgap length are also studied in detail. It shows that the optimal split ratio decreases measurably when the iron loss is considered. In addition, the increased airgap length increases its value in high speed

machines due to the decreased iron loss. The split ratio of high speed PM machines is optimized based on thermal resistance network in [FAN16]. The winding temperature rise is considered as the limitation, and both effects of iron loss and windage loss are taken into account. The optimal split ratio is also analytically determined in [LIQ14] and [WAN18], which accounts for the iron loss in the split ratio optimization directly. In addition, the influence of key design parameters are also investigated in these two papers, e.g. airgap length and rotor pole pairs, etc.

However, the effects of several key design parameters on the optimal split ratio have not been studied comprehensively, e.g. the slot/pole number combination, especially the comparison between 6-slot and 3-slot machines, the maximum stator flux density, the maximum stator allowed loss and the magnet remanence.

Moreover, the rotor loss, especially the rotor eddy current loss is almost neglected in the previous literatures. Since these papers mainly focus on relative large machines, and they assume the rotor eddy current loss can be effectively reduced by using manufacture techniques, e.g. PM segmentation. Nevertheless, the rotor employing magnet ring is usually adopted in small high speed PM machines due to its easy manufacture process, as stated in many literatures and applied widely in industry applications [WAN07] [BIA05] [XUS17] [BIN06] [BOR08] [BOR10] [ION14]. As a result, the segmentation can be hardly used in high speed PM machine with small size, which means the influence of rotor eddy loss is consequently much more significant and should be considered. In addition, the metallic sleeve is also usually used due to its high rigidity which is desirable for high speed machines. Nevertheless, it can have measureable eddy current loss which cannot be neglected when the machine volume is small.

In this chapter, the split ratio in high speed machines is optimized by taking both stator copper loss and iron loss into account at first. The influence of several key design parameters are investigated comprehensively as well. Then, the optimal split ratio in machines considering the rotor loss limitation only is investigated. In addition, a new analytical method is proposed for split ratio optimization in small high speed PM machines. Both stator and rotor loss limitations are taken into account. Moreover, the influence of several key design parameters, e.g. the slot/pole number combination, the magnet material and the magnet segmentation, are also investigated in details.

## 5.2 Split Ratio Optimization in Small High Speed Machine Considering Stator Loss Limitation Only

In this part, the split ratio will be optimized by considering stator loss limitation only. The loss calculation will be presented at first. Then, the output torque will be determined analytically. After that, the influence of key design parameters will be studied.

### 5.2.1 Loss Calculation

Comparing with the low speed machine, the stator iron loss cannot be neglected in high speed machines due to the high frequency, which can significantly worsen the thermal condition and decrease the total efficiency.

The iron loss density can be estimated by [BOG03] [LIN04] [ION07]:

$$W_{fe} = k_h f B_{\max}^{\chi} + k_c f^2 B_{\max}^2 + k_e f^{1.5} B_{\max}^{1.5} \quad (5.1)$$

Where  $W_{fe}$  is the iron loss density,  $k_h$ ,  $k_c$  and  $k_e$  are the hysteresis loss, classic eddy current loss and excess loss coefficients, respectively,  $f$  is the electrical frequency and  $B_{\max}$  is the maximum stator flux density. In order to ease the investigation, the value of  $\chi$  is chosen as a typical value, i.e. 2 [ZHO04] [ION07].

As a result, the stator iron loss can be calculated as:

$$P_{fe} = W_{Fe} m_{Fe} \quad (5.2)$$

where  $P_{fe}$  is the stator iron loss and  $m_{fe}$  is the mass of stator iron which can be calculated as:

$$m_{Fe} = A_{Fe} l_a \rho_{Fe} = \left[ (D_{so}^2 - D_{si}^2) \pi / 4 - A_s N_s \right] l_a \rho_{Fe} \quad (5.3)$$

where  $A_{fe}$  is the area of stator iron,  $l_a$  is the active length of machines,  $\rho_{fe}$  is the iron mass density,  $D_{so}$  and  $D_{si}$  are the outer and inner diameters of stator bore,  $A_s$  is the slot area and  $N_s$  denotes the number of slots.

The value of  $D_{si}$  can be calculated as

$$D_{si} = D_{so} \lambda + 2 \cdot (l_g + l_{sleeve}) \quad (5.4)$$

where  $l_g$  is the length of actual airgap,  $l_{sleeve}$  is the sleeve thickness and  $\lambda$  indicates the split ratio which is defined as

$$\lambda = D_{mo} / D_{so} \quad (5.5)$$

In (5.5),  $D_{mo}$  denotes the outer diameter of magnet. It should be noticed that  $D_{mo}$  is adopted in the definition of split ratio instead of the actual rotor outer diameter. Since the sleeve thickness should be also considered as a part of the rotor outer diameter. Nevertheless, non-magnetic materials are usually adopted for the sleeve, which indicates that the sleeve can be treated as equivalent airgap in magnetic circuit. Consequently,  $D_{mo}$  is employed here to ease the investigation.

As for the available slot area, it can be calculated as

$$A_s = \frac{\overbrace{\pi \cdot (D_{so}^2 - (D_{si} + 2h_t)^2)}^{\text{stator area/slot}}}{4N_s} - \frac{\overbrace{\pi \cdot D_{so}^2 - \pi \cdot (D_{so} - 2h_c)^2}^{\text{Back iron area/slot}}}{4N_s} - \underbrace{b_t \cdot (D_{so} / 2 - h_c - D_{si} / 2 - h_t)}_{\text{Stator tooth area}} \quad (5.6)$$

where  $h_c$ ,  $b_t$ , and  $h_t$  indicate the stator back-iron thickness, the tooth width and the tooth tip height, respectively.

For small high speed PM machines, 2-pole rotor with diametric magnetization is usually used for the lowest electrical frequency. As a result, the airgap flux density can be treated as sinusoidal ideally. Consequently, the values of  $h_c$  and  $b_t$  can be determined as

$$b_t = k_a \cdot h_c = \frac{D_{ag}}{2} \cdot \frac{B_{g\max}}{B_{\max}} \cdot \int_{-\pi/N_s}^{\pi/N_s} \cos \theta d\theta \quad (5.7)$$

where  $k_a$  is the coefficient depending on the slot/pole combinations. It is 1 for 6-slot/2-pole machine but 2 for 3-slot/2-pole machine,  $D_{ag}$  is the diameter of middle of equivalent airgap and  $B_{g\max}$  is peak value of the airgap flux density.

In terms of the relationship between  $D_{ag}$  and  $D_{mo}$ , according to (5.4), it can be expressed as

$$D_{ag} = D_{mo} + l_g + l_{sleeve} \quad (5.8)$$

As for the peak value of airgap flux density, i.e.  $B_{g\max}$ , it can be determined analytically by (5.9).

$$B_{g\max} = \frac{B_r}{2} \frac{1 - (D_{sh} / D_{mo})^2}{1 - (D_1 / D_{si})^2} \cdot \left[ (D_{mo} / D_{si})^2 + (D_{mo} / D_{ag})^2 \right] \quad (5.9)$$

where  $D_{sh}$  is the outer diameters of shaft.  $B_r$  is the remanence of magnet,  $D_1$  equals to  $D_{sh}$  when the shaft is magnetic and zero when the shaft is nonmagnetic.

It should be noticed that the motor is simplified as shown in Fig. 5. 1, which indicates that the permeability of the soft magnetic material is assumed to be infinite and the influence of slot opening is neglected.

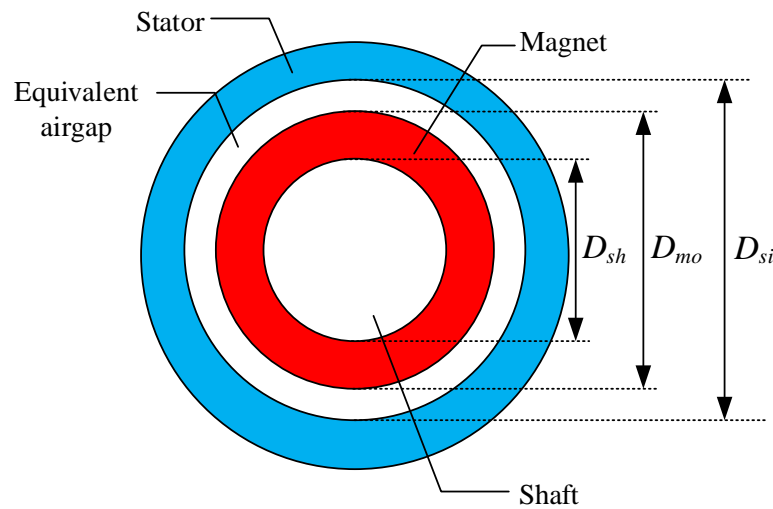


Fig. 5. 1 Simplified motor model.

In addition to the stator iron loss, the copper loss should be calculated as well. It should be noticed that only DC copper loss is considered here, which means the proximity effect and the eddy current in windings are neglected.

As for the DC copper loss, its value can be expressed as

$$P_{cu} = 2I^2 \rho_{r,c} \frac{2N_w (l_a + l_e)}{A_{coil}} \quad (5.10)$$

where  $N_w$  is the number of turns per phase,  $I$  is the amplitude of phase current,  $\rho_{r,c}$  is the resistivity of conductor,  $A_{coil}$  indicates the conductor area and  $l_e$  denotes the length of end winding .



The value of  $A_{coil}$  can be calculated as

$$A_{coil} = \frac{N_s \cdot K_s \cdot A_s / 2}{3N_w} \quad (5.11)$$

where  $K_s$  is the filling factor. Consequently, the total copper loss can be calculated as

$$P_{cu} = 24N_w^2 I^2 \rho_{r,c} \frac{(l_a + l_e)}{A_s K_s N_s} \quad (5.12)$$

In terms of the end winding length, it can be estimated by assuming the shape of end winding as the semicircle regardless the slot/pole combinations and winding configurations which is shown in Fig. 5. 2 [SHE08] [PAN06].

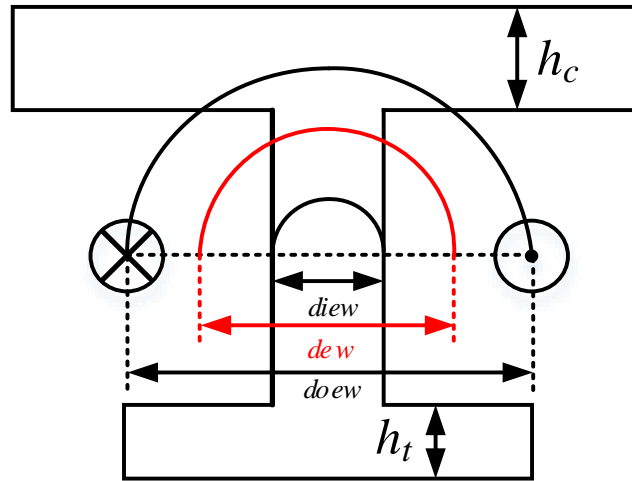


Fig. 5. 2 Illustration of end winding.

As a result, the diameter of end windings can be calculated by

$$\begin{aligned} d_{iew} &= b_t \\ d_{ow} &= \frac{(D_{so} - 2h_c + D_{si} + 2h_t) \pi}{2N_s} \\ d_{ew} &= \frac{d_{iew} + d_{ow}}{2} \end{aligned} \quad (5.13)$$

Therefore, the length of end winding can be calculated as

$$l_e = \frac{\pi}{4} \left\{ \left( \frac{D_{so} + D_{si}}{2} - h_c + h_t \right) \frac{\pi}{N_s} + b_t \right\} \quad (5.14)$$

As for the relationship between the copper loss and the stator iron loss, their sum should meet the stator thermal limitation.

In [BIA04], [WAN18], it is assumed that the temperature is evenly distributed in stator, and all stator losses are transferred by convection. As a result, the maximum allowed stator loss  $P_{stator,lim}$  can be roughly determined by the cooling capability of machines and calculated by

$$P_{stator,lim} = h_{stator} \Delta\tau_{stator,max} \pi D_{so} l_a \quad (5.15)$$

where  $\Delta\tau_{stator,max}$  is the maximum allowed stator temperature rise which mainly depends on the winding insulation class,  $h_{stator}$  indicates the stator overall heat transfer coefficient, its value usually ranges from  $25\text{W}/(\text{K}\cdot\text{m}^2)$  to  $100\text{W}/(\text{K}\cdot\text{m}^2)$  which depends on the cooling system [BIA04].

Consequently, the relationship between the copper loss and the stator iron loss can be expressed as

$$P_{stator,lim} = P_{cu} + P_{fe} \quad (5.16)$$

### 5.2.2 Torque Calculation

The output torque of a 3-phase BLDC machine can be expressed as [EDE01] [ZHU97]:

$$T = 2N_w D_{ag} l_a B_g K_{dp} I \quad (5.17)$$

where  $N_w$  is the number of turns per phase,  $D_{ag}$  is the diameter of middle of equivalent airgap,  $B_g$  is the airgap flux density and  $K_{dp}$  is the winding factor.

It should be noticed that the outer diameter of magnet is usually used for output torque calculation in large surface mounted permanent magnet machine, since the airgap length is usually much smaller than the rotor outer diameter. However, in high speed machine, especially for small high speed machine, due to the relative large airgap length and existence of retaining sleeve, the diameter of middle of equivalent airgap should be used for more accurate calculation.

Since the airgap flux density distribution is sinusoidal, while the machine works with BLDC drive mode, the torque calculation needs to be modified as

$$T = \frac{2 \int_{\theta_c}^{\pi-\theta_c} \overbrace{K_{dp} N_w D_{ag} l_g B_{g \max}}^{\text{phase back EMF}} \frac{\omega}{p} I \sin \theta d\theta}{2\pi/3} \quad (5.18)$$

$$= \frac{3\sqrt{3}}{\pi} D_{ag} l_a K_{dp} N_w I B_{g \max}$$

where  $\theta_c$  depends on the conduction angle, which is 60 degree here.

In addition, phase current  $I$  can be calculated as

$$I = \frac{1}{N_w} \sqrt{\frac{P_{cu} A_s K_s N_s}{24 \rho_{r,c} (l_a + l_e)}} \quad (5.19)$$

Consequently, the torque can be calculated as

$$T = \frac{3\sqrt{3}}{\pi} D_{ag} l_a B_{g \max} K_{dp} \sqrt{\frac{P_{cu} A_s K_s N_s}{24 \rho_{r,c} (l_a + l_e)}} \quad (5.20)$$

$$= \frac{3\sqrt{3}}{\pi} D_{ag} l_a B_{g \max} K_{dp} \sqrt{\frac{(P_{stator, \lim} - P_{fe}) A_s K_s N_s}{24 \rho_{r,c} (l_a + l_e)}}$$

The volume of the motor can be calculated as

$$V = \frac{D_{so}^2 \pi \cdot l_a}{4} \quad (5.21)$$

As a result, the torque density is

$$T/V = C \cdot \left( \lambda + \frac{l_g + l_{sleeve}}{D_{so}} \right) B_{g \max} \sqrt{\frac{A_s}{l_a + l_e}} \cdot \sqrt{P_{stator, \lim} - P_{Fe}} \quad (5.22)$$

$$C = \frac{3K_{dp}}{\pi^2 D_{so}} \sqrt{\frac{2K_s N_s}{\rho_{r,c}}} \quad (5.23)$$

Consequently, the optimal split ratio can be obtained by solving the differential equation as

$$\frac{\partial(T/V)}{\partial \lambda} = 0 \quad (5.24)$$

The cross section of the prototype machine is shown in Fig. 5. 3, and its detailed design parameters are listed in Table 5.1.

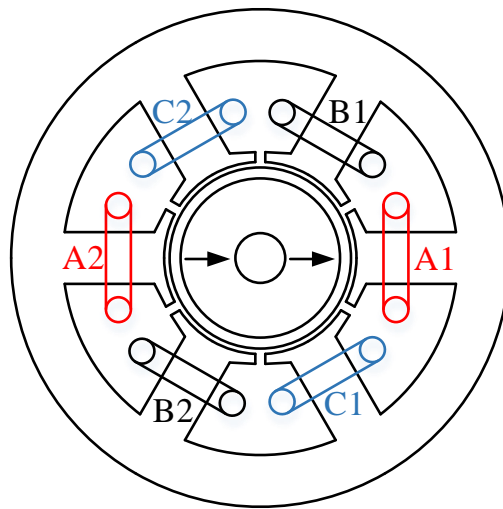


Fig. 5. 3 Cross section of 6-slot/2-pole high speed permanent magnet machine.

Table 5.1

Parameters of Prototype Machine

Stator outer diameter (mm)	50	Shaft diameter (mm)	5
Active length (mm)	12	Rotation speed (krpm)	110
Airgap length (mm)	1	Sleeve thickness (mm)	1
Tooth tip height (mm)	1	Slot opening width (mm)	2
Filling factor	0.4	Maximum stator allowed loss (W)	25
Remanence (T)	1.2		

The variation of output torque with split ratio in the prototype machine considering stator loss is shown in Fig. 5. 4.

As can be seen, the optimal split ratio exists when the stator loss is considered only. This is due to the fact that  $B_{gmax}$  increases with split ratio while the slot area represents an opposite trend as shown Fig. 5. 5.

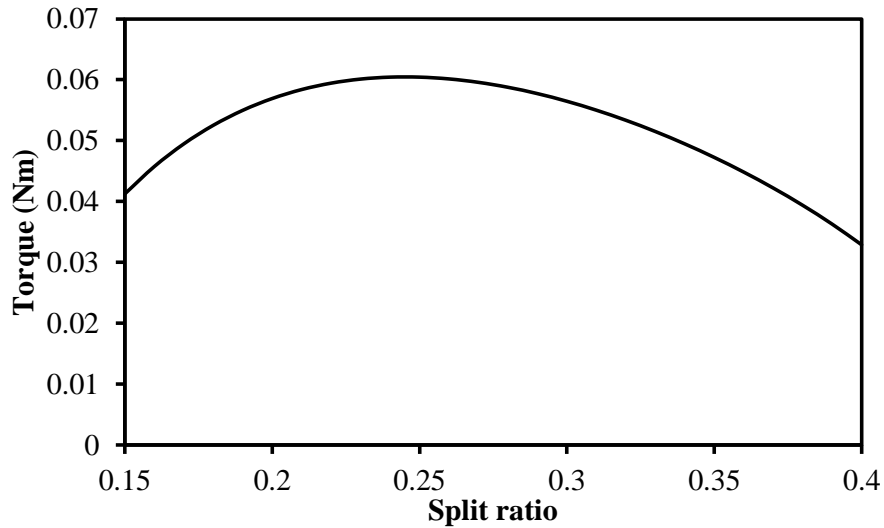


Fig. 5. 4 Variation of torque with split ratio in model considering stator loss only.

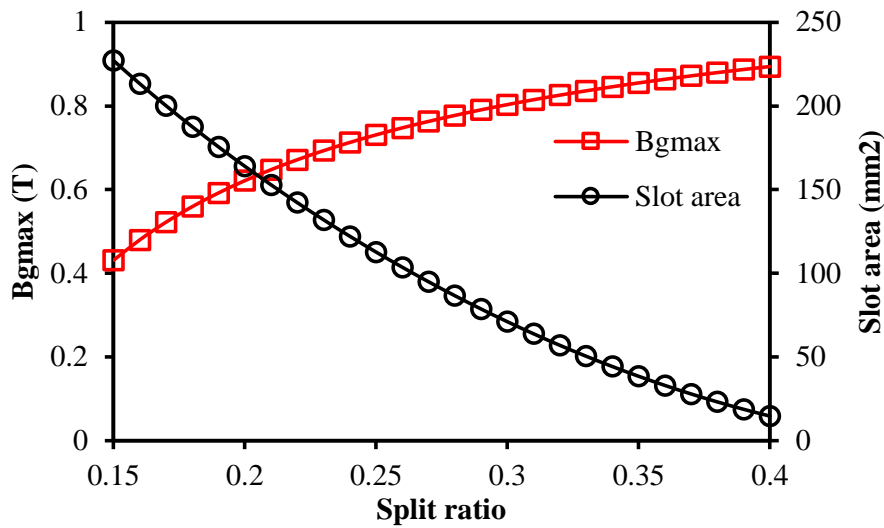


Fig. 5. 5 Variation of  $B_{gmax}$  and slot area with split ratio in model considering stator loss only.

As a result, the increased split ratio significantly increases the iron loss but decreases the copper loss as shown in Fig. 5. 6. Consequently, the phase ampere turns decrease with split ratio which is shown in Fig. 5. 7, and hence, the armature field.

Accordingly, there should be an optimal split ratio which can balance the PM field and the armature field so that the maximum output torque can be obtained.

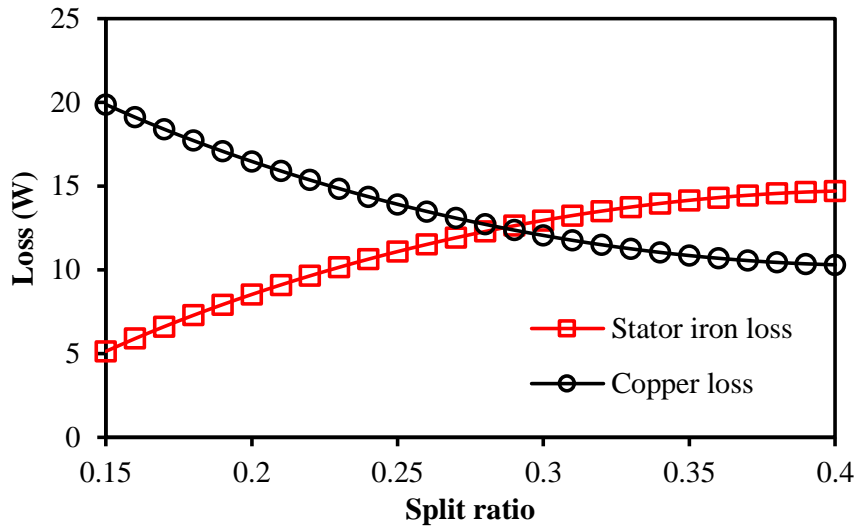


Fig. 5. 6 Variation of stator loss components with split ratio in model considering stator loss only.

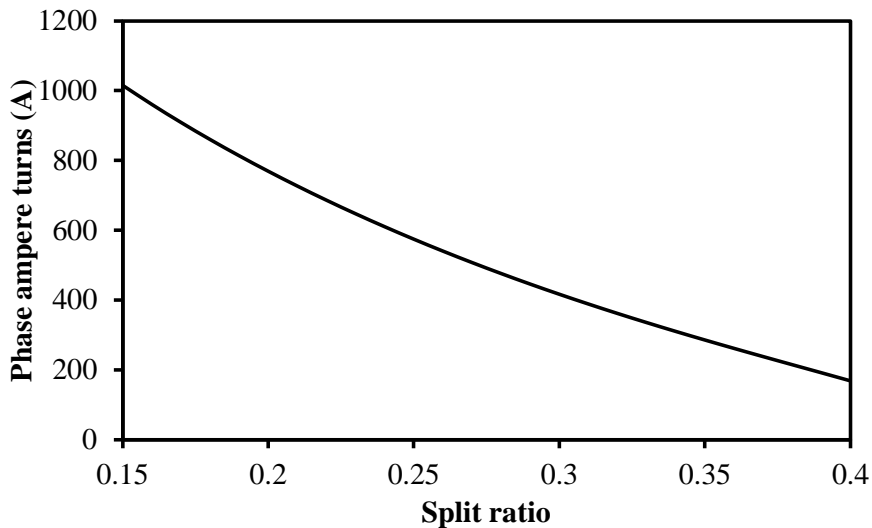


Fig. 5. 7 Variation of phase ampere turns with split ratio in model considering stator loss only.

It should be noticed that the phase ampere turns are used here instead of phase current. As the number of turns per phase related to many factors, i.e. slot area, diameter of wire, voltage limitation as well as parallel path, etc., which indicates that its value is hard to be determined at this design stage.

### 5.2.3 Influence of Key Design Parameters

In this part, the influence of several key design parameters will be investigated in detail. The 6-slot/2-pole machine is selected as the prototype machine while the influence of slot/pole number combinations will be investigate later.

### 5.2.3.1 Influence of $B_{\max}$

The influence of  $B_{\max}$  has been studied in [PAN04], in which it has been investigated by the flux density ratio defined as:

$$\gamma = \frac{B_g}{B_{\max}} \quad (5.25)$$

where  $B_g$  is the amplitude of the uniform airgap flux density. It states that the optimal split ratio decreases when  $\gamma$  ascends, since the increased  $\gamma$  can widen the stator tooth and increase the thickness of stator back-iron, which results in smaller slot area.

However, there is a specific assumption which assumes  $B_g$  can be kept as the same when the split ratio varies. However, this assumption can be hardly achieved in small high speed permanent magnet machines. Since the magnet thickness can vary significantly with split ratio in small high speed permanent magnet machines, and hence, the value of  $B_g$ .

In addition, since the airgap flux density is ideally sinusoidal in 2-pole high speed machines with diametric magnetization,  $B_{g\max}$  is used in later investigations instead of  $B_g$ . The variation of magnet thickness and  $B_{g\max}$  with split ratio is shown in Fig. 5. 8. As can be seen, the value of  $B_{g\max}$  increases with the split ratio due to significantly increased magnet thickness.

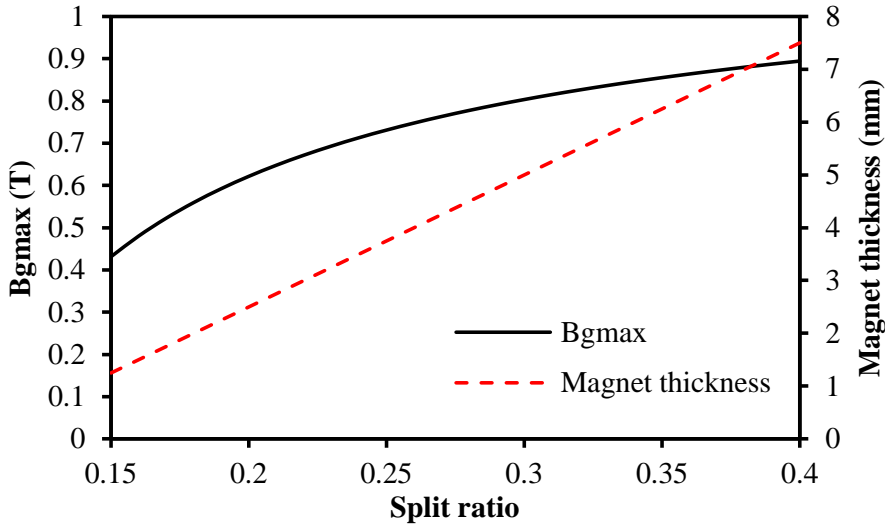


Fig. 5. 8 Variation of  $B_g$  and magnet thickness with different split ratio.

Consequently, the flux density ratio is not proper for optimization in small high speed machine, since  $\gamma$  becomes a function of split ratio. As a result, the influence of  $B_{\max}$  should be investigated directly.

As shown in (5.22), three variables having great influence on the optimal split ratio, i.e.  $A_s$ ,  $P_{cu}$  and  $l_a+l_e$ , are affected by  $B_{\max}$  significantly. Consequently, the influence of  $B_{\max}$  on these three variables should be studied in detail. The variations of  $A_s$ ,  $P_{cu}$  and  $l_a+l_e$  with different split ratio and  $B_{\max}$  are shown in Fig. 5. 9, Fig. 5. 10 and Fig. 5. 11, respectively.

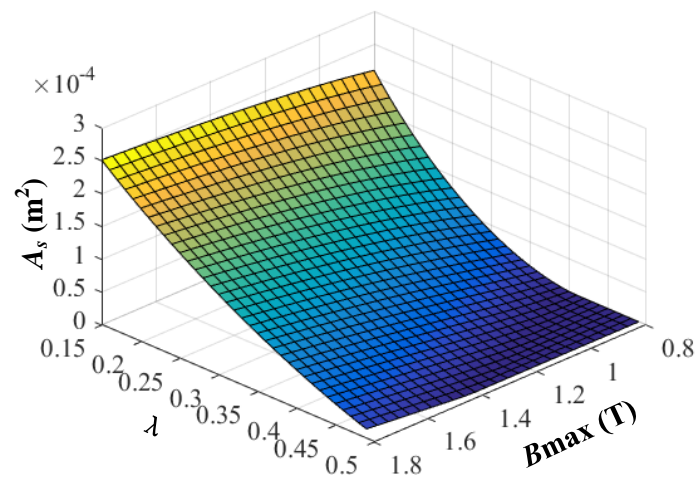


Fig. 5. 9 Variation of  $A_s$  with different  $\lambda$  and  $B_{\max}$ .

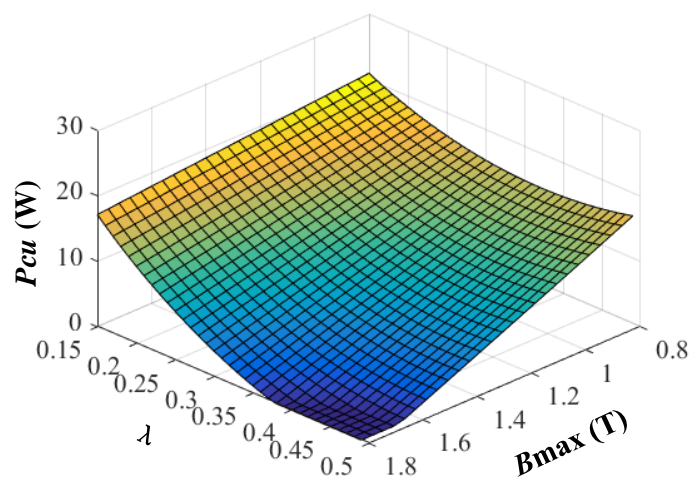


Fig. 5. 10. Variation of  $P_{cu}$  with different  $\lambda$  and  $B_{\max}$ .



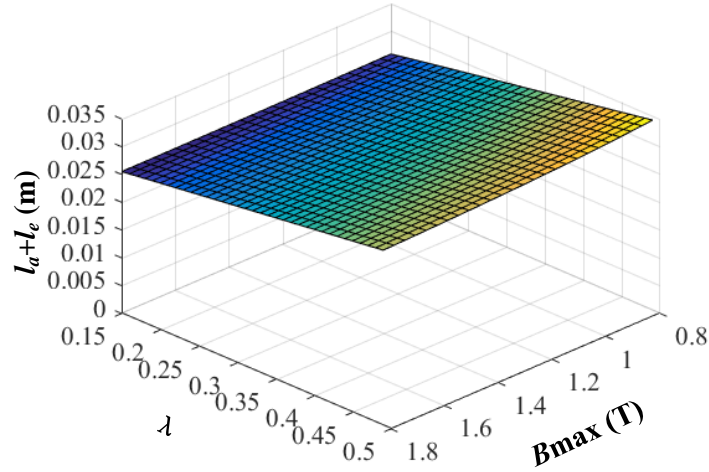


Fig. 5. 11 Variation of  $l_a+l_e$  with  $\lambda$  and  $B_{max}$ .

It should be noticed that there are certain regions where  $A_s$  and  $P_{cu}$  are zero, since at specific combinations of  $\lambda$  and  $B_{max}$ , the values of  $A_{iron}$  and  $P_{fe}$  could exceed the total stator area as well as  $P_{stator,lim}$ , which makes  $A_s$  and  $P_{cu}$  be zero.

As can be seen, both  $A_s$  and  $P_{cu}$  decrease with split ratio which is essentially due to the increased  $B_{gmax}$  and decreased stator area. However,  $B_{max}$  has opposite effect on  $A_s$  and  $P_{cu}$ . Since the increased  $B_{max}$  can decrease the width of stator tooth as well as the stator back-iron thickness,  $A_s$  will be increased significantly. Nevertheless, according to (5.1)-(5.3),  $P_{fe}$  is more sensitive to  $B_{max}$  instead of iron area. Consequently, the copper loss decreases significantly with the increase of  $B_{max}$ .

In contrast, the value of  $l_a+l_e$  increases with split ratio but decreases  $B_{max}$ . Since both  $d_{oew}$  and  $d_{iew}$  shown in (5.13) ascend with split ratio due to increased  $D_{si}$  and  $B_{gmax}$ , and hence,  $b_t$ . In contrast, with specific split ratio, the value of  $l_e$  decreases with  $B_{max}$ , since the increased  $B_{max}$  will shorten the stator tooth width, and hence,  $d_{iew}$ . Moreover,  $l_a+l_e$  is less sensitive to the variation of split ratio and  $B_{max}$ , which is due to the fact that the  $l_a$  is a constant.

It can be seen that  $B_{max}$  has different influence on these three variables. Therefore, there will be a tread-off among  $A_{slot}$ ,  $P_{cu}$  and  $l_a+l_e$  during the selection of  $B_{max}$ . As a result, there will be an optimal combination of  $B_{max}$  and split ratio for high speed machines.

The variation of torque with different  $B_{max}$  and  $\lambda$  is shown in Fig. 5. 12.

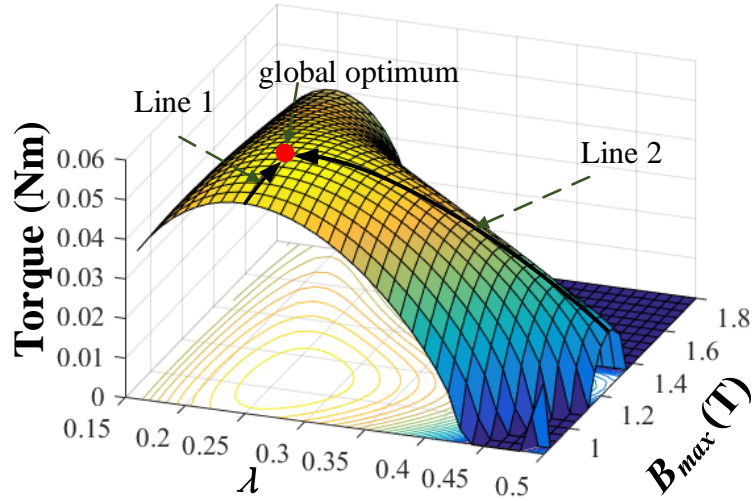


Fig. 5. 12 Variation of torque with  $\lambda$  and  $B_{max}$ .

As can be seen that the global optimum exists which can be reached by solving the differential equations set as

$$\begin{cases} \frac{\partial(T/V)}{\partial\lambda} = 0 \\ \frac{\partial(T/V)}{\partial B_{max}} = 0 \end{cases} \quad (5.26)$$

The line 1 and line 2 indicate the tracks of the optimal split ratio and the optimal maximum stator flux density, respectively.

### 5.2.3.2 Influence of $P_{stator,lim}$

In the previous sections,  $P_{stator,lim}$  is fixed as 25W. However, the value of  $P_{stator,lim}$  highly depends on the cooling system, which indicates that its value can be increased when more effective cooling method, e.g. water jacket, is used. Therefore, three different values of  $P_{stator,lim}$ , i.e. 25W, 35W and 45 W, are selected in this part of investigations.

The variation of torque with different  $\lambda$ ,  $B_{max}$  and  $P_{stator,lim}$  is shown in Fig. 5. 13. As can be seen, when  $P_{stator,lim}$  increases, not only the maximum output torque changes, but also the optimal combination of  $\lambda$  and  $B_{max}$ .

The variation of the optimal split ratio and  $B_{max}$  with different  $P_{stator,lim}$  is shown in Fig. 5. 14.

As shown, both these two parameters increase with  $P_{stator,lim}$ . Since  $P_{fe}$  is independent of  $P_{stator,lim}$ , which means its importance decreases with  $P_{stator,lim}$ . As a result, the influence of  $P_{fe}$  on the selection of  $B_{max}$  will descend with  $P_{stator,lim}$ . Ideally,  $P_{fe}$  will have negligible effect on the optimization when  $P_{stator,lim}$  is large enough. In this case,  $B_{max}$  will reach its maximum value which is only limited by the saturation condition. Consequently, the optimal split ratio will also achieve the maximum value due to the increased slot area which has been explained in [PAN04].

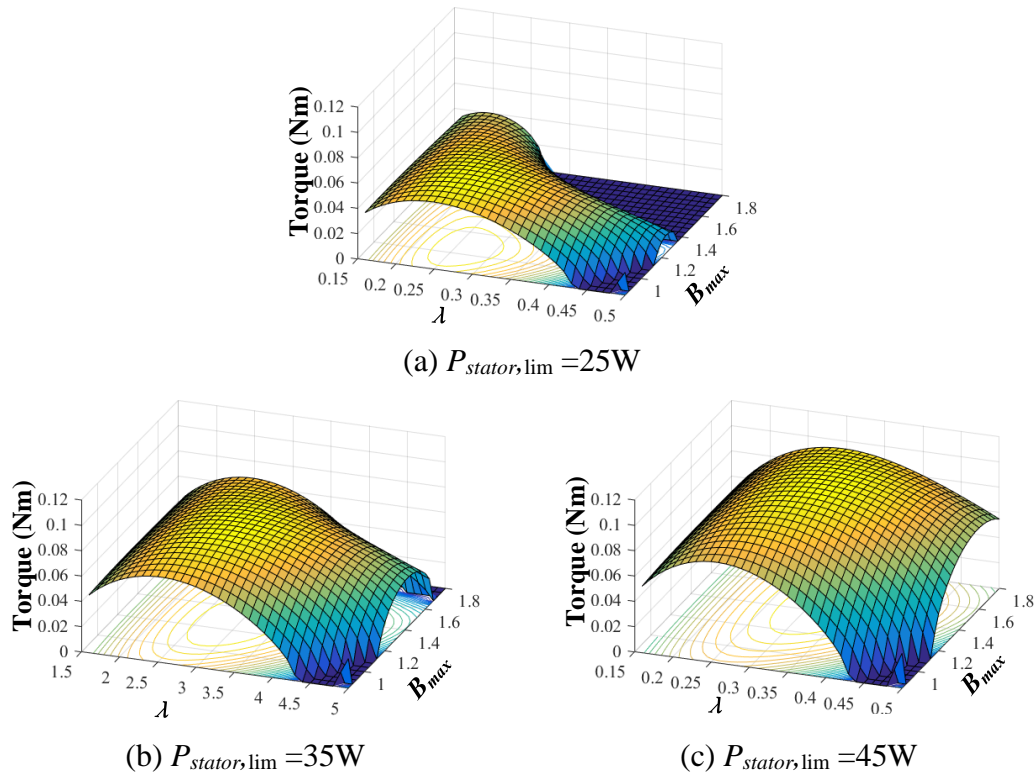


Fig. 5. 13 Variation of torque with  $\lambda$ ,  $B_{max}$ , and  $P_{stator,lim}$ .

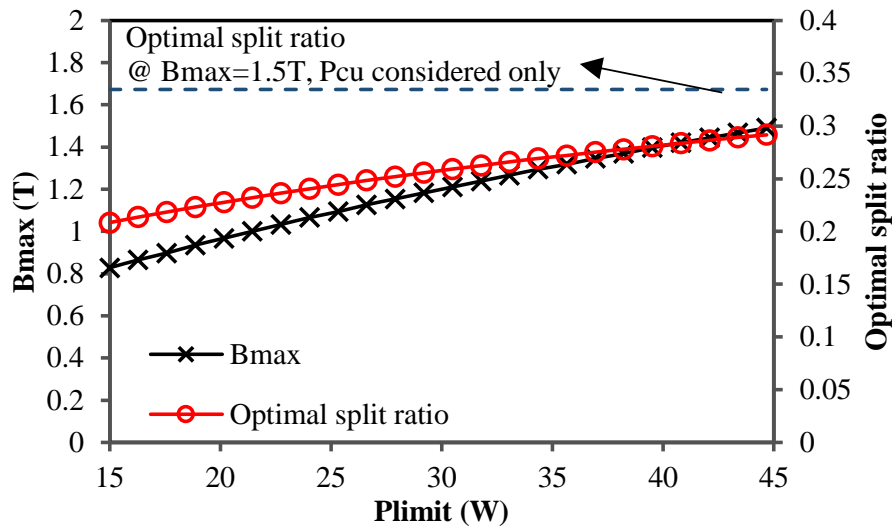


Fig. 5. 14 Variation of  $B_{max}$  and optimal split ratio with  $P_{stator,lim}$ .

### 5.2.3.3 Influence of Magnet Remanence

In the previous investigations, the remanence of the permanent magnet material is assumed to be a fixed value, i.e. 1.2T. However, in practice, the remanence varies with magnet material as well as temperature. As a result, the influence of remanence will be detailed in this part.

The variations of the optimal split ratio and the corresponding maximum output torque with different remanence are calculated and shown in Fig. 5. 15 and Fig. 5. 16, respectively. The value of  $P_{stator,lim}$  is assumed to be 25W. In terms of  $B_{max}$ , in order to ease the comparison, its value is fixed as the optimal value in machines having 1.2T remanence, i.e. 1.1T.

As can be seen, the optimal split ratio decreases with the remanence. This is mainly due to the fact that the PM field increases with remanence distinctly as shown in Fig. 5. 17. Consequently, with the same split ratio and  $B_{max}$ , the machine with the magnet having higher remanence will have relative thicker stator tooth and back iron, and hence, smaller  $A_s$  but larger  $P_{fe}$  and  $l_a+l_e$ . As a result, the armature field will be decreased. In this case, the optimal split ratio will decrease slightly, so that the increased PM field and the decreased armature field can be balanced.

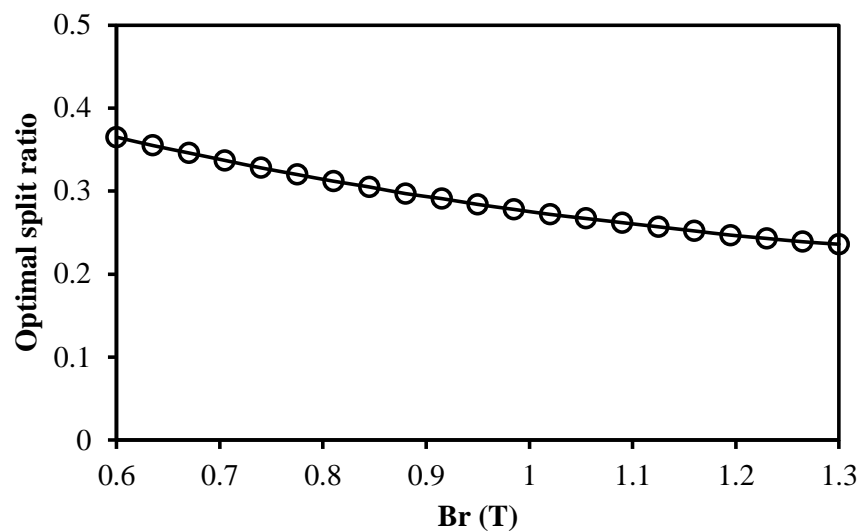


Fig. 5. 15 Variation of the optimal split ratio with remanence ( $P_{stator,lim}=25W$ ,  $B_{max}=1.1T$ ).

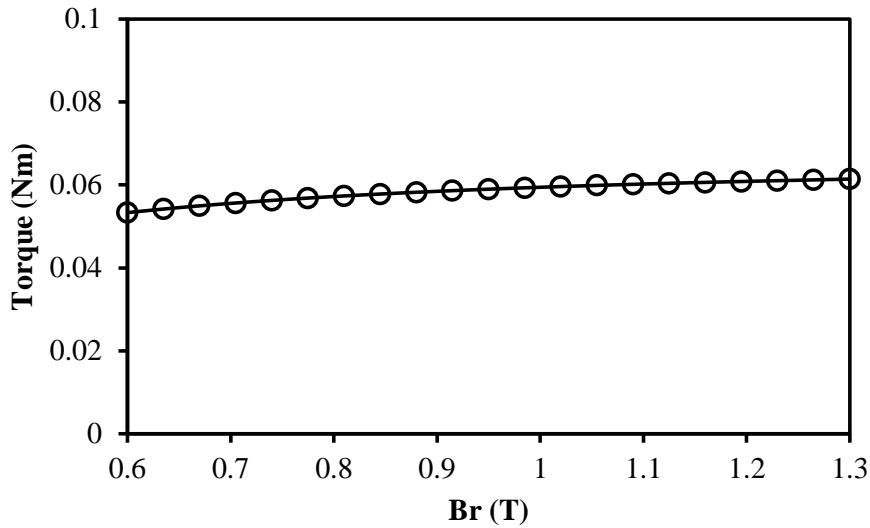


Fig. 5. 16. Variation of the maximum torque with remanence ( $P_{cu}=25W$ ,  $B_{max}=1.1T$ ).

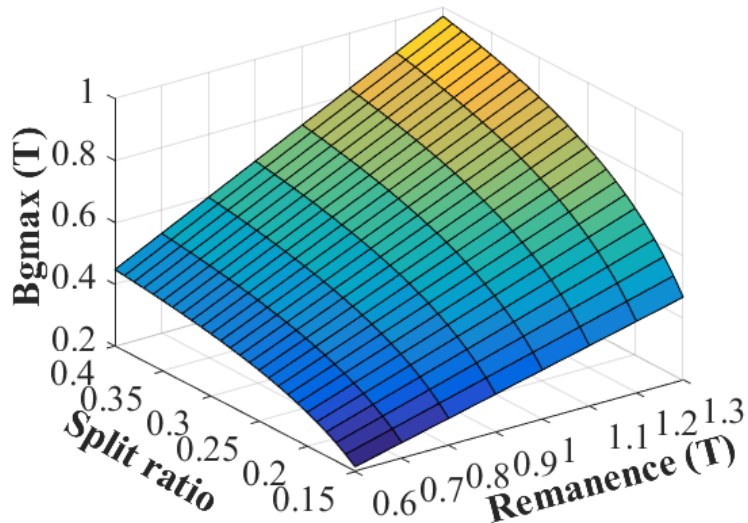


Fig. 5. 17 Variation of the loss components under optimal split ratio with remanence.

#### 5.2.3.4 Influence of Slot/Pole Combination

In the previous investigation, the 6-slot/2-pole machine is chosen as the prototype. In this part, the influence of slot/pole combinations on the optimal split ratio as well as the corresponding maximum output torque will be detailed. Both 6-slot/2-pole and 3-slot/2-pole machines are considered, of which the cross sections are shown in Fig. 5. 18.

The variations of output torque with split ratio in the machines having different slot/pole combinations are shown in Fig. 5. 19. In order to ease the investigation and comparison, the value of  $P_{stator,lim}$  is fixed as 25W in this part. In addition, the remanence and  $B_{max}$  are chosen as 1.2T and 1.1T, respectively.

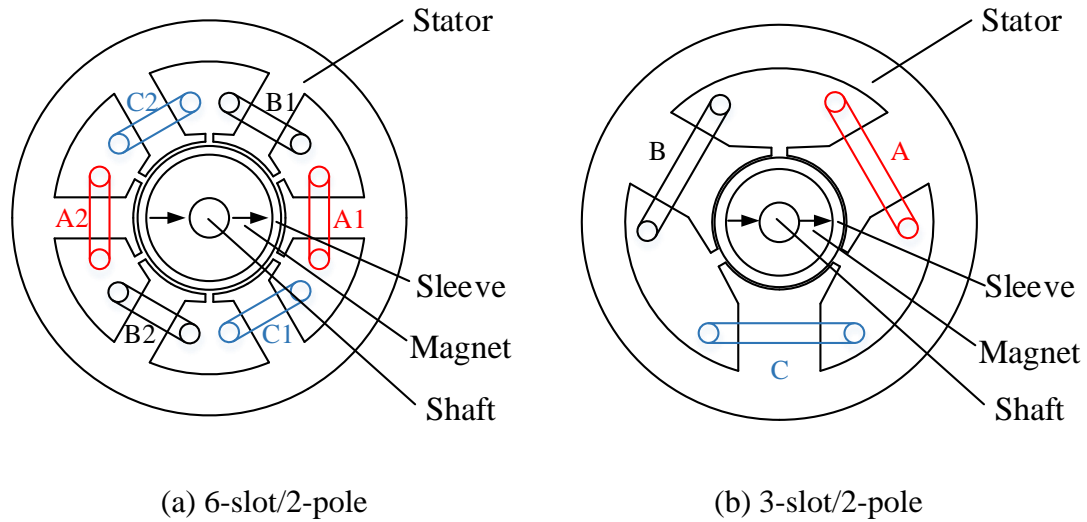


Fig. 5. 18 Cross sections of prototype machines.

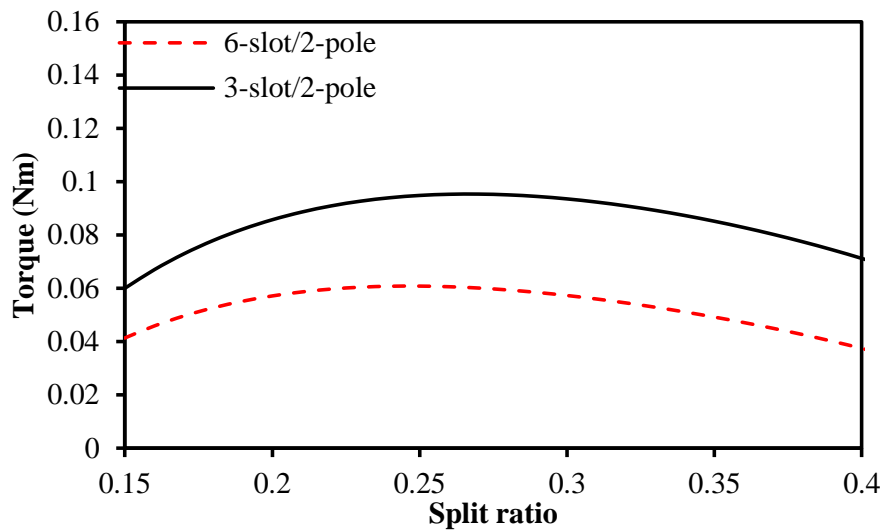


Fig. 5. 19. Variation of torque with split ratio ( $P_{stator,lim}=25W$ ,  $B_r=1.2T$ ,  $B_{max}=1.1T$ ). As can be seen, the 3-slot/2-pole machine has higher optimal split ratio. According to (5.6)-(5.7) and (5.13)-(5.14), the 3-slot/2-pole machine has relative larger slot area but shorter total end winding comparing with the 6-slot/2-pole machine when the split ratio and  $B_{max}$  are fixed, as shown in Fig. 5. 20 and Fig. 5. 21, respectively.

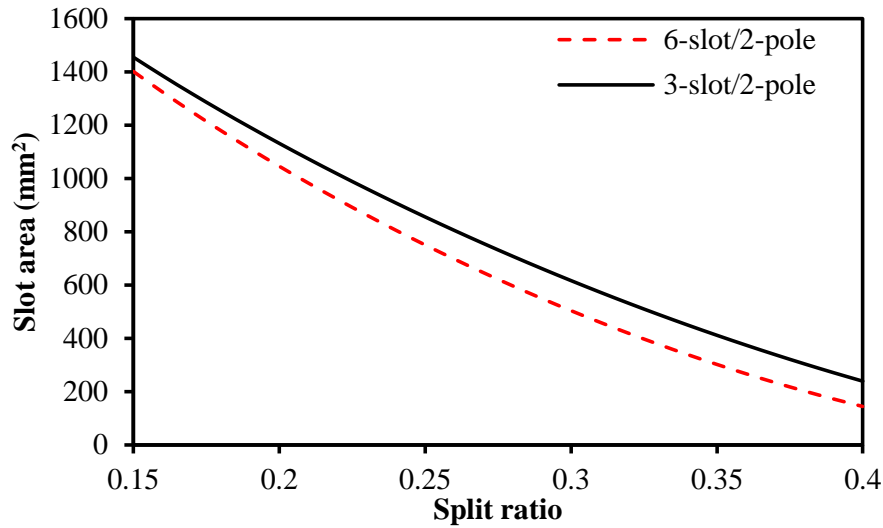


Fig. 5. 20. Variation of total slot area with split ratio ( $P_{stator,lim}=25W$ ,  $B_r=1.2T$ ,  $B_{max}=1.1T$ ).

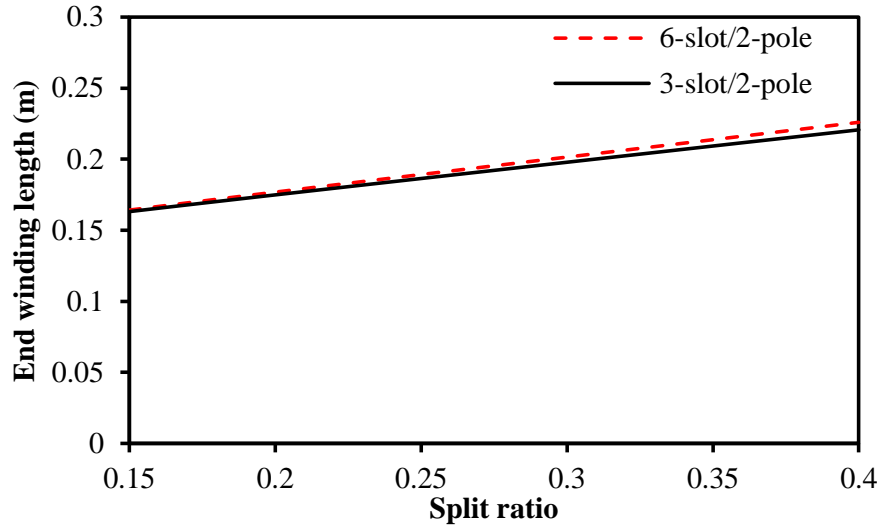


Fig. 5. 21 Variation of total end winding length with split ratio ( $P_{stator,lim}=25W$ ,  $B_r=1.2T$ ,  $B_{max}=1.1T$ ).

Consequently, with the specific split ratio and  $B_{max}$ , the 3-slot/2-pole machines should have higher  $P_{cu}$ . Although the phase ampere turns in the 3-slot/2-pole machine is still lower when the split ratio is small, which is due to relatively longer end winding per slot as shown in Fig. 5. 22, the high winding factor, i.e.  $\sqrt{3}/2$  for 3-slot/2-pole machines but 0.5 for 6-slot/2-pole machines, enhances the armature field significantly, and hence, output torque. As a result, the optimal split ratio in 3-slot/2-pole machines will be larger so that the PM field can be utilized further.

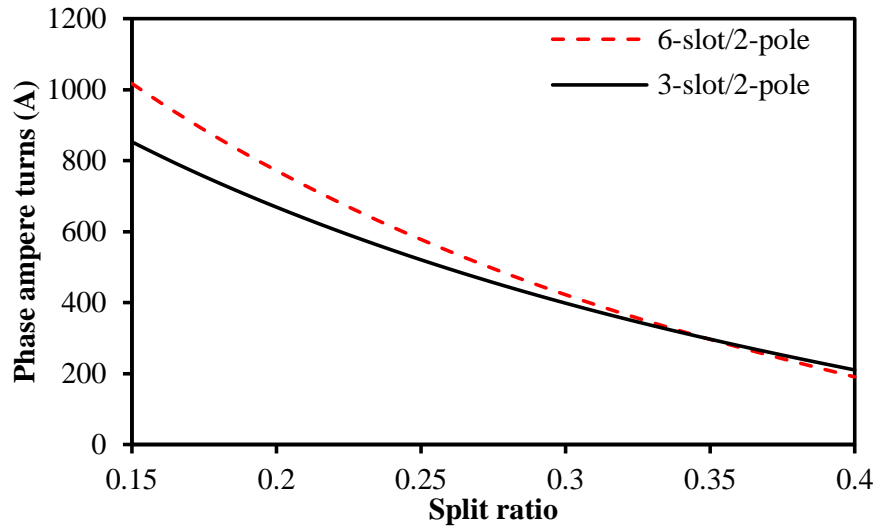


Fig. 5. 22 Variation of phase ampere turns with split ratio ratio ( $P_{stator,lim}=25W$ ,  $B_r=1.2T$ ,  $B_{max}=1.1T$ ).

However, it should be noticed that the 3-slot/2-pole machine suffers more serious local saturation comparing with the 6-slot/2-pole machine when the height of tooth tip is kept the same which is shown in Fig. 5. 23. Consequently, the tooth tip height should be designed as a larger value in 3-slot/2-pole machines.

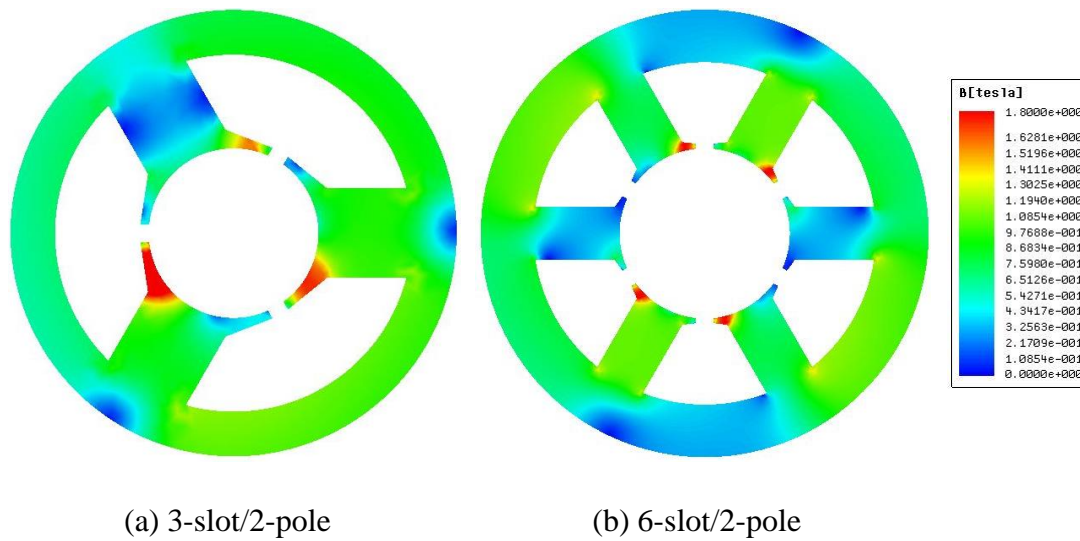


Fig. 5. 23 On-load flux density distribution ( $\lambda=0.3$ , ratio,  $P_{stator,lim}=25W$ ,  $B_{max}=1.1T$ ,  $B_r=1.2T$ , phase ampere turns=250A).

Therefore, the influence of tooth tip height should be investigated. The optimal split ratio and corresponding output torque with different tooth tip height in 3-slot/2-pole machines are shown in Fig. 5. 24.



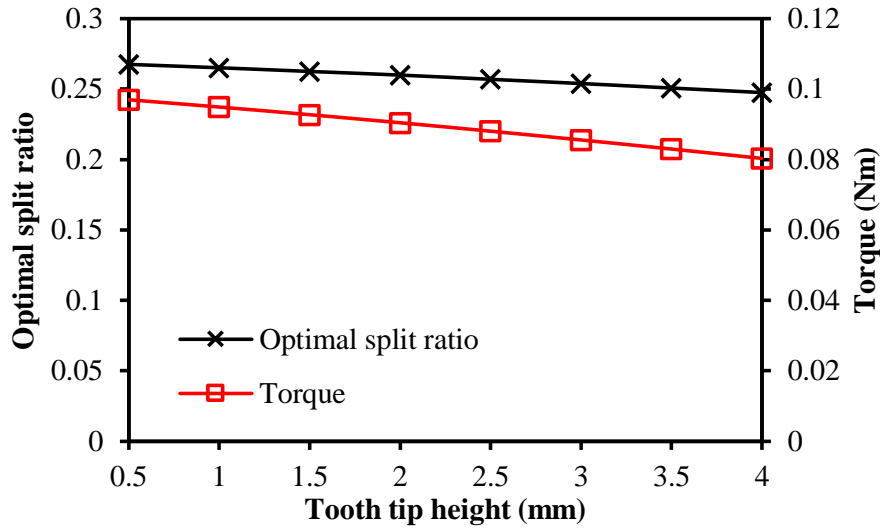


Fig. 5. 24 Variation of optimal split ratio and corresponding output torque with tooth tip height. ( $P_{stator,lim}=25W$ ,  $B_{max}=1.1T$ ,  $Br=1.2T$ )

As can be seen, with the increase of tooth tip heights, both the optimal split ratio and the corresponding output torque are decreased due to the reduced slot area, when the tooth tip height ranges from 0.5mm to 4mm, the drops of the optimal split ratio and output torque are 7.4% and 17.3%, respectively.

Consequently, in order to avoid serious local saturation, the tooth tip height in the 3-slot/2-pole machine is usually higher than that in the 6-slot/2-pole machine, which will reduce the optimal split ratio in 3-slot/2-pole machines.

#### 5.2.4 FE Validation

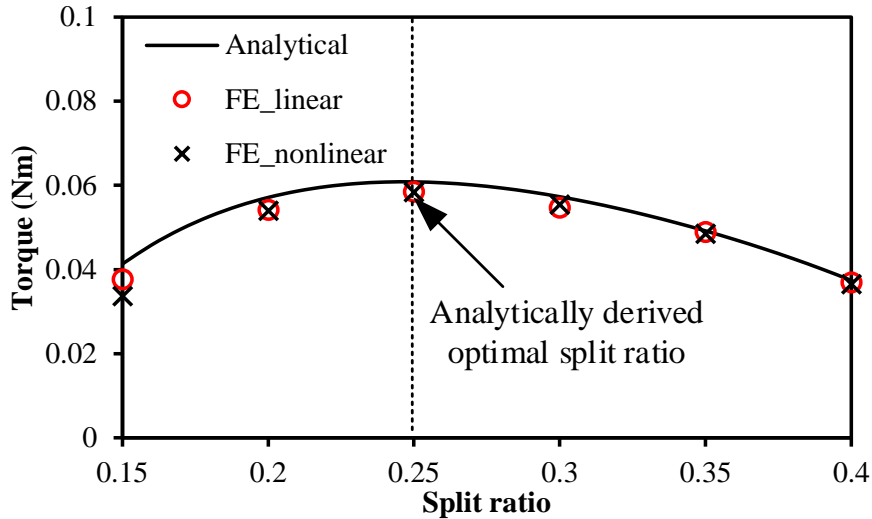
In this part, the FE verification is carried out to validate the analytical results. Both 6-slot/2-pole and 3-slot/2-pole machines are considered, and only the stator loss limitation is considered. The detailed parameters are the same as shown in Table 5.1, the other necessary parameters are listed in Table 5.2.

Table 5.2

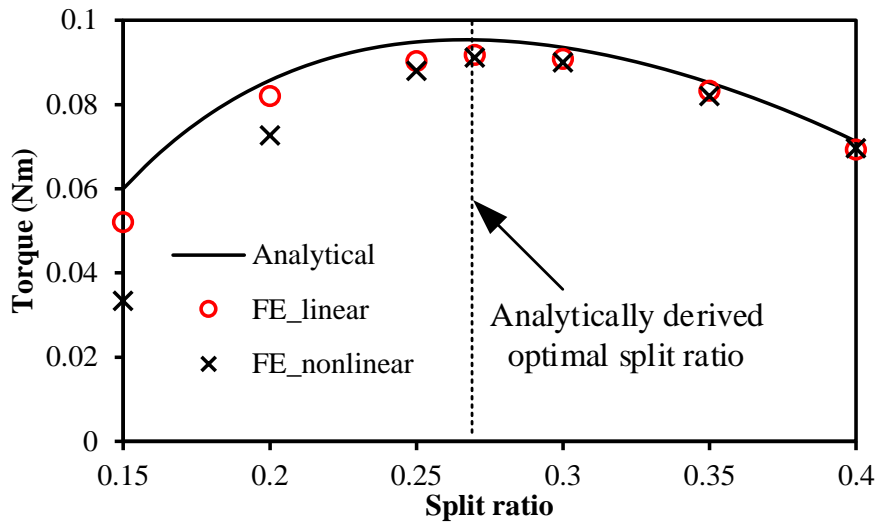
Parameters of Prototype Machine

Mass density of lamination ( $kg/m^3$ )	7872
Resistivity of copper ( $\Omega \cdot m$ )	$1.75 \times 10^{-8}$
Maximum stator flux density (T)	1.1
Lamination hysteresis loss coefficient ( $W/kg/Hz^2/T^2$ )	0.0198
Lamination eddy current loss coefficient ( $W/kg/Hz^2/T^2$ )	$1.517e-5$

The comparison between FE and analytical results is shown in Fig. 5. 25.



(a) 6-slot/2-pole



(b) 3-slot/2-pole

Fig. 5. 25. Comparison of analytical and FE predicted variations of torque with split ratio and optimal split ratio.

As can be seen, the output torque predicted by FE method is slightly lower, which is mainly due to the fact that the analytical method neglects the effect of armature field, the saturation, the flux leakage and the influence of tangential flux variation in the

airgap. Nevertheless, the difference is fairly small, and they have the same optimal split ratio, which shows the great effectiveness of the analytical method.

### 5.3. Split Ratio Optimization in Small High Speed Machine Considering Rotor Loss Limitation Only

As discussed in Section 5.1. The rotor loss is usually neglected in the split ratio optimizations. Nevertheless, it has significant influence on small high speed permanent magnet machines due to the employment of metallic sleeve and magnet ring. As a result, the split ratio optimization considering rotor loss only will be studied in this section. The rotor loss components will be calculated at first. Then, the optimal split ratio considering rotor loss limitation only will be investigated analytically.

#### 5.3.1 Loss Calculation

In terms of rotor loss, two loss components should be considered due to high rotating frequency and the adoption of magnet ring, i.e. windage loss and rotor eddy current loss, respectively.

As for the windage loss, it can be calculated by [AGL03]

$$P_{windage} = C_f \rho_{air} \pi \omega_{mech} r_{rotor}^4 l_a \quad (5.27)$$

where  $P_{windage}$  indicates the windage loss,  $\rho_{air}$  is the mass density of air,  $\omega_{mech}$  denotes the rotor angular velocity,  $r_{rotor}$  is the rotor outer radius including the sleeve thickness, and  $C_f$  is the friction coefficient which can be calculated as [AGL03]

$$C_f = \frac{0.0152}{R_{e\delta}^{0.24}} \left[ 1 + \left( \frac{8}{7} \right)^2 \left( \frac{4R_{ea}}{R_{e\delta}} \right)^2 \right]^{0.38} \quad (5.28)$$

where  $R_{ea}$  and  $R_{e\delta}$  are the Reynolds number for an axial flow through the air gap and the Couette Reynolds number for the tangential flow forced by the rotating rotor and the turbulence. Their values can be expressed as

$$R_{e\delta} = \frac{\rho_{air} \omega_{mech} r_{rotor} l_g}{\mu_{air}} \quad (5.29)$$

$$R_{ea} = \frac{\rho_{air} v_a 2l_g}{\mu_{air}} \quad (5.30)$$

In (5.29) and (5.30),  $\mu_{air}$  is the air dynamic viscosity and  $v_a$  indicates the axial speed of air.

In terms of the value of  $v_a$ , it can be roughly determined by

$$v_a = \frac{P_{rotor,lim}}{C_a \cdot \Delta\tau_a \cdot A_a} \quad (5.31)$$

where  $P_{rotor,lim}$  is the maximum allowed rotor loss, as shown later, it mainly depends on the cooling capability in the airgap and the maximum allowed rotor size,  $C_a$  is the specific heat capacity of coolant,  $\Delta\tau_a$  is the variation of the coolant temperature and  $A_a$  is the area of the airgap cross section. It should be noticed that the value of  $v_a$  depends on  $P_{rotor,lim}$  in practice. However, in order to ease the investigation,  $v_a$  is kept as the same in later studies, of which the value is determined under the most critical rotor thermal situation.

As for the rotor eddy current loss, it can be determined analytically or by using FE method. The analytical solution is presented in detail in [ZHU04].

Similar to stator part, the sum of rotor loss components should meet the rotor thermal limitation as well. In small high speed machine, in order to keep the rotor temperature to never reach the value which could demagnetize the magnet, the effective cooling in the airgap should be provided [AGL03]. According to [DON14], the stator and rotor parts can be approximately treated as thermal isolated due to the effective airgap cooling, which means the rotor loss can be also limited by a similar equation to (5.15) as

$$P_{rotor,lim} = h_{rotor} \Delta\tau_{rotor,max} \pi D_{ro} l_a \quad (5.32)$$

where  $h_{rotor}$  is the rotor overall heat transfer coefficient decided by the cooling method, and  $\Delta\tau_{rotor,max}$  is the maximum allowed rotor temperature variation which depends on the magnet material significantly.

Consequently, the sum of the rotor eddy current loss and the windage loss is restricted by  $P_{rotor,lim}$ , which can be expressed as

$$P_{rotor,lim} = P_{rotor,eddy} + P_{windage} \quad (5.33)$$

where  $P_{rotor,eddy}$  denotes the allowed rotor eddy current loss.

### 5.3.2 Torque Calculation Considering Rotor Loss Only

When the torque is limited by the rotor loss only, (5.18)-(5.23) can be also applied. Nevertheless, the current calculation which should be determined by the rotor loss, and the influence of temperature on magnet properties, e.g. magnet remanence, should be taken into account.

As for the relationship between the phase current and the rotor loss, since the influence of slot opening and saturation are neglected,  $P_{rotor,eddy}$  is determined by the phase current as well as the split ratio [ZHU04]. From another perspective, the phase current  $I$  limited by the  $P_{rotor,eddy}$  can be determined when the split ratio is specified. Consequently, the phase current can be expressed as

$$I = f^{-1}(P_{rotor,eddy}(I, \lambda)) \quad (5.34)$$

As a consequence, the output torque is calculated as

$$T = \frac{3\sqrt{3}}{\pi} N_w D_{ag} l_a B_{g \max} K_{dp} f^{-1}(P_{rotor,eddy}(I, \lambda)) \quad (5.35)$$

As can be seen, when the rotor loss dominates the input current, the slot area is not shown in the output torque equation, which means it has no influence on the optimal split ratio.

In addition, temperature affects the magnet properties, and hence, the rotor loss significantly. As a result, the calculation of airgap flux density should take the influence of temperature into account, which can be expressed as

$$B_{g \max} = \frac{B_{r,temp}}{2} \frac{1 - (D_{sh} / D_{mo})^2}{1 - (D_1 / D_{si})^2} \cdot \left[ (D_{mo} / D_{si})^2 + (D_{mo} / D_{ag})^2 \right] \quad (5.36)$$

where  $B_{r,temp}$  is the remanence with specific magnet temperature.

By this way, the variation of torque with different split ratio in the model only considering the rotor loss can be calculated, and the result is shown in Fig. 5. 26.

As shown, the output torque increases with split ratio monotonously. This is due to the fact that the allowed  $P_{rotor,eddy}$  increases with split ratio shown in Fig. 5. 27, which increases the phase ampere turns when the split ratio is small, and hence, the output torque.

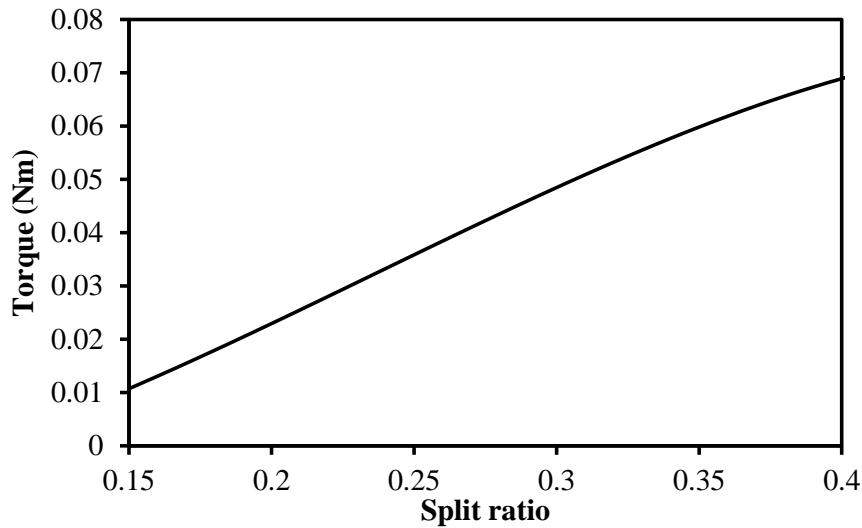


Fig. 5. 26 Variation of torque with split ratio in model considering rotor loss only.

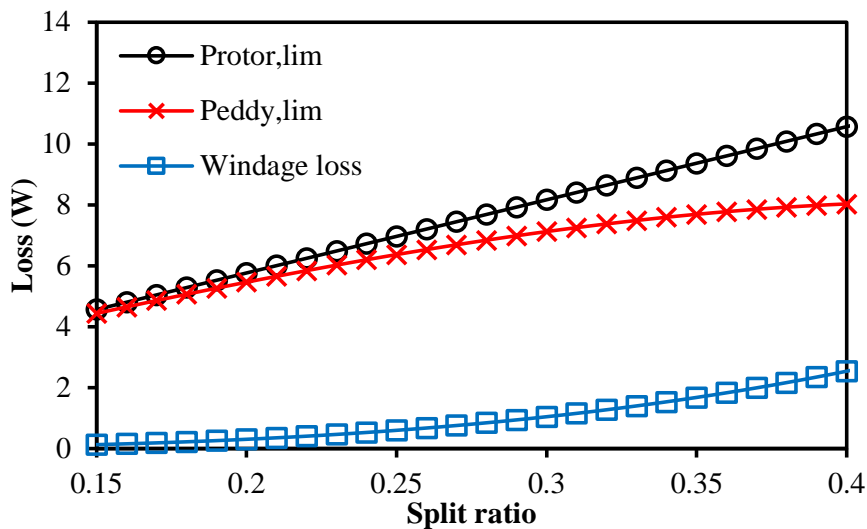


Fig. 5. 27 Variation of rotor loss components with split ratio in model considering rotor loss only.

Although the value of phase ampere turns decreases slightly when the split ratio is relatively large as shown in Fig. 5. 28, the torque still increases due to the enhancement of  $B_{gmax}$  and  $D_{ag}$  caused by increased split ratio.

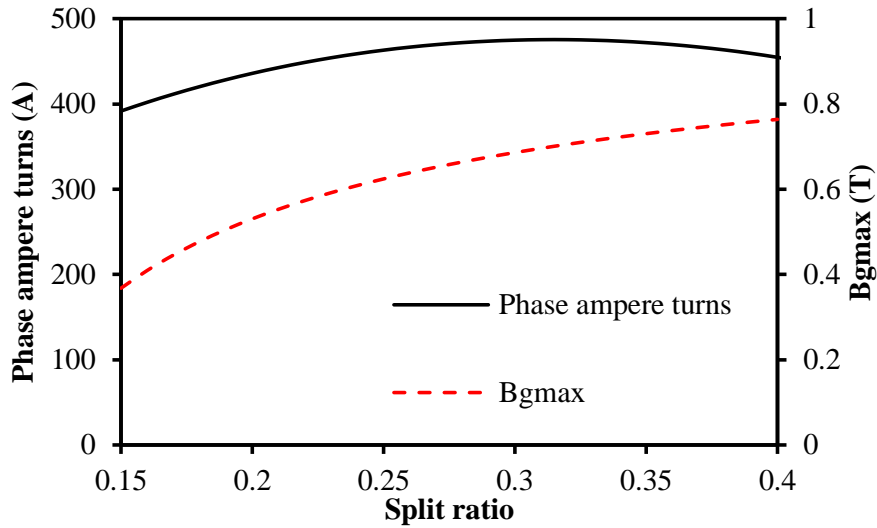


Fig. 5. 28 Variation of phase ampere turns and  $B_g$  with split ratio in model considering rotor loss only.

#### 5.4 Split Ratio Optimization in Small High Speed Machine Considering Both Stator and Rotor Loss Limitations

As shown, the variation of torque with split ratio represents very different behavior when the limitations are different. In order to calculate the optimal split ratio and corresponding maximum output torque practically, both stator and rotor loss limitations should be considered simultaneously, which will be detailed in this section. The optimal split ratio calculation and its characteristics will be investigated at first. Then, the influence of several key design parameters will be studied. Finally, the FE validation is carried out

##### 5.4.1 Optimal split ratio Calculation and Its Characteristics

In terms of calculation, since the analytical solution for the optimal split ratio considering both stator and rotor limitations is almost impossible, its value is calculated by a flow chart shown in Fig. 5. 29. The variation of torque with split ratio in the machines with different optimization models is shown in Fig. 5. 30. The Model 1 refers to the conventional model accounting the stator iron and copper losses, while Model 2 is the model considering both stator and rotor loss limitations.

As can be seen, Model 2 has relative smaller maximum output torque but larger optimal split ratio. More importantly, the torque optimized by Model 2 increases almost linearly at first, but drops suddenly after specific point. In order to investigate it in more detail,

different regions are divided according to the variation of torque and current, which are shown in Fig. 5. 31 and Fig. 5. 32, respectively.

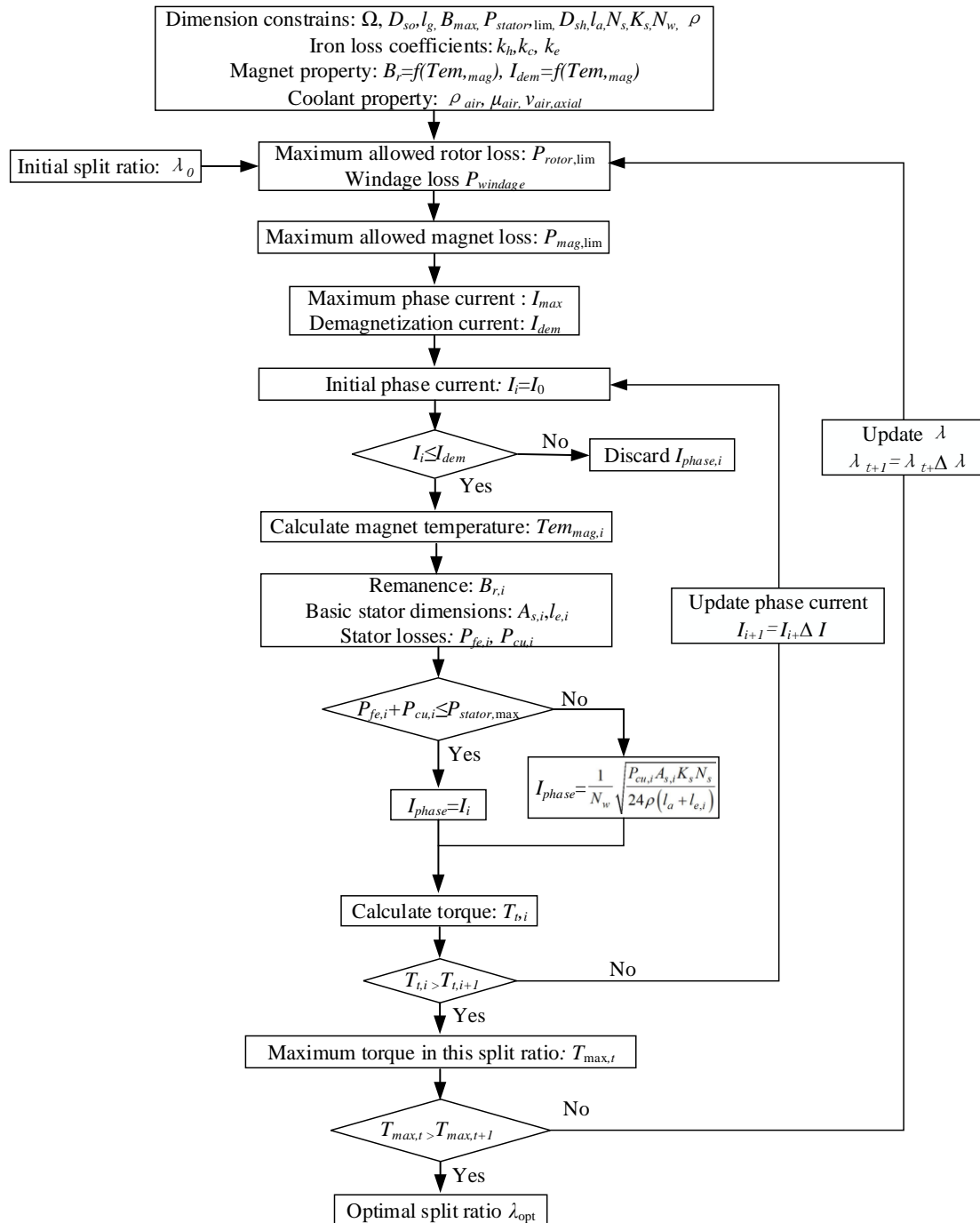


Fig. 5. 29 Optimization process for split ratio in small high speed permanent magnet machine.



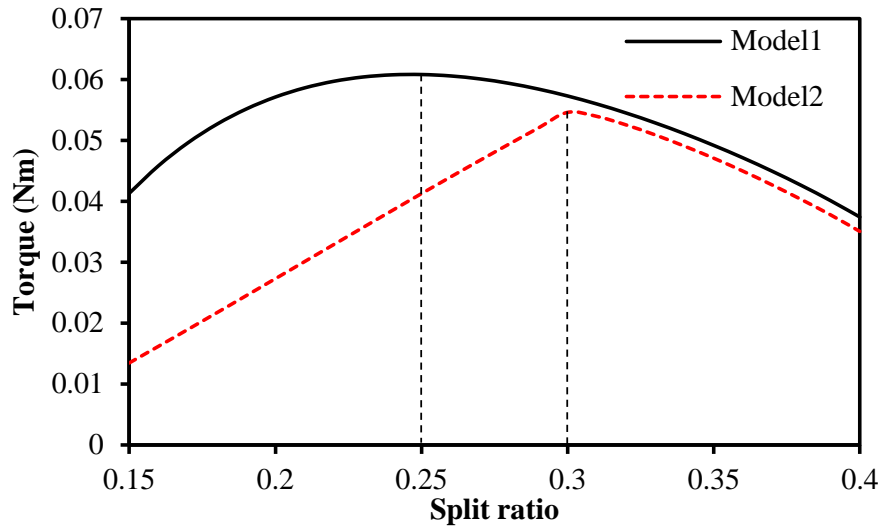


Fig. 5. 30 Variation of torque with different split ratio ( $P_{\text{stator,lim}}=25\text{W}$ ,  $B_{\text{max}}=1.1\text{T}$ )

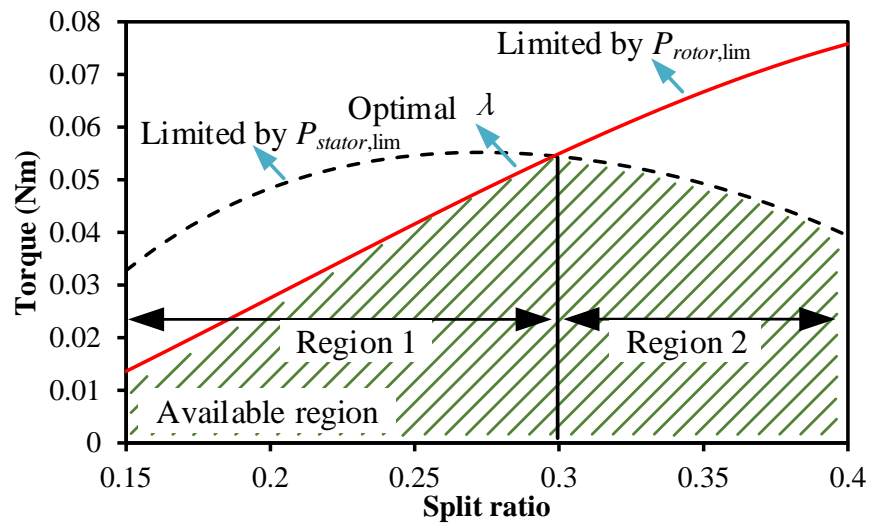


Fig. 5. 31 Different regions of torque-split ratio curve. ( $P_{\text{stator,lim}}=25\text{W}$ ,  $B_{\text{max}}=1.1\text{T}$ ).

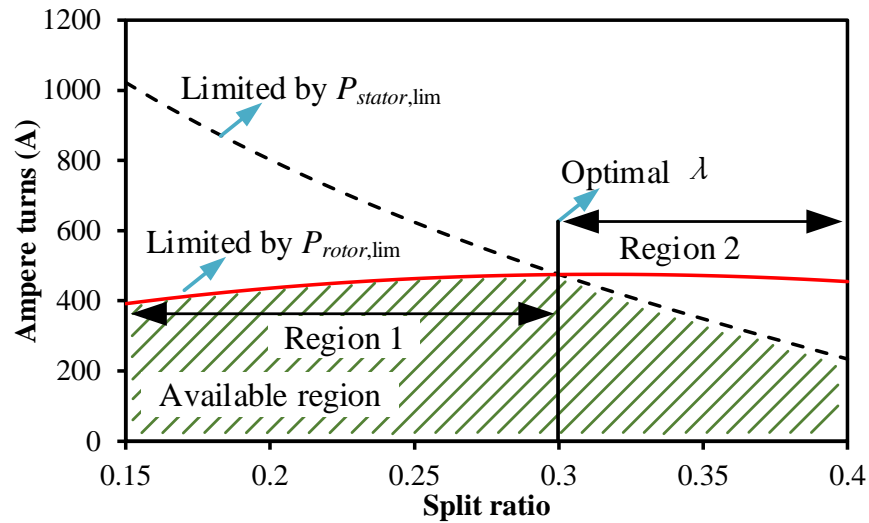
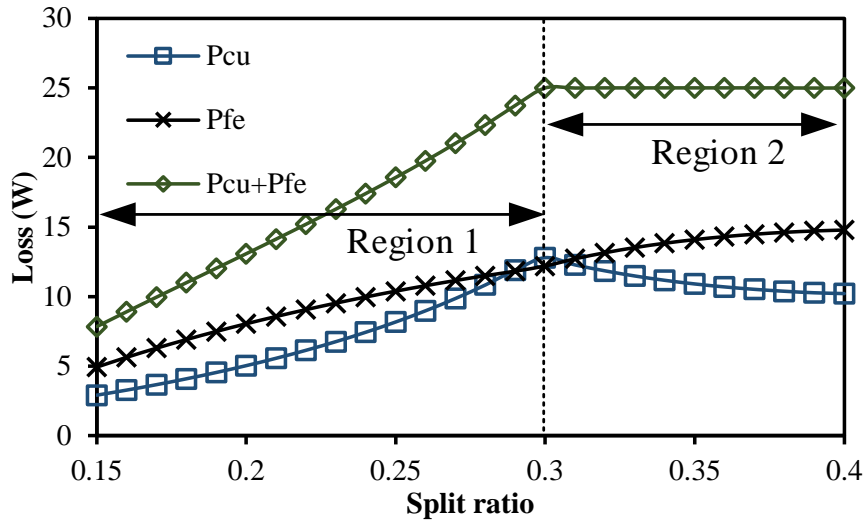
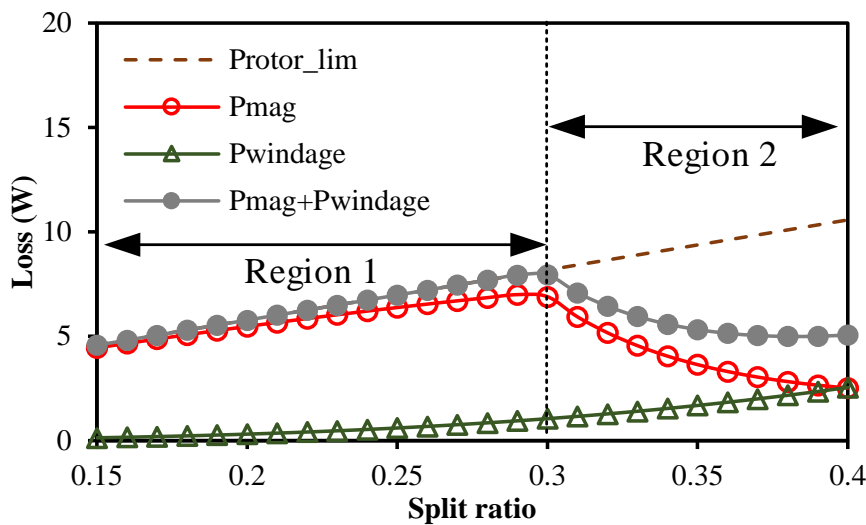


Fig. 5. 32 Different regions of current-split ratio curve. ( $P_{\text{stator,lim}}=25\text{W}$ ,  $B_{\text{max}}=1.1\text{T}$ ).

It can be seen that in region 1, the torque and current are limited by the  $P_{rotor,lim}$ , while in the region 2, the torque and current are restrained by the  $P_{stator,lim}$ . Since different loss limitation is the main reason, the variations of different loss components with split ratio are shown Fig. 5. 33, so that more details can be studied.



(a) Stator loss components



(b) Rotor loss components

Fig. 5. 33 Variation of different loss components with different split ratio. ( $P_{stator,lim}=25W$ ,  $B_{max}=1.1T$ ).

As shown, the iron loss increases with the split ratio all the time. In contrast, the copper loss increases with split ratio from a small value in region 1. Since in that region, the stator loss limitation can result in high value of phase ampere turns, which leads to unacceptable rotor loss. As a result, the rotor loss limitation is more crucial for phase ampere turns in this region. Accordingly, the phase ampere turns increase with split

ratio due to more allowed  $P_{rotor,lim}$ , and it results in ascending copper loss as well as output torque.

Meanwhile, with the increase of split ratio,  $P_{rotor,lim}$  ascends measurably according to (5.32), which results in significant increase of phase ampere turns, and hence, copper loss. As a result, the sum of copper loss and stator iron loss reaches  $P_{stator,lim}$  at the beginning of region 2. Consequently, the phase ampere turns and output torque starts to be restrained by stator loss limitation in this region.

#### **5.4.2 Influence of Design Parameters**

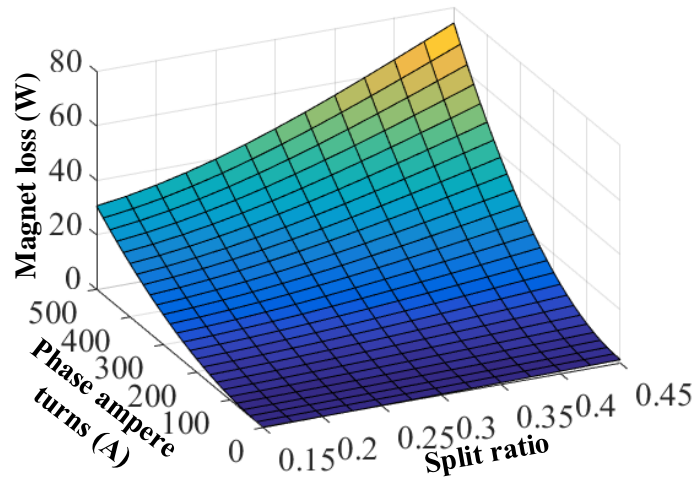
In previous parts, the split ratio is optimized considering both stator and rotor loss limitations. In this part, the influence of several key design parameters, e.g. slot pole combinations, magnet materials and segmentations.

##### **5.4.2.1 Influence of Slot/Pole Number Combinations**

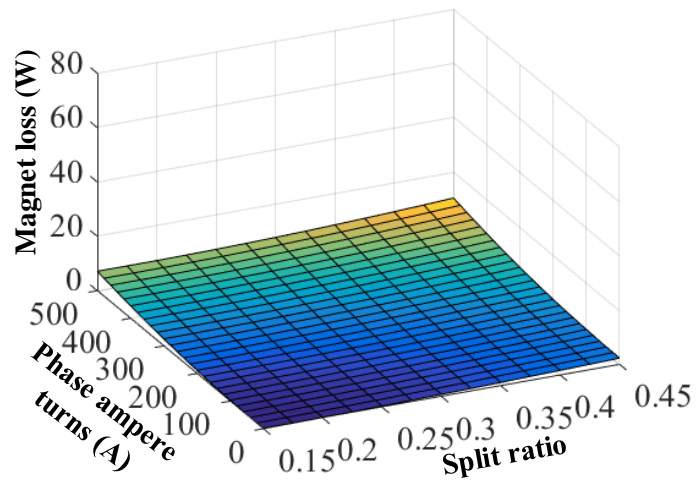
In the previous investigation, the 6-slot/2-pole machine has been chosen as the prototype machine. Nevertheless, other possible slot/pole number combinations can be competitive candidates for small high speed PM machines, e.g. 3-slot/2-pole, etc. Therefore, the influence of slot/pole combinations is studied here, and both 2-pole machines with 3 slots and 6 slots are considered which share the same specifications shown in previous sections.

The comparison of rotor eddy current loss with split ratio and phase ampere-turns in machines with different slot/pole combinations is shown in Fig. 5. 34.

As can be seen, the 3-slot/2-pole machine has much larger rotor eddy current loss comparing with the machine having 6-slot/2-pole when the phase ampere-turns and the split ratio are the same. This is due to the fact that there are abundant low order even harmonics in airgap flux density in a 3-slot/2-pole machine, which is caused by the unbalanced winding structure and asymmetric stator topology [MAJ18a]. Consequently, the rotor eddy current loss should affect more significantly in the machine having 3-slot/2-pole.



(a) 3-slot/2-pole



(b) 6-slot/2-pole

Fig. 5. 34 Variation of rotor eddy current loss with different phase ampere-turns and split ratio.

The variation of torque with split ratio in machines having different slot/pole combinations is shown in Fig. 5. 35. It can be seen that the machine with 3-slot/2-pole has almost the same output torque but higher optimal split ratio comparing with the 6-slot/2-pole machine.

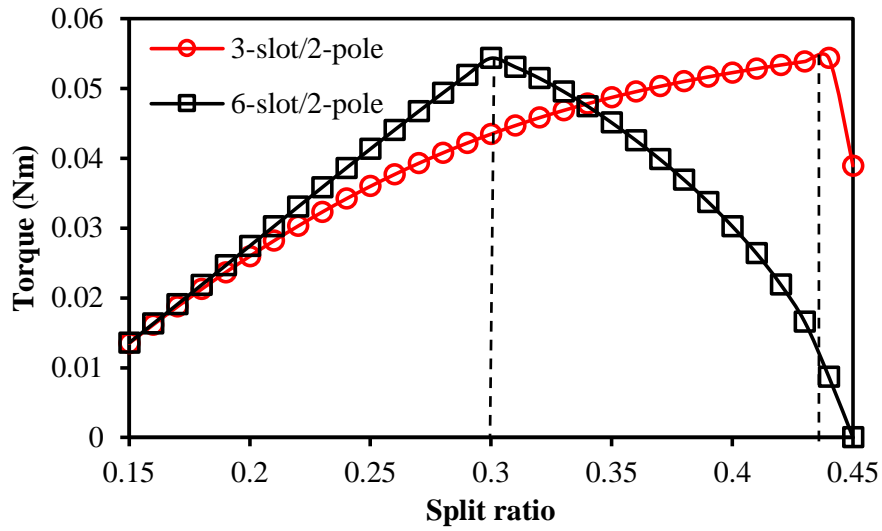
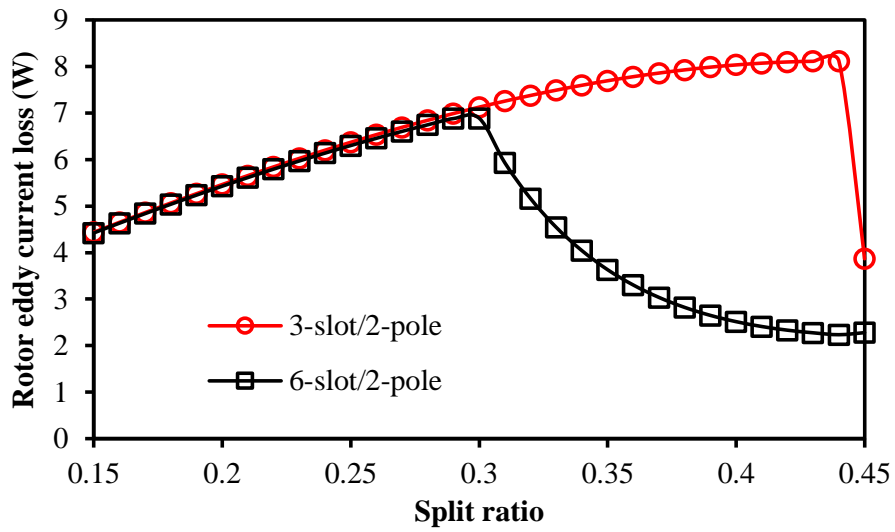
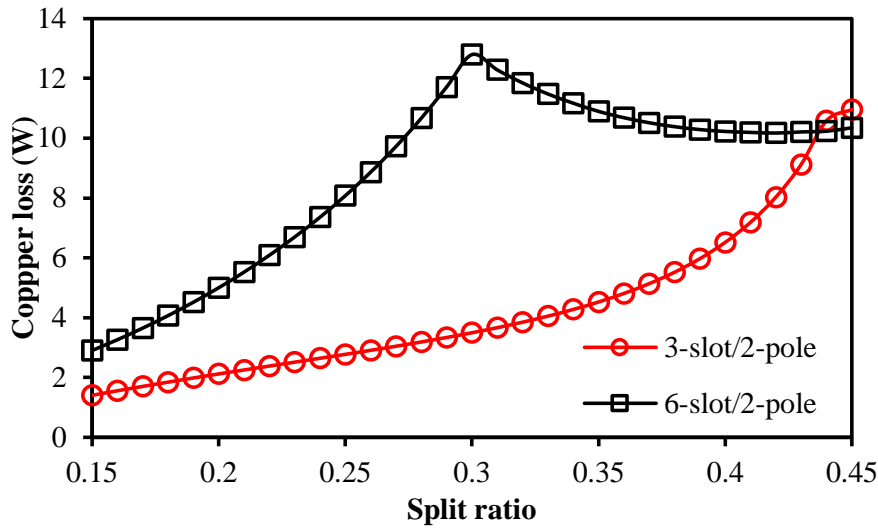


Fig. 5.35 Variation of torque with split ratio in machines with different slot/pole combinations ( $P_{\text{stator,lim}}=25\text{W}$ ,  $B_{\text{max}}=1.1\text{T}$ ).

To study in more details, the variations of loss components and phase ampere turns with split ratio are shown in Fig. 5.36 and Fig. 5.37, respectively.



(a) Rotor eddy current loss



(b) Copper loss

Fig. 5. 36 Variation of loss components with split ratio in machines with different slot/pole combinations ( $P_{\text{stator,lim}}=25\text{W}$ ,  $B_{\text{max}}=1.1\text{T}$ ).

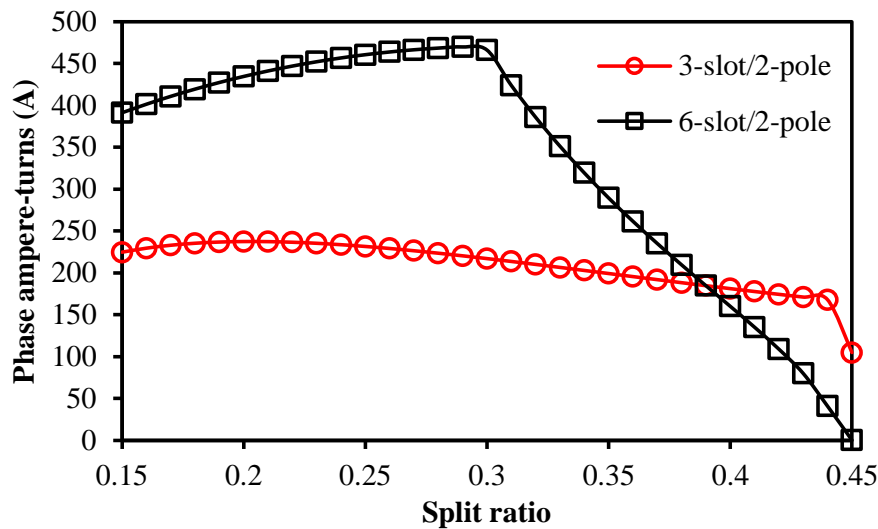


Fig. 5. 37 Variation of Input phase current loss with different split ratio in machines with different slot/pole combinations ( $P_{\text{stator,lim}}=25\text{W}$ ,  $B_{\text{max}}=1.1\text{T}$ )

As can be seen, the rotor eddy current losses increase with the same track in both 3-slot/2-pole and 6-slot/2-pole machines when the split ratio is small. Since these two machines share the same rotor structure, which indicates that they have the same  $P_{\text{rotor,lim}}$  when the split ratio is specified. However, since the 3-slot/2-pole machine has larger rotor eddy current loss, it will have much smaller phase ampere turns at specific split ratio when  $P_{\text{rotor,lim}}$  is the limitation. In addition, the 3-slot/2-pole machine has relatively shorter total ending winding length but larger total slot area as shown in Fig. 5. 38.

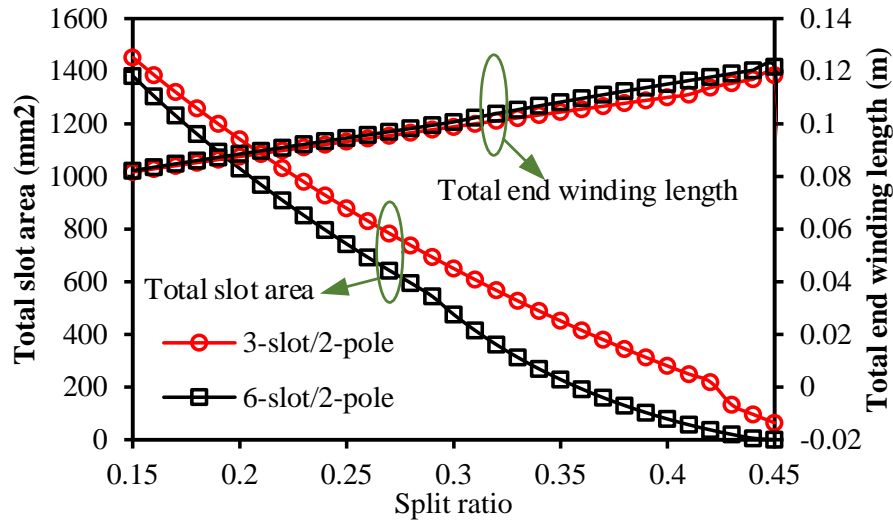


Fig. 5. 38 Variation of total slot area and total ending length with split ratio in machines with different slot/pole combinations ( $P_{stator,lim}=25W$ ,  $B_{max}=1.1T$ ).

As a result, the increase of copper loss will be much slower in the 3-slot/2-pole machine. Therefore,  $P_{stator,lim}$  will restrain the phase ampere turns at a larger split ratio in the 3-slot/2-pole machine, where the optimal split ratio occurs.

Meanwhile, due to the low level of phase ampere turns but higher winding factor, i.e.  $\sqrt{3}/2$  for 3-slot/2-pole but 0.5 for 6-slot/2-pole machines, and relative larger optimal split ratio, the maximum output torque of the 3-slot/2-pole machine has almost the same value comparing with the machine having 6-slot/2-pole.

#### 5.4.2.2 Influence of Magnet Material

In the previous sections, the NdFeB35UH is chosen as the magnet material. However, the magnet material could be changed with different applications, which can result in significant difference in terms of the machine performance. As a result, the comparison of different magnet materials will be investigated in this section.

Here two different permanent magnet materials are chosen which are the NdFeB35UH and SmCo Recoma18, respectively. Variation of material properties with temperature is shown Fig. 5. 39. As shown, different from NdFeB35UH, SmCo Recoma18 can provide better demagnetization performance when the temperature is high, while it has lower remanence. In addition, SmCo Recoma18 can also provide higher working temperature which is set as 250°C.

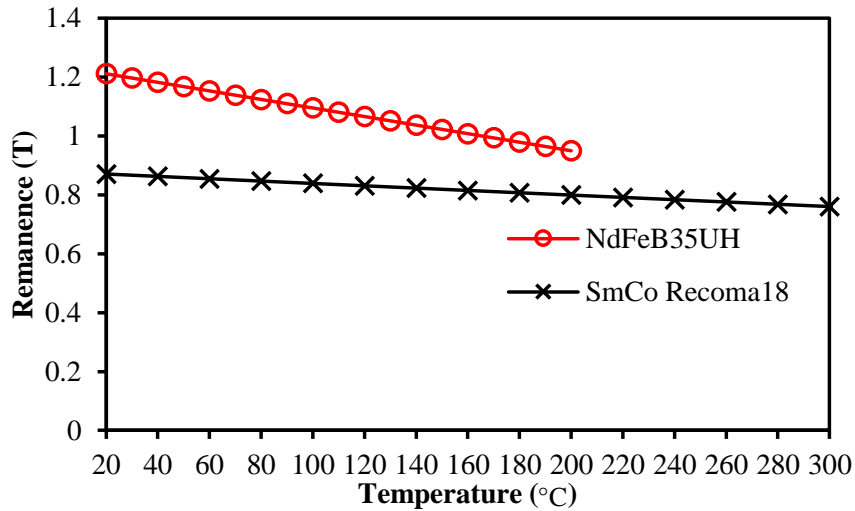


Fig. 5. 39. Variation of magnet properties with different magnetization.

The variation of torque with split ratio in machines having different magnet materials is shown in Fig.49. As can be seen that comparing with machine having NdFeB35UH, the rotor loss has very limit influence on the optimal split ratio when the SmCo Recoma18 is adopted, which only shows on the magnet temperature and remanence shown in Fig. 5. 40. This is due to the fact that the torque starts to be limited by  $P_{stator,lim}$  before the optimal split ratio determined by  $P_{stator,lim}$  occurs.

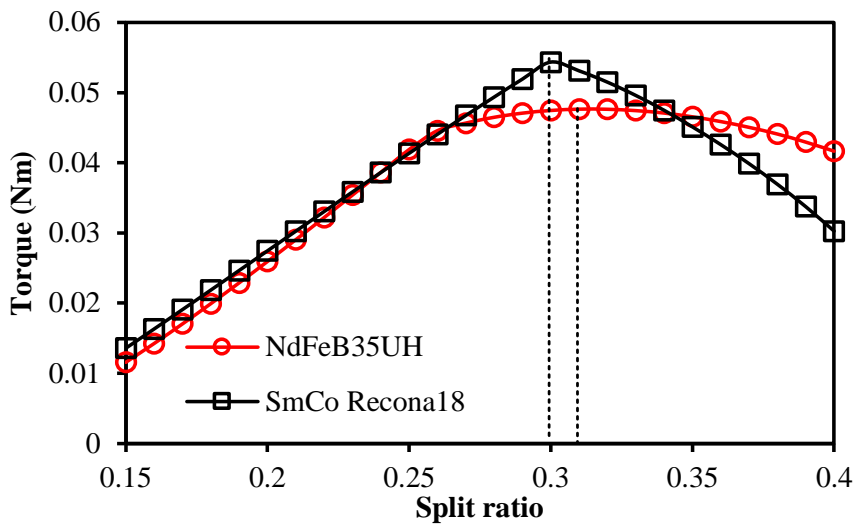


Fig. 5. 40 Variation of torque with different split ratio in machines with different magnet materials ( $P_{stator,lim}=25W$ ,  $B_{max}=1.1T$ ).

In order to explain in more detail, the variation of loss with split ratio is investigated and shown in Fig. 5. 41. In addition, the rotor temperature and remanence with different split ratio are shown in Fig. 5. 42.



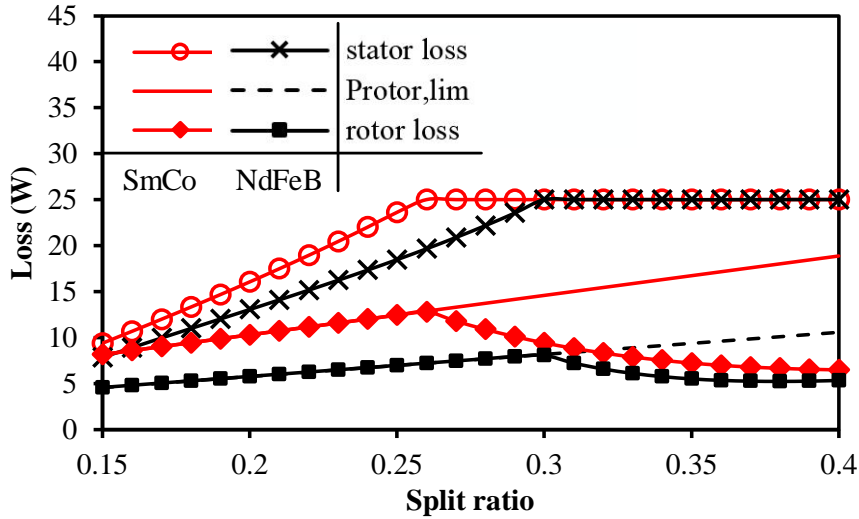
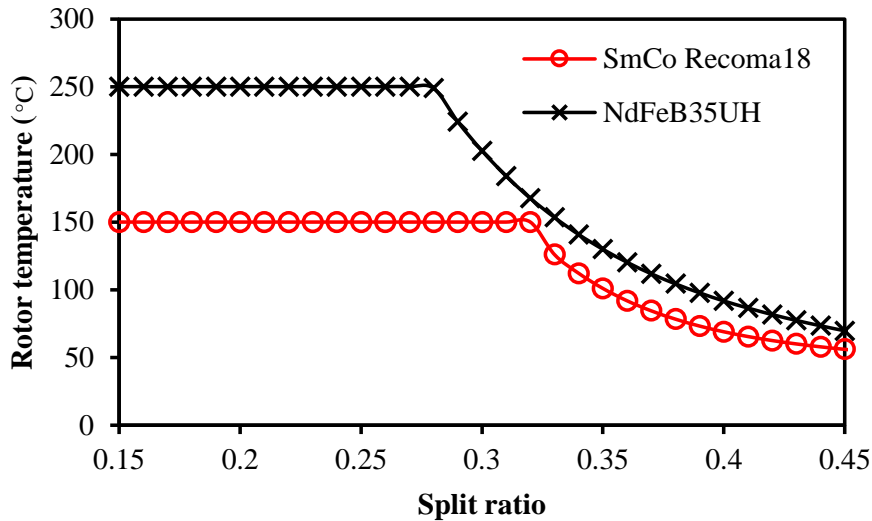
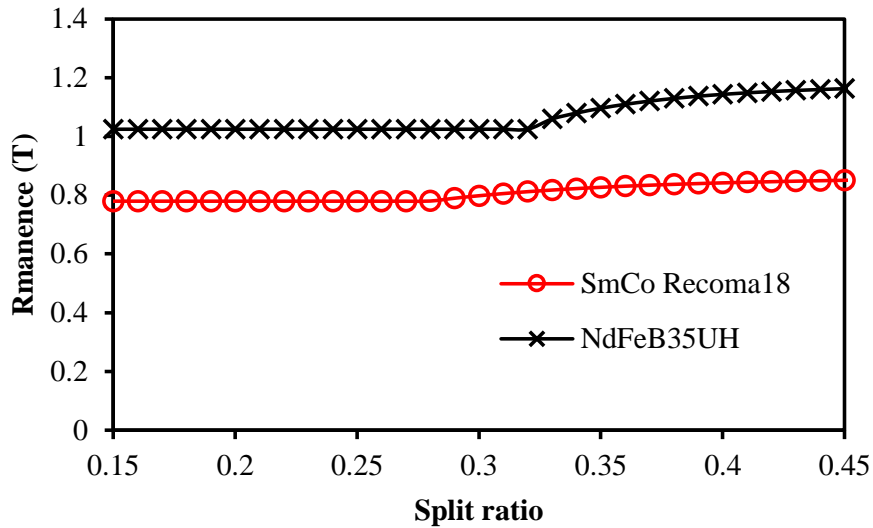


Fig. 5. 41 Variation of different loss components with split ratio in machines having different magnet materials ( $P_{stator,lim}=25W$ ,  $B_{max}=1.1T$ ).

As shown, in machine with SmCo Reconal18, the allowed rotor loss is much higher due to the larger maximum allowed working temperature of magnet. As a result, the machine with SmCo Reconal18 has higher phase ampere turns in region 1 comparing with machine having NdFeB35UH. Consequently, with the increase of phase ampere turns,  $P_{stator,lim}$  will restrain the phase ampere-turns quickly due to the rapidly ascended copper loss, even before the optimal split ratio determined by  $P_{stator,lim}$  only occurs.



(a) Rotor temperature



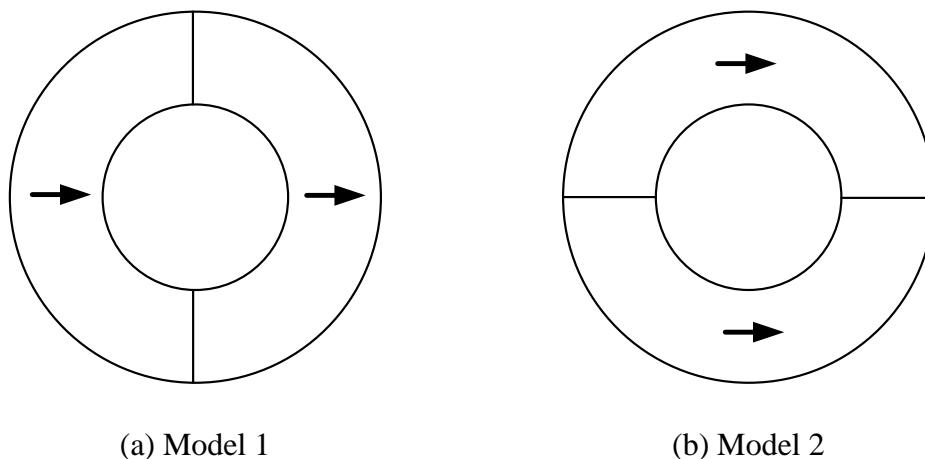
(b) Remanence

Fig. 5. 42 Variation of magnet properties with split ratio ( $P_{\text{stator,lim}}=25\text{W}$ ,  $B_{\text{max}}=1.1\text{T}$ ).

### 5.4.2.3 Influence of PM Segmentation

Although the magnet ring is usually adopted for small high speed permanent magnet machines. In order to make the investigation more comprehensively. The influence of PM segmentation will be investigated in this part. Considering the small volume of the PM material, only the rotor with two segments is investigated. Nevertheless, the method can be applied on any other number of PM segments.

It should be noticed that there are two different segmentation methods for the magnet ring when two segments are required, which are shown in Fig. 5. 43.



(a) Model 1

(b) Model 2

Fig. 5. 43 Cross sections of rotors with 2 PM segments.

In Model 1, the magnet is equally segmented along the perpendicular direction of the PM field. In contrast, the magnet is equally segmented with the same direction of the PM field in Model 2.

Since the segmentation mainly aims to reduce the magnet eddy current loss, the influence of sleeve is not considered at first, while its impact will be studied later. The comparison of magnet eddy current loss with rotor position is shown in Fig. 5. 44. The split ratio and ampere turns are the optimal value when both stator and rotor loss limitations are considered.

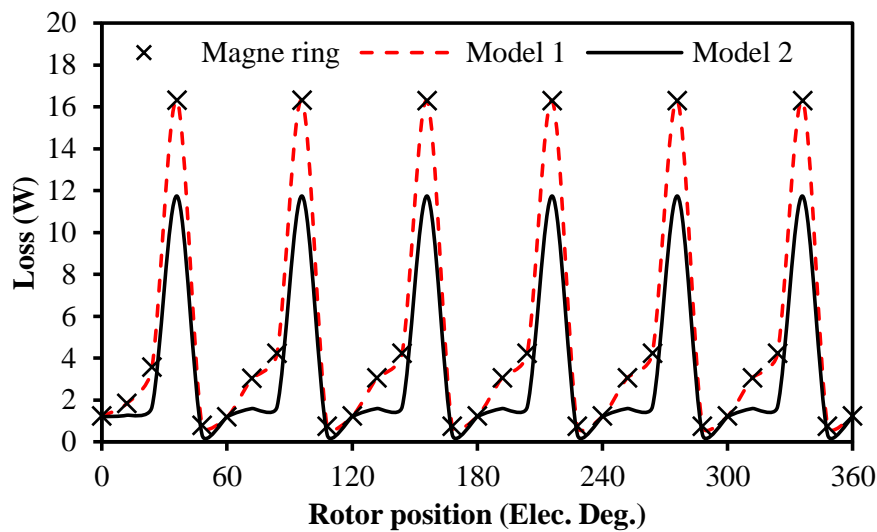


Fig. 5. 44 Variation of magnet eddy current loss with rotor positions. ( $\lambda=0.3$ , phase ampere turns=572)

As can be seen, Model 1 has slight influence on the magnet eddy current reduction while the Model 2 can reduce this part of loss significantly. In order to show more details, the loss distribution is compared in Fig. 5. 45. It should be noticed that the magnet eddy current loss varies with rotor position significantly due to the time harmonics. Consequently, the distributions of maximum magnet eddy current loss are shown, where the rotor position equals to 36 electrical degrees.

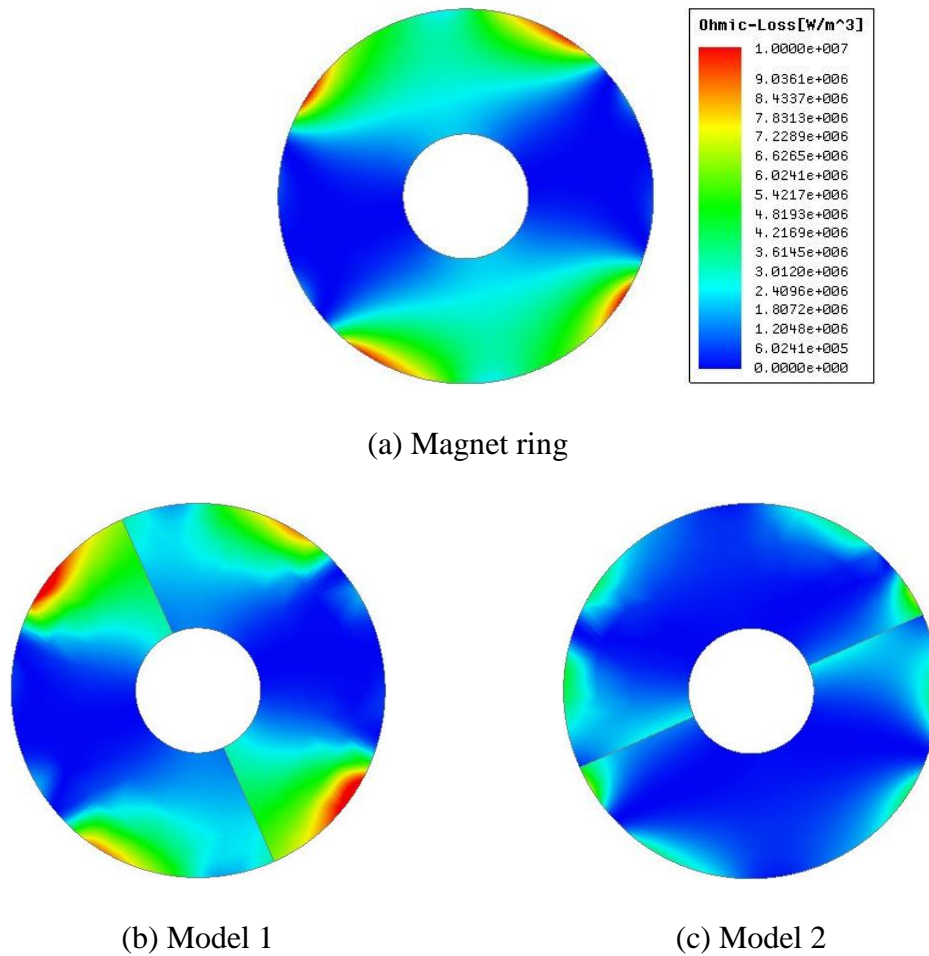


Fig. 5. 45 Magnet eddy current loss distribution ( $\lambda=0.3$ , phase ampere turns=572, rotor position=36 electrical degrees).

Comparing with the magnet ring, Model 1 only changes the distribution of magnet eddy current loss slightly. In contrast, the reduction of this part of losses is notable in Model 2. In order to explain the reason, the illustration of rotor eddy current is shown in Fig. 5. 46, where  $Direction_{ar}$ ,  $Direction_{PM}$ ,  $Direction_{eddy}$   $Direction_{rotating}$  indicate armature field direction, PM field direction, rotor eddy current direction and rotating direction, respectively. The reference plane equally divides the rotor along the same direction of PM field. Since the influence of PM field on rotor eddy current loss is very small which has been shown in Chapter 3 and Chapter 4. Only the influence of armature field on rotor eddy current is considered here. In addition, it should be noticed that due to the zero current angle, the armature field is perpendicular to PM field.

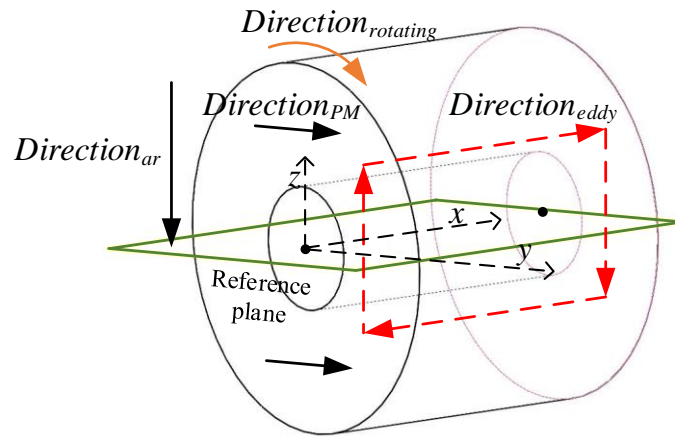
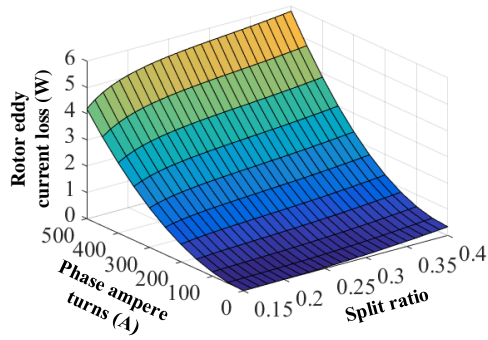


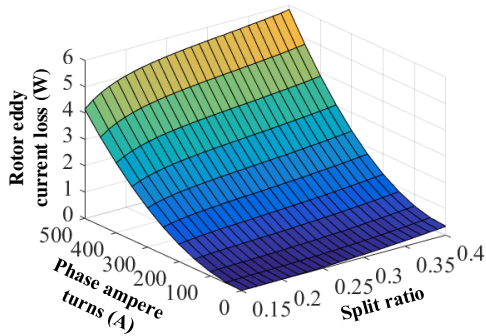
Fig. 5. 46. Illustration of rotor eddy current loss.

As a result, the eddy current of the rotor along the  $z$ -axis higher than the reference plane has inward direction, and the rotor lower than the reference plane in the  $z$ -axis has the opposite eddy current direction. Therefore, Model 1 segments the rotor along the eddy current direction, which indicates that the equivalent resistance can be hardly improved by Model 1. As a result, Model 2 can offer better performance in terms of rotor eddy current loss reduction.

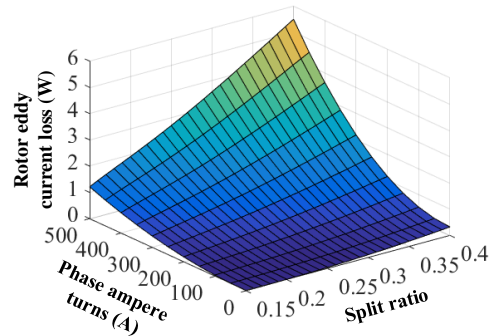
The variation of magnet eddy current loss with phase ampere turns and split ratio is shown in Fig. 5. 47.



(a) Magnet ring



(b) Model 1



(c) Model 2

Fig. 5. 47 Variation of rotor eddy current loss with phase ampere turns and split ratio. The variation of torque with split ratio is shown in Fig. 5. 48. It should be noticed that since the machine with magnet ring has very similar performance comparing with Model 1, its torque will not be shown here.

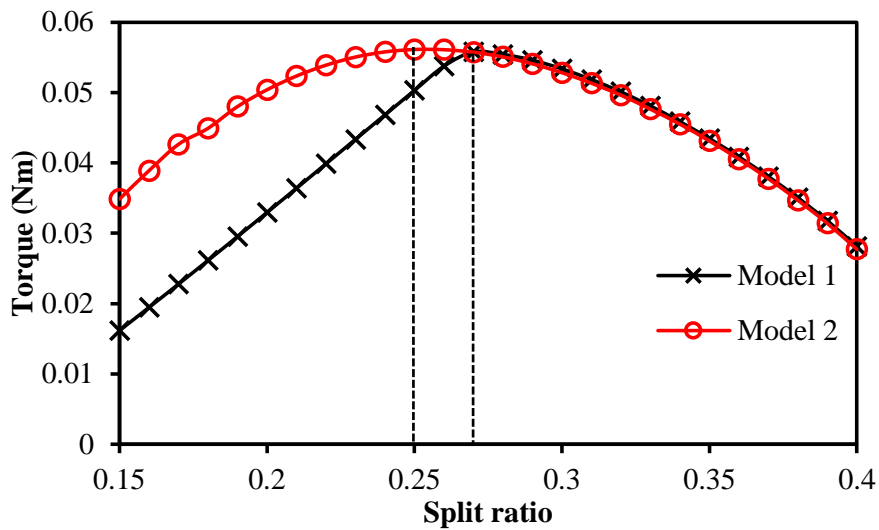


Fig. 5. 48 Variation of torque with different split ratio.

As can be seen, the rotor loss has negligible influence on the machine with Model 2 rotor, which results in lower optimal split ratio but higher maximum output torque comparing with Model 1. In order to investigate it in more details, the variation of loss components with split ratio is shown in Fig. 5. 49.

Since the magnet eddy current loss is small in Model 2 and the influence of sleeve on the rotor loss is not considered, the allowed phase ampere turns in Model 2 can be higher as shown in Fig. 5. 50. Consequently, Model 2 reaches  $P_{stator,lim}$  very quickly, and the rotor loss has negligible impact on the optimal split ratio as well as output torque.

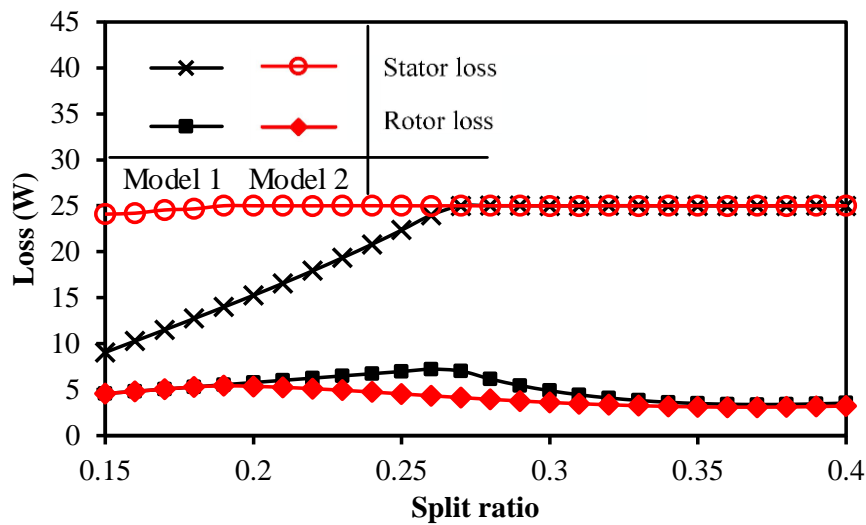


Fig. 5. 49 Variation of loss components with different split ratio.

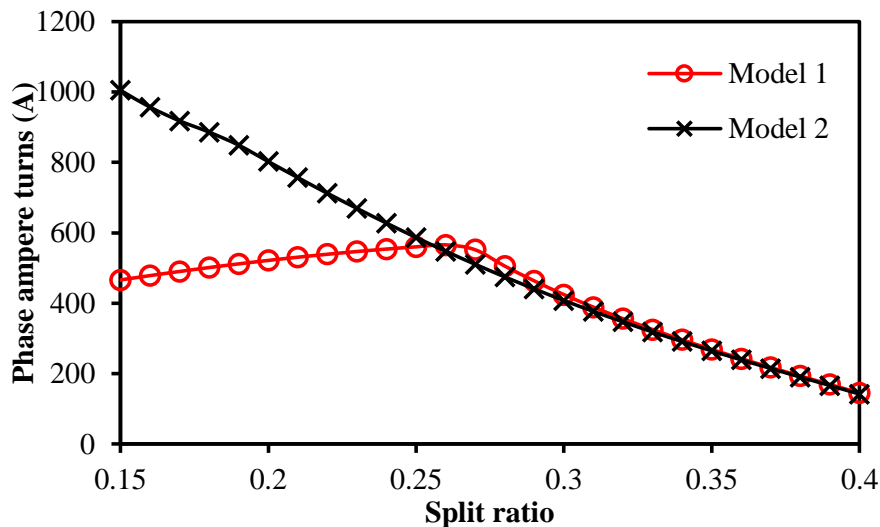


Fig. 5. 50 Variation of phase ampere turns with different split ratio.

Nevertheless, when the influence of Inconel 718 sleeve is considered, the eddy current loss will mainly focus on the sleeve due to its high conductivity. As a result, the influence of segmentation can be different. The variation of rotor eddy current loss with rotor positions are shown in Fig. 5. 51Fig. 5. 50. As shown, comparing with the magnet ring, Model 1 has the similar loss while the Model 2 has even a higher value.

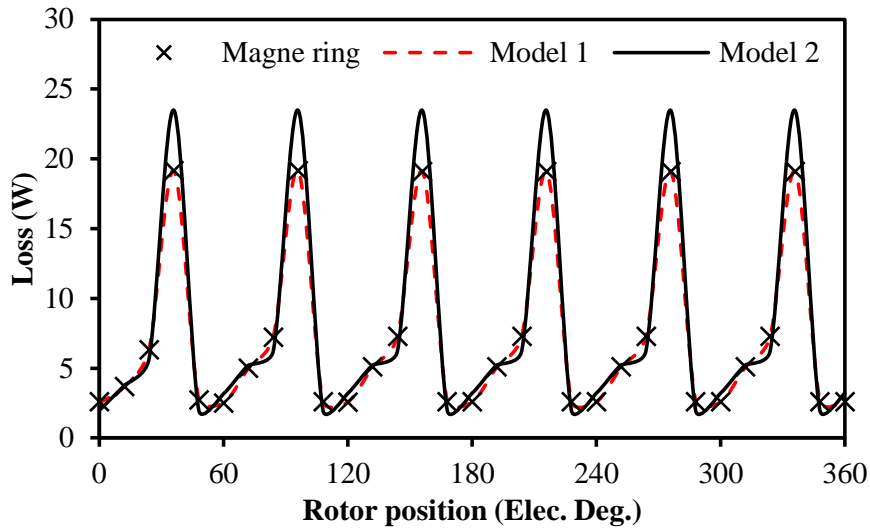


Fig. 5. 51 Variation of rotor eddy current loss with rotor positions ( $\lambda=0.3$ , phase ampere turns=572).

In order to show more details, the loss distributions of magnet ring and model 2 are shown in Fig. 5. 52. The label of loss density is identical to Fig. 5. 45. As can be seen, most of loss concentrates on the sleeve instead of magnet. Although the segmentation can reduce part of the magnet eddy current loss in Model 2, the eddy current reaction is also reduced, which results in more significant loss in the sleeve.



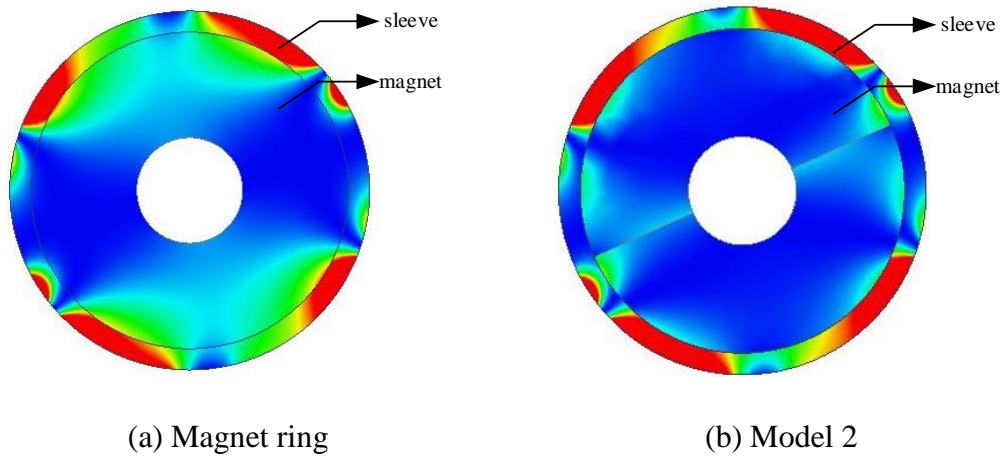


Fig. 5. 52 Rotor eddy current loss distribution ( $\lambda=0.3$ , phase ampere turns=572, rotor position=36 electrical degrees).

### 5.4.3 FE Validation

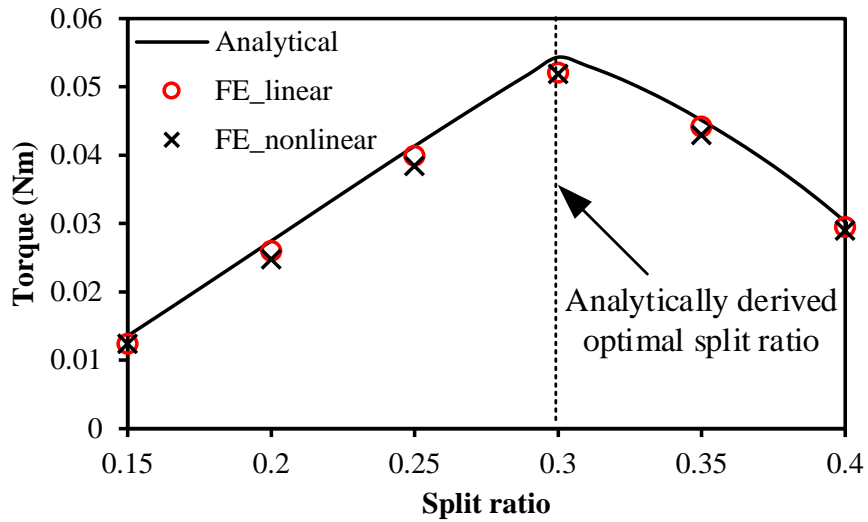
The FE results are carried out in this section for validation. Both 3-slot/2-pole and 6-slot/2-pole machines considering stator and rotor loss limitations are considered, the detailed parameters are the same shown in Table 5.1 and Table 5.2, and NdFeB35UH is employed. The other necessary parameters are listed in Table 5.3.

Table 5.3

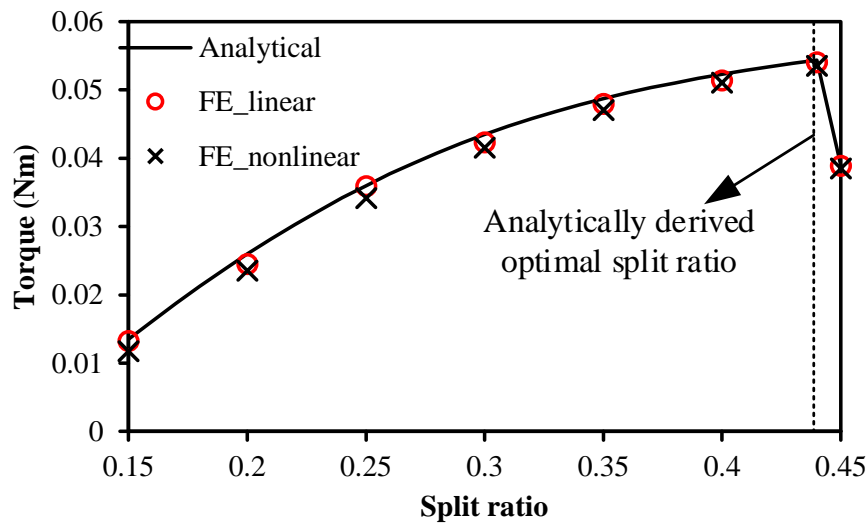
Parameters of Prototype Machine

Air mass density ( $\text{kg}/\text{m}^3$ )	1.20
Air dynamic viscosity ( $\text{kg}/\text{m}\cdot\text{s}$ )	$1.82 \times 10^{-5}$
Air specific heat capacity ( $\text{J}/(\text{kg}\cdot\text{K})$ )	1100
Rotor overall heat transfer coefficient ( $\text{W}/(\text{K}\cdot\text{m}^2)$ )	100

The variations of torque predicted by analytical and FE methods are calculated and shown in Fig. 5. 53.



(a) 6-slot/2-pole



(b) 3-slot/2-pole

Fig. 5. 53 FE validation of variation of torque with different split ratio.

Both linear and non-linear soft magnetic materials are considered, which are marked as circle and cross, respectively. As shown, the difference between analytical and FE predictions is very small regardless if the saturation is considered or not. This is due to the fact that  $B_{\max}$  is typically chosen very small in high speed machine to avoid large iron loss. In addition, the phase ampere turns are limited by both stator and rotor loss limitations, which has relatively low value in all split ratio range. Consequently, the influence of saturation can be almost neglected.

#### 5.4.4 General Determination of Optimal Split Ratio in Small High Speed Permanent Magnet Machine Considering Both Stator and Rotor Loss

In the previous sections, the optimal split ratio in small high speed permanent magnet machines considering both stator and rotor loss limitations is investigated. It shows there are generally two different scenarios which are shown in Fig. 5. 54.

As can be seen, in scenario 1, the optimal split ratio occurs when the track of torque restrained by  $P_{rotor,lim}$  crosses the torque track limited by  $P_{stator,lim}$ . In this scenario, the optimal split ratio can be identified when the current meets the equation as

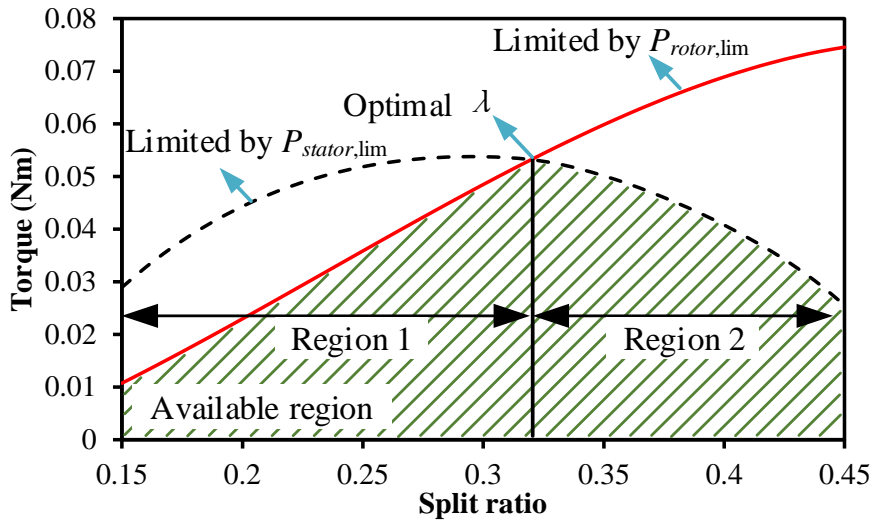
$$I_a = f^{-1}(P_{eddy,lim}(I_a, \lambda)) = \frac{1}{N_w} \sqrt{\frac{(P_{stator,lim} - P_{fe}) A_s K_s N_s}{24 \rho (l_a + l_e)}} \quad (5.37)$$

In contrast, in scenario 2, the optimal split ratio is mainly determined by  $P_{stator,lim}$ , and  $P_{rotor,lim}$  affects the remanence of magnet material only. Consequently, the optimal split ratio in scenario 2 can be determined in a very similar way as shown in Section 5.2.

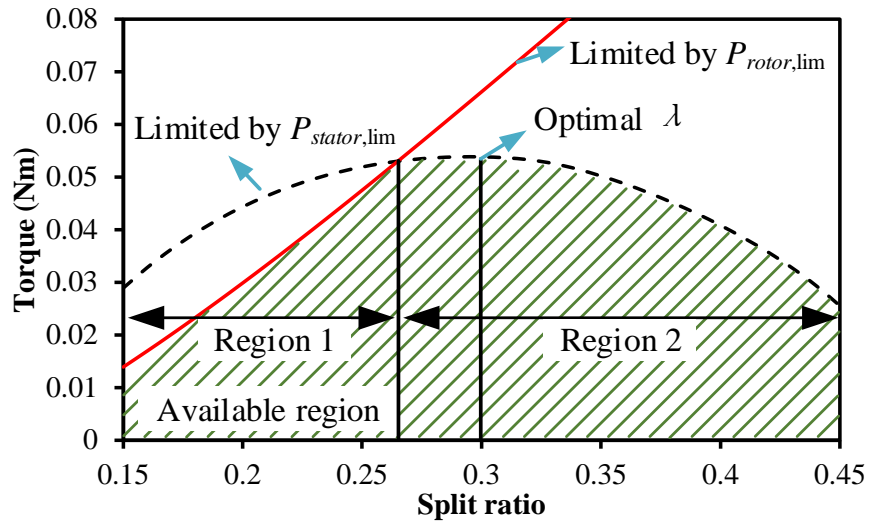
This scenario can be reached by two different ways, either reducing the rotor loss, which can be achieved by rotor optimizations, e.g. PM segmentation, rotor shaping, novel sleeve structures, etc., or increasing  $P_{rotor,lim}$ , which can be accomplished by changing the magnet material or enhancing the cooling ability.

In order to distinguish the optimal split ratio in scenarios 1 and 2 separately, they are identified as  $\lambda_{opt1}$  and  $\lambda_{opt2}$ , respectively. In practice, the overall optimal split ratio  $\lambda_{opt,overall}$  should be calculated by

$$\lambda_{opt,overall} = \max(\lambda_{opt1}, \lambda_{opt2}) \quad (5.38)$$



(a) Scenario 1



(b) Scenario 2

Fig. 5. 54 Different scenarios of optimal split ratio in small high speed permanent magnet machines considering both stator and rotor loss limitations.

### 5.5. Summary

In this chapter, the split ratio in small high speed machines is optimized. The stator loss limitation is considered only at first. Both loss and output torque are calculated analytically. Moreover, the influence of several design parameters are investigated as well. It shows there will be an optimal combination for split ratio and  $B_{max}$ . In addition, all  $P_{stator,lim}$ , slot/pole number combinations and the magnet remanence have significant influence on the optimal split ratio and the corresponding maximum output torque.

Then, the output torque is calculated by considering rotor limitation only. It shows the torque increases with split ratio monotonously, which is mainly due to the increased rotor cooling ability. Finally, the optimal split ratio in small high speed machines considering both stator and rotor loss limitations is studied. It shows two different regions can be divided. The torque is limited by the rotor loss limitation in region 1 but stator loss limitation in region 2. Moreover, the influence of slot/pole number combinations, magnet materials and PM segmentations has been investigated in details. It shows that the 3-slot/2-pole machine is affected by the rotor eddy current loss more seriously comparing with the machine having 6-slot/2-pole. In addition, the rotor eddy current loss has less importance in machines with SmCo Recoma18 or specific rotor segmentations.

It should be noticed that the optimal split ratio obtained in this chapter is only for small size high speed PM machines. When the machine size increases, the electric loading usually increases as well, which will result in higher optimal split ratio.

# CHAPTER 6

## GENERAL CONCLUSIONS AND FUTURE WORK

### 6.1 General Conclusions

#### 6.1.1 Performance Improvement

In this thesis, the electromagnetic performance of high speed permanent magnet motors, with particular reference to the mitigation of parasitic effects (i.e. the UMF and the magnet eddy current loss reduction), the influence of key design parameters and the improved optimization method.

For UMF mitigation in 3-slot/2-pole high speed PM machines, three machines with different types of auxiliary slots are investigated and compared. In the first two machines, namely Machine 1 and Machine 2, the auxiliary slots are inserted in the middle of stator teeth, while their sizes are optimized under different working conditions, i.e. no-load and rated on-load conditions. In contrast, both position and size of auxiliary slots are optimized under rated on-load condition in the third machine, i.e. Machine 3. It shows the Machine 1 can offer the best performance in terms of the no-load UMF reduction due to the balanced airgap permeance distribution. In contrast, Machine 3 can almost eliminate the rated on-load UMF, since the auxiliary slots in Machine 3 can make F1 and F2 which are the UMFs caused by the self-interaction of PM field and mutual interaction between PM and armature fields, have almost the same amplitude but the opposite phase, which results in significant cancelling effect. Although the existence of auxiliary slots increases the equivalent airgap length, which reduces the output torque. The relevant electromagnetic performance under rated working condition for four different machines are compared in Table 6.1.

Table 6.1

Electromagnetic performance comparison of different machines under rated working condition

	UMF	Flux linkage	Back EMF	Cogging torque	Average torque	Torque ripple
Conventional	23.8N	14.3mWb	20.9V	3.7mNm	212.9mNm	9.3mNm
Machine 1	21.6N	14.2mWb	20.7V	1.5mNm	210.3mNm	5.8mNm
Machine 2	11.7N	12.4mWb	18V	10.2mNm	184.3mNm	26.1mNm
Machine 3	0.8N	13.8mWb	20.1V	2.7mNm	205.2mNm	4.2mNm

However, As shown in Chapter 2, the variation of working conditions have significant influence on the effectiveness of auxiliary slots in Machine 3, since different working conditions change the phase and amplitude of F2, which results in the decreased cancelling effect between F1 and F2. In addition, Machine 3 has higher rated on-load UMF when BLDC drive mode is adopted due to the impact of additional time harmonics. Nevertheless, the reduction is still significant which is higher than 65%. It also shows Machine 3 can be only applied to unidirectional applications, since the armature field reverses when the rotating direction changes while the PM field is hardly affected, which turns the cancelling effect between F1 and F2 to the additive effect. Another type of auxiliary slots is proposed to solve this problem, which has two auxiliary slots per stator tooth and they are symmetrical along the middle of the tooth. Both the size and the position of auxiliary slots are optimized under rated on-load working condition. The rated on-load UMF reduced by this type of auxiliary slots is about 33%. The comparison in terms of the main electromagnetic performance among different machines are shown in Table 6.2.

Table 6.2

Main electromagnetic performance comparison of different machines under rated working condition

	UMF	Average torque
Machine 1	23.8N	212.9mNm
Machine 3 +	0.8N	205.2mNm
Machine 3 -	36.5N	207.5mNm
Machine 4	15.8N	203.5mMm

Furthermore, the auxiliary slots with the optimal size and position are also proposed for reducing the magnet eddy current loss. A MMF-permanence model is employed for explaining the working mechanism from the harmonics reduction perspective. It shows that this method can effectively reduce the rated on-load magnet eddy current loss over 80%. The electromagnetic performance of the conventional and the proposed machines are compared in Table 6.3.

Table 6.3

Electromagnetic performance comparison of different machines under rated working condition

	Magnet eddy current loss	Flux linkage	Back EMF	Cogging torque	Average torque	Torque ripple
Conventional	8.5W	13.6mWb	85.4V	1.9mNm	201.6mNm	5.9mNm
Proposed	1.6WN	12.9mWb	81.2V	2mNm	193mNm	2.8mNm

However, the proposed method is also affected by working conditions due to the modified amplitude and phase of armature field harmonics. In addition, the influence of airgap length is also investigated. The magnet eddy current loss and torque in both conventional and proposed machines under rated working condition with several different airgap lengths are compared in Table 6.4 and Table 6.5.

Table 6.4

Comparison of magnet eddy current loss between machines in Chapter 3

Airgap length	0.5mm	0.7mm	0.9mm
Conventional	13W	10.9W	9.4W
Proposed	3.6W	2.5W	1.8W
Reduction percentage	72.5%	77.5%	80.6%

Table 6.5

Comparison of torque between machines in Chapter 3

Airgap length	0.5mm	0.7mm	0.9mm
Conventional	214.3mNm	209.2mNm	204.2mNm
Proposed	207.2mNm	200.9mNm	195.7mNm
Reduction percentage	3.3%	3.7%	4.1%

It shows that the machines with larger airgap length can benefit more from this method, since the proposed method can only suppress specific harmonics content instead of all of them, while the contribution of high order harmonics decreases with airgap length, which increases the effectiveness of the proposed method. Although the increased airgap length will reduce the output torque, the reduction is very low in all situations due to relative small airgap variation.

In terms of the influence of drive mode, the effectiveness decreases when BLDC drive mode is used due to the abundant time harmonics. Nevertheless, the reduction of rated



on-load magnet eddy current loss is about 40%. Moreover, this method can be also applied to other slot/pole number combinations and winding configurations.

It should be noticed that the optimizations in Chapter 2 and Chapter 3 only have one goal during the optimization, i.e. the minimum rated on-load UMF or the minimum average rated on-load magnet eddy current loss, respectively. Nevertheless, since the optimal stator structure and corresponding electromagnetic performance can be different according to different optimization goal, they should be balanced in practice, which indicates that the multi-objective optimization should be employed.

In order to show the influence of the optimization goal, three stator structures are compared in Fig.6.1, in which M1 indicates the conventional machine employed in Chapter 3, M2 is optimized to minimize the maximum rated on-load UMF and M3 is optimized to obtain the minimum average rated on-load magnet eddy current loss. Their electromagnetic performance are compared and shown in Table 6.6.

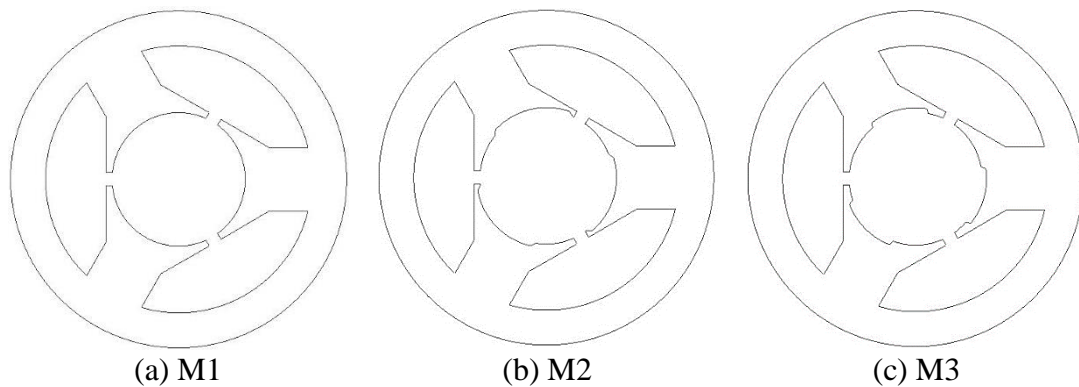


Fig. 6.1 Comparison of stator structures with different optimization goal.

Table 6.6

Comparison of electromagnetic performance among machines with different optimization goals

	Output torque	Maximum rated on-load UMF	Average rated-on load magnet eddy current loss
M1	201.7 mNm	21.5 N	8.3 W
M2	193.1 mNm	3.2 N	1.3 W
M3	193.4 mNm	0.6 N	2 W

As can be seen, the proposed method can reduce the maximum rated on-load UMF and average rated on-load magnet eddy current loss simultaneously. Nevertheless, the optimal stator structures and electromagnetic performance still have slight difference

when the optimization goal changes. Consequently, the electromagnetic performances which should be balanced in practice according to their importance.

### 6.1.2 Influence of Design Parameters

Due to the small volume of the rotor size, the magnet thickness has much more significant influence on the electromagnetic performance of small high speed PM machines, which has been studied comprehensively in this thesis. Its influence on magnetic fields has been studied at first. It shows that the PM field increases significantly with the magnet thickness while the armature field represents an opposite trend when the output torque is fixed. Moreover, the machines with thicker magnet benefit from lower on-load UMF, lower magnet eddy current loss as well as better demagnetization withstand capability, which are essentially due to the weakened armature reaction. Nevertheless, the thick magnet also results in high value of back EMF, which may make the phase voltage exceeds the limitation. In addition, the inductance and magnet usage efficiency also decrease with the magnet thickness. As a result, the magnet thickness should be carefully selected to balance different design considerations. In order to show more details, the electromagnetic performance of the prototype machine with several different magnet thicknesses is compared in Table 6.7.

Table 6.7

Comparison of electromagnetic performance of prototype machines in Chapter 4				
Magnet thickness	1mm	2mm	3mm	4mm
Current	17.4A	12.1A	10.5A	9.8A
Flux linkage	4.1mWb	5.6mWb	6.5mWb	6.8mWb
Back EMF	25.5V	35.5V	40.6V	43.1V
UMF	19.4N	14.0N	12.2N	11.5N
Self-inductance	4.1mH	2.3mH	1.8mH	1.5mH
Mutual inductance	-1.8mH	-1mH	-0.8mH	-0.6mH
Stator iron loss	8.72W	7.3W	8.5W	9.2W
Magnet eddy current loss	34.3W	11.6W	6.1W	4W
Magnet usage efficiency	0.16Nm/USD	0.09Nm/USD	0.06Nm/USD	0.05Nm/USD

### 6.1.3 Improved Optimization Method

An improved optimization method has been proposed in this thesis, which has considered different loss limitations, i.e. stator loss limitation only, rotor loss limitation only and both stator and rotor loss limitations. The loss limitations are calculated based on thermal considerations. The model considering stator loss limitation only has been investigated at first. All magnetic fields, loss components and output torques have been calculated analytically. It shows there is an optimal combination of split ratio and the maximum stator flux density when the maximum allowed stator loss is fixed, while the optimal value is affected by many design parameters, e.g. values of the maximum allowed stator loss, the magnet remanence and slot/pole number combinations, etc. In contrast, the output torque increases with split ratio monotonously in a very wide range when the rotor loss limitation has been considered only. Since the rotor cooling ability increases with the rotor size, which results in higher allowed the maximum allowed rotor loss, and hence, higher phase ampere turns. Although the phase ampere turns decrease slightly when the split ratio is large, thanks to the increased PM field and the rotor outer diameter, the output torque still increases.

Nevertheless, both stator and rotor loss limitations should be considered in practice, which has been investigated finally. It shows that the optimal split ratio exists in this situation. Moreover, 3-slot/2-pole high speed PM machines are affected by rotor loss limitation more comparing with machines with 6-slot/2-pole. Since the abundant even order spatial harmonics in 3-slot/2-pole machines result in much higher rotor eddy current loss. Consequently, the rotor loss limitation will constrain the output torque more. In addition, the machine with SmCo material is less sensitive to the effect of the rotor loss limitation comparing with the machines having NdFeB material. This is due to the fact that the allowed working temperature of SmCo is much higher than NdFeB. Consequently, the maximum allowed rotor loss in the machines having SmCo material is also larger, which leads to higher phase ampere turns when the split ratio is small, and the stator loss limitation will constrain the output torque very quickly. Finally, the effect of segmentations has been investigated. It shows that the segmentation could result in lower rotor eddy current loss when the sleeve is not considered, and hence, the lower influence of the rotor loss limitation. Nevertheless, when the metallic sleeve is employed, the most of rotor loss occurs on sleeve. As a result, the segmentation has very limited effect in this situation.

In order to summarise this chapter in more detail, the optimal split ratio and corresponding maximum output torque with different optimization conditions are compared in Table 6.8. The maximum stator loss is chosen as 25W, the maximum stator flux density is chosen as 1.1T and the magnet material is selected as NdFeB35UH. Although the variation of design parameters can significantly affect the optimal split ratio, and hence, the output torque. It will be very complicated and lengthy to summary the effect of all design parameters into several tables. Consequently, only the most common stator loss limitation, the magnet material and the optimal maximum stator flux density are used here.

Table 6.8

Comparison of optimal split ratio in machines with different slot/pole combinations and optimization conditions

	Stator loss limitation only	Rotor loss limitation only	Both stator and rotor limitations
Optimal split ratio	0.24	0.4	0.3
Maximum output torque	60.8mNm	70.3mNm	54.3mNm

## 6.2 Future Work

Based on the investigations in this PhD thesis, several future work can be suggested as follows:

Firstly, although the auxiliary slots with the optimal size and position can decrease the parasitic effects significantly without sacrificing the rotor mechanical strength. This method may decrease the stator mechanical strength, which may result in several problems, e.g. vibrations and stator tooth bending, etc. Consequently, the stator mechanical limitation in machines using this type of auxiliary slots needs to be investigated.

Secondly, the variation of magnet thickness also has influence on the rotor nature frequency as well as the sleeve thickness, which should be investigated in detail.

Thirdly, the thermal limitation used for the machine optimization is relatively simple, which may lead to certain error. Consequently, more accurate thermal model can be used for further improving the accuracy.

## References

- [ACA96] P. P. Acarnley, B. C. Mecrow, J. S. Burdess, J. N. Fawcett, J. G. Kelly, and P. G. Dickinson, "Design principles for a flywheel energy store for road vehicles," *IEEE Trans. Ind. Appl.*, vol. 32, no. 6, pp. 1402–1408, Nov./Dec. 1996.
- [AHO07] T. Aho, "Electromagnetic design of a solid rotor steel rotor motor for demanding operation environments," Ph.D. dissertation, Lappeenranta Univ. Technol., Lappeenranta, Finland, 2007.
- [ALA17] M. M. J. Al-ani, S. M. Barrans and J. Carter, "Electromagnetic and mechanical analysis of high speed SPM rotor with copper shield," 2017 *IEEE International Electric Machines and Drives Conference (IEMDC)*, Miami, FL, pp. 1-8, 2017.
- [ALA17a] F. B. Alam, B. Rezaeealam, and J. Faiz, "Unbalanced magnetic force analysis in eccentric surface permanent-magnet motors using an improved conformal mapping method", *IEEE Trans. Energy Convers.*, vol. 32, no. 1, pp. 146-154, 2017.
- [AUB12] J. Aubry, H. B. Ahmed, and B. Multon, "Sizing optimization methodology of a surface permanent magnet machine-converter system over a torque-speed operating profile: Application to a wave energy converter," *IEEE Trans. Ind. Electron.*, vol. 59, no. 5, pp. 2116–2125, May 2012.
- [AZA12] Z. Azar, Z. Q. Zhu, and G. Ombach, "Influence of electric loading and magnetic saturation on cogging torque, back-EMF and torque ripple of PM machines," *IEEE Trans. Magn.*, vol. 48, no. 10, pp. 2650-2658, Oct. 2012.
- [BAI09] C. Bailey, D. M. Saban and P. Guedes-Pinto, "Design of High-Speed Direct-Connected Permanent-Magnet Motors and Generators for the Petrochemical Industry," *IEEE Trans. Ind. Appl.*, vol. 45, no. 3, pp. 1159-1165, May-June 2009.

- [BEL13] Z. Belli and M. R. Mekideche, "Optimization of magnets segmentation for eddy current losses reduction in permanent magnets electrical machines," in *8th International Conference and Exhibition on Ecological Vehicles and Renewable Energies 2013 (EVER)*, pp. 1-7, 2013.
- [BEL14] Z. Belli, "Optimization of stator slots shape for eddy current losses reduction in permanent magnets synchronous machine," *2014 9th Int. Conf. on Ecological Vehicles and Renewable Energies (EVER)*, pp. 1-7, 2014.
- [BIA04] N. Bianchi, S. Bolognani, and F. Luise, "Potentials and limits of high speed PM motors," *IEEE Trans. Ind. Appl.*, vol. 40, no. 6, pp. 1570–1578, Nov. 2004.
- [BIA05] N. Bianchi, S. Bolognani, and F. Luise, "Analysis and design of a PM brushless motor for high speed operations," *IEEE Trans. Energy Convers.*, vol. 20, no. 3, pp. 629-637, 2005
- [BIA07] A. Binder and T. Schneider, "High-speed inverter-fed AC drives," in *Proc. ACEMP*, Sep. 2007, pp. 9-16.
- [BIA98] N. Bianchi, and S. Bolognani, "Magnetic models of saturated interior permanent magnet motors based on finite element analysis," in *IEEE IAS Annu. Meet.*, St. Louis, U.S., Oct. 1998, pp. 27-34.
- [BIC96] Bi, C., Liu, Z.J., Low, T.S, "Analysis of unbalanced-magnetic-pulls in hard disk drive spindle motors using a hybrid method", *IEEE Trans. Magn.*, 1996, 32, (5), pp. 4308–4310.
- [BIN06] A. Binder, T. Schneider, and M. R. Klohr, "Fixation of buried and surface-mounted magnets in high-speed permanent-magnet synchronous machines," *IEEE Trans. Ind. Appl.*, vol. 42, no. 4, pp. 1031–1037, Jul./Aug. 2006.
- [BIN07] A. Binder and T. Schneider, "High-speed inverter-fed AC drives," in *Proc. ACEMP*, pp. 9–16, Sep. 2007.

- [BOG03] A. Boglietti, A. Cavagnino, M. Lazzari, and M. Pastorelli, "Predicting iron losses in soft magnetic materials with arbitrary voltage supply: An engineering approach," *IEEE Trans. Magn.*, vol. 39, no. 2, pp. 981–989, Mar. 2003.
- [BOI14] J. Boisson, F. Louf, J. Ojeda, X. Mininger, and M. Gabsi, "Analytical approach for mechanical resonance frequencies of high-speed machines," *IEEE Trans. Ind. Electron.*, vol.61, no. 6, pp. 3081-3088, 2014.
- [BOR08] A. Borisavljevic, H. Polinder, and B. Ferreira, "Overcoming limits of high-speed PM machines," *18th Int. Conf. Electrical Machines (ICEM)*, pp. 1-6. 2008.
- [BOR10] A. Borisavljevic, H. Polinder, and J. A. Ferreira, "On the speed limits of permanent-magnet machines," *IEEE Trans. Ind. Electron.*, vol. 57, no. 1, pp. 220-227, 2010.
- [BOR10a] J. F. A. Borisavljevic, and H. Polinder, "Enclosure design for a highspeed permanent magnet rotor", *The 5th IET International Conference on Power Electronics, Machines and Drives (PEMD 2010)*, 2010.
- [BOR12] A. Borisavljevic, *Limits, Modeling and Design of High-Speed Permanent Magnet Machines*, 2013 edition. Berlin; New York: Springer, 2012.
- [BOR14] A. Borisavljevic, S. Jumayev, E. Lomonova, "Toroidally-wound permanent magnet machines in high-speed applications," *IEEE International Conferences on Electrical Machines (ICEM)*, pp. 2588-2593, 2014.
- [BUM06] J. R. Bumby, E. Spooner, and M. Jagiela, "Equivalent circuit analysis of solid-rotor induction machines with reference to turbocharger accelerator applications," *Proc. IEE Elect. Power Appl.*, vol. 153, no. 3, pp. 31–39, Jan. 2006.

- [BUM06a] J. R. Bumby, E. Spooner, and M. Jagiela, "Solid rotor induction machines for use in electrically-assisted turbochargers," in *Proc. Int. Conf. PEMD*, Apr. 2006, vol. 1, pp. 341–345.
- [CAP05] M. Caprio, V. Lelos, J. Herbst, and J. Upshaw, "Advanced induction motor end ring design features for high speed applications," in *Proc. IEMDC*, vol. 1, pp. 993–998, May, 2005.
- [CEN10] M. Centner and U. Schafer, "Optimized design of high-speed induction motors in respect of the electrical steel grade," *IEEE Trans. Ind. Electron.*, vol. 57, no. 1, pp. 288–295, Jan. 2010.
- [CHA10] S. H. Chai, B. Y. Lee, J. J. Lee, and J. P. Hong, "Reduction eddy current loss design and analysis of in-wheel type vehicle traction motor," *2010 Int. Conf. on Electrical Machines and Systems (ICEMS)*, pp. 1264–1267, 2010.
- [CHA12] N. Chayopitak, R. Pupadubsin, S. Karukanan, P. Champa, P. Somsiri, and Y. Thinphowong, "Design of a 1.5 kW high speed switched reluctance motor for electric supercharger with optimal performance assessment," in *Proc. 15th ICEMS*, pp. 1–5, Oct. 2012.
- [CHA15] S. Chaithongsuk, N. Takorabet, and S. Kreuawan, "Reduction of eddy-current losses in fractional-slot concentrated-winding synchronous PM motors," *IEEE Trans. on Magn.*, vol. 51, no. 3, 2015.
- [CHE07] A. Chebak, P. Viarouge, and J. Cros, "Analytical model for design of high-speed slotless brushless machines with SMC stators," in *Proc. IEEE IEMDC*, pp. 159–164, 2007.
- [CHE14] L. L. Chen, and C. S. Zhu, "Rotor strength analysis for high speed permanent magnet machines," *2014 17th Int. Conf. Electrical Machines and Systems (ICEMS)*, pp. 65–69, 2014.
- [CHE15] A. Chebak, P. Viarouge, and J. Cros, "Improved analytical model for predicting the magnetic field distribution in high-speed slotless permanent magnet machines," *IEEE Trans. Magn.*, vol. 51, no. 3, pp. 1–4, 2015.



- [CHO11] H. W. Cho, K. J. Ko, J. Y. Choi, H. J. Shin, and S. M. Jang, "Rotor natural frequency in high-speed permanent-magnet synchronous motor for turbo-compressor application," *IEEE Trans. Magn.*, vol. 47, no. 10, pp. 4258-4261, 2011.
- [CHU12] W. Q. Chu, Z. Q. Zhu, "Optimal split ratio and torque comparison of surface-mounted permanent magnet machines having inner or outer rotor", in *Proc.6th IET Int. Conf. on Power Electr., Machines and Drives*, Bristol, U.K, pp. 1-6, Mar, 2012.
- [CHU13] W. Q. Chu and Z. Q. Zhu, "Average torque separation in permanent magnet synchronous machines using frozen permeability," *IEEE Trans. Magn.*, vol. 49, no. 3, pp. 1202–1210, Mar. 2013
- [CRE10] L. Cremer and B. Petersson, *Structure-Borne Sound: Structural Vibrations and Sound Radiation at Audio Frequencies*. New York, NY, USA: Springer-Verlag, 2010.
- [CUI15] Chenjum Cui, Gang Liu, Kun Wang, and Xinda Song, "Sensorless Drive for High-Speed Brushless DC Motor Based on the Virtual Neutral Voltage," *IEEE Trans. Power Electro.*, vol. 30, no. 6, pp. 3275-3285, Jun. 2015.
- [DAJ12] G. Dajaku, and D. Gerling, "Low costs and high-efficiency electric machines." *2012 2nd Int. Conf. Electric Drives Production Conference (EDPC)*, pp. 1 – 7, 2012.
- [DAJ12a] G. Dajaku, and D. Gerling, "Different novel methods for reduction of low space harmonics for the fractional slot concentrated windings." *2012 15th Int. Conf. Electrical Machines and Systems (ICEMS)*, pp.1 – 6, 2012.
- [DAJ13] G. Dajaku, and D. Gerling, "Different novel electric machine designs for automotive applications", *2013 World Electric Vehicle Symposium and Exhibition (EVS27)*, pp. 1 – 7, 2013.

- [DAJ14] G. Dajaku, and D. Gerling, "Analysis of different PM machines with concentrated windings and flux barriers in stator core", *2014 Int. Conf. Electrical Machines (ICEM)*, pp. 375 – 384, 2014.
- [DAM03] D. Kowal, P. Sergeant, L. Dupre, and L. Vandenbossche, "The effect of the electrical steel properties on the temperature distribution in direct-drive PM synchronous generators for 5 MW wind turbines," *IEEE Trans. Magn.*, vol. 49, no. 10, pp. 5371-5377, 2003.
- [DAN08] J. B. Danilevich, I. Y. Kruchinina, V. N. Antipov, Y. P. Khozikov, and A. Ivanova, "Some problems of the high-speed permanent magnet miniturbogenerators development," in *Conf. Rec. 18th IEEE ICEM*, pp. 1–4, 2008.
- [DON13] J. Dang, S. Haghbin, Y. Du, C. Bednar, H. Liles, J. Restrepo, J. Mayor, R. Harley, and T. Habetler, "Electromagnetic design considerations for a 50,000 rpm 1kw Switched Reluctance Machine using a flux bridge," in *Electric Machines Drives Conference (IEMDC)*, pp. 325–331, May 2013.
- [DON14] J. Dong et al., "Electromagnetic and thermal analysis of open-circuit air cooled high-speed permanent magnet machines with gramme ring windings," *IEEE Trans. Magn.*, vol. 50, no. 11, pp. 1–4, Nov. 2014.
- [DON14] J. Dong, Y. Huang, L. Jin, B. Guo, H. Lin, J. Dong, M. Chen, H. Yang, "Electromagnetic and thermal analysis of opencircuit air cooled high-speed permanent magnet machines with gramme ring windings," *IEEE Trans. Magn.*, vol. 50, no. 11, Art. ID 8104004, Nov. 2014.
- [DON16] J. Dong, Y. Huang, L. Jin, and H. Lin, "Comparative study of surface mounted and interior permanent-magnet motors for high-speed applications," *IEEE Trans. Appl. Supercond.*, vol. 26, no. 4, pp. 1–4, Jun. 2016.
- [DON16a] M. S. Donea and D. Gerling, "Design and calculation of a 300 kW high-speed PM motor for aircraft application," *2016 International*

*Symposium on Power Electronics, Electrical Drives, Automation and Motion (SPEEDAM)*, Anacapri, pp. 1-6, 2016.

- [DON16b] Dong, Y. K. Huang, L. Jin, B. C. Guo, H. Y. Lin, J. Y. Dong, M. Cheng and H. Yang, "Electromagnetic and thermal analysis of open-circuit air cooled high-speed permanent magnet machines with gramme ring windings," *IEEE Trans. Magn.*, vol. 50, no. 11, pp. 1–4, Nov. 2014.
- [DZI16] A. Dziechciarz, C. Oprea, C. Martis, "Multi-physics design of synchronous reluctance machine for high speed applications", *IECON 2016 – 42nd Annual Conference of the IEEE Industrial Electronics Society*, pp. 1704-1709, 2016
- [EDE01] J. D. Ede, Z. Q. Zhu, and D. Howe, "Optimal split ratio for high-speed permanent magnet brushless DC motors", *International Conference on Electrical Machines and Systems (ICEMS)*, vol. 2, pp. 909-912, 2001.
- [EDE02] J. Ede, Z. Zhu, and D. Howe, "Rotor resonances of high-speed permanent-magnet brushless machines," *IEEE Trans. Ind. Appl.*, vol. 38, no. 6, pp. 1542–1548, Nov. 2002.
- [ELR10] A. M. El-Refai, "Fractional-slot concentrated-windings synchronous permanent magnet machines: Opportunities and challenges," *IEEE Trans. Ind. Electron.*, vol. 57, no. 1, pp. 107–121, Jan. 2010.
- [EWA09] J. Ewanchuk, J. Salmon, and A. Knight, "Performance of a high-speed motor drive system using a novel multilevel inverter topology," *IEEE Trans. Ind. Appl.*, vol. 45, no. 5, pp. 1706–1714, Sep./Oct. 2009.
- [FAN16] X. G. Fan, R. H. Qu, B. Zhang, J. Li, and D. W. Li, "Split ratio optimization of high-speed permanent magnet synchronous machines based on thermal resistance network," *Int. Conf. on Electr. Machines*, pp. 2059-2065, Sept. 2016.
- [FAN19] H. Y. Fang, D. W. Li, R. H. Qu, J. Li, C. Wang, and B. Song, "Rotor design and eddy-current loss suppression for high-speed machines with a solid PM rotor," *IEEE Trans. Ind. Appl.*, vol.55, no.1, pp. 448-457, 2019.

- [FER94] Ferreira, J.A. "Improved analytical modeling of conductive losses in magnetic components" *IEEE Trans. on Power Electron.*, vol.9, no.1, pp.127,131, Jan 1994.
- [FER17] N. Fernando, G. Vakil, P. Arumugam, E. Amankwah, C. Gerada, and S. Bozhko, "Impact of soft magnetic material on design of highspeed permanent-magnet machines," *IEEE Trans. Ind. Electron.*, vol. 64, no. 3, pp. 2415–2423, March 2017.
- [FOD14] D. Fodorean, "Study of a high-speed motorization with improved performances dedicated for an electric vehicle," *IEEE Trans. Magn.*, vol. 50, no. 2, pp. 921–924, Feb. 2014.
- [GAL15] S. J. Galioto, P. B. Reddy, A. M. EL-Refaie and J. P. Alexander, "Effect of magnet types on performance of high-speed spoke interior-permanent-magnet machines designed for traction applications," *IEEE Trans. on Ind. Appl.*, vol. 51, no. 3, pp. 2148-2160, May-June 2015.
- [GAV02] H. Gavrilă and V. Ionita, "Crystalline and amorphous soft magnetic materials and their applications—Status of art and challenges," *J. Optoelectron. Adv. Mater.*, vol. 4, no. 2, pp. 173–192, Jun. 2002.
- [GER11] D. Gerada, A. Mebarki, N. L. Brown, K. J. Bradley, and C. Gerada, "Design aspects of high-speed high-power-density laminated-rotor induction machines," *IEEE Trans. Ind. Electron.*, vol. 58, no. 9, pp. 4039–4047, Sep. 2011.
- [GER12] D. Gerada, A. Mebarki, N. L. Brown, H. Zhang, and C. Gerada, "Design, modelling and testing of a high speed induction machine drive," in *Proc. ECCE*, Sep. 2012, pp. 4649–4655.
- [GER14] D. Gerada, A. Mebarki, N. L. Brown, C. Gerada, A. Cavagnino, and A. Boglietti, "High-speed electrical machines: technologies, trends, and developments," *IEEE Trans. Ind. Electron.*, vol. 61, no. 6, pp. 2041-2059, 2014.

- [GIE12] J. F. Gieras and J. Saari, "Performance calculation for a high-speed solid-rotor induction motor," *IEEE Trans. Ind. Electron.*, vol. 59, no. 6, pp. 2689–2700, Jun. 2012.
- [GIE14] J. F. Gieras, "Design of permanent magnet brushless motors for high speed applications," *2014 17th Int. Conf. Electrical Machines and Systems (ICEMS)*, pp. 1-16, 2014.
- [GIL16] A. Gilson, F. Dubas, D. Depernet, and C. Espanet, "Comparison of high-speed PM machine topologies for electrically-assisted turbocharger applications," *2016 19th International Conference on Electrical Machines and Systems (ICEMS)*, Art. ID 16650645, 2016.
- [GOL03] L. Goldstein, B. Hedman, D. Knowles, S. I. Freedman, R. Woods, and T. Schweizer, "Gas-fired distributed energy resource technology characterizations," Nat. Renewable Energy Lab., Golden, CO, USA, Tech. Rep. NREL/TP-620-34783, Nov. 2003.
- [GON14] D. A. Gonzalez, D. M. Saban, "Study of the copper losses in a high-speed permanent-magnet machine with form-wound windings," *IEEE Trans. Ind. Electron.*, vol. 61, no. 6, pp. 3038-3045, 2014.
- [GON17] C. Gong, and T. Habetler, "A novel rotor design for ultra-high speed switched reluctance machines over 1 million rpm," *IEMDC, 2017*.
- [GUO03] Y. G. Guo, J. G. Zhu, P. A. Watterson, and W. Wu, "Comparative study of 3-D flux electrical machines with soft magnetic composite cores," *IEEE Trans. Ind. Appl.*, vol. 29, pp. 1696–1703, Nov./Dec. 2003.
- [HUA10] W. Y. Huang, A. Bettayeb, R. Kaczmarek, and J. C. Vannier, "Optimization of magnet segmentation for reduction of eddy current losses in permanent synchronous machine," *IEEE Trans. Energy Convers.*, vol. 25, no. 2, pp. 381-387, 2010.
- [HUA16] Z. Y. Huang and J. C. Fang, "Multiphysics design and optimization of high speed permanent-magnet electrical machines for air blower applications," *IEEE Trans. Ind. Electron.*, vol. 63, no. 5, pp. 2766–2774, May 2016.

- [HUA17] H. Hua, Z. Q. Zhu, C. Wang, M. Zheng, Z. Z. Wu, D. Wu, and X. Ge, "Partitioned stator machines with NdFeB and Ferrite magnets," *IEEE Trans. Ind. Appl.*, vol. 53, no. 3, pp. 1870-1882, May 2017.
- [HUP04] J. Hupponen, "High-speed solid-rotor induction machine—Electromagnetic calculation and design," Ph.D. dissertation, Lappeenranta Univ. Technol., Lappeenranta, Finland, 2004.
- [IKE90] M. Ikeda, S. Sakabe, and K. Higashi, "Experimental study of high speed induction motor varying rotor core construction," *IEEE Trans. Energy Convers.*, vol. 5, no. 1, pp. 98–103, Mar. 1990.
- [ION07] D. M. Ionel, M. Popescu, M. I. McGilp, T. J. E. Miller, S. J. Dellinger, and R. J. Heideman, "Computation of core losses in electrical machines using improved models for laminated steel," *IEEE Trans. Ind. Appl.*, vol. 43, no. 6, pp. 1554–1564, Nov. 2007.
- [ISH05] D. Ishak, Z. Q. Zhu, and D. Howe, "Eddy-current loss in the rotor magnets of permanent-magnet brushless machines having a fractional number of slots per pole," *IEEE Trans. on Magn.*, vol. 41, no. 9, pp. 2462–2469, Sept 2005.
- [IWA09] S. Iwasaki, R. Deodhar, Y. Liu, A. Pride, Z. Q. Zhu, and J. Bremner, "Influence of PWM on the proximity loss in PM brushless AC machines," *IEEE Trans. Ind. Appl.*, vol. 45, no. 3, pp. 1359–1367, 2009.
- [JAN01] Seok-Myeong Jang, Sang-Sub Jeong, Dong-Wan Ryu, Sang-Kyu Choi, "Design and analysis of high speed slotless PM machine with Halbach array", *IEEE Trans. on Magn.*, vol.37, no.4, pp.2827-2830, Jul. 2001.
- [JAN07] S.-M. Jang, H.-W. Cho, and S.-K. Choi, "Design and analysis of a highspeed brushless DC motor for centrifugal compressor," *IEEE Trans. Magn.*, vol. 43, no. 6, pp. 2573–2575, Jun. 2007.
- [JAN10] Seok-Myeong Jang, Ji-Hwan Choi, Kyoung-Jin Ko, Dae-Joon You, Jeong-Phil Lee, "Characteristic analysis of slotless synchronous motor/generator with Halbach array PM for 30kW flywheel energy

storage system," *2010 International Conference on Electrical Machines and Systems (ICEMS)*, pp.1197-1200, 10-13 Oct. 2010.

- [JAN11] X. Jannot, J.-C. Vannier, C. Marchand, M. Gabsi, J. Saint-Michel, and D. Sadarnac, "Multiphysic modeling of a high-speed interior permanentmagnet synchronous machine for a multiobjective optimal design," *IEEE Trans. Energy Convers.*, vol. 26, no. 2, pp. 457–467, Jun. 2011.
- [JAN91] G. Jang and D. Lieu, "The effect of magnet geometry on electric motor vibration," *IEEE Trans. Magn.*, vol. 27, pp. 5202–5204, Nov. 1991.
- [JAN93] G. Jang and D. Lieu, "Vibration reduction in electric machine by interlocking of the magnets," *IEEE Trans. Magn.*, vol. 29, pp. 1423–1426, Mar. 1993.
- [JAS12] M. Y. Jason, P. H. Mellor, R. Wrobel, J. D. Booker, and S. G. Burrow, "Analysis of semipermeable containment sleeve technology for high-speed permanent magnet machines," *IEEE Trans. Energy Convers.*, vol. 27, no. 3, pp. 646-653, 2012.
- [JIA04] G. Jiao and C. D. Rahn, "Field weakening for radial force reduction in brushless permanent-magnet DC motors," *IEEE Trans. Magn.*, vol. 40, no. 5, pp. 3286–3292, Sep. 2004.
- [JUM13a] S. Jumayev, A. Borisavljevic, K. Boynov, J. Pyrhonen, and E. Lomonova, "Comparative analysis of inductances of air-gap windings," in *Electromagnetic Fields in Mechatronics, XVI Int. Symp. on (ISEF 2013)*, Sep 2013.
- [JUM14] S. Jumayev, A. Borisavljevic, K. Boynov, E. A. Lomonova, and J. Pyrhonen, "Analysis of rotor eddy current losses in slotless high-speed permanent magnet machines," in *Proc. 16th Eur. Conf. Power Electron. Appl. (EPE-ECCE Europe)*, Aug. 2014, pp. 1–10.
- [JUM15] S. Jumayev, M. Merdzan, K. O. Boynov, J. J. H. Paulides, J. Pyrhonen, and E. A. Lomonova, "The effect of PWM on rotor eddy-current losses

- in high-speed permanent magnet machines,” *IEEE Trans. Magn.*, vol. 51, no. 11, Nov. 2015, Art. ID 8109204.
- [JUN15] H. W. Jun, J. Lee, H. W. Lee and W. H. Kim, "Study on the optimal rotor retaining sleeve structure for the reduction of eddy-current loss in high-speed SPMSM," *IEEE Trans. Magn.*, vol. 51, no. 3, pp. 1-4, March 2015.
- [KAN09] G.-H. Kang, J. Hur, W.-B. Kim, and B.-K. Lee, “The shape design of interior type permanent magnet BLDC motor for minimization of mechanical vibration,” in *Proc. Energy Convers. Congr. Expo.*, Sep. 2009, pp. 2409–2414.
- [KOL13] R. Kolano et al., “Amorphous soft magnetic materials for the stator of a novel high-speed PMSBLDC motor,” *IEEE Trans. Magn.*, vol. 49, no. 4, pp. 1367–1371, Apr. 2013.
- [KRO11] J. Krotzsch, T. Ley, and B. Piepenbreier, “Reduction of torque and radial force fluctuation in permanent magnet synchronous motors by means of multi-objective optimization,” in *Proc. 1st Int. Electr. Drives Prod. Conf. (EDPC)*, Sep. 2011, pp. 40–48.
- [KUN10] J. Kunz, S. Cheng, Y. Duan, J. Mayor, R. Harley, and T. Habetler, “Design of a 750,000 rpm switched reluctance motor for micro machining,” in *IEEE Energy Conversion Congress and Exposition*, Atlanta, Georgia, USA, pp. 3986–3992, Sep. 2010.
- [LAH00] J. Lahteenmaki and V. Soitu, “Comparison of solid steel rotors with a copper coating or with a copper cage for a 60kW 60 000 RPM compressor,” in *Proc. ICEM*, vol. 2, pp. 623–626, Aug. 2000.
- [LAH02] J. Lähteenmäki, “Design and voltage supply of high-speed induction machines,” Ph.D. dissertation, Dept. Electr. Commun. Eng., Helsinki Univ. Technol., Espoo, Finland, 2002.
- [LAT09] R. Lateb, J. Enon, and L. Durantay, “High speed, high power electrical induction motor technologies for integrated compressors,” in *Proc. ICEMS*, pp. 1438–1442, Nov. 2009.



- [LEC04] J.-P. Lecointe, R. Romary, J.-F. Brudny, and T. Czaplá, “Five methods of stator natural frequency determination: Case of induction and switched reluctance machines,” *Mech. Syst. Signal Process.*, vol. 18, no. 5, pp. 1133–1159, Sep. 2004.
- [LEI11] X. Lei, W. Liao, and L. Zhang, “Design of a two-spindle CNC machine tool applications for dental restoration,” in *Proc. 3rd IEEE Int. Conf. Meas. Technol. Mechatron. Autom.*, pp. 934–937, 2011.
- [LIG14] G. J. Li, Z. Q. Zhu, W. Chu, M. Foster, and D. Stone, “Influence of flux gaps on electromagnetic performance of novel modular PM machines” *IEEE Trans. Energy Convers.*, vol. 29, no. 3, pp. 716-726, 2014.
- [LIG14a] G. J. Li, Z. Q. Zhu, W. Chu, M. Foster, and D. Stone, “Comparative studies of modular and unequal tooth PM machines either with or without tooth tips,” *IEEE Trans. Magn.*, vol. 50, no. 7, pp. 1-10, 2014.
- [LIJ07] J. T. Li, Z. J. Liu, and L. H. A. Nay: “Effect of radial magnetic forces in permanent magnet motors with rotor eccentricity”, *IEEE Trans. Magn.*, vol. 43, no. 6, pp. 2525–2527, 2007.
- [LIN04] D. Lin, P. Zhou, W. N. Fu, Z. Badics, and Z. J. Cendes, “A dynamic core loss model for soft ferromagnetic and power ferrite materials in transient finite element analysis,” *IEEE Trans. Magn.*, vol. 40, no. 2, pp. 1318–1321, Mar. 2004.
- [LIQ11] Q. Li, “A novel analytical method of calculating of stator natural frequency for axial flux permanent magnet machines,” in *Proc. ICEMS*, pp. 1–3, Aug. 2011.
- [LIQ15] Q. W. Li, M. F. Dou, C. Fang, “Analytical determination of optimal split ratio for high speed permanent magnet brushless motors,” *Int. Conf. on Electrical Machines and Systems (ICEMS)*, Oct. 2015.
- [LIY16] Y. Li, D. Han, N. Altintas, and B. Sarlioglu, “Design of high-speed toroidal winding surface PM machine with SiC-based inverters,” in *XXII International Conference on Electrical Machines (ICEM)*, pp. 1559–1565, 2016.

- [LIY17] Y. X. Li, Q. F. Lu, and Z. Q. Zhu, “Unbalanced magnetic force prediction in permanent magnet machines with rotor eccentricity by improved superposition method,” *IET Electric Power Applications*, vol. 11, no. 6, 2017.
- [LIY17a] Y. X. Li, and Z. Q. Zhu, “Cogging torque and unbalanced magnetic force prediction in PM machines with axial-varying eccentric by superposition method,” *IEEE Trans. Magn.*, vol. 53, no. 11, 2017.
- [LOV04] E. Lovelace, T. Jahns, T. Keim, and J. Lang, “Mechanical design considerations for conventionally laminated, high-speed, interior PM synchronous machine rotors,” *IEEE Trans. Ind. Appl.*, vol. 40, no. 3, pp. 806–812, May/Jun. 2004.
- [MAE95] A. Maeda and H. Tomita, “Power and speed limitations in high speed electrical machines,” in *Proc. IPEC-Yokohama*, pp. 1321–1326, 1995.
- [MAJ17] J. Ma, Z. Q. Zhu, and L. J. Wu, “Influence of slot/pole combination and magnet thickness on unbalanced magnetic force in PM machines with different rotor eccentricities and magnetizations,” *International Conference on Electrical Machines and Systems (ICEMS)*, 2017.
- [MAJ17a] J. Ma, and Z. Q. Zhu, “Effect of magnet thickness on electromagnetic performance of high speed permanent magnet machines,” *International Conference on Electrical Machines and Drives (IEMDC)*, 2017.
- [MAJ17b] J. Ma, and Z. Q. Zhu, “Unbalanced magnetic force mitigation in 3-slot/2-pole permanent magnet machines by inserting auxiliary slots,” *International Conference on Electrical Machines and Drives (IEMDC)*, 2017.
- [MAJ17c] J. Ma, and Z. Q. Zhu, “Magnet eddy current loss reduction in a 3-slot/2-pole permanent magnet machine,” *Int. Conf. on Electric. Machines and Drives (IEMDC)*, pp. 1-8, 2017.
- [MAJ18] J. Ma and Z. Q. Zhu, “Mitigation of unbalanced magnetic force in a PM machine with asymmetric winding by inserting auxiliary slots,” *IEEE Trans. Ind. Appl.*, vol. 54, no. 5, pp. 4133-4146, 2018.

- [MAJ18a] J. Ma and Z. Q. Zhu, "Magnet eddy current loss reduction in permanent magnet machines," *IEEE Trans. Ind. Appl.*, early access, pp. 1-1, 2018.
- [MAR14] A. N. Marashi, K. Abbaszadeh, and F. R. Alam, "Analysis and reduction of magnet eddy current losses in surface mounted permanent magnet machines", *IEEE 22nd Iranian Conference on Electrical Engineering (ICEE 2014)*, pp. 782-786, 20-22 May 2014.
- [MEL91] P. H. Mellor, D. Roberts, D. R. Turner, "Lumped parameter thermal model for electrical machines of TEFC design," *IEE Proceedings B - Electric Power Applications*, vol. 138, no. 5, pp. 205 – 218, Sept. 1991.
- [MER15] M. Merdzan, J. J. H. Paulides, and E. A. Lomonova, "Comparative analysis of rotor losses in high-speed permanent magnet machines with different winding configurations considering the influence of the inverter PWM," in *Proc. 10th IEEE Int. Conf. Ecol. Vehicles Renew. Energies (EVER)*, Monte Carlo, Monaco, Mar./Apr., pp. 1–8, 2008.
- [MEY94] T. Meydan, "Application of amorphous materials to sensors," *J. Magn. Mater.*, vol. 133, nos. 1–3, pp. 525–532, May 1994.
- [MIR10] M. Mirzaei, A. Binder, and C. Deak, "3D analysis of circumferential and axial segmentation effect on magnet eddy current losses in permanent magnet synchronous machines with concentrated windings," *19th Int. Conf. on Electrical Machines (ICEM)*, Rome, Italy, Sep. 6–8, 2010.
- [MOR00] L. Morel, H. Fayard, H. Vives Fos, A. Galindo, and G. Abba, "Study of ultra-high speed switched reluctance motor drive," in *IEEE Industry Applications Conference*, Rome, Italy, pp. 87–92, Oct. 2000.
- [MYE00] J. Seok-Myeong, J. Sang-Sub, R. Dong-Wan and C. Sang-Kyu, "Comparison of three types of PM brushless machines for an electro-mechanical battery," *IEEE Trans. Magn.*, vol. 36, no. 5, pp. 3540-3543, 2000.

- [MYE01] J. Seok-Myeong, J. Sang-Sub, R. Dong-Wan and C. Sang-Kyu, "Design and analysis of high speed slotless PM machine with Halbach array," *IEEE Trans. Magn.*, vol. 37, no .4, pp. 2827-2830, 2001.
- [NAG06] A. S. Nagorny, R. H. Jansen, and D. M. Kankam, "Experimental performance evaluation of a high speed permanent magnet synchronous motor and drive for a flywheel application at different frequencies," in *Conf. Rec. 17th IEEE ICEM*, 2006, pp. 1–6.
- [NAR15] M. Di Nardo, M. Galea, C. Gerada, M. Palmieri, and F. Cupertino, "Multi-physics optimization strategies for high speed synchronous reluctance machines," in *Proc. IEEE Energy Convers. Congr. Expo.*, pp. 2813–2820, 2015.
- [NAR18] M. D. Nardo, G. L. Calzo, M. Galea, and C. Gerada, "Design optimization of a high-speed synchronous reluctance machine," *IEEE Trans. Ind . Appl.*, vol. 54, no. 1, pp. 233-243, Jan/Feb. 2018.
- [PAL59] A. Palmgren, *Ball and Roller Bearing Engineering*. Philadelphia, PA, USA: SKF Industries Inc., 1959
- [PAN06] Y. Pang, Z. Q. Zhu, and D. Howe, "Analytical determination of optimal split ratio for permanent magnet brushless motors", *IEE Proceedings Electric Power Appl.*, vol. 153, no. 1, pp. 7-13, 2006.
- [PAN14] Y. Pang, and Z. Q. Zhu, "Reduction of unbalanced magnetic force in 2-pole 3-slot permanent magnet machine," *7th IET Int. Conf. Power Electronics, Machines and Drives (PEMD 2014)*, 2014, pp. 1-6.
- [PER79] M. P. Perry, "Multiple layer series connected winding design for minimum losses," *IEEE Trans. Power App. Syst.*, vol. PAS-98, pp. 116–123, Jan./Feb. 1979.
- [PET10] D. S. Petrovic, "Non-oriented electrical steel sheets," *Mater. Technol.*, vol. 44, no. 6, pp. 317–325, 2010.
- [PFI10] P. Pfister and Y. Perriard, "Very-high-speed slotless permanent-magnet motors: Analytical modeling, optimization, design, and torque

- measurement methods," *IEEE Trans. Ind. Electron.*, vol. 57, no. 1, pp. 296–303, Jan. 2010.
- [PHY12] H. N. Phyu, and B. Chao, "Effect of magnetization on high-speed permanent magnet synchronous motor design," *2012 15th Int. Conf. Electrical Machines and Systems (ICEMS)*, pp. 1-6, 2012.
- [POW05] D. J. Powell, G. W. Jewell, S. D. Calverley, and D. Howe, "Iron loss in a modular rotor switched reluctance machine for the "more-electric" aero-engine," *IEEE Trans. Magn.*, vol. 41, no. 10, pp. 3934–3936, Oct. 2005.
- [PRI16] Dany Prieto, Philippe Dessante, Jean-Claude Vannier, Benjamin Dagusé, Xavier Jannot, Jacques Saint-Michel, "Multi-physic analytical model for a saturated permanent magnet assisted synchronous reluctance motor", *Electric Power Applications IET*, vol. 10, no. 5, pp. 356-367, 2016.
- [PYI10] P. D. Pfister and Y. Perriard, "Very high speed slotless permanent magnet motors: Analytical modeling, optimization, design, and torque measurement methods," *IEEE Trans. on Electron.*, vol. 57, no. 1, pp. 296–303, 2010.
- [PYR10] J. Pyrhonen, J. Nerg, P. Kurronen, and U. Lauber, "High-speed, high output, solid-rotor induction motor technology for gas compression," *IEEE Trans. Ind. Electron.*, vol. 57, no. 1, pp. 272–280, Jan. 2010.
- [RAH04] M. A. Rahman, A. Chiba, and T. Fukao, "Super high speed electrical machines—Summary," in *Proc. IEEE Power Eng. Soc. Gen. Meeting*, vol. 2, pp. 1272–1275, Jun. 6–10, 2004.
- [RAO14] J. Rao, R. Qu, J. Ma and W. Xu, "Investigate the influence of magnetic bridge design on mechanical strength and electromagnetic characteristics in high speed IPM machines," *2014 17th International Conference on Electrical Machines and Systems (ICEMS)*, Hangzhou, pp. 22-27, 2014.

- [RED08] Reddy, P.B., Z.Q. Zhu, S.H. Han, and T.M. Jahns, "Strand-level Proximity Losses in PM Machines Designed for High-Speed Operation", in *Proc. of 38th Intl Conf. on Elec. Mach.*, Sept 2008.
- [REF14] A. M. El-Refaie, J. P Alexander, S. Galioto, P. Reddy, H. Hum-Kang, P. de Bock, and S. Xiochun, "Advanced high power-density interior permanent magnet motor for traction applications," *IEEE Trans. Ind. Appl.*, vol. 50, no. 5, pp. 3253–3248, Sep/Oct. 2014.
- [REI13] Thomas Reichert, Thomas Nussbaumer, Johann W. Kolar, "Split ratio optimization for high-torque PM motors considering global and local thermal limitations", *IEEE Trans. Energy Convers.*, vol. 28, no. 3, pp. 493-501, 2013.
- [SAA94] J. Saari and A. Arkkio, "Losses in high speed asynchronous motors," *Int. Conf. Electrical Machines. (ICEM)*, vol. 3, pp. 704–708, Sep. 1994.
- [SCH14] A. Schoppa, and P. Delarbre, "Soft magnetic powder composites and potential applications in modern electrical machines and devices," *IEEE Trans. Magn.*, vol. 50, pp. 1613-1616, 2014
- [SHA96] N. D. Sharma, R. Anbarasu, J. Nataraj, A. Y. Dangore, and B. Bhattacharjee, "Experimental investigations on high speed solid and composite rotor induction motor," in *Proc. Int. Conf. Power Electron., Drives Energy Syst. Ind. Growth*, vol. 2, pp. 913–919, Jan. 1996.
- [SHE11] Y. Shen, Z. Q. Zhu, and L. J. Wu, "Analytical determination of optimal split ratio for overlapping and none-overlapping winding external rotor PM brushless machines", *IEEE International Electric Machine & Drive Conference*, pp. 41-46, 2011.
- [SHE13] J. Shen, H. Hao, M. Jin, and C. Yuan, "Reduction of rotor eddy current loss in high speed PM brushless machine by grooving retaining sleeve," *IEEE Trans. Magn.*, vol. 49, no. 7, pp. 3973–3976, Jul. 2013.
- [SHO16] S. Kasai, M. Namikawa, and T. Hiratani, "Recent progress of high silicon electrical steel in JFE steel," JFE Steel Res. Dept., Tokyo, Japan, Tech. Rep., no.4, 2016.

- [SOO00] W. L. Soong, G. B. Kliman, R. N. Johnson, R. A. White, and J. E. Miller, "Novel high-speed induction motor for a commercial centrifugal compressor," *IEEE Trans. Ind. Appl.*, vol. 36, no. 3, pp. 706–713, May/Jun. 2000.
- [SPA15] S. Spas, G. Dajaku, and D. Gerling. "Eddy current loss reduction in PM traction machines using two-tooth winding," *Vehicle Power and Propulsion Conference (VPPC)*, pp. 1-6, 2015.
- [TAK94] I. Takahashi, T. Koganezawa, G. Su, and K. Ohyama, "A super high speed PM motor drive system by a quasi-current source inverter," *IEEE Trans. Ind. Appl.*, vol. 30, no. 3, pp. 683–690, 1994.
- [TEN14] A. Tenconi, S. Vaschetto, and A. Vigliani, "Electrical machines for high-speed applications: design considerations and tradeoffs," *IEEE Trans. Ind. Electron.*, vol. 61, no. 6, pp.3022-3029, Jun. 2014.
- [TIP87] Hesmondhalgh, D.E., Tipping, D., and Amrani, M.: "Design and construction of a high-speed high-performance direct-drive handpiece", *IEE Proc. B Electr. Power Appl.*, 134, (6), pp. 286–296. 1987.
- [TOD04] H. Toda, Z. Xia, J. Wang, K. Atallah, and D. Howe, "Rotor eddy current loss in permanent magnet brushless machines," *IEEE Trans. on Magn.*, vol. 40, no. 4, pp. 2104–2106, 2004.
- [UZH14] N. Uzhegov, N. Uzhegov, J. Nerg, and J. Pyrhönen, "Design of 6-slot 2-pole high-speed permanent magnet synchronous machines with tooth-coil windings," in *Proc. Electrical Machines (ICEM)*, 2014.
- [VAN97] J. L. F. Van der Veen, L. J. J. Offringa and A. J. A. Vandenput, "Minimising rotor losses in high-speed high-power permanent magnet synchronous generators with rectifier load," *IEE Proceedings Electric Power Applications*, vol. 144, no. 5, pp. 331-337, Sep., 1997.
- [VRA68] J. Vrancik, "Prediction of windage power loss in alternators," NASA Technical Note, 1968.
- [WAN07] T. Wang, F. Wang, H. Bai, and J. Xing, "Optimization design of rotor structure for high speed permanent magnet machines," in *Proc. Int.*

- Conf. Elect. Mach. Syst.*, Seoul, Korea, Oct. 8–11, pp. 1438–1442, 2007.
- [WAN09] F. Wang, D. Zhang, J. Xing, and Y. Xu, “Study on air friction loss of high speed PM machine,” in *Proc. IEEE Int. Conf. Ind. Technol.*, pp. 1–4, 2009.
- [WAN10] Jiabin Wang, K. Atallah, R. Chin, W. M. Arshad and H. Lendenmann, “Rotor eddy-current loss in permanent-magnet brushless AC machines,” *IEEE Trans. on Magn.*, vol. 46, no. 7, pp. 2701–2707, 2010.
- [WAN14] K. Wang, Z. Q. Zhu, and G. Ombach, “Synthesis of high performance fractional-slot permanent-magnet machines with coil-pitch of two slot-pitches,” *IEEE Trans. Energy Convers.*, vol. 29, no. 3, pp. 758–770, May 2014.
- [WAN18] Y. Wang, J. H. Feng, S. Y. Guo, Y. F. Li, Z. C. Chen, Y. Wang, and Z. Q. Zhu, “Investigation of optimal split ratio for high-speed permanent magnet brushless machines,” *IEEE Trans. Magn.*, vol. 54, no. 11, 2018.
- [WIT11] P. Witczak, “Analytical method for calculation of eigenfrequencies and modes of stator cores in AC machines,” *Maszyny Elektryczne, Zeszyty problemowe*, no. 92, pp. 1–6, 2011.
- [WON08] S. H. Won, J. Choi, and J. Lee, “Windage loss reduction of high speed SRM using rotor magnetic saturation,” *IEEE Trans. on Magn.*, vol. 44, no. 11, pp. 4147–4150, Nov. 2008.
- [WUL09] L. J. Wu, Z. Q. Zhu, J. T. Chen, Z. P. Xia, and G. W. Jewell, “Optimal split ratio in fractional-slot interior permanent-magnet machines with non-overlapping windings,” *IEEE Trans. Magn.*, vol. 46, no. 5, pp. 1235–1242, 2009.
- [WUL10] L. J. Wu, Z. Q. Zhu, J. T. Chen, and Z. P. Xia, “An analytical model of unbalanced magnetic force in fractional-slot surface-mounted permanent magnet machines,” *IEEE Trans. Magn.*, vol. 46, no. 7, pp. 2686–2700, Jul. 2010.



- [WUL13] L. J. Wu, Z. Q. Zhu, M. L. M. Jamil, "Unbalanced magnetic force in permanent magnet machines having asymmetric windings and static/rotating eccentricities," *International Conference on Electrical Machines and Systems (ICEMS)*, 2013.
- [WUL16] L. J. Wu, Z. Q. Zhu, Y. Fang, and X. Huang, "Influence of magnet height on unbalanced magnetic force of surface-mounted permanent magnet machines," *13th IEEE. Int. Conf. Vehicle Power and Propulsion Conference (VPPC 2016)*, pp. 1-6, 2016.
- [WUL17] L. J. Wu, Z. Q. Zhu, Y. T. Fang, and X. Y. Huang, "Difference in unbalanced magnetic force of fractional-slot PM machines between internal and external rotor topologies," *CES Transactions on Electrical Machines and Systems*, vol. 1, no. 2, pp. 154-163, 2017.
- [XIA04] Z. P. Xia, Z. Q. Zhu, D. Howe, "Analytical magnetic field analysis of Halbach magnetized permanent magnet machines," *IEEE Trans. Magn.*, vol. 40, no. 4, pp. 1864-1872, 2004.
- [XIA16] Y. Xia, J. Li, Ronghai Qu, and Haiyang Fang, "Comparison of two rotor topologies for high-speed permanent magnet synchronous machines," *2016 XXII Int. Conf. Electrical Machines (ICEM)*, ID number: 16444223, 2016.
- [XUE12] S. S. Xue, H. P. Xu, and C. Fang, "The effect of stator slot and air gap length on high speed brushless PM motor," *2012 7th int. conf. Power Electronics and Motion Control Conference (IPEMC)*, pp. 281-285, 2012.
- [XUS17] S. Xu, X. Liu, and Y. Le, "Electromagnetic design of a highspeed solid cylindrical permanent-magnet motor equipped with active magnetic bearings," *IEEE Trans. Magn.*, vol. 53, no. 8, Art. No. 8203715, Apr. 2017.
- [YAM09] K. Yamazaki, M. Shina, Y. Kanou, M. Miwa, and J. Hagiwara, "Effect of eddy current loss reduction by segmentation of magnets in

- synchronous motors: Difference between interior and surface types," *IEEE Trans. on Magn.*, vol. 45, no. 10, pp.4756- 4959, 2009.
- [YAM62] Y. Yamada, "Torque resistance of a flow between rotating co-axial cylinders having axial flow," *Bulletin of Japan Society of Mechanical Engineers (JSME)*, vol. 5, no. 20, pp. 634-642. 1962.
- [YAN14] H. Yang and Y. Chen, "Influence of radial force harmonics with low mode number on electromagnetic vibration of PMSM," *IEEE Trans. Energy Convers.*, vol. 29, no. 1, pp. 38–45, Mar. 2014.
- [YUS06] S. Yu, R. Tang, "Electromagnetic and mechanical characterizations of noise and vibration in permanent magnet synchronous machines," *IEEE Trans. on Magn.*, vol.42, no.4, pp.1335-1338, 2006.
- [ZHA07] G. Zhang, F. Wang, and Y. Shen, "Reduction of rotor loss and cogging torque of high speed PM machine by stator teeth notching," in *Proc. Int. Conf. Elect. Mach. Syst. (ICEMS)*, Seoul, Korea, pp. 856–859, Oct. 2007.
- [ZHA15] J. Zhang et al., "Evaluation of applying retaining shield rotor for highspeed interior permanent magnet motors," *IEEE Trans. Magn.*, vol. 51, no. 3, Art. ID 8100404, Mar. 2015.
- [ZHA15a] Y. Zhang, Q. Li, Y. Wang, Z. Ren, J. Xia, and D. Xie, "Anisotropic magnetostriction of nonoriented silicon steel sheet and its frequency dependence," *IEEE Trans. Magn.*, vol. 51, no. 11, pp. 1–4, Nov. 2015.
- [ZHA15b] F. G. Zhang, G. H. Du, T. Y. Wang, G. W. Liu, and W. P. Cao, "Rotor retaining sleeve design for a 1.12-MW high-speed PM machine," *IEEE Trans. Ind. Appl.*, vol. 51, no. 5, pp. 3675–3685, Sep./ Oct. 2015.
- [ZHU01] Z. Q. Zhu, K. B. Ng, N. Schofield, and D. Howe, "Analytical prediction of rotor eddy current loss in brushless machines equipped with surfacemounted permanent magnets. i. magnetostatic field model," in *Proceedings of the Fifth International Conference on Electrical Machines and Systems, 2001. ICEMS 2001.*, vol. 2, pp. 806–809 vol.2, Aug 2001.

- [ZHU01a] Z. Q. Zhu, K. B. Ng, N. Schofield, and D. Howe, “Analytical prediction of rotor eddy current loss in brushless machines equipped with surface-mounted permanent magnets. ii. accounting for eddy current reaction field,” in *Proceedings of the Fifth International Conference on Electrical Machines and Systems, 2001. ICEMS 2001.*, vol. 2, pp. 810–813 vol.2, Aug 2001.
- [ZHU04] Z. Zhu, K. Ng, N. Schofield, and D. Howe, “Improved analytical modelling of rotor eddy current loss in brushless machines equipped with surface-mounted permanent magnets,” *Electric Power Applications, IEE Proceedings*, vol. 151, no. 6, pp. 641–650, Nov. 2004.
- [ZHU06] Z. Q. Zhu, S. Ruangsinchaiwanich, and D. Howe, “Synthesis of cogging torque from a single stator slot in permanent magnet machines,” *IEEE Trans. Ind. Appl.*, vol. 42, no. 3, pp. 650–657, 2006.
- [ZHU07] Z. Q. Zhu, D. Ishak, D. Howe, and J. T. Chen, “Unbalanced magnetic forces in permanent-magnet brushless machines with diametrically asymmetric phase windings,” *IEEE Trans. Ind. Appl.*, vol. 43, no. 6, pp. 1544–1553, 2007.
- [ZHU09] Z. Q. Zhu, “A simple method for measuring cogging torque in permanent magnet machines,” in *IEEE Power & Energy Society General Meeting*, Calgary, U.S., pp. 1-4., 2009.
- [ZHU13] Z. Q. Zhu, M. L. M. Jamil, L. J. Wu, “Influence of slot and pole number combinations on unbalanced magnetic force in PM machines with diametrically asymmetric windings,” *IEEE Trans. Ind. Appl.*, vol.49, no.1, pp.1-1, 2013.
- [ZHU97] Z. Q. Zhu, K. Ng, and D. Howe, “Design and analysis of high-speed brushless permanent magnet,” in *Proc. of Electrical Machines and Drives (EMD) Conf.*, pp. 381–385, Sep. 1–3, 1997.
- [ZWY05] C. Zwysig, J. W. Kolar, W. Thaler, and M. Vohrer, “Design of a 100 W 500 000 rpm permanent-magnet generator for mesoscale gas

turbines,” in *Conf. Rec. 40th IEEE IAS Annu. Meeting*, Hong Kong, pp. 253–260, 2005.

- [ZWY09] C. Zwysig, J. W. Kolar, and S. D. Round, “Megaspeed drive systems: Pushing beyond 1 million r/min,” *IEEE/ASME Trans. Mechatronics*, vol. 14, no. 5, pp. 564–574, Oct. 2009.

## APPENDIX I

### FROZEN PERMEABILITY METHOD

In this thesis, the frozen permeability method is employed to separate the PM and armature fields under different working conditions. In order to show the necessity of this method, the influence of different excitations on relative permeability is illustrated at first, which is shown in Fig. A1. The operation points A, B and C are excited by both PM and armature currents, only PM and only armature currents, respectively. As can be seen, with the change of excitations, the relative permeability of soft magnetic material varies significantly, of which the values at operation points B and C can be very different comparing with the resultant working point A. Consequently, if  $\mu_{PM}$  and  $\mu_{armature}$  which are the relative permeabilities under operation points B and C are used for calculating the PM and armature fields, the real saturation cannot be reflected. As a result, the frozen permeability method has to be employed.

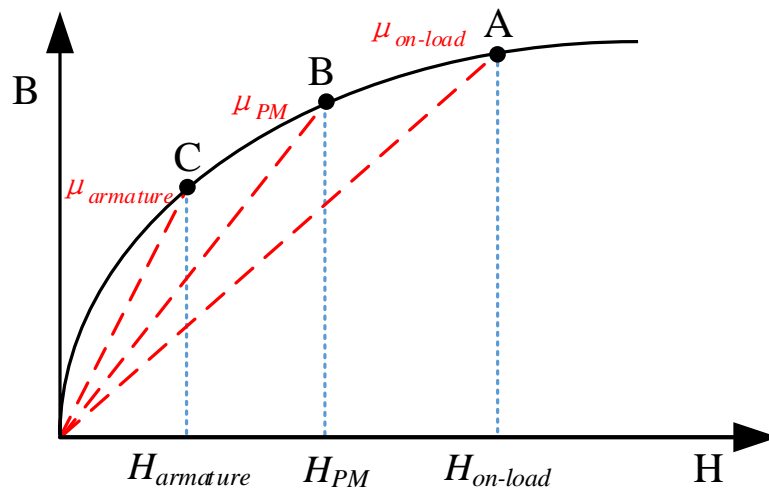


Fig. A1 Influence of different excitations on relative permeability [CHU13].

The working principle of frozen permeability method has been illustrated in many literatures [BIA98] [AZA12] [CHU13]. After the normal calculation under operation point A with non-linear soft magnetic material in finite element analysis, the permeability of each element will be saved. Then, the PM and armature currents are used as excitations separately for models sharing the same saved permeability. By this way, each magnetic fields can be separated precisely.

## APPENDIX II

### STATIC TORQUE MEASURING METHOD

The static torque can be measured by the method proposed in [ZHU09]. The schematic diagram is shown in Fig. B 1 and the test rig is shown in Fig. B 2. As can be seen, the shaft is fixed with a rigid beam by using a fixing screw. In addition, the weight locates at the end of the beam so that the beam can be kept as still when the direction of output torque is clockwise. Moreover, the spirit level should be used to keep the beam as level position. The scale is employed to measure the force in vertical direction, and the torque with specific load and rotor position can be calculated by

$$T = L_{lever} \cdot (m_{on-load} - m_{weight}) \cdot g \quad (\text{B.1})$$

where  $L_{beam}$  is the length between the end of the beam and the middle of the shaft,  $m_{on-load}$  is the reading shown on the scale when currents are input,  $m_{weight}$  is the mass of the weight and  $g$  is the gravity acceleration.

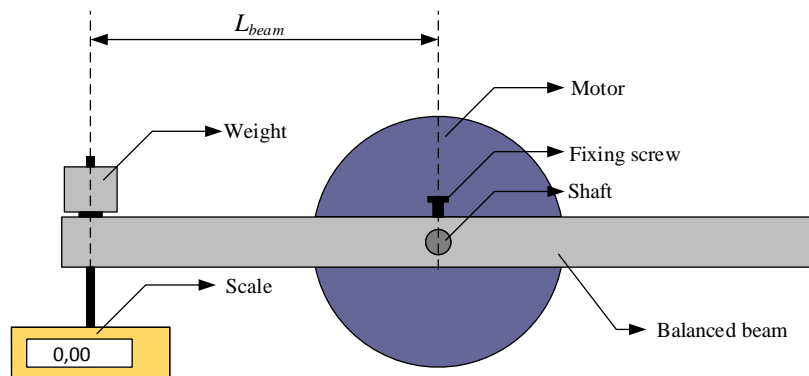


Fig. B 1 Schematic diagram of static torque measurement [ZHU09].

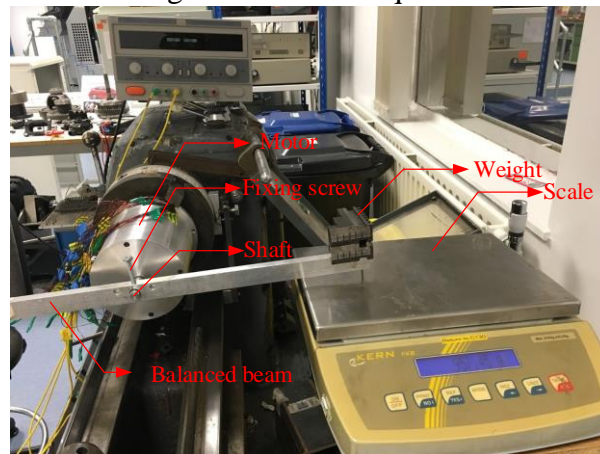


Fig. B 2 Test rig for static torque measurement.

# APPENDIX III

## CAD DRAWINGS OF PROTOTYPES

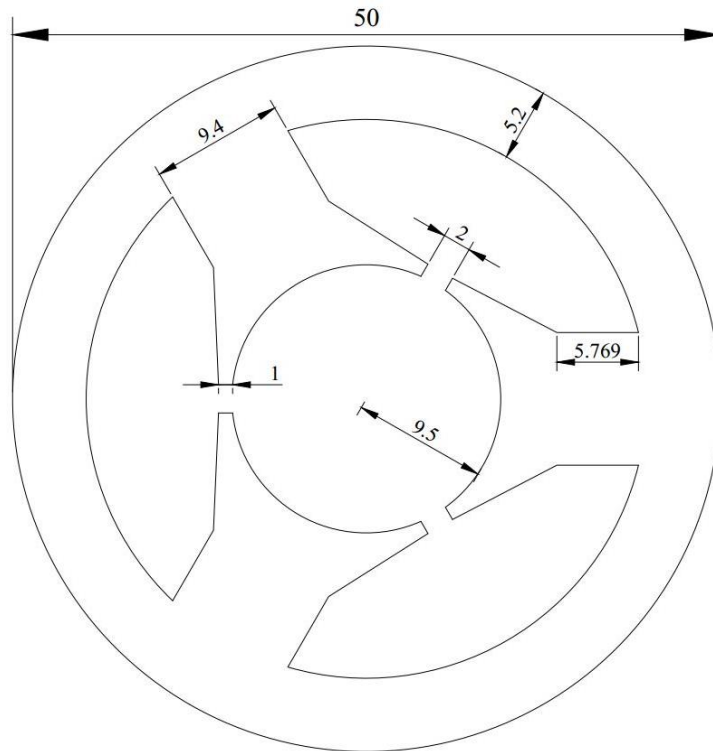


Fig. C 1 Stator lamination for conventional machine in Chapter 2.

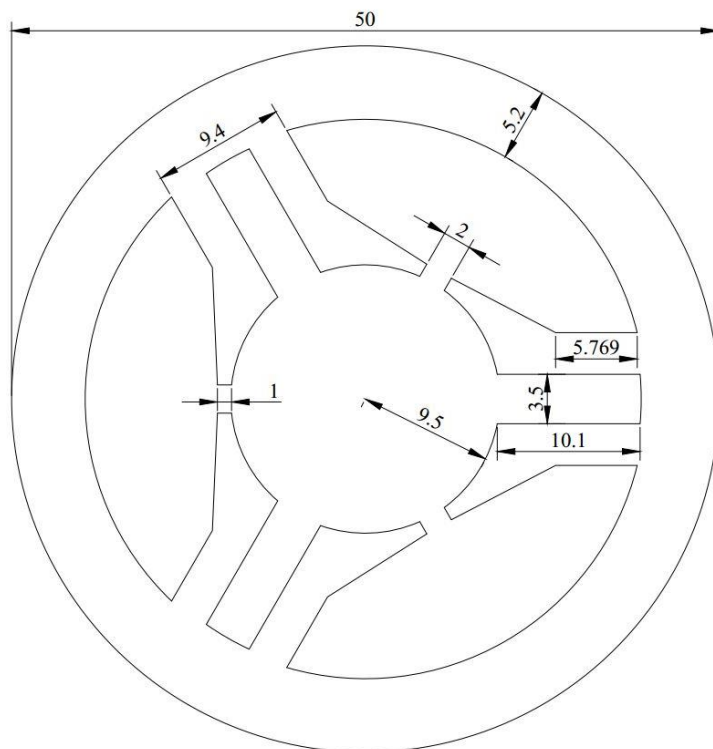


Fig. C 2 Stator lamination for Machine 2 in Chapter 2.

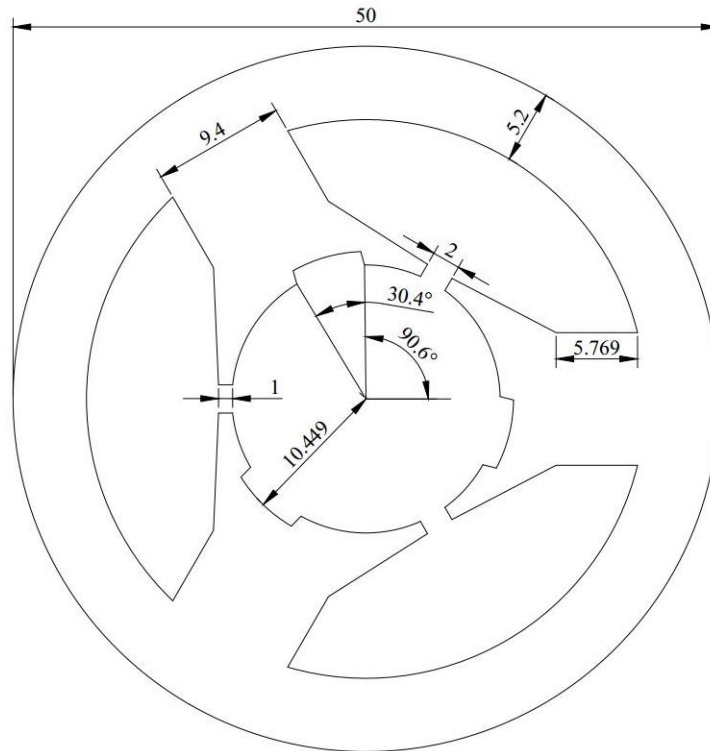


Fig. C 3 Stator lamination for Machine 3 in Chapter 2.

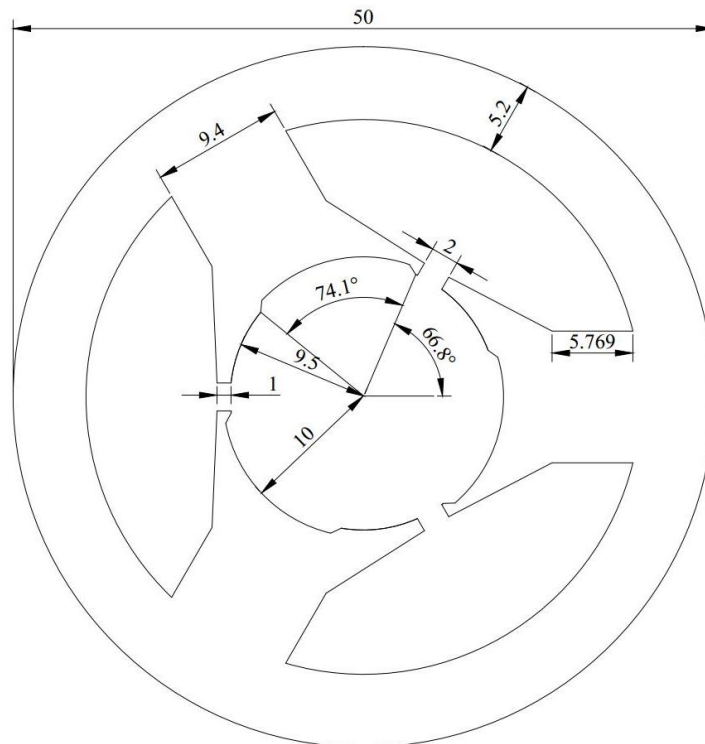


Fig. C 4 Stator lamination for proposed prototype machine in Chapter 3.



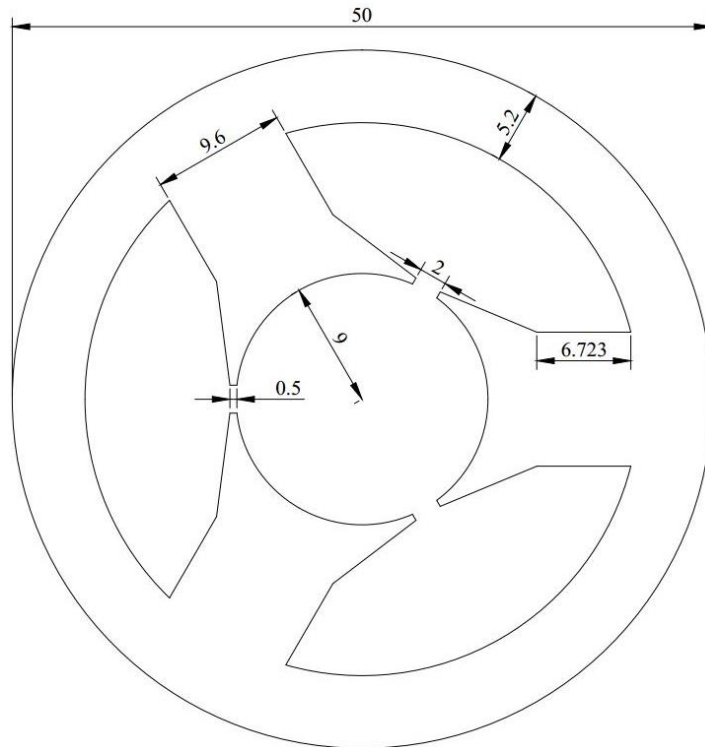
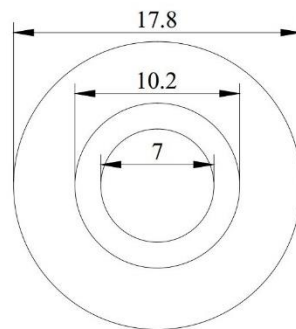
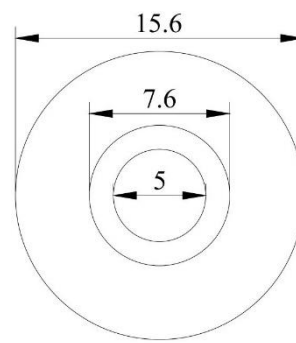
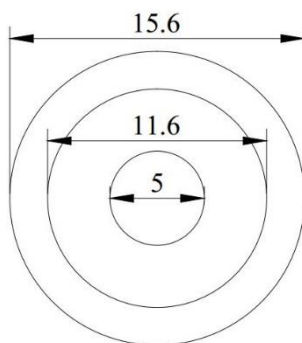


Fig. C 5 Stator lamination for prototype machine in Chapter 4.



(a) Chapter 2 and Chapter 3



(b) Chapter 4 (magnet thickness=2mm)      (b) Chapter 4 (magnet thickness=4mm)

Fig. C 6 Rotor structures for prototype machines.

## Appendix IV

### CALCULATION OF THE OPTIMAL SLEEVE THICKNESS

In this appendix, the optimal sleeve thickness will be calculated. In order to determine the optimal sleeve thickness, the stress between each rotor components, i.e. the sleeve, the magnet and the shaft, should be determined, which can be accomplished by using the displacement technique [BOR08]. The outer machine outer diameter in this appendix is chosen as 50mm. The split ratio is defined as the ratio between outer diameters of magnet and stator bore. The rotating speed is selected as 110krpm. Nevertheless, the method introduced in this appendix can be also applied on other machine size and rotating speed.

$$u_i = M_i r + \frac{N_i}{r} - (1 - \nu^2) \frac{\rho_i r \Omega^2}{8 E_i}, i = 1, 2, 3 \quad (D.1)$$

$$\sigma_{radial,i} = \frac{E_i}{1 - \nu_i} M_i - \frac{E}{1 + \nu_i} \frac{N_i}{r^2} - \frac{3 + \nu_i}{8} \rho_i r^2 \Omega^2, i = 1, 2, 3 \quad (D.2)$$

$$\sigma_{\theta,i} = \frac{E_i}{1 - \nu_i} M_i + \frac{E}{1 + \nu_i} \frac{N_i}{r^2} - \frac{1 + 3\nu_i}{8} \rho_i r^2 \Omega^2 - \alpha E \cdot \Delta T, i = 1, 2, 3$$

where  $u$  is the displacement,  $r$  is the radius,  $\rho$  denotes the mass density,  $\Omega$  indicates the mechanical angular velocity,  $E$  is the Young's modulus,  $\sigma_{radial}$  is the radial stress,  $\sigma_{\theta}$  indicates the tangential stress,  $\nu$  is the Poisson's ratio,  $\alpha$  indicates the coefficient of linear thermal expansion,  $\Delta T$  denotes the variation of temperature,  $M$  and  $N$  are the coefficients, respectively. In addition, the number of  $i$  indicates different rotor parts, the numbers of 1, 2 and 3 represent shaft, magnet and sleeve, respectively.

In order to get the value of coefficients  $M$  and  $N$ , the boundary conditions should be applied as

$$\begin{aligned} \sigma_{radial,1}(0) &\neq \infty \\ \sigma_{radial,2}(ro_1) &= \sigma_{radial,1}(ro_1) \\ u_2(ro_1) &= u_1(ro_1) \\ \sigma_{radial,3}(ro_2) &= \sigma_{radial,2}(ro_2) \\ u_3(ro_2) &= u_2(ro_2) + \delta_{fit} \\ \sigma_{radial,3}(ro_3) &= 0 \end{aligned} \quad (D.3)$$

where  $\delta_{fit}$  indicates the pre-fit. By this way, the contact pressure can be solved. However, in order to ensure the machine can work safely, the limit condition can be expressed as:

$$\begin{aligned}\sigma_{radial,2}(r_{o1}) &= \sigma_{R,lim} \quad (0 \leq \Omega \leq \Omega_{max}) \\ \sigma_{ref,3}^{vM}(r_{o2}) &= \sigma_U \cdot k \quad (0 \leq \Omega \leq \Omega_{max})\end{aligned}\quad (D.4)$$

where  $\sigma_{R,lim}$  is the maximum normal stress in the inner surface of magnet,  $\sigma_U$  is the sleeve yield stress,  $k$  is the safety coefficient which should be 0.5-0.7 [WAN07] [BIN06] and  $\sigma_{ref}^{vM}$  is the von-Mises reference stress which can be calculated by.

$$\sigma_{ref}^{vM}(r) = \sqrt{\sigma_{radial}^2(r) + \sigma_{\theta}^2(r) - \sigma_{radial}(r) \cdot \sigma_{\theta}(r)} \quad (D.5)$$

By applying the limit condition, the optimal sleeve thickness for different split ratio can be determined. In order to ease the understanding, the flowchart of optimal sleeve thickness calculation is shown in Fig. D1.

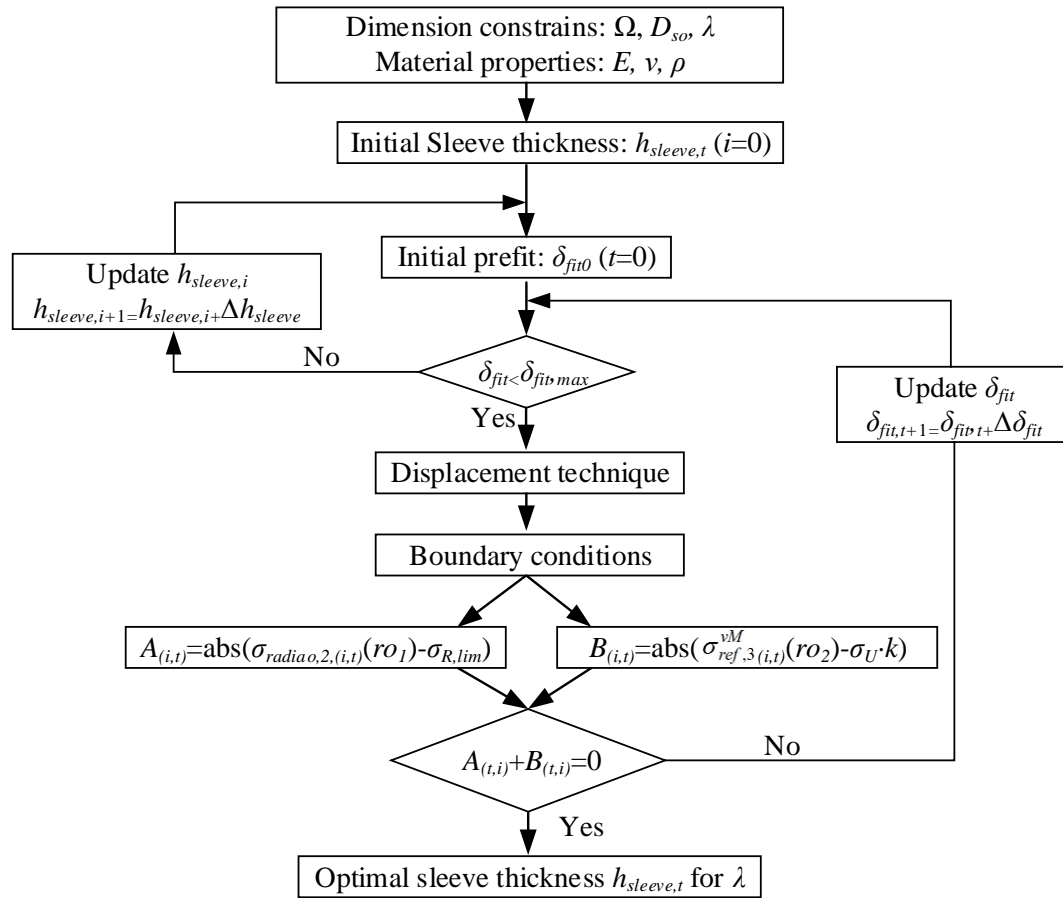


Fig. D1. Flowchart of optimal sleeve thickness calculation.

In order to show the effectiveness of the analytical method, the finite element (FE) validation for stress model under 20°C is shown in Fig. D2, in which the split ratio is chosen as 0.35 and Inconel718 is used as sleeve material. The properties of different sleeve materials are listed in Table D1. The outer radius of sleeve and the interference fit are calculated by (D.1)-(D.6) which are 9.162mm and 43.2μm, respectively.

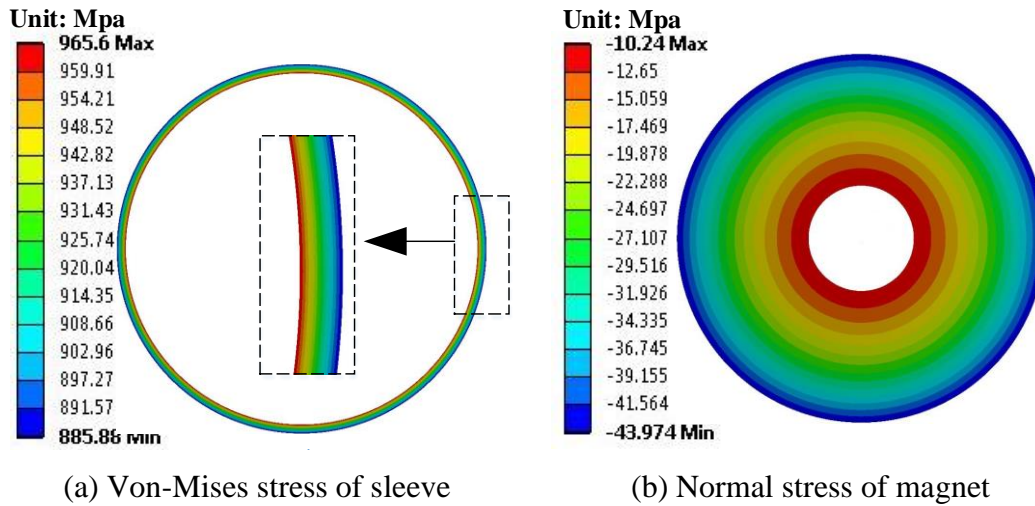


Fig. D2. FE validation.

Table D1

Mechanical parameters of sleeve and magnet materials [HUA16] [BOR10a]

	NdFeB35	Carbon fiber	Inconel 718	Stainless steel
$E$ (Gpa)	190	186	199	196.5
$\nu$	0.3	0.3	0.3	0.3
$\rho$ (Kg/m <sup>3</sup> )	8400	1550	8240	8000
$\sigma_U$ (Mpa)	-	1400	1400	505

As can be seen, the maximum von-Mises reference stress is 965.6Mpa occurring in the sleeve inner surface which has good agreement with the maximum reference stress for Inconel718 sleeve, i.e. 980Mpa. In addition, the normal stress in the inner surface of magnet is -10.24Mpa which is also very close to the chosen value, i.e. -7.5Mpa.

It should be noticed that in practice, different materials can be chosen as the sleeve material. Consequently, the influence of sleeve materials should be also studied. The variations of optimal sleeve thickness with different split ratio in machines with different sleeve materials are shown in Fig. D3.

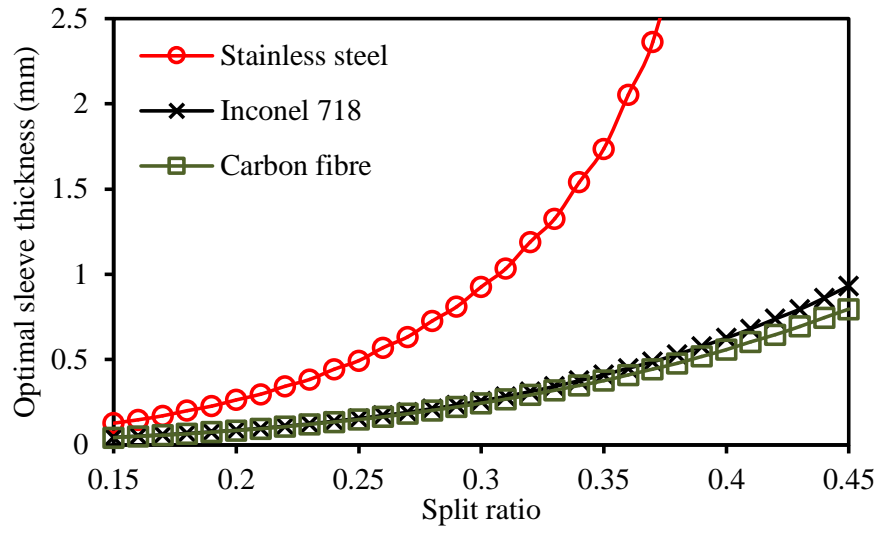


Fig. D3. Variation of optimal sleeve thickness with different split ratio.

## APPENDIX V

### PUBLICATION RESULTED FROM PHD STUDY

#### Journal Publications:

- [1] **J. Ma**, and Z. Q. Zhu, “Mitigation of unbalanced magnetic force in a PM machine with asymmetric winding by inserting auxiliary slots,” *IEEE Trans. Ind. Appl.*, vol. 54, no. 5, pp. 4133-4146, 2018.
- [2] **J. Ma**, and Z. Q. Zhu, “Magnet eddy current loss reduction in permanent magnet machines,” *IEEE Trans. Ind. Appl.*, early access, pp. 1-1, 2018.
- [3] **J. Ma**, and Z. Q. Zhu, “Optimal split ratio in small high speed PM machines considering both stator and rotor limitations,” *CES Transactions on Electrical Machines and Systems*, vol.3, no.1, pp.3-11, Apr 2019.
- [4] G. J. Li, B. Ren, Z. Q. Zhu, Y. X. Li, **J. Ma**, “Cogging torque mitigation of modular permanent magnet machines,” *IEEE Trans. Magn.*, vol. 52, no. 1, article ID: 8100210, 2016.

#### Conference Publications:

- [1] **J. Ma**, and Z. Q. Zhu, “Magnet eddy current loss reduction in a 3-slot/2-pole permanent magnet machine,” *Int. Conf. on Electric. Machines and Drives (IEMDC)*, Miami, FL, USA, article ID: 17096983, 2017.
- [2] **J. Ma**, and Z. Q. Zhu, “Unbalanced magnetic force mitigation in 3-slot/2-pole permanent magnet machines by inserting auxiliary slots” *Int. Conf. on Electric. Machines and Drives (IEMDC)*, Miami, FL, USA, article ID: 17083867, 2017.
- [3] **J. Ma**, and Z. Q. Zhu, “Effect of magnet thickness on electromagnetic performance of high speed permanent magnet machines” *Int. Conf. on*

*Electric. Machines and Drives (IEMDC)*, Miami, FL, USA, article ID: 17083861, 2017.

- [4] **J. Ma**, Z. Q. Zhu, and Lijian Wu, “Influence of slot/pole combination and magnet thickness on unbalanced magnetic force in PM machines with different rotor eccentricities and magnetizations,” *2017 20th Int. Conf. Electrical Machines and Systems (ICEMS)*, Sydney, Australia, article ID: 17239577, 2017.